RAY, Dipak Kumar, 1933-

GEOCHEMISTRY AND PETROLOGY OF THE MT. TRIDENT ANDESITES, KATMAI NATIONAL MONUMENT, ALASKA.

University of Alaska, Ph.D., 1967
Geology

University Microfilms, Inc., Ann Arbor, Michigan

GEOCHEMISTRY AND PETROLOGY OF THE MT. TRIDENT ANDESITES, KATMAI NATIONAL MONUMENT, ALASKA

A

DISSERTATION

Presented to the Faculty of the

University of Alaska in Partial Fulfillment

of the Requirements

for the Degree of

Doctor of Philosophy

by

Dipak Kumar Ray, B.Sc., M.Sc.,

College, Alaska

May, 1967

GEOCHEMISTRY AND PETROLOGY OF THE MT. TRIDENT ANDESITES,

KATMAI NATIONAL MONUMENT, ALASKA

APPROVED:

Carl E. Benson

W. Bly

W. Dean Pilkington

D. C. Burnell

Robert B. Forbes
Chairman

Department Head

APPROVED: Earl A. Beistline DATE January 6, 1967
Dean of the College of Earth Sciences
and Mineral Industry

G. Rae

Vice President for Research and
Advanced Study

ABSTRACT

Five andesite flows were erupted from the new vent of Trident Volcano, Katmai National Monument, Alaska, during the period 1953-1963. The recent lavas are olivine bearing two pyroxene andesites.

Bulk chemical analyses show that these andesites are more highly siliceous than typical andesites erupted by circum-Pacific orogenic volcanoes, and perhaps transitional to dacites. The range in wt.% of SiO_2, FeO and Fe_2O_3 of all andesites in the series is greater than that determined by several specimens from one flow (1958), but the comparative variation in wt.% of Al_2O_3, MgO, CaO, Na_2O and K_2O is not significant.

Coexistent plagioclase (phenocrysts and groundmass), pyroxenes, magnetite and groundmass glass were successfully separated and analyzed from six representative andesites. X-ray diffraction analyses were done on the pyroxene and magnetite phases, and unit cell parameters, volumes and packing indices were derived.

The Si-Al content of Trident clinopyroxenes is similar to that of clinopyroxenes from alkali basalts. The coexistent orthopyroxenes are Ca-rich (wt.% CaO = 2.63 - 6.89). Reinterpretation of experimental phase equilibrium data seems to support the stability of high-Ca orthopyroxene in volcanic rocks. Phenocrystal and groundmass plagioclase plus groundmass glass display sympathetic compositional variations, which indicate a cognate origin for the phenocrysts.

From mineral phase and bulk chemical data the Trident andesites are considered to be a differentiated sequence from a parental magma, which was slightly undersaturated in silica. Some differentiation seems to have occurred in the magma reservoir during two periods before each of the two

eruptive sub-cycles of 1953-1954 and 1957-1963. Chemical variation in the mineral phases and bulk composition was dominantly controlled by high partial pressure of oxygen, which is expressed in compositional trends throughout the suite. High partial pressure of oxygen encouraged the development of the jadeite molecule in clinopyroxene and the sub-solidus oxidation of magnetite to maghemite. Plagioclase crystallization appears to have been rapid under these conditions; and coexistent orthopyroxene, which crystallized later in the sequence, contains Ca-Tschermak's molecule. Cyclic pre-eruption increases in water pressure, to the detriment of partial oxygen pressure, seem to have been responsible for the bulk compositional variation within a single flow unit (enrichment in iron and alumina). Pyroxenes which crystallized under these conditions were characterized by the presence of Ca-Tschermak's molecule in the monoclinic, and the jadeite molecule in the orthorhombic members. Plagioclase and magnetite crystallization was retarded, and magnetite sub-solidus oxidation was from ulvöspinel to magnetite.

The proposed parent magma would have high-alumina and alkali basalt affinities. Such melts could be derived from the partial fusion of basaltic layer at the base of the crust. Undersaturation vs. saturation in respect to silica, in such melts, may be controlled by temperature and pressure gradients along the base of the crust from the oceanic to stable continental areas, and the Andesite Line could be an expression of this relationship.

TABLE OF CONTENTS

LIST OF TABLES

LIST OF ILLUSTRATIONS

LIST OF PLATES

CHAPTER I

INTRODUCTION

LOCATION OF STUDY AREA

Mt. Trident (58°13'42" N: 155°07'16" W), located in Katmai National Monument, Alaska, is one of several active volcanoes located in the Aleutian Range of the Alaska Peninsula (fig. 1). The volcanoes of the Alaska Penninsula (fig. 2) represent the northeastern continental extension of the arcuate volcanic belt of the Aleutian Archipelago. The new vent which led to the development of the cone and flows, discussed in this paper, was initiated on the south flank of ancestral Mt. Trident in 1953.

HISTORIC VOLCANIC ACTIVITY IN THE KATMAI AREA

Katmai Eruption of 1912

Mt. Katmai erupted violently on June 6, 1912, and for several days thereafter, covering the area with heavy ash and pumice falls. During this period the now-famous ash flow was deposited in the valley north of Katmai Pass, thus creating the Valley of Ten Thousand Smokes (Griggs, 1922). Griggs and Fenner (1923) believed that the deposition of ash flow preceded the main Katmai eruption, while Williams (1954) and Curtiss (1955) are of the opinion that the Novarupta vent was the chief center of activity. Fenner (op.cit.) estimated the total volume of erupted pyroclastics (including the ash flow) at 1 mile^3.

The pre-historic and recent lavas and pyroclastics erupted from Mt. Katmai and the neighbouring volcanoes, Mts. Mageik, Martin, Knife Peak and Novarupta volcanoes were studied by Fenner (1920, 23, 26 and 50).

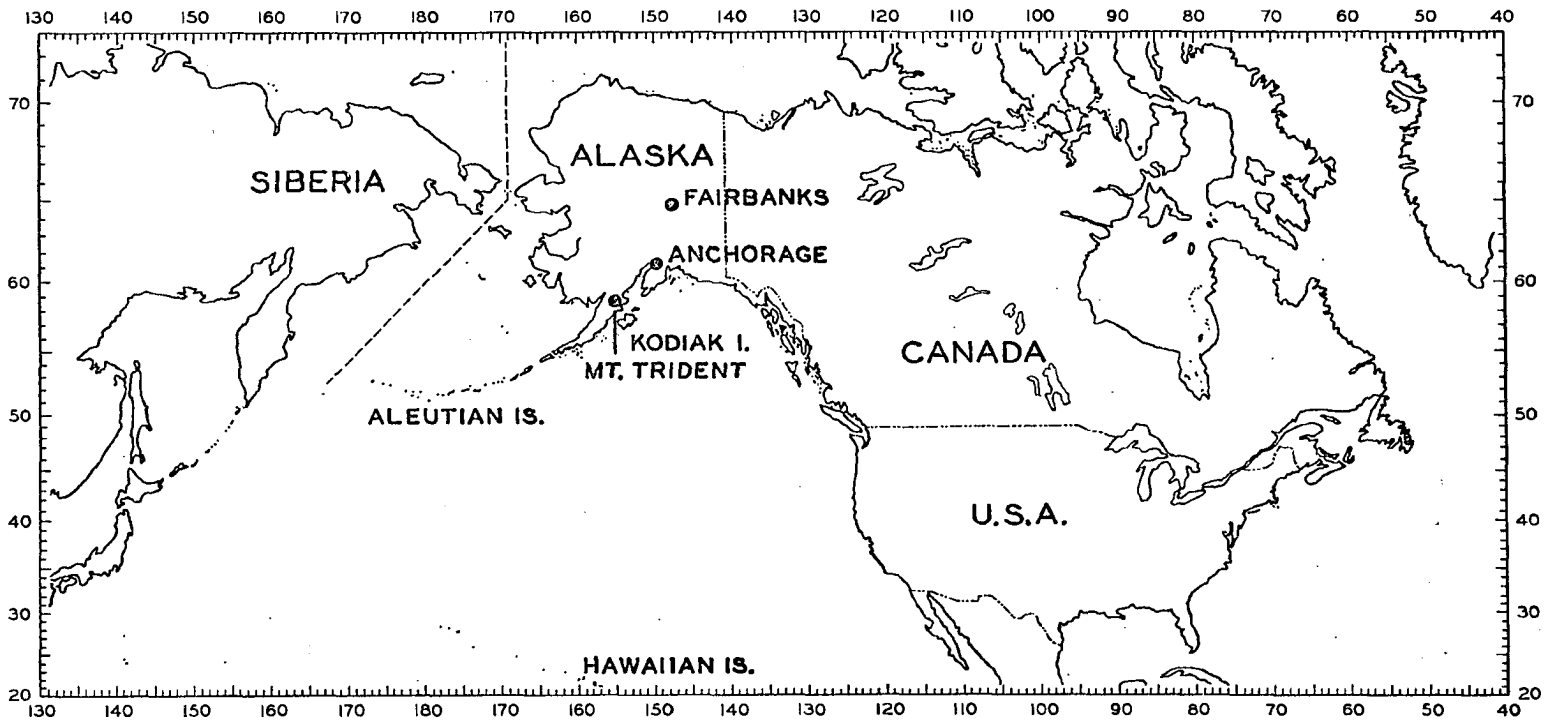

Fig. 1. Map of N. America showing location of Mt. Trident, Katmai National Monument, Alaska.

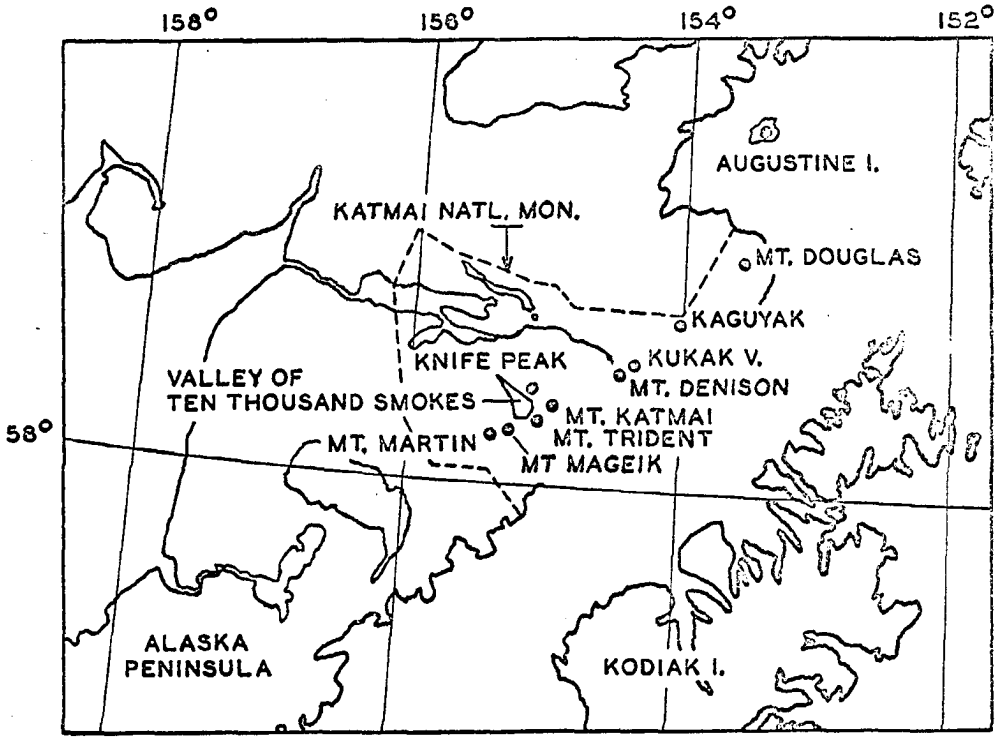

Fig. 2. Map of the Northeastern Alaska Peninsula showing volcanoes of the Katmai group.

His conclusions,as taken from several papers, are:

(1) The composition of the 1912 Katmai magma was highly siliceous (SiO_2 - 76.53%). Earlier lavas (pre-historic?) were distinctly andesitic to dacitic in composition (Fenner, 1926, pp. 695, 676, 685),

(2) The Katmai volcanic suite displays consanguinity (Fenner, op.cit., p. 771),

(3) The linear trends defined by the variation of major chemical components do not correlate favorably with the trends of Bowen, and Fenner (ibid. p.,772) questioned the validity of crystallization differentiation in the genesis of rock types in the Katmai volcanic suite.

Fenner (ibid.) also challenged the importance of crystallization differentiation as a universal process in the evolution of the basalt-andesite-dacite-rhyolite series of the orgenic volcanoes. He believed that other mechanisms were important such as assimilation-contamination (1923, p. 61); and he presented strong evidence for the digestion of old lavas in the new magma (ibid.,p. 59) as seen in the structure of layered pyroclastics. Later, he was also convinced that a considerable volume of basic volcanics had been partially assimilated by acid magma (1950, p. 724).

Fenner (1920, p. 569) has also noted that the more recently erupted lavas of the Aleutian volcanic chain are basic andesites in contrast to the rhyodacitic lavas and pyroclastics of the 1912 eruption of Katmai. It would appear that this trend is continuing, as all known post-1912 eruptive products have been andesitic.

Eruptions of Mt. Trident

Reliable records are not available for the volcanic activity of Mt. Trident prior to 1953. Since 1953 Mt. Trident has been the most active volcano in the Katmai area. A resume of the Trident eruptive history is given in table 1. The 1953 eruption was the best documented event and information about the other events have been obtained from reports from U.S. National Park Service rangers, sporadic air reconnaissance missions and chance observations from both military and private sources. A summary of available information on the volcanic activity of Mt. Trident is given in Appendix I.

The lava flows and block avalanches were mapped and studied during the field investigations of 1965 and 1966. Areas occupied by lava and blocks are shown in fig. 3. The map shown as fig. 3 includes modified flow boundaries as previously shown by Decker (1963).

Based on documentary reports (Appendix I) and field investigations the sequence of eruption of the lavas and the block avalanches appear to be as follows:

(1) February, 1953 - June, 1954 flow,

(2) Block avalanche (?) 1954-57

(3) 1957 flow,

(4) 1958 flow,

(5) 1959-60 flow,

(6) August, 1960 overflow and

(7) April, 1963 blocky avalanche.

For the sake of brevity the above units are referred to hereafter as (i) 1953 flow, (ii) 1954 blocks, (iii) 1957 flow, (iv) 1958 flow, (v) 1959 flow, (vi) 1960 flow and (vii) 1963 blocks. Specimen localities

Table 1

Eruptive History of Mt. Trident

July, 1951	Aerial photos showed linear fumarole line near site of 1953 vent.
February 15, 1953	30,000 ft column of ash and gas.
February 18, 1953	Vent on Mt. Trident situated at about 3,600 ft on the south west flank; blocky lava flow over an area of 800 x 700 ft.
June 17, 1953	Lava flow continued.
June 30, 1953	Activity reduced to an ash plume only.
June 18, 1954	Lava flow increased in size.
August, 1957	Left arm flow complete, must have originated earlier.
September, 1958	New lava flow partially over-riding 1953-53 flow.
Winter (?), 1959	Right arm flow, in place by August, 1960.
August 10, 1960	Two successive gas blow-offs; 20,000 ft vapor-ash column; lava blocks thrown 1000 ft or more; carapace formed and destroyed; reconnaissance showed flow which was emplaced during winter 1959-60.
June 30, 1961	Suspected gas and ash blow-out; later reconnaissance detected plug in vent.
January, 1962	Cone diameter had doubled.
June 10, 1962	20,000 ft ash-charged vapor column; plug blown out, and new crater formed.
April 1, 1963	40,000 ft ash and gas column; crater cleaned out,ash fall.
May 31, 1964	Mushroom cloud erupted to over 20,000 ft; ash fall-out zone to west; pyroclastic debris in Mageik valley; cone breached.

are shown in fig. 3. Descriptions of the lavas and the hand specimens are discussed in Chapter II (Petrography). A sketch, shown as fig. 4 shows the lavas and the location of the specimens, selected for geochemical studies.

Activity State of Mt. Trident as Observed during Field Investigation of 1965 and 1966.

During the summer of 1965 attempts to visit Trident crater were repeatedly beaten back by high winds and poor visibility. Incomplete reports on volcanic activity in the area can be principally blamed on poor accessibility and bad weather. A camp established above Katmai Pass (with Dr. R. B. Forbes and Mr. Jürgen Kinele) was demolished by gale winds on July 7; and the area was not visited until July 25, 1965.

During the month of July, 1965 all lava flows were degassing and fumaroles were abundant. The eastern rim of the crater was cut by fissures which were emitting gas (predominantly water vapor) at high pressure (see plate 1a). The crater and the cone did not show much change from the descriptions given by Decker (1963), with the exception of the fissures and the presence of an incipient plug in the vent. Sulphurous fumes were strong within the crater. The southwestern rim of the crater was covered with a number of blocks (source of specimen 'TC'). The maximum depth of the crater was around 75 ft and the plug was about 10 ft high.

On August 24, 1966, it was noted that the plug had risen to a height of about 50 ft. Earlier in the field season it was about 15 ft high (verbal communication - Mr. J. Kienle). Plate 1b shows the character of the plug during the last week of August, 1966. Gas activity

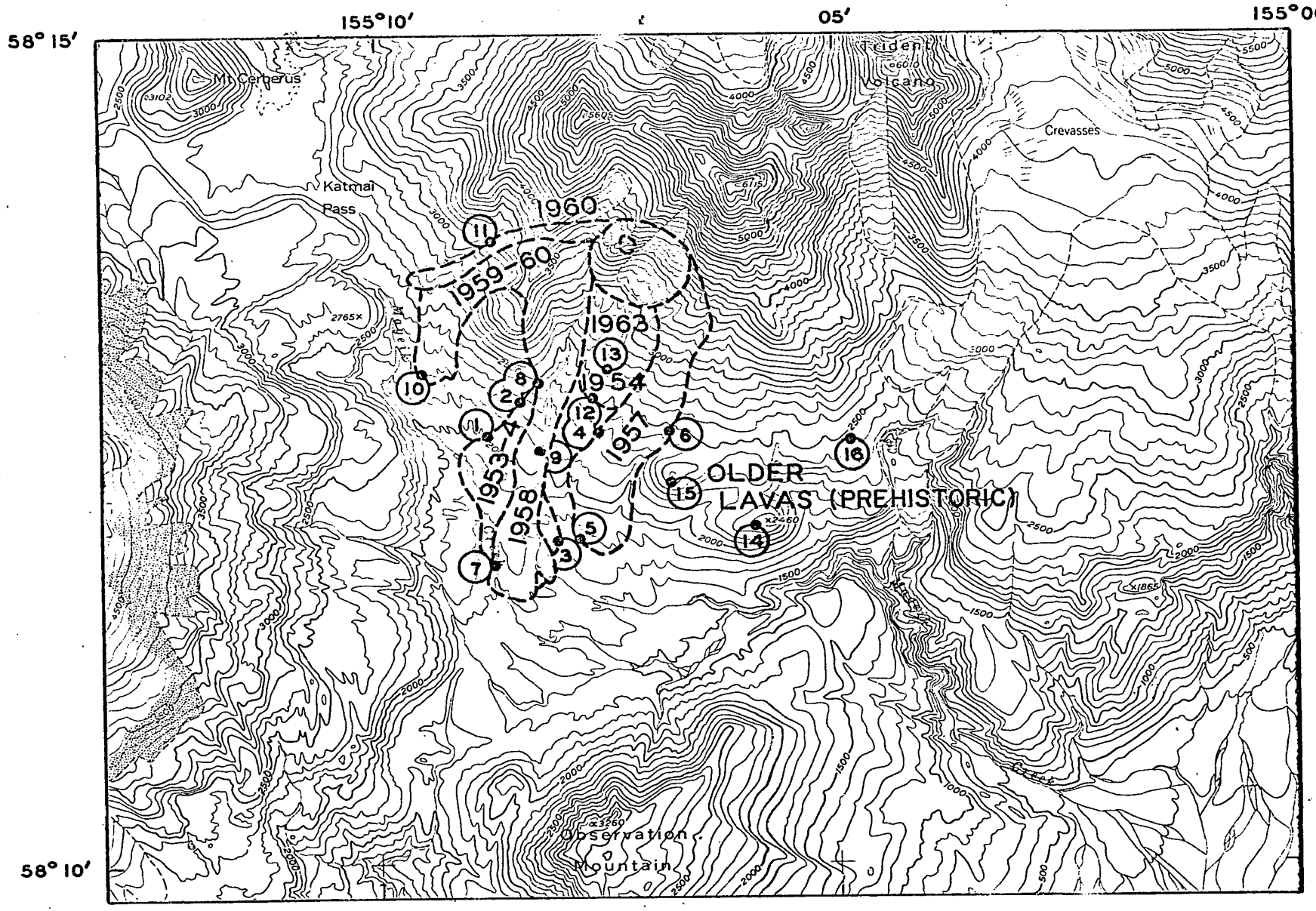

Fig. 3. Map of Mt. Trident showing the location of the cone, recent lavas and block avalanches (circled numbers indicate specimen localities), scale - 1:63,360. (Taken from U.S. Geological Survey topographic map, Mt. Katmai, A-4, Quadrangle).

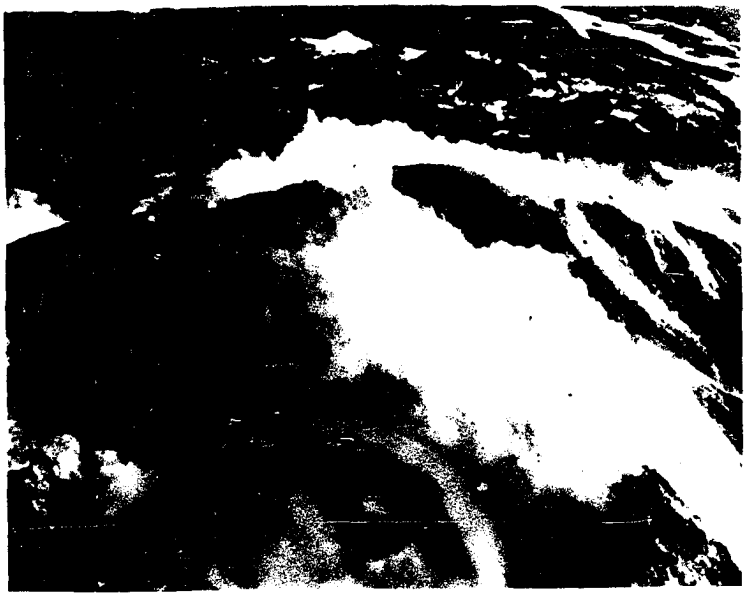

Plate 1a. Aerial view of the rim of the crater showing intense fumarolic activity (July, 1965).

Plate 1b. The enlarged plug, Trident crater, August, 1966 (Photo - Capt. S. Silber, U.S.A.F.).

in the crater was of much greater intensity than noted during summer, 1965. During July and early August, 1966, there were sporadic eruptions of smoke and ash (verbal communication - Mr. and Mrs. J. Kienle, Geosphical Institute, College, and P. Molnar, Lamont Geological Observatory).

Since 1959-60, the activity of Trident valcano seems to have undergone a profound change. Decker (op. cit., p.39) commented that after 1959-60 volcanic activity consisted of one or more explosive eruptions each year which destroyed the spine and the lava dome, producing peripheral fall out lobes of ash and fragments. There have been no lava flows since 1960. Recent observations agree with this trend. The material errupted in 1963 consisted largely of blocks and (bread-crust bombs). The development of plugs commenced after the cessation of lava flows.

Activity of Neighboring Volcanoes during June-August, 1965 and August, 1966.

June-August, 1965: The crater of Mt. Mageik continued to discharge steam throughout the whole period. Mt. Martin displayed intermittent vapor plumes. The huge plug occupying Novarupta crater was degassing slowly, and the solfatara field on the west rim of the crater showed the usual activity. Several mildly active fumaroles were observed on the west slope of Mt. Trident. A new fumarole field has been observed on the west flank (at about 7,000 ft) of Mt. Griggs (Knife Peak), which includes at least 7 vents. Two of these are discharging gas under considerable pressure; and sulphur stains are abundant around these vents. Kaguyak volcano was quiet. Fumarolic activity in the Valley of Ten Thousand Smokes is restricted to the west flank of Baked Mountain, the saddle between Baked and Broken Mountains, Broken Mtn. and the ridge between Broken Mtn. and Novarupta.

August, 1966: Volcanic activity in the Katmai area was similar to that observed in 1965. The fissure fumaroles on Mt. Griggs were less active than observed in 1965.

REGIONAL GEOLOGY AND TECTONIC SETTING

Contributions to the general geology of the Katmai area, other than the 1912 eruption date back to 1898 (Spurr, 1900). Recurrent U.S. Geological Survey field work in the area continued up to 1953, when the survey completed a 1:250,000 scale reconnaissance geological map of the area. A compilation of previous and recent work is contained in U.S. Geological Survey Bulletin 1058-G (Keller and Reiser, 1959).

Late Jurassic (Naknek Formation), late Cretaceous (Kaguyak Formation) and Eocene sedimentary rocks are exposed throughout most of the area. A NE-SW trending fault separates the Mesozoic and Cenozoic sediments from Lower and Middle Jurassic dioritic intrusive complex to the northwest. The latter are associated with some pre-Middle Jurassic sediments and crystalline schists in the western part of the Katmai area. Tertiary and Quaternary andesite-dacite and basalt volcanic piles overlie the Jurassic and Cretaceous sediments along the volcanic belt. Tertiary sediments (Kenai Formation of Eocene (?) age) and Eocene volcanics (with associated hypabyssal intrusives) are exposed in the eastern part of the area (fig. 5) eastwards to the Shelikof Strait.

Tertiary volcanism in the area was predominantly basaltic (Bordet, 1963, op. cit., p. 12); and was manifest along two NE-SW trending zones. Recent volcanism (predominantly andesitic) is concentrated in the more eastern one of the two zones.

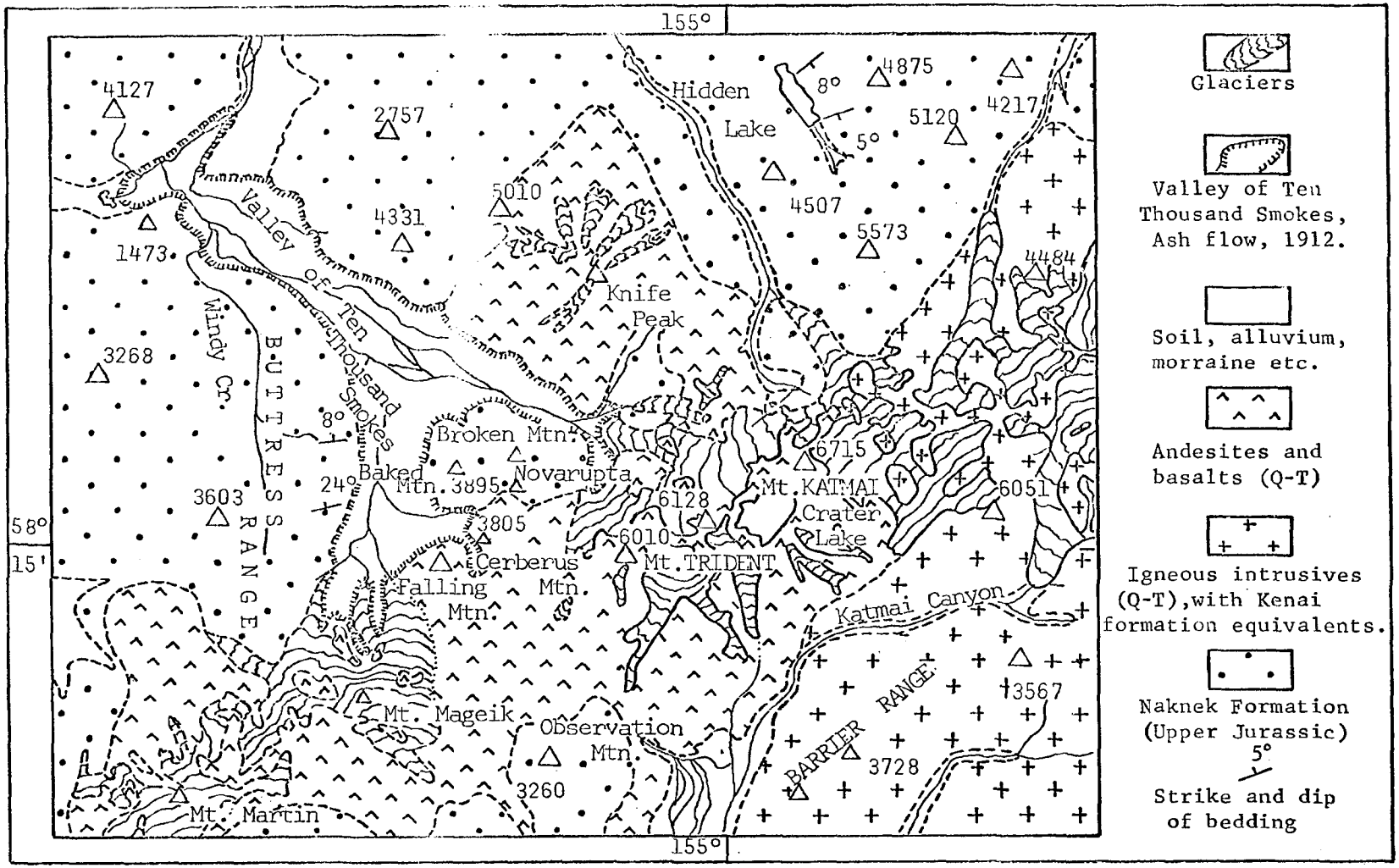

Fig. 5. Geological Map of Katmai area, modified after Keller and Reiser (1959), scale - 1: 250,000.

The basal unit of the Naknek Formation is a conglomerate which is overlain by 6,000-9,000 ft of fossiliferous sandstone, siltstone, conglomerate and shale; and these units form the sub-volcanic basement of the volcanoes. The Kaguyak Formation is composed of a basal succession of 2,000 ft of fossiliferous siltstone, overlain by sandstone, siltstone and shale (± 1,090 ft); and upper units of littoral sandstone and siltstone (± 1,460 ft).

The Tertiary sequence is largely continental and coal-bearing. The regional trend is NE-SW; and the tendency toward a gentle SE regional dip is occasionally disturbed by mild and broad anticlinal and synclinal warps.

Marine transgressions occurred during late Jurassic and late Cretaceous time; and the major regression was of Eocene age. A major orogenic event between Eocene and Pleistocene ages has been proposed by Keller et al (op. cit., p. 261).

A fairly comprehensive summary of regional tectonics has been given by Payne (1955). The following are the relevant geologic data pertaining to the Katmai area, as gathered from Payne and other sources (fig. 6).

The principal tectonic units of southwestern Alaska are expressed as alternating 'geanticlines' and 'geosynclines'. The sequence includes from NW to SE, the Talkeetna geanticline, Matanuska geosyncline, Seldovia geanticline and Chugach geosyncline. The Shelikof and Cook Inlet troughs lie between the Matanuska and Seldovia structures, while the Chugach geosyncline is flanked on the southeast by the Shumagin, Middleton and Yakataga troughs. The Talkeetna geanticline is overlapped on the south by the Nushagak basin. The Katmai volcanic chain is located on the margin of the Matanuska and Shelikof structures.

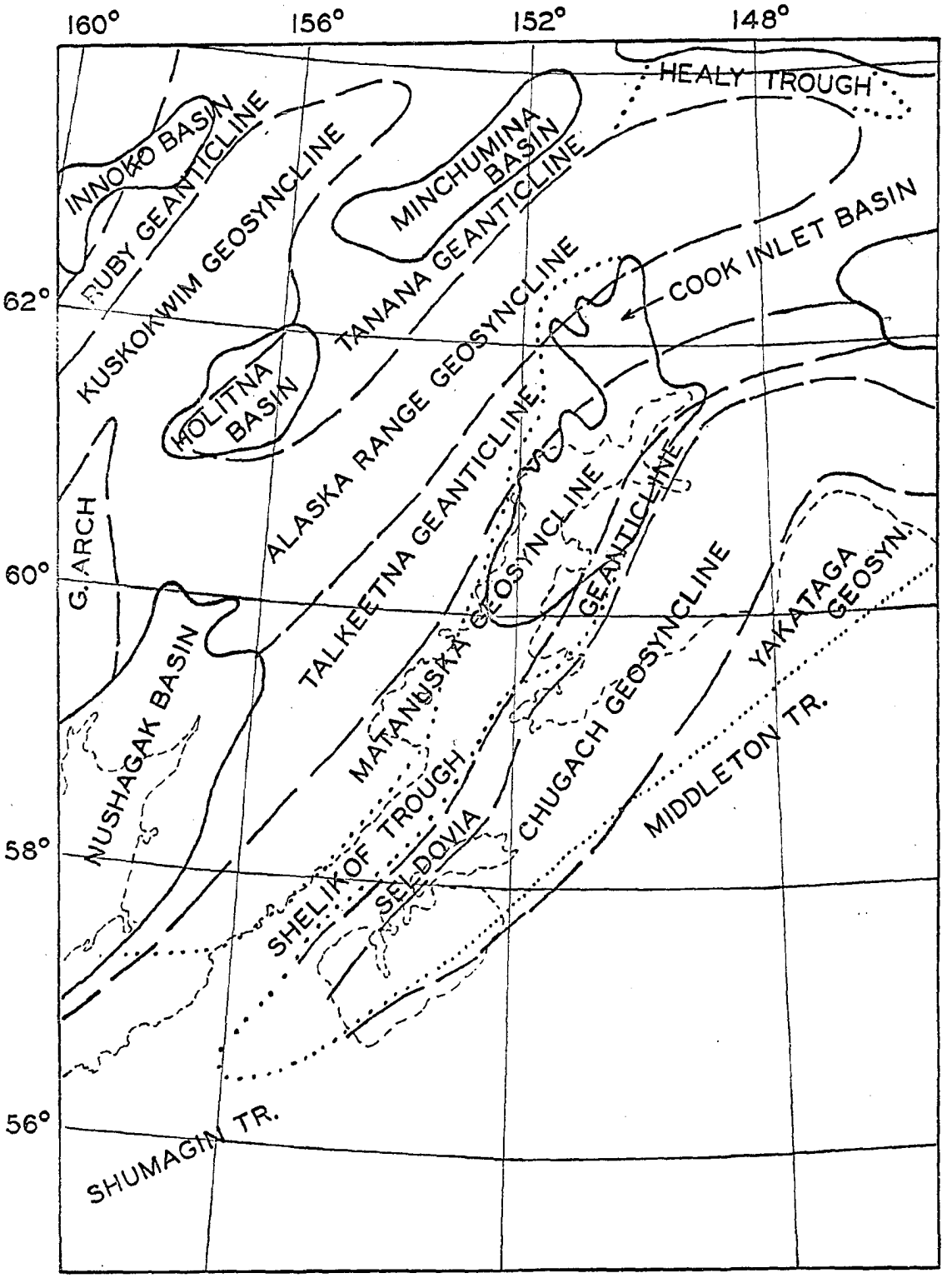

Fig. 6. Principal tectonic units of southwestern Alaska (generalized after Payne, 1955), scale - 1:5,000,000.

Payne's 'geanticlines' and 'geosynclines' are similar to the intrageanticlines and intrageosynclines of Beloussov (1962, pp. 301-2) or ridges and furrows of Aubouin (1965, pp. 39-40). The deformation of the Seldovia and Talkeetna geanticlines has been correlated with the Nevadan orogenic events leading to the development of the Matanuska and Chugach geosynclines. Laramide or time-equivalent orogenic events led to the uplift of the Matanuska and Chugach geosynclines, which was followed by the development of the Nushagak, Shelikof-Cook Inlet, Shumagin, Middleton and Yakataga depressions. Pliocene (? Pacific) orogenesis initiated the uplift of the former Shelikof-Cook Inlet and Yakataga troughs. Burk (1965) in his comprehensive account of the geology and tectonics of the Alaska Peninsula, does not recognize any typical geosynclinal sedimentation in these areas beyond the Cretaceous. According to Payne (op.cit.) and Burk (op. cit.) the history is as follows:

(1) Eugeosynclinal sedimentation ceased by Cretaceous time.

(2) Late tectonic volcanism (basalt-andesite) commenced in the Matanuska furrow in the Eocene, pari passu, with the waning orogenesis.

(3) The Shelikof marginal depression was uplifted to the maximum during orogenesis and andesitic volcanism commenced in the Quaternary east of the present volcanic belt.

(4) Migration of late-tectonic/post-tectonic volcanism toward WNW with successive consolidation of the tectonic units.

(5) Marginal andesitic volcanism accompanying the post-Laramide consolidation.

(6) Post-Pliocene eugeosynclinal subsidence has probably migrated to the southeast.

As suggested above volcanism in the Katmai chain is probably related to a period of waning orogenesis which commenced in Pliocene or later time.

THE ANDESITE PROBLEM

Sixteen years have elapsed since C. E. Tilley (1950, p. 59), concluded an address to the Geological Society of London, with remarks on the status of the andesite problem at that time:

> "In the field of volcanic petrogenesis no more pressing problem awaits intimate investigation than this - the study of geochemistry and the chemical variation within the basalt-andesite suites of the orogens, and in particular the systematic attack on their phase chemistry, phenocryst and groundmass mineral and vitrous residuum alike - for it is from such research, in cooperation with field investigation, that we may acquire the data requisite to solve the status of voluminous andesite of the orogen, and of intermediate magma, effusive or deep-seated, in igneous rock evolution."

Various mechanisms had been proposed to explain the petrogenesis of andesite.Holmes (1932), Daly (1933) and Fenner (1948) had suggested modes of origin ranging from the basification of granitic melts and allied processes, to the mixing of immiscible magmas and the assimilation of crustal rocks by basaltic magmas.

Essential differences between basalt (iron enrichment) and andesite trends (iron depletion) of fractionation were defined and attributed to compositional differences in the parental magma by Tilley (op. cit.,p. 54), although the possibility of intermediate parental magma types was discussed. Tilley (op. cit., p.54) appears to favor a genesis involving parental basaltic magma.

During the period 1950-54 Kuno (1950, p. 993; 1952, pp. 229-230; 1953, p. 270; 1954a, pp. 242, 261-264) favored the generation of andesitic magmas both by fractionation and sialic contamination of andesites of basaltic melts. The pigeonitic and hypersthenic series of the Hakone District, Honshu, Japan, according to Kuno, were produced respectively

by the fractional crystallization and fractional crystallization + sialic contamination of a high alumina tholeiitic basalt magma. In a world-wide study of the chemical composition of andesites, Nockolds and Allen (1953, p. 139) proposed that primitive or parental andesite magmas were basaltic andesite, with an average silica content of 53-54%. Waters (1955, pp. 712-714) pointed out the possibility of an intermediate magma type generated by differential crustal fusion, to explain the basalt andesite-dacite-rhyolite suite of effusives. Laboratory experiments conducted by Osborn (1959, p. 634) showed that both tholeiitic basalts and members of the calc-alkali series could be derived from a parental olivine-tholeiite magma under varying oxygen partial pressure in the stable and mobile zones of the earth's crust.

Several aspects of the andesite problem deserve additional comment. Andesites appear to prefer the mobile belts and they characteristically occur in the late to post-orogenic phases of such belts.

True andesites are allegedly absent from the volcanic suites of the intraoceanic archipelagos, - an empirical observation, which led Marshall to define the 'Andesite line'. The circum-Pacific belt of orogenic andesitic volcanoes is coincident with island arcs, and orogenic belts which lie along continental margins and peninsulae. Andesites dominate the rocks of the circum-Pacific volcanic belt as shown by the comparative volumetric data given below, as computed by Daly, and cited by Tilley (op. cit., p. 50).

Rhyolite - 22%,
Pyroxene andesites - 41%,
Other andesites - 4%,
Total andesites - 45%,
Basalt - 32% and
Rest - 1%.

Not much is known regarding regional variations in the bulk composition of andesites. Circum-oceanic belts of andesitic volcanism are also underlain by zones of unstable crust and upper mantle as shown by their high seismicity. Here, crustal structures may be undergoing the most significant changes. Thus, andesite magmas are significantly associated with epicontinental orogenic belts and the zone of transition from continental to oceanic crust. Detailed discussions on andesites from circum-Pacific (Japan, Kuno, op. cit.) and epicontinental mobile belts (Larsen, 1936, 1938) are available, but data on andesites from transitional peninsular areas are meager and/or inadequate. Consequently the andesite lavas of Mt. Trident are of particular interest.

After many years of neglect, the andesite problem has been attracting increasing interest. Kosminskaya, et al (1963, p. 11) and Shor (1964, p. 21-23) have indicated the absence of continental crust under some of the island arcs of circum-Pacific island arcs (Kuriles and Aleutians), where andesites abound. Compston (cited in Taylor and White, 1965) has pointed out the low initial strontium isotope ratios of many andesites. Green and Ringwood (1966, p. 105) have demonstrated that 50% partial melting of eclogite under dry conditions at 25-40 kb produces a melt of andesitic composition. Derivation of the calc-alkali series of rocks from the partial melting of eclogites at depths of 100-140 km has been suggested by the same authors. All of these contributions should be tempered by the fact that undersaturated analogues of andesites do occur in both continental and oceanic provinces.

PLAN OF RESEARCH, TRIDENT ANDESITES

The new cone, lava flows and/or block avalanches of Trident volcano represent a ten year span of activity. This suite offers a unique opportunity for the chemical and mineralogical studies of 5 sequential andesite lava flows, erupted from a common vent over a very short period of time (1953-1960).

No other known Pacific rim locality other than Paricutin volcano (Wilcox, 1954) has offered analogous opportunities for the study of such flows in regard to their genesis as separate "batches" of melt vs recurrent pulses of magma from a parent reservoir. The recent age of the flows and the transitional structural and petrogenetic setting are of additional importance.

Field work was chiefly done during the summer of 1965, and a brief recheck of field relations was accomplished during August, 1966. During the 1965 field season, the field relations of the cone and flows were studied, and specimens were collected for geochemical and petrological studies. The activity state of Trident and other volcanoes in the area was also monitored.

Laboratory research included the following investigations of:

(1) The comparative mineralogy and bulk chemistry of the Trident eruptive phases.

(2) The comparative chemistry of the constituent crystalline and glass phases of the andesites with particular attention given to the lattice structure and chemistry of coexisting pyroxenes.

(3) Mineral paragenesis, phase relations and physiochemical chemical parameters effecting the genesis and crystallization of the Trident andesites.

(4) Application of the above data to the theoretical aspects of the "andesite problem", and the genesis of andesites in orogenic belts.

ACKNOWLEDGEMENTS

The supervision and guidance received from Professor R. B. Forbes, Geology Department and Geophysical Institute, University of Alaska, during the course of this work is hereby acknowledged with a deep sense of gratitude and indebtedness. Help received from Drs. C. Benson and E. Berg (Geophysical Institute), H. D. Pilkington (Geology Department) and D. Burrell (Institute of Marine Sciences) through discussions and critical reading of the thesis is gratefully acknowledged. Thanks are due to Dr. T. Katsura of Department of Chemistry, Tokyo Institute of Technology, who, not only performed some of the chemical analyses of rocks and mineral phases, but also offered valuable guidance during the X-ray diffraction studies. X-ray diffraction analyses of the magnetite were actually done by him. Dr. H. Matsumoto, Kumamoto University, and Mr. H. Haramura, Geological Institute, University of Tokyo, Japan, performed the chemical analyses of the rocks and mineral phases, and words are inadequate to express gratitude to their excellent work.

Assistance received from Mr. and Mrs. J. Kienle (both of Geophysical Institute) during field investigations is acknowledged with sincere gratitude. Thanks are also due to Miss Ruth McCoy, Mr. L. Zarvais and Miss Jean Ingraham for the assistance rendered by them in the laboratory. The helicopter and fixed wing support provided by the 5017th Operational Squadron, Alaskan Air Command, through Elmendorf and King Salmon Air Force Bases was superior, and without this support, field investigations of Mt. Trident would not have been possible.

This support was arranged through the cooperation and interest of Dr. E. Berg, Principal Investigator in charge of the Katmai Seismic and

Gravity Programs (AFOSR Grant No. 701-64), through the approval of Mr. W. J. Best, Chief of Geophysical Division, Air Force Office of Scientific Research. Particular thanks are extended to Captains W. Kuschel, N. Miller, S. Silber, R. McGeechan, J. Keel, L. Ballinger, W. Fox, T. Argo and H. Rhodes for their cooperation and kindness.

Field and laboratory work was supported by research grant from the National Science Foundation (GF-185, Dr. R. B. Forbes, Principal Investigator) under the provisions of the U.S.-Japan Cooperative Research Program. The writer extends his profound gratitude to Professor K. B. Mather, Director, Geophysical Institute, for the continued support he has received from the Institute including his appointment as senior research assistant during his two years of resident research and study.

CHAPTER II

FIELD AND PETROGRAPHIC DESCRIPTION OF THE TRIDENT ANDESITES

LAVA FLOWS AND SPECIMEN LOCALITIES

The terminal lobes of the lava flows are usually less than 60 ft thick. Near the vent, due to over-riding and roll-overs, the cumulative thickness exceeds 200 ft. As seen in the photographs (plate 2) the surface of the lava flows is characteristically blocky. All flows are still degassing (plate 2b). Sampling was restricted to the more accessible areas. Contacts between flows are rarely as distinct as that seen in plate 2b. This problem was magnified by snow cover which remained on the upper segments of some of the flows throughout the summer of 1965, with the exception of areas where degassing is intense. A description of localities and specimens is summarized in table 2. Specimen locations are shown in figs. 3 and 4.

The 1953 and younger andesites will be referred to hereafter as "Trident andesites". The specimen prefix KT (Katmai-Trident) will be omitted in the text and the specimens will be mostly referred to by number only.

PETROGRAPHY

The prehistoric and historic lavas of Trident volcano, as studied to date, are two pyroxene andesites, which are mineralogically and texturally similar. The andesites are vesicular, porphyritic to glomeroporphyritic, with pilotaxitic or hyalopilitic groundmasses, which are rarely vitrophyric. Modal quartz is absent. Spherulites, when present, are variolites of Plagioclase. Exotic inclusions of sedimentary or plutonic rocks have not been recognized. Andesite inclusions (megascopic in 1953-1957 flows and microscopic in younger flows) and monomineralic aggregates are present.

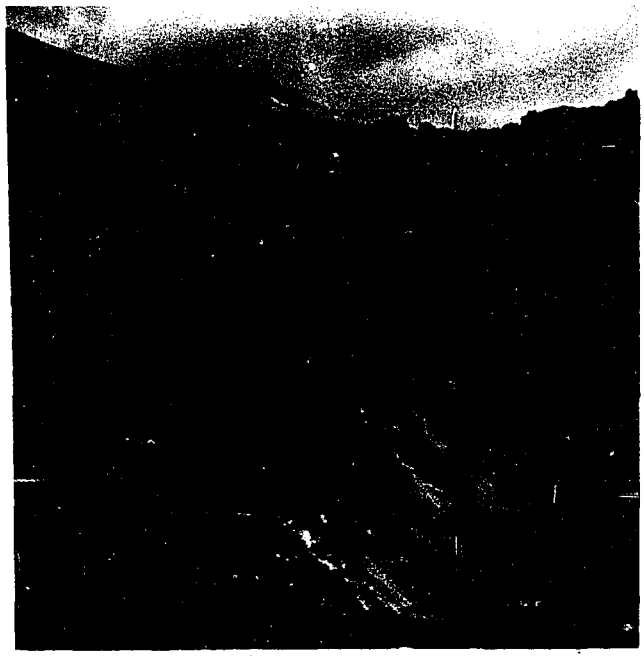

Plate 2a. Typical blocky surface of the Trident lavas (August, 1966).

Plate 2b. 1958 flow over-riding 1953 flow, with degassing activity along contact (July, 1965).

Table 2. Specimen Localities and Descriptions.

Locality Nos.	Description of Localities	Specimen Nos.
	1953 Flow	
1	Andesite coarse grained and porphyritic, ∿ 50 ft, a 25 ft roll-over on a 25 ft basal flow; top is vesicular	KT-7,8 and 9
2	Similar to above; roll-over not distinct	KT-11
3	Porphyritic andesite; ∿ 40 ft; vesicular to scoriaceous toward top	KT - 56 and 57
	1957 Flow	
4	Porphyritic and vesicular andesite; basal flow not exposed; ∿ 70 ft	KT - 14 and 15
5	Vesicular andesite with rare dacitic inclusions; ∿ 50 ft; three variations:	
	(a) highly vesicular	KT-58
	(b) coarsely porphyritic	KT-59
	(c) irregular blocks from the 1953 flow	KT-60
6	Dark colored andesite with rare dacitic inclusions; vesicular and porphyritic	KT-61 (vesicular) KT-62 (porphyritic)
	1958 Flow	
7	Banded flow with vesicular top; ∿ 50 ft; poor in vesicles at base; upper 15 ft composed of irregular blocks.	KT-1,2 and 3
8	More porphyritic than above lavas	KT-10
9	Boundary with 1953 flow indistinct; copious fumaroles; ∿ 80 ft; 2 flow units (?)	KT-16 and 17

Table 2. Specimen Localities and Descriptions (Cont'd.)

Locality Nos.	Description of Localities	Specimen Nos.
	1959 Flow	
10	Porphyritic, vesicular andesite; ∿ 50 ft	KT-5 and 6
	1960 Flow	
11	Alternate zones of porphyritic and vesicular andesite; ∿30 ft	KT-22 and 23
	1954 Block Avalanche	
12	Blocks of andesite; banded structure	KT-12 and 13
	1963 Block Avalanche	
13	400 ft above loc. 12; irregular and rotated blocks; intense fumarolic activity, porphyritic and vesicular; occasionally pumicous like.	KT-29 and 30
	Older Lavas of Ancestral Mt. Trident	
14	Andesite, partially mantled by pumice blanket	KT-20 and 24
15	Andesite, partially covered by pumice; with dacite and rhyolite-pumice inclusions; banded structure; probably same unit as 14.	KT-25-28
16	Porphyritic andesite on the NNE-SSW trending ridge to the east of Mt. Trident, rarely aphanitic; not similar to units 14 and 15.	KT-18 and 19

These are considered to be cognate cumulates. Detailed mineralogical studies were confined to the 1953-63 eruptives. The mineralogy of the andesites including the pre-historic lavas and a sample of andesite ('TC') collected from the rim of the active crater is summarized below.

1953-63 Lavas and Block Avalanches

Modes and modal averages are shown in table 3. The compositional ranges of major crystalline phases (based on optical determinations) for each specimen are given in table 4. The modes of occurrence and textural relations of the individual components are as follows:

Olivine:

Olivine is common minor constituent in the earlier lavas but occur less frequently in some younger flows. Subhedral to rounded microphenocrysts of olivine occur both with and without reaction rims of tangential needles and prisms of orthopyroxene (plate 3a); or irregular growth of clinopyroxene and vermicular magnetite. Olivine cores have also been observed in clinopyroxene phenocrysts (plate 3b). Glomeroporphyritic aggregates of olivine with plagioclase $\pm$ clinopyroxene and rare orthopyroxene are also common (plate 4). Alteration to iddingsite is rare as compared to alteration rims composed of magnetite and/or limonite.

Olivine composition determinations based on optic axial angles (from curves of Winchell et al, 1964, p. 500) are given in table 5. These determinations carry an error of $\pm$ 3-4 mol.% Fo, as discussed by Chudoba and Frechen (1943, p. 183). Olivine occurs as a minor to trace constituent and it was not possible to isolate this phase for chemical analysis.

Table 3. Modal Analyses of the Trident Andesites
(Point Count Method; ∿ 1000 points)

S. Nos.	Olivine	Ortho-pyroxene	Clino-pyroxene	Plagio-clase	Magne-tite	Glassy Mesostasis
1953 Flow						
7	--	4.6	2.4	27.6	4.4	61.0
8	0.1	3.1	4.2	30.7	1.7	60.2
9	0.8	5.2	4.5	30.9	3.2	55.4
11	0.6	4.2	4.5	30.1	1.9	58.7
56	0.2	5.5	1.9	26.8	2.8	62.9
57	-	3.5	4.1	27.3	2.7	62.5
Average	0.4	4.4	3.6	28.9	2.8	60.1
1957 Flow						
14	0.4	5.0	2.8	32.0	2.8	56.9
15	1.1	3.2	5.9	33.1	5.9	50.8
58	0.3	2.4	2.0	28.3	2.0	65.0
59	0.7	3.8	2.6	26.6	2.0	64.3
*60	0.4	3.4	4.3	24.7	1.6	65.6
61	0.3	2.4	4.4	34.4	2.0	56.6
62	0.5	4.0	4.3	34.0	2.9	54.3
Average (excluding 60)	0.6	3.5	3.7	31.4	2.9	58.0
1958 Flow						
1	1.4	3.7	3.5	30.5	1.4	59.5
2	0.3	5.8	3.0	30.1	2.1	58.8
3	0.3	4.6	3.4	23.5	1.8	66.4
10	1.4	3.3	4.0	32.6	1.6	57.1
56	0.9	4.2	3.6	31.6	2.6	57.1
57	0.3	4.3	3.3	31.7	2.8	57.6
Average	0.8	4.3	3.5	30.0	2.1	59.4
1959 Flow						
5	0.2	4.6	3.5	28.4	2.8	60.5
6	0.5	3.6	2.2	33.8	4.4	55.5
Average	0.4	4.1	2.9	31.1	3.6	58.0
1960 Flow						
22	0.6	2.1	6.6	29.9	4.1	56.7
23	0.1	4.2	2.1	27.5	3.1	63.0
Average	0.4	3.2	4.4	28.7	3.6	59.9
1954 Block Avalanche 12	-	4.4	3.2	30.7	2.0	59.7
13	0.4	2.3	3.7	30.8	1.2	61.6
1963 Block Avalanche 29	-	1.9	2.5	26.4	1.5	67.8
30	-	4.5	3.6	33.8	3.1	55.1

*may be a bomb

Table 4. Range of Composition of Major Crystalline Constituents in the Different Flow Units.

	Olivine	Clinopyroxene			Orthopyroxene	Plagioclase
	Mol.% Fo	Mol.% Wo	Mol.% CEn	Mol.% CFs	Mol.% En	Mol.% An
1953 Flow						
Av. Comp. Range	73-63	48-42	42-38	16-14	65-58	63-42
Rare extremes	91				80, 50	90, 12
1957 Flow						
Av. Comp. Range	79-62	44-43	44-41	16-13	65-55	58-29
Rare extremes	91, 57				73, 50	90, 21
1958 Flow						
Av. Comp. Range	85-67	46-43	41-38	19-15	65-60	70-43
Rare extremes					70, 50	90, 23
1959 Flow						
Av. Comp. Range	87	45-43	40-30	18-16	66	51-48
Rare extremes					50	90. 23
1960 Flow						
Av. Comp. Range	77-62	46-43	41-39	18-16	62-58	63-43
					72	84, 28

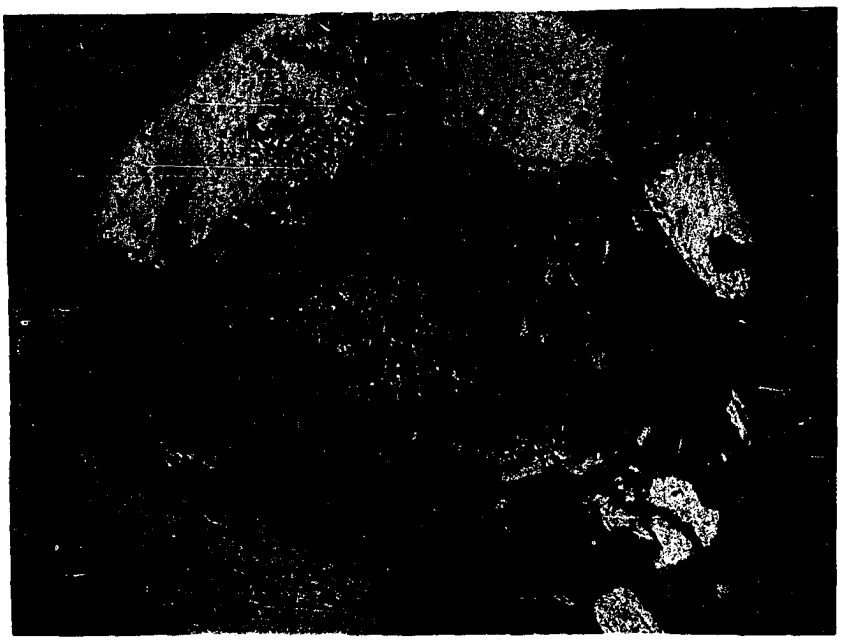

(60X)

Plate 3a. Olivine (ol) surrounded by reaction rims composed of slender prisms and needles of orthopyroxene (o).

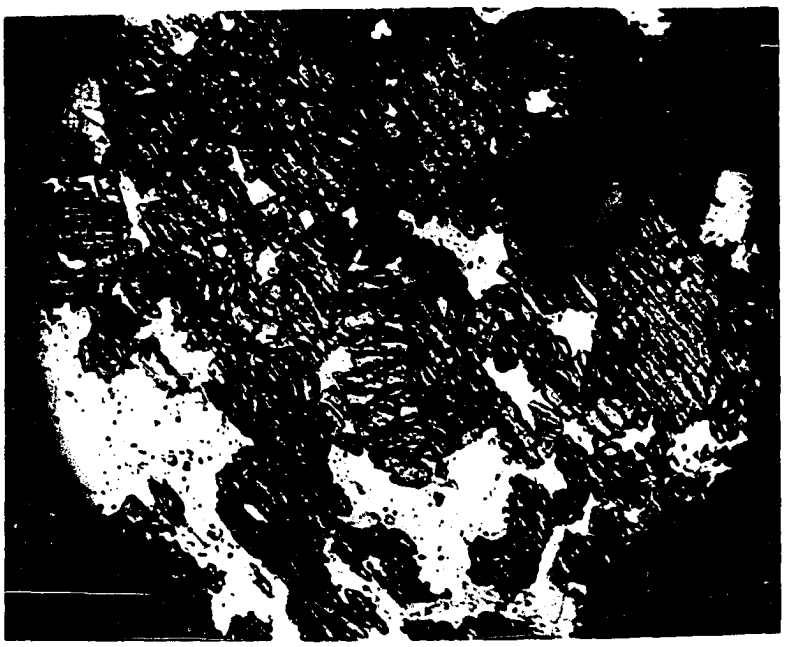

(17X)

Plate 3b. Olivine (ol) core surrounded by clinopyroxene (c).

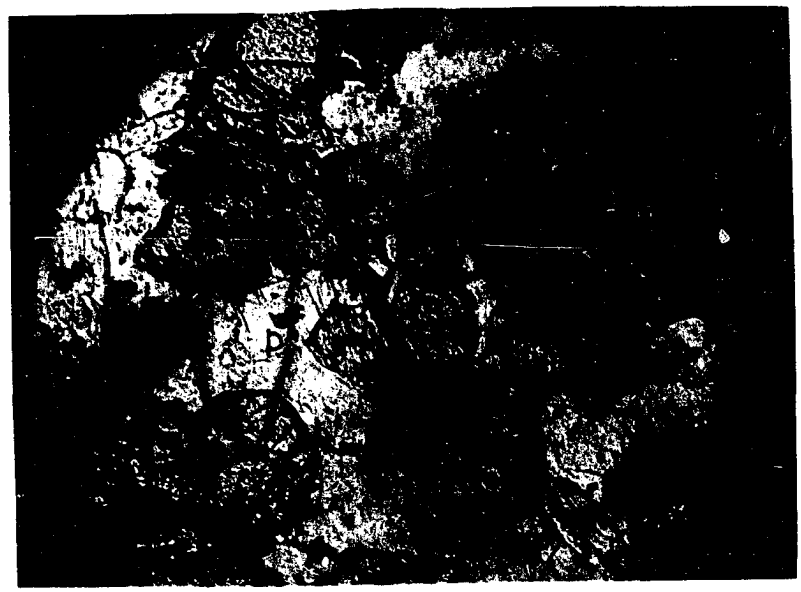

(60X)

Plate 4a. Glomeroporphyritic aggregate of olivine (ol) and plagioclase (p)

(17X)

Plate 4b. Glomeroporphyritic aggregate of olivine (ol), clinopyroxene (c) and plagioclase (p).

Table 5. Optical Axial Angles and Estimated Composition of Olivine (discrete grains).

	S. Nos.	$2V_x \pm 1°$	Mol.% Fo (± 2%)	Group Range Mol.% Fo
1953 Flow				
	7	85°	68	
	8	83°-85°	68-62	91-62
	9	93°	91	
	56	87°	73	
1957 Flow				
	14	83°	62	
	15	84°-89°	79-65	
	58	81°	57	
	59	93°	91	91-57
	60	87°	73	
	61	87°-92°	88-73	
	62	86°-88°	77-70	
1958 Flow				
	1	91°	85	
	10	91°	87	87-67
	16	85°	67	
	17	90°-91°	85-83	
1959 Flow				
	6	91°	87	∿ 87
1960 Flow				
	22	87°-88°	77-73	77-62
	23	83°-85°	67-62	
1954 Block Avalanche	12	83°	62	62-57
	13	81°	57	

Orthopyroxene :

Orthopyroxene (hypersthene), which is generally the dominant pyroxene, occurs as euhedral to subhedral phenocrysts and microphenocrysts in the groundmass. Zoning is quite common. In normally zoned grains (plate 5a) the marginal zones are stained reddish-brown. These stained zones are characterized by unusually low optic axial angles. Lewis (1960, p. 1125) believes that these phenomena are due to oxidation. Reverse zoning is rare. Clinopyroxene rims and jackets occur (plate 5b) but hypersthene grains with clinopyroxene cores occur more frequently (plate 6a). Thick alteration rims of hydrous iron oxide are commonly present and vermicular areas of microgranular magnetite frequently fill hypersthene phenocrysts.

The optic axial angles, refractive indices and composition (mol.% En) of orthopyroxenes based on optical data and curves by Kuno,(1954b, p.40) are listed in table 6. Data in table 6 show that there is a fair degree of uniformity in the composition of phenocrystal and groundmass orthopyroxene.

The optic axial angles were determined for two orthopyroxene grains from an inclusion in sample KT-17. In one phenocryst $2V_x$ was measured at 68.5 $\pm$ 1° (En_{74}) while in the other, with reverse zoning, $2V_x$ increased from 57 $\pm$ 1° (En_{62}) in the core, to 66 $\pm$ 1° (En_{72}) in the rim.

Clinopyroxene :

The clinopyroxene phase in the Trident andesites is augite. No pigeonite has been observed. Augite is present as euhedral to subhedral phenocrysts and microphenocrysts, and subhedral to anhedral groundmass grains. Orthopyroxene cores are rare, and augite cores in orthopyroxene

(60X)

Plate 5a. Microphenocrysts of zoned hypersthene (o) with reddish-brown stained rims.

(17X)

Plate 5b. Orthopyroxene (o) core in clinopyroxene (c).

(crossed Nicols, 17X)

Plate 6a. Clinopyroxene (c) core in orthopyroxene (o) phenocryst.

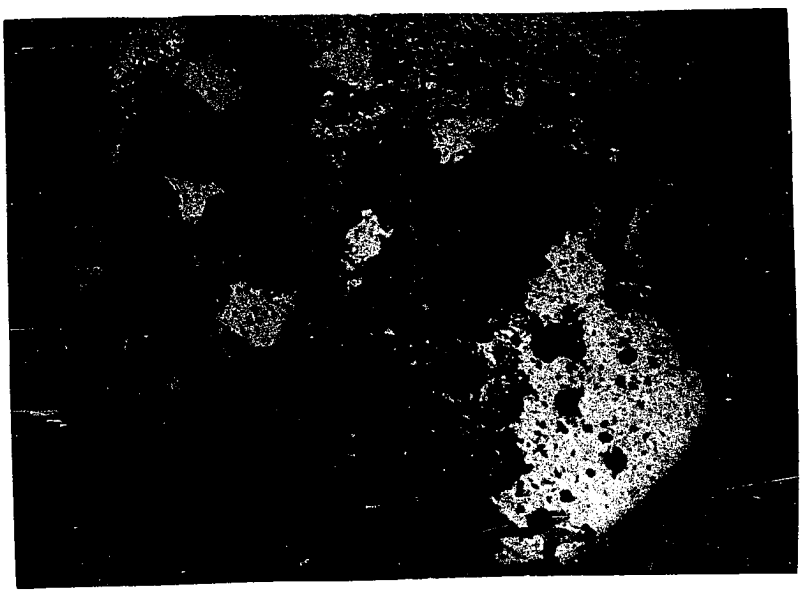

(60X)

Plate 6b. Clinopyroxene (c) - plagioclase (p) aggregate.

Table 6. Optical Properties and Estimated Composition of Orthopyroxene.

	S.Nos.	$2V_x \pm 1°$						R.I (Type 3) ± .001		*Mol.% of En			
		Type 1	Type 2	Type 3	Type 4			N_z	N_x	Type 1	Type 2	Type 3	Type 4
					Core	Zone 1	Zone 2						
1953 Flow	7			51	54	42		1.701	1.690			50	55
	8			59-58	78	63		1.702	1.690			64-63	80-69
	9			59-57				1.704	1.691			64-62	
	11			55				1.704	1.691			58	
	56		66-60	60-57				1.702	1.690		71-65	65-62	
	57		67	58	56	52					73	63	60-?
1957 Flow	14			58-56				1.701	1.688			63-60	
	15	68-60		55				1.703	1.690	73-65		58	
	58			56	55/57	36/46		1.704	1.691			60	58-?/62-?
	59	60		57,48	56	49	45	1.703	1.691	66		62,?	60-?-?
	60			56-55				1.703	1.690			60-58	
	61	56		54	54	40		1.702	1.690	60		55	55-?
	62			57	56/50	61/41		1.702	1.688			65	61-67/?-?
1958 Flow	1			56				1.707	1.694			60	
	2			59				1.706	1.693			63	
	3	59	64					1.704	1.691	-63	69.5		
	10		60	59-57	61/57	73/51		1.703	1.691		65	65-62	67-77/62-?
	16			57				1.706	1.693			62	
	17			59				1.704	1.692			65	
1959 Flow	5			60	57/58	42/47		1.705	1.693			66	62-?/63-?
	6				57/57	52/45		1.709	1.696				62-?/62-?
1960 Flow	22		62	56				1.702	1.690		68	60	
	23		66-63	57-55				1.706	1.693		72-69	62-58	
1954 Block Avalanche	12			56	56	61		1.701	1.688			60	60-67
	13			57				1.703	1.690			62	
1963 Block Avalanche	29			57				1.703	1.689			62	
	30			56				1.702	1.690			60	

Type 1: Orthopyroxene core in clinopyroxene; Type 2: Large phenocrysts (>1 mm.); Type 3: Average phenocrysts, microphenocrystal and groundmass orthopyroxene; and Type 4: Zoned phenocrysts (normal and reverse).
*Estimated composition of types 1, 2 and 4 are approximate only.

grains are more frequent (plate 6a). Glomeroporphyritic clinopyroxene aggregates with plagioclase laths ± olivine and small aggregates of clinopyroxene + magnetite are also present (plates 6b & 7_a). Inclusion-like monomineralic aggregates of clinopyroxene are common (plate 7b), which show clear contact relations with the groundmass of the host andesite. Interesting graphic intergrowths of clinopyroxene and plagioclase were also observed (plate 8a). There are also rare examples of partially resorbed clinopyroxene phenocrysts (KT-23, plate 8b).

The augite is weakly pleochroic(X = pale brownish green, Y = pale bluish green and Z = pale brownish green).

The optical properties of the clinopyroxenes are listed in table 7 along with the estimated compositions based on curves by Hess (1949, p. 634). It is evident that there are small but meaningful differences in the comparative composition of phenocrystal and groundmass augite. Large phenocrysts (type 1, table 7) display a larger $2V_z$. Normal zoning, with decreasing $2V_z$ toward the rim was observed in KT-58, where the range of $2V_z$ from core to rim was 62° to 52° (± 1°). Adjacent twin lamellae may have slightly different compositions as observed in a phenocryst in KT-57. Adjacent twin lamellae produced a $2V_z$ of 53° and 55° respectively (± 1°). The optical properties of the augites from the inclusions (andesites) are similar to those of the phenocrysts.

Plagioclase:

Plagioclase occurs in the Trident andesites as euhedral to subhedral phenocrysts, microphenocrysts and small prismatic or equant grains in the groundmass. Glomeroporphyritic aggregates of plagioclase with the other mineral phases have been described above. Monomineralic aggregates of

(60X)

Plate 7a. Clinopyroxene (c) - magnetite aggregate.

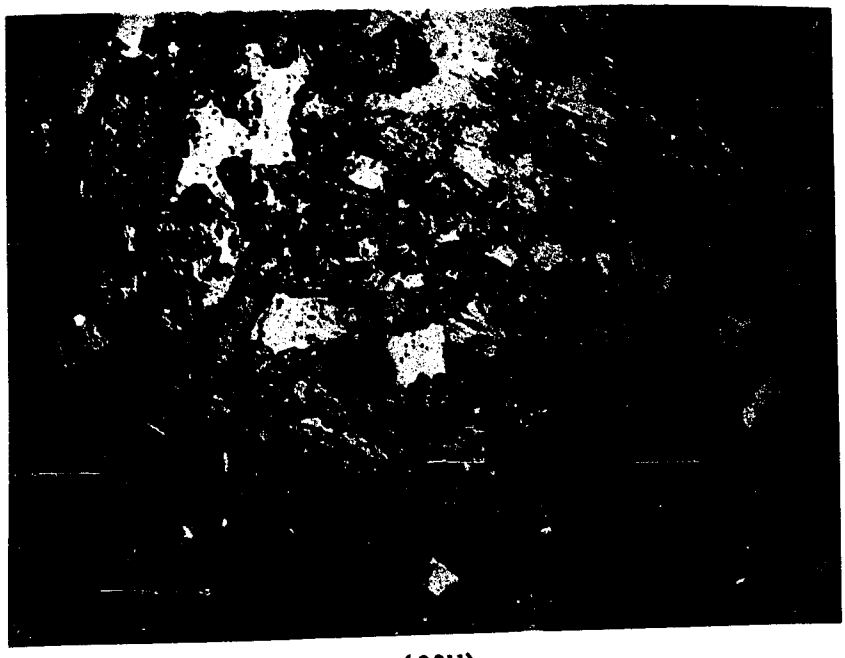

(60X)

Plate 7b. Inclusion-like aggregate of clinopyroxene (c).

(60X)

Plate 8a. Graphic (?) intergrowth of clinopyroxene (c) and plagioclase (p).

(17X)

Plate 8b. Partially resorbed clinopyroxene (c), KT-23.

Table 7. Optical Properties and Estimated Composition of Clinopyroxene

	S.Nos.	$2V_z \pm 1°$			R.I. $N_y \pm .001$	$Z \wedge c$	Composition (Hess, 1949, p. 634)					
		Type 1	Type 2	Type 3	(Type 2)	(Type 2)	Type 2			*Type 3		
							Mol.% Wo	Mol.% CEn	Mol.% CFs	Mol.% Wo	Mol.% CEn	Mol.% CFs
1953 Flow	7		53-51		1.690	48°	44-42	40-42	16			
	8	66	58-55	55-46	1.690	47°	52-48	36-38	12(?)-14	48-39	38-43	14-18
	9		56-53	48-46	1.690	51°	48-44	38-41	14-15	40-39	43	17-18
	21		59-56		1.691	34°?	48	38	14			
	56		59-56	58	1.690	41°	48	38	14	52	36	12
	57		56-53			43-44	48-44	38-41	14-15			
1957 Flow	14		58	57	1.688	44°	52	35	13	(?)50	36	14
	15			53-52	1.690	44-45				44-43	41	15-16
	58	62-52 (zoned)	53		1.691	44°	43	41	16			
	59		52	48	1.688	43°	43	43	14	40	45	15
	60		53		1.687	43°	44	43	13			
	61		53		1.690	44°	44	41	15			
	62		52		1.687	43°	43	44	13			
1958 Flow	1	64-61	58		1.694	48°	(?) 52	34	14			
	2		52		1.694	41°	43	38	19			
	3			50-41	1.691	46°				41-35	42-45	17-20
	10		54		1.693	44°	45	38	17			
	16		55		1.691	39°	46	39	15			
	17		52	49	1.691	45°	43	41	16	41	42	17
1959 Flow	5		53		1.691	48°	44	40	16			
	6		54-52		1.693	51°	45-43	38-39	17-18			
1960 Flow	22		52		1.690	42°	43	41	16			
	23		55-53		1.691	44°	46-44	39-40	15-16			
1954 Block Avalanche	12	70-63	56	57	1.688	44°	48	40	12	50	39	11
	13			55-54	1.688	45°				46-45	41-42	13
1963 Block Avalanche	29	61		50	1.688	41-42°				42	43	15
	30		55	51	1.689	49°	46	40	14	42	43	15

Type 1: Large phenocrysts (>1mm); Type 2: Average phenocrysts and microphenocrysts, and Type 3: Groundmass augite.
*Composition approximate only.

small equant plagioclase grains form inclusions which display sharp contacts with the groundmass of the host rock.

Minute inclusions of glass, clinopyroxene and more rarely magnetite and orthopyroxene also occur in the phenocrysts. Phenocrysts have been subdivided into inclusion-bearing and inclusion-free types; and the former can be further subdivided as follows:

(1) Grains with dusty inclusions of glass, ± clinopyroxene, ± opaques in a zone penultimate to the grain boundary (rarely in the core or intermediate zones) (plate 9a),

(2) Grains displaying inclusions resulting in a honey-comb structure, (plate 9b).

Plagioclase composition was determined from extinction angles using the Rittman Zone Method (Chudoba, 1933) and high-temperature plagioclase curves given by Tröger (1956, p. 111). The determinations for the different types of phenocrysts and groundmass plagioclase are listed in tables 8, 9 and 10. The error associated with these determinations is estimated at ± 2% An.

Inclusion-free phenocrysts are either homogenous, or display normal and oscillatory zoning. The An content of the homogeneous phenocrysts may represent the pre-eruption plagioclase equilibrium with the magma. The compositional variation of these grains in a single flow or in different flows is small (table 8). The total range in composition of homogeneous phenocrysts is An_{70-29}. Various phenocrysts rarely display optically distinct rims (presumably late). The compositional range of these rims (table 8) is An_{68-33}, which is similar to that of the homogeneous phenocrysts.

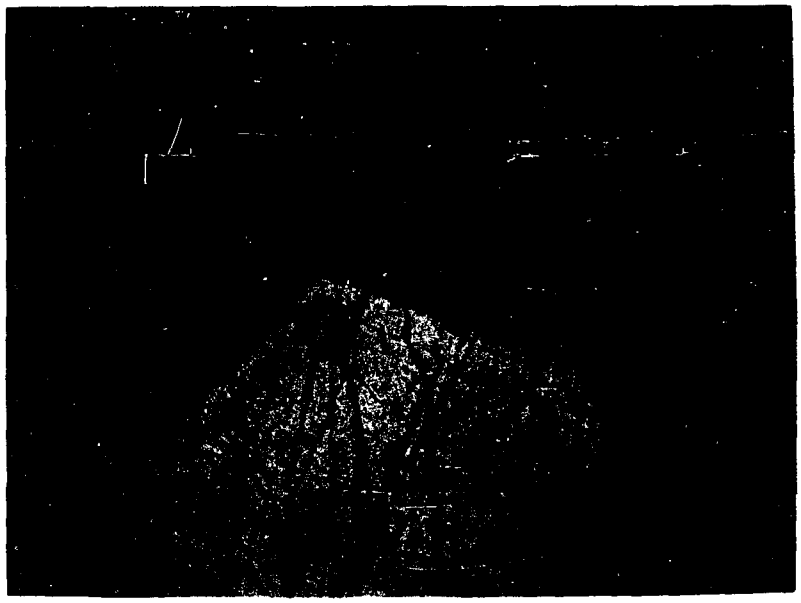

(crossed Nicols, 60X)

Plate 9a. Plagioclase phenocryst with a marginal zone filled with glassy inclusions.

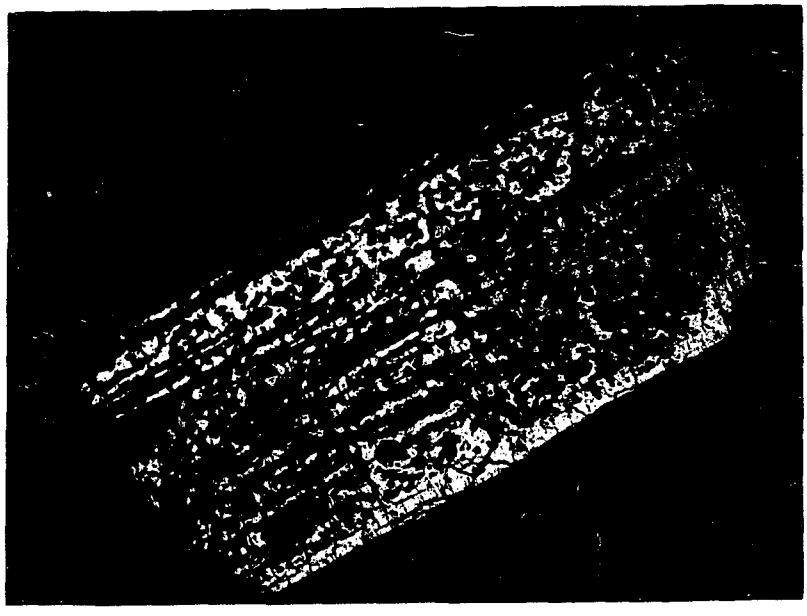

(crossed Nicols, 60X)

Plate 9b. Plagioclase phenocryst with honey-comb structure formed by glassy inclusions.

Table 8. An Mol.% Composition of Phenocrystal and Groundmass Plagioclase (optical determinations).

	S. Nos.	Range in Mol.% An			
		Zoned	Homogeneous	Late Rims	Groundmass Plagioclase
1953 Flow					
	7	63-28	63-49	52	49-44
	8	70-25			49-40
	9	70-19	52-48		46-40
	11	70-42	50-42	58-56	49-45
	56	90-40	55		51-46
	57	70-42	46	54	48-44
1957 Flow					
	14	56-21	58-29	33	44-41
	15		84-61		59-57
	58	80-31	52		43-43
	59	48-36	54-42		52-46
	60	99-31		58	46-40
	61	74-48	58-45	54	51-46
	62	90-40	58-51	69-45	51-45
1958 Flow					
	1	65-23	70	56-31	52-42
	2	90-24	54	56-49	51-43
	3	80-27	47	54-41	52-41
	10		68-47	47-25	51-45
	16	58-43	45		52-36
	17	68-43	50-43		51-41
1959 Flow					
	5	87-28	51-48	57-37	51-45
	6	84-34	49	49	51-40
1960 Flow					
	22	84-28	63-54		56-49
	23	69-39	54-43		49-41
1954 Block Avalanche	12	70-40	58-37	63	45-41
	13	80-32	59-45		47-46
1963 Block Avalanche	29	84-41	48-37	46	46-36
	30	84-31	54-36	54-40	52-45

Table 9. An (Mol.%) Composition of Plagioclase Phenocrysts with Poikilitic Marginal Zones (optical determinations).

	S. Nos.	Range in Mol.% An		
		Whole Phenocryst	Poikilitic Zone	Outer Rim
1953 Flow				
	7	90-61	90	61
	8	74-37	70-37	58-47
	9	70-43	63-51	58-52
	11	66-42	56-45	66-52
	56	68-51	68-63	52-51
	57	53-46	46	53
1957 Flow				
	14	63-40	58-40	63-32
	15	70-28	63-33	70-43
	58	63-43	58-50	63-54
	60	80-26	70-29	80-33
	61	67-50	67-54	66-58
	62	68-35	68-45	65-56
1958 Flow				
	1	61-45	61-56	52
	2	45-35	41	45
	3	70-40	57-48	58-50
	10	66-43	66	43
	17	61-44	56-55	61-58
1959 Flow				
	5	84-33	68-45	70-46
	6	59-46	54-53	59-56
1960 Flow				
	22	80-36	80-46	80-54
	23	70-36	61-48	70-35
1954 Block Avalanche	12	84-54	74	54
	13	84-43	84-52	54-52
1963 Block Avalanche	29	42-31	42	31
	30	61-47	54	61

Table 10. An (Mol.%) Composition of Phenocrysts with 'Honey-comb' Structure, and/or Patchy or Irregular Cores (optical determinations).

S. Nos.		Range in Mol.% An		
		1	2	3
1953 Flow				
	7	84-21	46-23	36-33
	8	50-35	84-50	56
	9	58-54		
	11	84-26		
	56	56-31	58-45	58
	57	90-54		
1957 Flow				
	14	63-54	74-43	48-43
	15	90-63		
	58	84-56		
	59	70-32		
	60	41-29		
	61	84-32	84-34	84 (?)
	62	90-70		
1958 Flow				
	1	80-29	77-41	46
	2	84-43		
	3		58-42	58
	10		50-29	35
	16	75-49	63-28	47
	17	75-58	66-42	66
1959 Flow				
	5	75-31	74-45	52-48
	6	90-42		
1960 Flow				
	22	73-28		
	23		63-45	
1954 Block Avalanche	12	74-23	66-38	40
	13	52-40		
1963 Block Avalanche	29	58-40		
	30	70-61		

Col. 1: Phenocrysts with 'honey-comb' structure,
Col. 2: Phenocrysts with patchy cores, and
Col. 3: Core sector of phenocrysts (Col. 2).

Inclusion bearing phenocrysts show considerable variation in zoning i.e. normal, oscillatory and reverse. Amongst these, in type 1, reverse zoning is more common. The outermost zone is generally more calcic than the intermediate and adjacent inclusion bearing zone (table 9). Partial fusion of less calcic plagioclase and subsequent growth in contact with a more basic melt would explain these features. As suggested by Kuno (1950, p. 968), phenocrysts with honey-comb structure may represent an advanced stage of the above process. Reverse zoning is also present in type 2 phenocrysts.

In phenocrysts with irregular cores, the cores range in composition between 66 and 33 mol.% An (table 10) - a range which is compositionally similar to that of the homogeneous phenocrysts.

The variation in the composition of the groundmass plagioclase is small (table 8) and there is little difference in composition(10 mol.% An) between these grains and the homogeneous phenocrysts. The An composition of the groundmass plagioclase may be related to the molar concentration of An in the immediate post-eruptional stage of the lava.

The range of composition of plagioclase microphenocrysts from inclusions is An_{57-48} (megascopic inclusions) and An_{48-29}(microscopic inclusions).

Magnetite:

Magnetite occurs as euhedral to subhedral microphenocrysts, small disseminated grains in the groundmass and vermicular intergrowths with orthopyroxene and olivine.

No exsolved or discrete ilmenite could be detected in direct light. Hematite - goethite alteration is associated with granular magnetite.

Glassy Mesostasis:

The glassy mesostasis is heavily charged with microlites of feldspar (? plagioclase), pyroxene granules and opaque dust. It is usually pale brown to brown in color. Deep brown glass is common in 1957 flows. 1958 flows sometimes show alternate bands of pale brown and colorless glass. The glassy mesostases of the andesites from the block avalanches are predominantly colorless. Inclusions contain blebs of pale brown to colorless glass.

Pre-historic Lavas

Subhedral to anhedral microphenocrysts of olivine occur in minor amounts with frequent reaction rims of slender orthopyroxene needles. Olivine grains are partially altered to iddingsite and/or iron oxides. Hypersthene phenocrysts with a high $2V_x$ are frequently filled with vermicular patches of magnetite. Iron-stained rims are common. Euhedral to subhedral phenocrysts of augite ($Z \wedge c$ - 41-45°) contain rare cores of orthopyroxene. Euhedral to subhedral plagioclase phenocrysts of both types (inclusion-bearing and inclusion-free) occur. Inclusion-free homogeneous phenocrysts have a compositional range of An_{50-42}. Microphenocrysts and small,but discrete, grains of magnetite are disseminated throughout the pilotaxitic groundmass. The glassy mesostasis, mostly colorless to pale brown, is charged with small laths of plagioclass (An_{38-26}) and minor pyroxene.

Cognate inclusions are mineralogically similar. They are composed of microphenocrysts of plagioclase (An_{48-29}), augite ($Z \wedge c$- 49-39°) and hypersthene embedded in a pilotaxitic to hyalopilitic glassy groundmass, which is pale brown in color.

Andesite Blocks on the Crater Rim

These porphyritic two-pyroxene andesites contain euhedral to subhedral phenocrysts and microphenocrysts of hypersthene (dominant pyroxene), augite, plagioclase (av. An_{34}) and magnetite embedded in a pilotaxitic groundmass with colorless glass. Minor olivine was observed. Cognate cumulates of plagioclase and clinopyroxene $\pm$ orthopyroxene are present.

CHAPTER III

CHEMICAL MINERALOGY

Coexistent pyroxenes plagioclase, magnetite and groundmass glass phases were separated from selected andesite specimens taken from each of the following flow units, as shown below:

1953	flow	S. No. KT-56
1954	block avalanche	" KT-13
1957	flow	" KT-14
1958	"	" KT- 1
1959	"	" KT- 6
1960	"	" KT-23

Procedures and techniques used in mineral separations are discussed in Appendix II.

In the section to follow, separated mineral phases will be identified by the numbers of the parent rock specimens as listed above with prefixes M,O,C,PP,GP and GM (for magnetite, orthopyroxene, clinopyroxene, plagioclase phenocrysts, groundmass plagioclase and groundmass glass respectively) rather than KT.

MAGNETITE

Thirteen samples of magnetite from eight rock specimens were separated and analyzed. The purity of the samples ranged from 93 to 98%. Magnetite was analyzed for wt.% FeO, Fe_2O_3 and TiO_2. Chemical analyses and accompanying recalculations are given in table 11.

The 'a' unit cell parameters and packing indices, calculated from the (440), (511), (400) and (311) X-ray reflections (obtained with a Norelco X-ray diffractometer, Fe$K\alpha$ radiation) are also included in table 11.

Table 11. Chemical Composition and Cell Parameters of Magnetite.

S. Nos.	M-11	M-11g	M-56	M-14(1)	M-14(2)	M-14(3)	M-1	M-5	M-6	M-23(1)	M-23(2)	M-13(2)	M-13(2)
Wt.%													
FeO	38.79	37.98	38.64	34.24	34.27	34.34	36.69	30.64	36.92	32.70	32.53	36.33	36.19
Fe_2O_3	46.94	47.33	48.08	49.81	53.28	52.41	51.89	57.32	48.62	55.01	53.90	49.64	47.82
TiO_2	10.00	9.87	10.17	8.92	9.31	9.24	9.64	10.23	9.07	9.81	9.68	9.16	9.02
											Analysts:	T. Katsura and H. Haramura.	
Atomic proportions on 32-oxygen basis													
Fe^2	10.33	10.16	10.15	9.32	8.92	9.03	9.46	7.76	9.94	8.40	8.48	9.71	9.90
Fe^3	11.25	11.39	11.36	12.21	12.48	12.40	12.04	13.06	11.78	12.71	12.65	11.93	11.77
Ti	2.40	2.37	2.40	2.18	2.18	2.18	2.24	2.33	2.20	2.27	2.27	2.20	2.22
Total Cation	23.98	23.92	23.91	23.71	23.58	23.61	23.74	23.15	23.92	23.38	23.40	23.84	23.89
Deficiency	0.02	0.08	0.09	0.29	0.42	0.39	0.26	0.85	0.08	0.62	0.60	0.16	0.11
Mol.%													
FeO	38.79	37.98	38.64	34.24	34.27	34.34	36.69	30.64	36.92	32.70	32.53	36.33	36.19
Fe_2O_3	46.94	47.33	48.08	49.81	53.28	52.41	51.89	57.32	48.62	55.01	53.90	49.64	47.82
TiO_2	13.05	13.02	13.18	12.40	12.57	12.54	12.62	14.01	12.18	13.31	13.30	12.31	12.32
$\Sigma Fe/(\Sigma Fe+Ti)$	0.9001	0.9008	0.9000	0.9079	0.9075	0.9076	0.9058	0.9000	0.9082	0.9031	0.9029	0.9077	0.9072
$Ti/(\Sigma Fe+Ti)$	0.0999	0.0992	0.1000	0.0921	0.0925	0.0924	0.0942	0.1000	0.0918	0.0969	0.0971	0.0923	0.0928
a(Å)	8.424		8.422		8.418		8.408	8.397	8.401	8.399		8.426	
Packing index	53.84		53.84		53.77		53.89	53.98	54.23	54.04		53.71	

M-11g - (-200) mesh fraction

Analyses were repeated on separates extracted from the same rock specimen. The analytical data listed in table 11 are based on the diffraction patterns obtained on the purest separates of those isolated from the host rocks. All of the analyzed magnetite, as indicated by the X-ray studies, are primarily composed of a single phase (spinel). However, a trace of the rhombohedral phase was detected in M-5, 6 and 23.

Composition and Nomenclature

The magnetite analyses have been plotted on a FeO-Fe_2O_3-TiO_2 diagram in fig. 7. According to this diagram the analyzed magnetites can be classified as 'titano-magnetite' as suggested by Katsura (1964, p. 223). The cation deficiency in the analyzed magnetites does not exceed 0.85 (total cations = 23.15 on 32 oxygen basis).

In fig. 8, a $\Sigma Fe/(\Sigma Fe+Ti)$ - 32 $(\Sigma Fe+Ti)/O$ diagram of analyzed magnetite, the plots define two vertical fields with $\Sigma Fe/(\Sigma Fe+Ti)$ values ranging from 0.900 - 0.908. This behavior (analogous to observations by Katsura and Kushiro, 1961, p. 142, fig. 3) furnishes another example from a natural system of oxidation of ulvöspinel (Usp-Fe_2TiO_4) - magnetite Mt-$Fe_3O_4)_{ss}$ to produce intermediate titanomagnetite. In fig. 8 the trends of the above binary solid solution series, Usp-Mt and $\gamma FeTiO_3$ - Hematite (Ht-Fe_2O_3), have been indicated. The trends defined by the composition of these magnetites do not correlate with the solid solution variations.

Buddington and Lindsley (1964, p. 334) have emphasized the paragenetic relations and position of magnetite in the sequence of crystallization (op. cit., pp. 329-330) in igneous rocks. But these features are complicated by other modes of origin, for example,

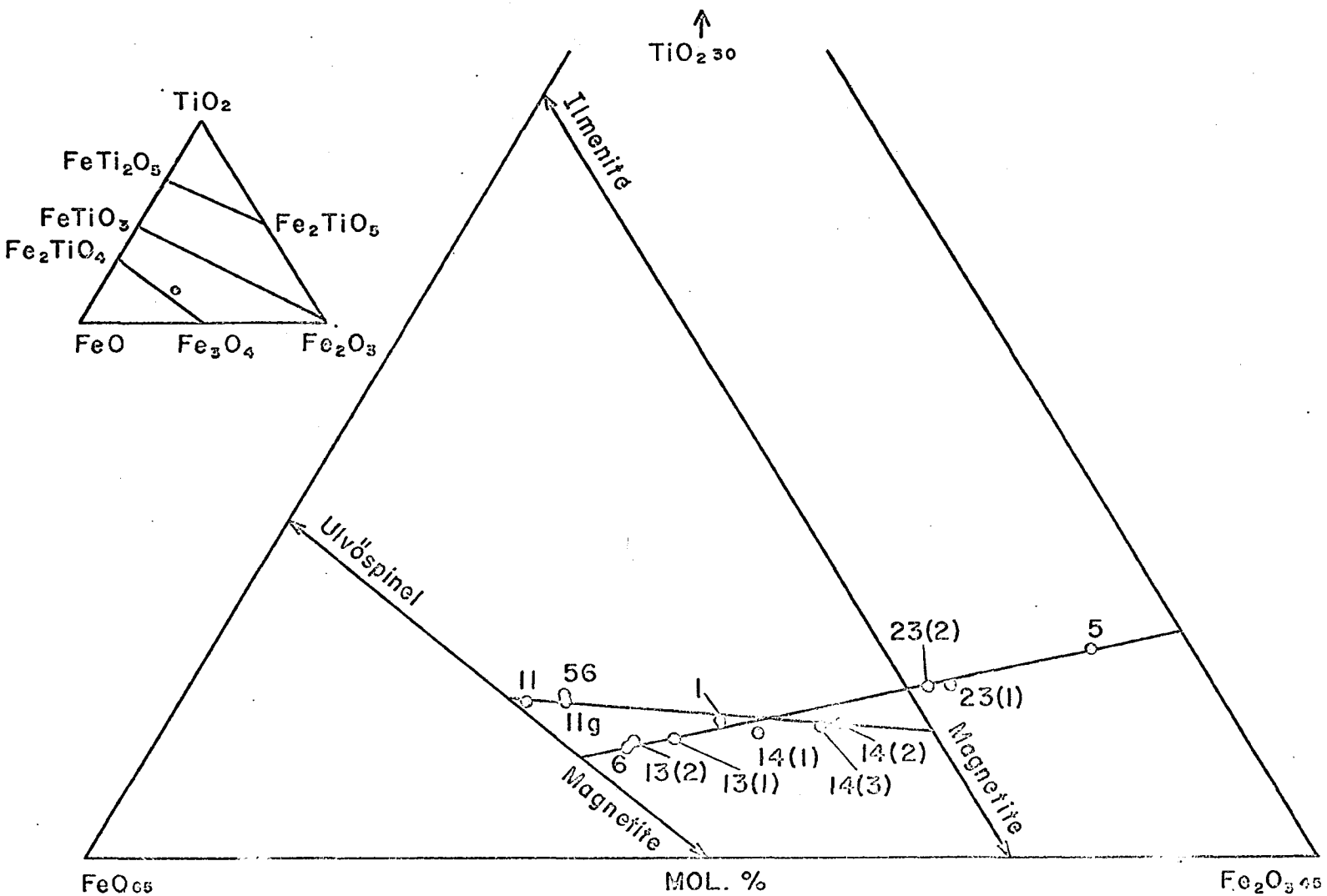

Fig. 7. FeO_{65}-$Fe_2O_{3\ 45}$ - $TiO_{2\ 30}$ field from FeO-Fe_2O_3-TiO_2 diagram showing the analyzed magnetite.

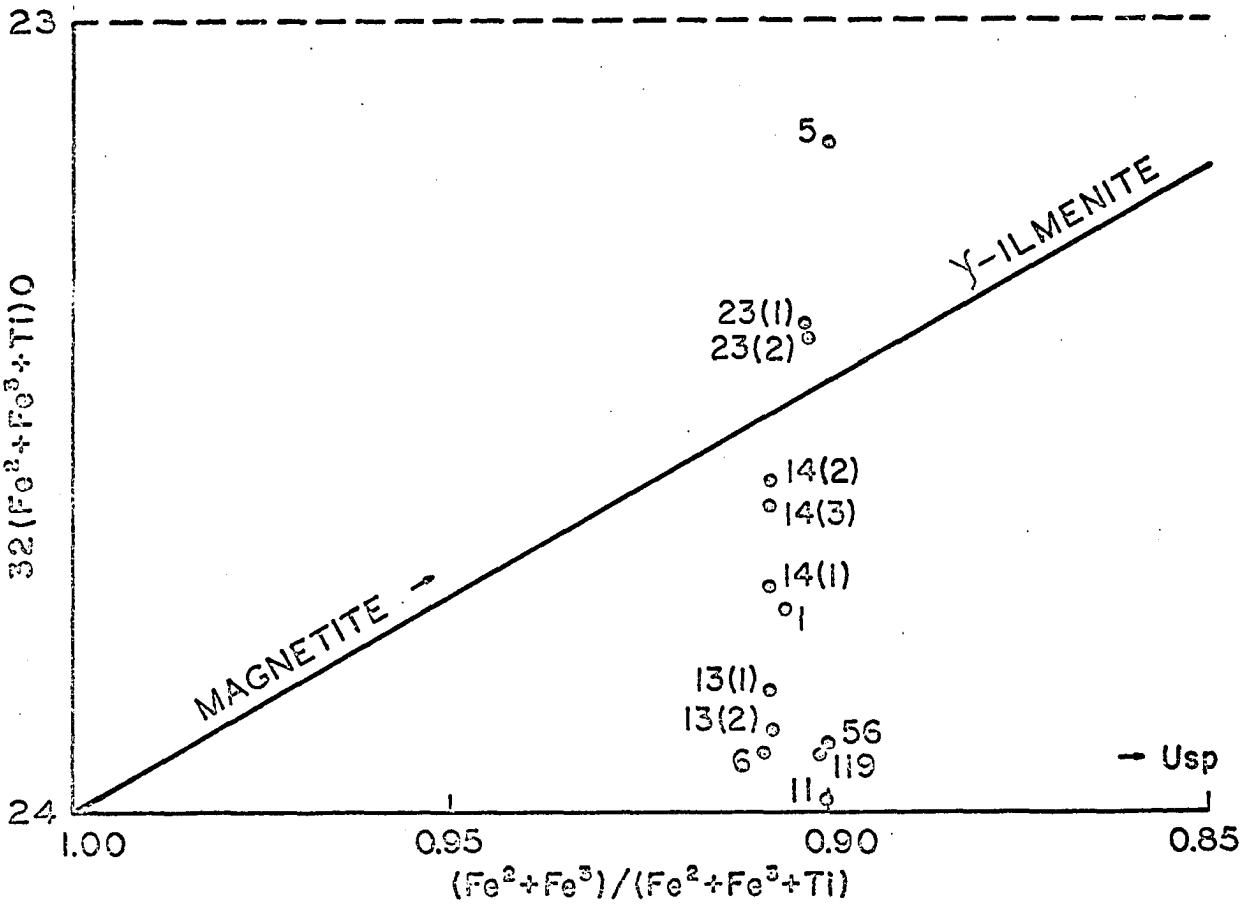

Fig. 8. Diagram showing the oxidation trend of analyzed magnetite and the lack of correlation of the plots with magnetite-ilmenite join.

(1) Reaction relation of olivine (Kuno, 1950, p. 971; Muir, Tilley and Scoon, 1957, p. 252) leading to vermicular magnetite swarms.

(2) Progressive oxidation relations shown by olivine and magnesioferrite, where

olivine enstatite magnesioferrite

$$2Mg_2SiO_4 + Fe^2_2SiO_4 + 1/2\ O_2 = 3MgSiO_3 + MgFe^3_2O_4$$ (Yoder and Tilley, 1962, p. 426)

is followed by the reaction

olivine magnesioferrite enstatite magnetite

$$Mg_2SiO_4 + 2Fe_2SiO_4 + MgFe^3_2O_4 + 1/2\ O_2 = 3MgSiO_3 + 2Fe^2Fe^3_2O_4$$

(Ödman, 1932; Ramdohr, 1940; Muan and Osborn, 1956; Yoder and Tilley, op. cit.):

(3) Oxidation of clinopyroxene (Yoder and Tilley, op. cit.)

hedenbergite Magnetite wollastonite + increasing Di mol.

$$6\ CaFe^2Si_2O_6 + O_2 = 2\ Fe_3O_4 + 6\ CaSiO_3 + 6\ SiO_2$$

Under the microscope magnetite chiefly occurs as individual grains, aggregates and microphenocrysts. Magnetite of types (1) and (2) mentioned above is not quantitatively important in the Trident samples. Magnetite of the type, described in (3) above, seems to be absent. The minor ilmenite-hematite peaks detected in the diffraction patterns of M-5, 6 and 23 could be due to a coexistent primary rhombohedral phase or incipient exsolution of rhombohedral phase subsequent to sub-solidus oxidation. The latter origin is preferred. The presence of a trace rhombohedral phase is not of major significance in the interpretation of the compositional data.

Unit Cell Dimension and Chemical Composition

From Katsura and Kushiro's observations (op. cit., pp. 142, 144) and from table 11 it is apparent that the 'a' unit cell parameter of magnetite, varies inversely with 32 (ΣFe+Ti)/O and also with the ratio ΣFe/(ΣFe+Ti) to some extent. Among the solid solution series in the $FeO-Fe_2O_3-TiO_2$ system, the only spinel phases are ulvöspinel (Usp), magnetite (Mt) and maghemite (Mht), and Mht is the only phase with a cation deficiency (Verwey, 1935, cited in Deer, Howie and Zussman, 1962, v.5, p. 58) cation deficiency observed in the analyzed magnetite can, thus, be attributed to the presence of Mht, held in solid solution, or, these particular magnetites could be considered as solid solutions of Usp, Mt and Mht. The variation in unit cell dimensions should show some systematic correlation with the molecular proportions of the components; and magnetite analyses should be recalculated in terms of the three end members before any correlation between chemical composition and geometry of the unit cell is attempted.

Considerable controversy attends the end member composition of magnetite, as recalculated from chemical analyses, with specific accent on single phase homogeneous magnetite from volcanic rocks. If, however, the cation deficiency is entirely due to the presence of the Mht, and if the excess mol.% Fe_2O_3, which remains after the composition is recalculated in terms of Usp and Mt molecules, shows a linear covariance with vacancies, the recalculated composition is acceptable.

Recalculated magnetite analyses are listed tables 12 and 13. Considering the inverse spinel structure of the Usp, Mt and Mht end members, the cations would be distributed between the tetrahedral and octahedral sites of the Usp and Mt members in the manner shown in table 12.

Table 12. Distribution of Cations (32-oxygen basis) in Tetrahedral and Octahedral Sites in Magnetite.

S. Nos.	Tetrahedral Site		Octahedral Site			Fe^3	Total
	Ti (Usp)	Fe^3 (Mt)	Fe^2 (Mt)	Fe^2 (Mt)	Fe^2 (Usp)	Assigned to Mht (γ-Fe_2O_3)	Cation Deficiency
M-11	2.40	5.53	5.53	5.53	4.80	0.19	0.02
M-56	2.40	5.35	5.35	5.35	4.80	0.66	0.09
M-14(2)	2.18	4.56	4.56	4.56	4.36	3.36	0.42
M-1	2.24	4.98	4.98	4.98	4.48	2.08	0.26
M-5	2.33	3.30	3.30	3.30	4.66	6.46	0.85
M-6	2.20	5.54	5.54	5.54	4.40	0.70	0.08
M-23(1)	2.27	3.86	3.86	3.86	4.54	4.99	0.62
M-13(1)	2.20	5.31	5.31	5.31	4.40	1.31	0.16

Table 13. End Member Composition of Analyzed Magnetite.

S. Nos.	Mol. %.		
	Usp	Mt	Mht
M-11	30.02	69.18	0.80
M-56	30.11	67.12	2.77
M-14(2)	27.73	58.01	14.26
M-1	28.30	62.93	8.77
M-5	30.19	42.76	27.05
M-6	27.59	69.48	2.93
M-23(1)	29.12	49.52	21.36
M-13(1)	27.68	66.82	5.50

Table 14. Calculated vs. Observed Cell Parameters (a Å) of Analyzed Magnetite.

S. Nos.	Calculated Cell Parameter a(Å)	Observed Cell Parameter a(Å)
M-11	8.436	8.424
M-56	8.434	8.422
M-14(2)	8.425	8.418
M-1	8.429	8.408
M-5	8.421	8.397
M-6	8.431	8.401
M-23(1)	8.423	8.399
M-13(1)	8.430	8.426

Excess Fe_2O_3 (Fe^3) and the cation deficiencies are also listed in table 12. The diagram shown as fig. 9, documents the covariant relationship between the maghemite molecule and cation deficiencies in the magnetite lattice, and confirms the fact that the analyzed magnetites are Usp-Mt-Mht solid solutions. The close agreement between calculated and measured cell dimensions (deviation <0.4%), as shown in table 14, reinforces the validity of the recalculated compositions and further indicates that the 'a' unit cell parameter is related to the relative molecular proportions of Usp, Mt and Mht.

The above correlation is further explored in figs. 10 and 11, where the 'a' parameter has been plotted against $Fe^2/ (Fe^2+Fe^3)$ and 32 $(Fe^2+Fe^3)/0$ respectively. This demonstrates the inverse relation between 'a' and (Mt+Mht) mol.%. Two distinct trends are defined by plots of magnetite samples 11-56-1, 13-14 and 6-23-5. The former corresponds to the Usp-Mt transformation (cf. Lindsley, 1965a, p.145, fig. 45) and the latter to Mt-Mht transformation. The separation between these two trends is more distinct in fig. 11. In the former trend the effect of a change in ΣFe is greater as compared to that in the latter group. Normally transformations within the Usp-Mt-Mht series due to sub-solidus oxidation would not involve a change in ΣFe unless exsolution of the Fe_2O_3 bearing phase occurs, which is related to the rate of cooling. Incipient exsolution of Fe_2O_3 from Fe-Ti spinels would be aided by slow cooling and retarded or avoided during rapid cooling following crystallization. Thus, magnetite samples 11, 56, 1, 13 and 14 were apparently crystallized when the cooling was more rapid and the latter group during a period of slow cooling. The presence of sub-solidus oxidation of Usp→Mt in the former group suggests a low partial pressure of oxygen, while the Mt→Mht trend

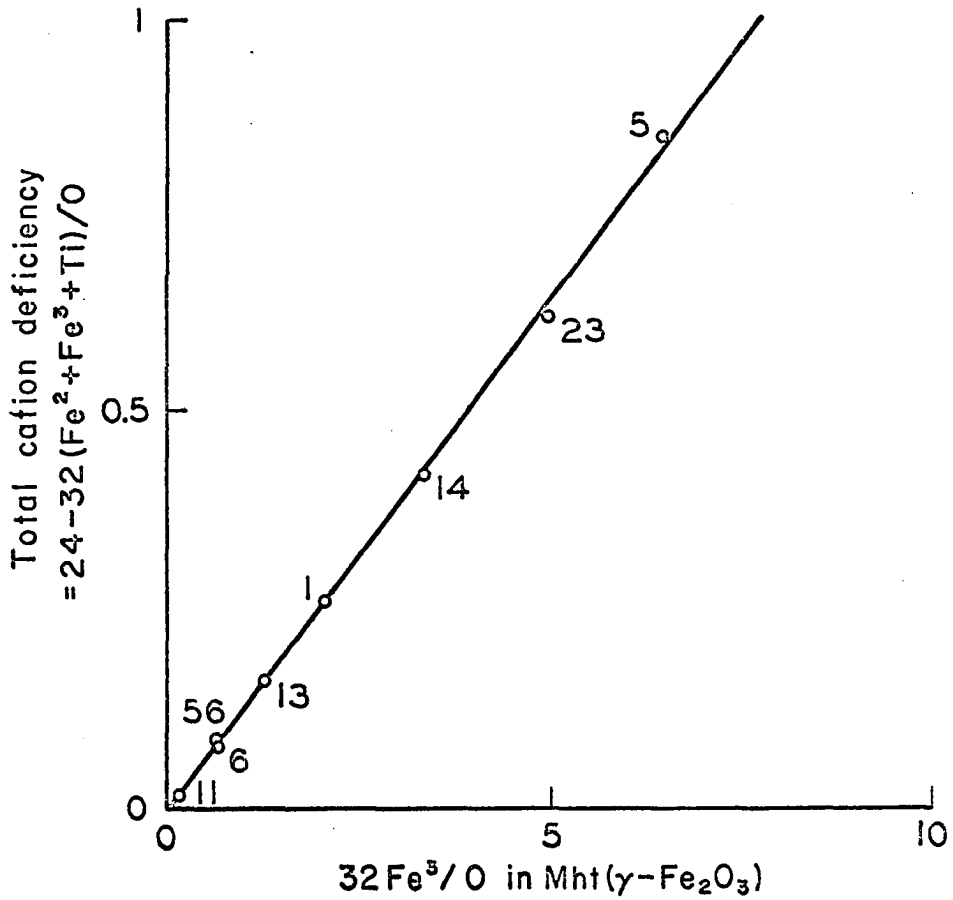

Fig. 9. Diagram showing the correlation between the atomic proportion of Fe^3 in maghemite solid solution vs. calculated cation deficiency.

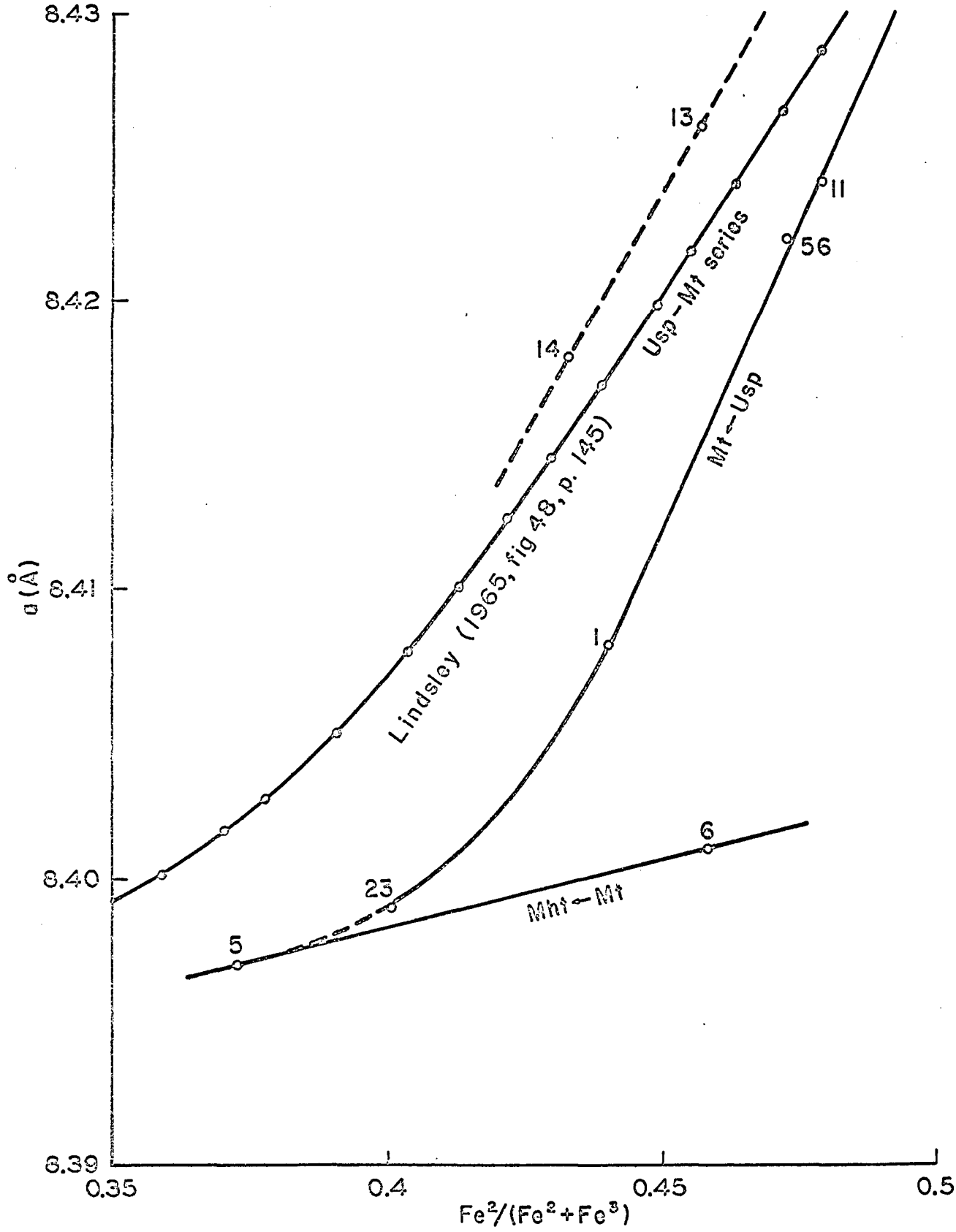

Fig. 10. Plot showing correlation between lattice parameter and $Fe^2/(Fe^2+Fe^3)$ ratio of analyzed magnetite from the Trident andesites. Note parallelism of Usp-Mt trend with the curve obtained by Lindsley (1965a, fig. 48, p. 145) for the synthetic members in the Usp-Mt series.

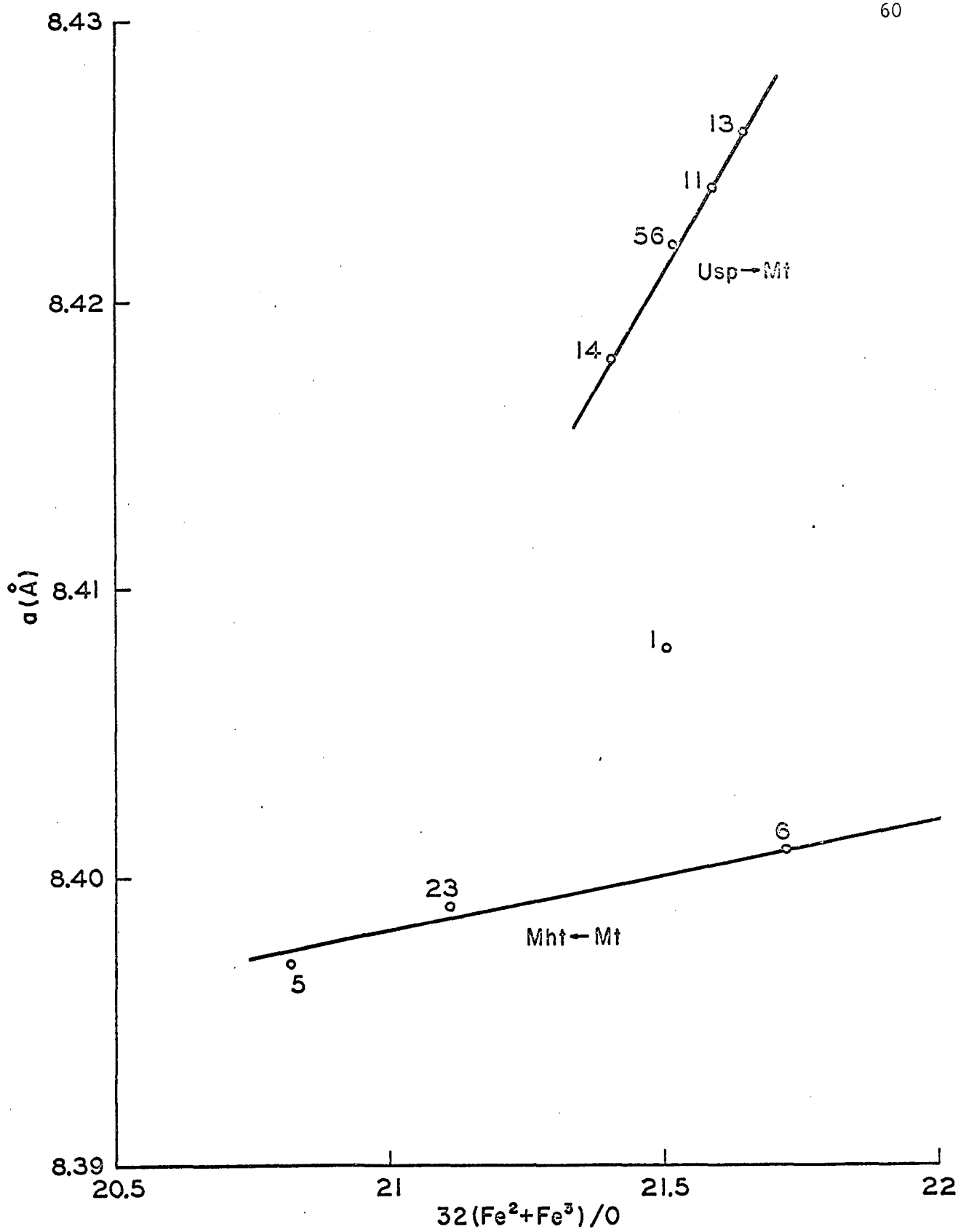

Fig. 11. Plot showing correlation between the 'a' lattice parameter and atomic proportions of ΣFe in analyzed magnetite. Note separation of the Usp-Mt and Mt-Mht trends.

of the latter group infers higher P_{O_2}, as interpreted from Usp and Mt oxidation trends, discussed by Buddington and Lindsley (1964, pp. 349 and 354). In crystallization sequence magnetite specimens 6, 23 and 5 must have crystallized relatively earlier than those in the other group as indicated by P_{O_2} conditions (Yoder and Tilley, 1962, p. 384; Muan and Osborn, 1956, p. 133). P_{O_2} variations are usually related to variations in water pressure; and increasing water pressure with no escape of H_2 may effectively reduce P_{O_2}. It is possible that the magnetites 11, 56, 1, 13 and 14 may have crystallized under conditions of increasing water pressure. Such conditions would not only retard the oxidation to Usp→Mt only, but would prevent the formation of Fe_2O_3 bearing rhombohedral phases also (David and Welch, 1956) and thus prevent exsolution.

Packing Index:

The packing indices of the magnetite have been plotted against Fe^3 as Mht in fig. 12. The parameters of the three end member components are Usp-8.53 Å, Mt-8.396 Å and Mht-8.34 Å (Deer et al,op.cit.,p.55). Thus, increasing proportions of the Mht molecule would tend to reduce the cell volume and increase the packing index and the cation deficiency. The trends defined by plots of magnetite specimens 11, 56, 1, 13 and 14 in fig. 12 follow this concept. Fe_2O_3 has been retained. The reverse trend shown by 6, 23 and 5 imply an incipient exsolution of some Fe_2O_3 as rhombohedral phase, whereby cell volume increased and packing index decreased.

Packing Indices and Sequence of Crystallization

Packing indices are related to temperature and pressure, and with progressive fractionation, the packing indices of clinopyroxenes decrease (Yamaguchi, 1964, p. 208). As a thermodynamic consideration, the packing

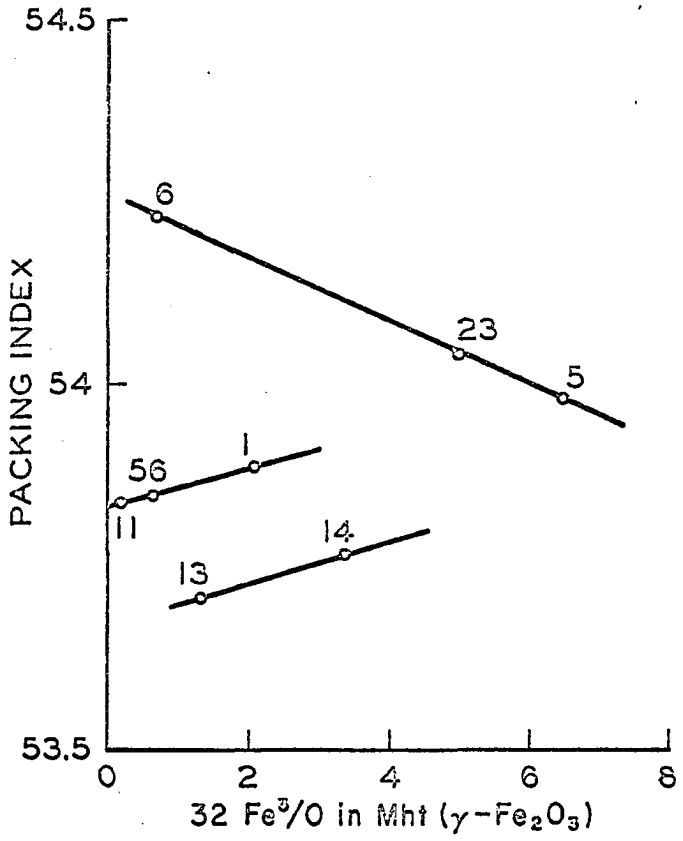

Fig. 12. Plot showing the divergent relations of the two groups of analyzed magnetite in respect of Fe^{3} in maghemite vs. packing indices.

index may be meaningful in other solid solution series. In these magnetites the sequence of decreasing packing indices is 6, 23, 5, 1, 56, 11, 14 and 13. If the parent andesites (1953-63) of these magnetite samples are considered to be derived from the same parent magma, then this sequence of crystallization assumes special significance.

Three factors may be of importance in deciphering the relative sequence of crystallization of magnetite including packing indices; Usp content in mol.% (as implied by Buddington and Lindsley, op. cit., p.345); and cation deficiency or Mht content in mol.% (Katsura, 1964, p. 228). Table 15 below, evaluates the comparative order of crystallization, as indicated by these three parameters:

Table 15. Comparative Order of Crystallization of the Analyzed Magnetite as Indicated by Different Parameters.

	Packing Index	Usp mol.%	Cation deficiency/Mht mol.%
Late	13	6	5
	14	13	23
	11	14	14
	56	1	1
	1	23	13
	5	11	6
	23	56	56
Early	6	5	11

Dates of eruption of the host andesites : M-11, 56 - 1953; M-13 - 1954; M-14 - 1957, M-1 - 1958; M-5,6 - 1959; M-23 - 1960.

As discussed earlier, calculated cation deficiencies are largely determined by oxidation of Fe^2 and, therefore, of questionable significance under varying P_{O_2}. Usp mol.% content is related to temperature and the molar concentration of TiO_2 at the time of crystallization. TiO_2 concentrations do not decrease uniformly during fractionation (Wager, 1960), and this factor introduces an element of unreliability in the status of the Usp content of magnetite as a meaningful index. Packing indices, besides their thermodynamic significance, combines the effects of the two other parameters, and are, therefore, believed to be more directly related to order of crystallization than Usp/Mht content.

Petrogenetic Significance

In fig. 7 two distinct magnetite trends were defined by group 1 (specimens 6, 23 and 5) which crystallized under high P_{O_2} and group 2 (specimens 11, 56 and 14) which crystallized under under lower P_{O_2} and increased water pressure. Magnetite specimens 1 and 13 occupy intermediate positions. Katsura (op. cit., p.227) has compared the compositional fields of titanomagnetite from Hawaiian Alkali-olivine basalts and rocks of the Japanese calc-alkali series. The trend shown by the former, considered by Katsura to be an oxidation trend, is parallel to (1) above. Katsura observed that magnetites from the calc-alkali series of Japan define a trend which is close to Usp-Mt join; and with continued differentiation there is a decrease in TiO_2 content (ibid., p.228). He also noted the absence of highly oxidized phases. The trend shown by group (2) above parallels Katsura's calc-alkali magnetite trend. Although these trends are parallel, the composition of the analyzed Trident magnetites are dissimilar to the magnetites from the alakali basalts or calc-alkali rocks discussed by Katsura. The coexistence of both trends in one series of andesites

contradicts the implied uniqueness of such trends for a particular rock suite.

The initial composition of nucleated magnetite in the Usp-Mt series is essentially determined by temperature and the molar concentration of TiO_2; and the final composition, as implied by the preceding discussions, is controlled by variance in oxygen and water pressures during crystallization and sub-solidus oxidation, and also by the thermal gradients during final cooling. The two trends described above must therefore, be interpreted as Mt→Mht and Usp→Mt oxidation trends occurring under high vs low oxygen pressures, and/or low and high water pressures respectively. These trends are probably controlled by local thermodynamic environments and they may not be unique petrogenetic indices of a particular suite, such as the calc-alkali series.

ORTHOPYROXENE

The chemical analyses, structural formulae and related data for orthopyroxenes from Trident andesites are listed in tables 16-18. The composition of the orthopyroxenes has been plotted on a standard Ca-Mg-(Fe^{2}+Fe^{3}+Mn) diagram shown as fig. 13. The plots are all in the compositional field of magnesian pigeonite.

In the calculation of the structural formulae of the orthopyroxenes (table 17), it has been assumed that the Z - site should be filled (Kuno, 1954b, p.32). From the data presented in tables 17 and 18 it can be seen that the analyzed orthopyroxenes are Al-deficient with the exception of specimens 6R and 23. In the former case, following convention, Ti has been added to Si, and the remaining requirements of the Z-site have been filled with Al, and Fe^{3} when necessary.

Table 16, Chemical Composition of Analyzed Orthopyroxene.

S. Nos. / Component	0-56	0-14	0-1	0-6R	0-6	0-23	0-13
SiO_2	51.62	51.87	50.60	51.90	50.71	52.95	51.74
TiO_2	0.78	0.44	0.73	0.84	0.88	0.88	0.68
Al_2O_3	1.25	1.46	2.71	1.73	1.02	2.88	1.41
Fe_2O_3	2.45	1.18	3.48	2.09	5.15	2.99	1.70
FeO	18.18	18.81	15.64	16.91	13.75	15.16	18.18
MnO	0.75	0.74	0.70	0.78	0.63	0.63	0.78
MgO	21.92	22.04	21.24	20.09	19.91	19.06	21.11
CaO	2.77	2.63	4.56	4.69	6.89	4.26	3.67
Na_2O	0.37	0.52	0.43	0.38	0.51	1.06	0.36
K_2O	0.12	0.14	0.26	0.19	0.17	0.10	0.14
H_2O^-	0.00	0.00	0.00	0.00	0.00	0.05	0.00
H_2O^+	0.08	0.12	0.04	0.10	0.12	0.12	0.11
P_2O_5	0.06	0.14	0.15	0.09	0.12	0.11	0.13
Total	100.35	100.09	100.54	99.79	99.86	100.25	100.01
Ni	0.011	0.009	0.017	0.026	0.011	0.011	0.021
Cr	0.013	0.008	0.013	0.018	0.017	0.023	0.0096
Mol.%							
Ca	5.58	5.32	9.24	9.78	13.95	9.42	7.48
Mg	61.25	62.11	59.93	58.32	56.04	58.69	59.87
$Fe^{2+}+Fe^{3+}+Mn$	33.17	32.57	30.83	31.90	30.01	31.89	32.63

Analyst: H. Haramura

Table 17. Structural Formulae of Analyzed Orthopyroxene, Based on 6-oxygens.

S. Nos: / Cations	0-56	0-14	0-1	0-6R	0-6	0-23	0-13
Si	1.916	1.927	1.870	1.932	1.895	1.945	1.927
Al	0.055	0.061	0.110	0.068	0.045	0.055	0.054
		0.003	0.008	0.008		0.069	0.008
Ti	0.022	0.012	0.020	0.024	0.025	0.024	0.019
Fe^{3+}	0.007	0.033	0.097	0.059	0.035	0.083	0.048
	0.062				0.110		
Fe^{2+}	0.566	0.587	0.485	0.528	0.431	0.467	0.568
Mn	0.024	0.023	0.022	0.025	0.020	0.019	0.025
Mg	1.217	1.226	1.174	1.119	1.113	1.047	1.176
Ca	0.111	0.105	0.181	0.188	0.277	0.168	0.147
Na	0.027	0.038	0.031	0.028	0.037	0.076	0.026
K	0.006	0.007	0.012	0.009	0.008	0.005	0.007
P	0.002	0.004	0.005	0.003	0.004	0.003	0.004
Ni	0.0004	0.0003	0.0006	0.001	0.0004	0.0004	0.001
Cr	0.0006	0.0003	0.0006	0.0008	0.0007	0.0009	0.0004
Z	2.000	2.000	2.000	2.000	2.000	2.000	2.000
XY	2.016	2.026	2.016	1.993	2.001	1.962	2.010

Table 18. Cation Proportions Recalculated to 4 and Molecular Norm of Analyzed Orthopyroxene.

	0-56	0-14	0-1	0-6R	0-6	0-23	0-13
Si	1.908	1.914	1.862	1.935	1.895	1.963	1.922
Al	0.055	0.064	0.118	0.076	0.045	0.125	0.062
Ti	0.022	0.012	0.020	0.024	0.025	0.024	0.019
Fe^{3+}	0.069	0.033	0.097	0.059	0.145	0.084	0.048
Fe^{2}	0.564	0.583	0.483	0.529	0.431	0.471	0.567
Mn	0.024	0.023	0.022	0.025	0.020	0.019	0.025
Mg	1.212	1.218	1.169	1.121	1.113	1.057	1.173
Ca	0.111	0.104	0.180	0.188	0.277	0.170	0.146
Na	0.027	0.038	0.031	0.028	0.037	0.077	0.026
K	0.006	0.007	0.012	0.009	0.008	0.005	0.007
D	0.002	0.004	0.005	0.003	0.004	0.003	0.004
Ni	0.0004	0.0003	0.0006	0.001	0.0004	0.0004	0.001
Cr	0.0006	0.0003	0.0006	0.001	0.0007	0.0009	0.000
$\frac{100(Fe^{2}+Fe^{3}+Mn)}{\Sigma Fe + Mg}$	35.15	34.41	33.99	35.35	34.87	35.19	35.30
$100Fe^{2}/(Fe^{2+}+Mg)$	31.76	32.37	29.23	32.06	27.91	30.82	32.59
Qz	0.00	0.00	0.00	0.19	0.72	1.44	0.00
Or	0.70	0.82	1.52	1.13	1.01	0.59	0.83
Ab	3.32	4.66	3.84	3.44	4.61	9.53	3.24
An	1.39	1.23	4.67	2.47	0.00	2.81	1.82
Ne	0.00	0.00	0.00	0.00	0.00	0.00	0.00
Di	9.56	8.70	13.49	16.33	27.00	14.12	12.49
Hy	77.94	74.08	65.82	72.84	59.70	66.90	75.21
En	54.18	50.24	47.93	50.34	45.30	47.71	51.24
Fs	23.76	23.83	17.88	22.50	14.40	19.18	23.96
Ol	3.27	8.35	5.69	0.00	0.00	0.00	3.37
Fo	2.27	5.66	4.14				2.30
Fa	0.99	2.68	1.54				1.07
Mt	2.56	1.23	3.62	2.20	5.43	3.13	1.78
Il	1.08	0.61	1.01	1.18	1.23	1.22	0.95
Ap	0.12	0.29	0.31	0.18	0.25	0.23	0.27

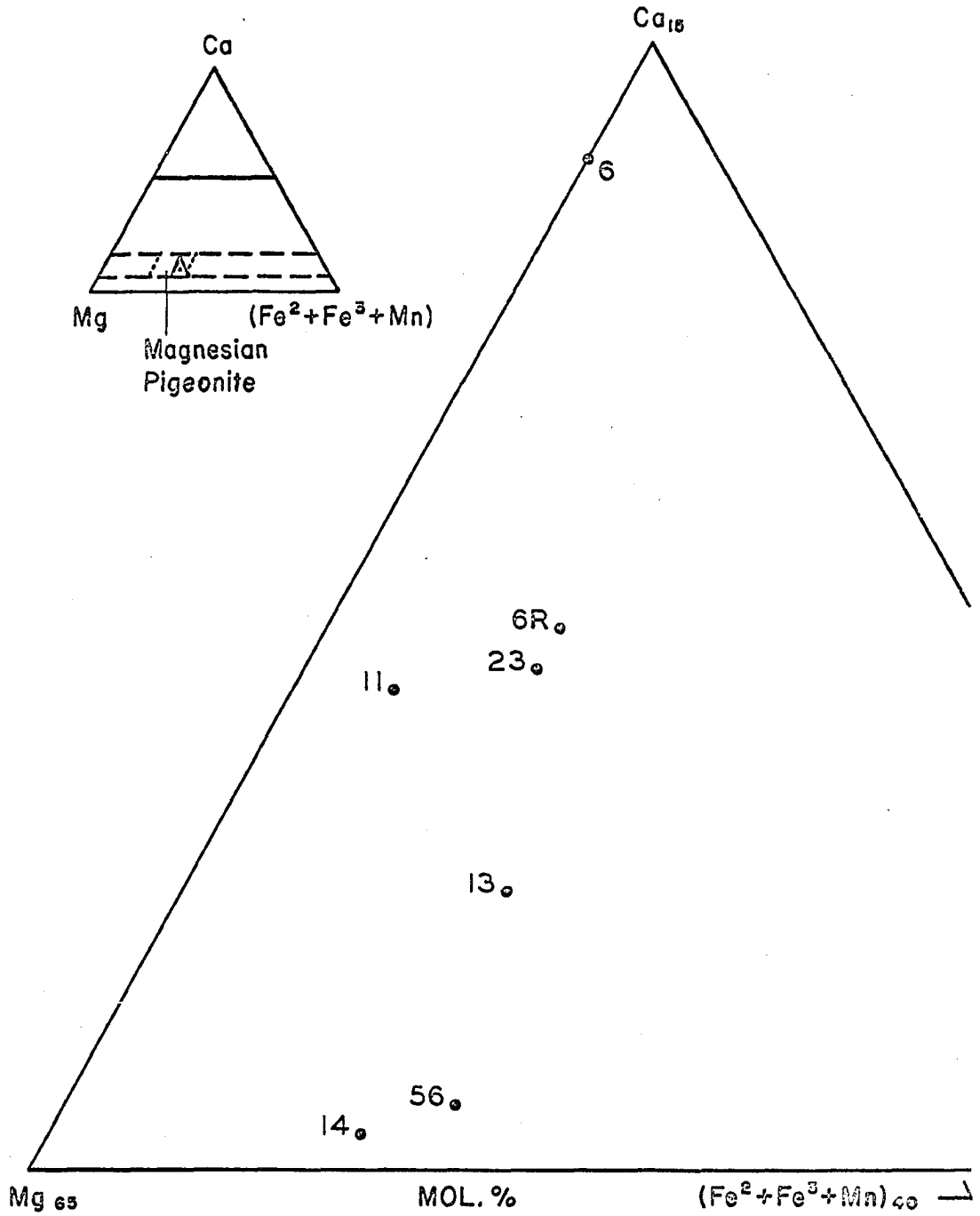

Fig. 13. Chemical composition of analyzed orthopyroxene from the Trident andesites as plotted on a standard Ca-Mg-(Fe^{2}+ Fe^{3}+Mn) diagram. The plots fall in the field of magnesian pigeonite as shown in the inset triangle covering the complete pyroxene field.

Optical Properties and Chemical Composition

As discussed in Chapter II, orthopyroxenes from the same rock display a range in optical properties, which is related to compositional variations. The chemically analyzed orthopyroxene separates represent the average composition of both phenocrysts and microphenocrysts. The optical properties and the molecular ratios of the end members of the analyzed orthopyroxenes are listed in table 19.

Kuno (op. cit.) in his studies of orthopyroxenes from volcanic rocks, has given data for compositionally similar orthopyroxenes (table 20). Generally the data in tables 19 and 20 are comparable, indicating fair correlation between the indices of refraction and the Fe:Mg ratios. Correlation based on the $2V_x$ of the analyzed orthopyroxenes appears to be less reliable, although the actual plots (those in table 20 being mean values) in Kuno's diagram (op. cit., fig. 1, p.40) define a field which includes $2V_x$ values measured in the Trident orthopyroxenes.

Hess (1952) and Kuno (op. cit.) had observed that increasing Al content (> 0.070) is accompanied by an increase in N_Z; a tendency shown by 0-1, 0-6R and 0-23 (table 21). The above authors have suggested that high Ca content does not affect N_Z; a proposal which seems to be refuted by the correlation offered by the data in table 21. In orthopyroxenes with Al>0.070 there is an apparent inverse correlation between Al content and N_Z. There also appears to be an inverse covariance between Ca and Al. Deer et al (Vol. 2, 1963, p.29) and Hess (op. cit.) have also suggested that high Ca content might be related to higher optic axial angles of orthopyroxenes from volcanic rocks. However, the data in table 21 reveal an inverse relation defined by increasing Ca content vs a decrease in $2V_x$.

Table 19. Optical Properties and Chemical Composition of Analyzed Orthopyroxene.

S. Nos.	$2V_x$	N_x	N_z	100 Fe: (Fe+Mg)	Mol. % $Ca_2Si_2O_6$	$Mg_2Si_2O_6$	$(Fe)_2Si_2O_6$
O-56	60-57	1.690	1.702	35.15	5.58	61.25	33.17
O-14	58-56	1.688	1.701	34.41	5.32	62.11	32.57
O-1	56	1.694	1.707	33.99	9.24	59.93	30.83
O-6R	57-52	1.696	1.709	35.35	9.78	58.32	31.90
O-6	57-45			34.87	13.95	56.04	30.01
O-23	57-55	1.693	1.706	35.19	9.42	58.69	31.89
O-13	57	1.690	1.703	35.30	7.48	59.87	32.63

Table 20. Optical Properties and Chemical Composition of Orthopyroxene from Dacites, Andesite and Amphibolite, cited in Kuno, (1954b, p. 39.)

S. Nos.	$2V_x$	N_x	N_z	Range of N_z	Fe:(Fe + Mg)	6Al/O	6Ca/O
9-Dacite	60.5°	1.6915	1.7055	0.0045	34:66	0.084	0.024
10- "	63.5°	1.6955	1.7075	0.0025	34:66	0.040	0.029
11-Andesite	60.0°	1.6945	1.7075	0.0025	35:66	0.018	0.033
12-Amphibolite	58.0°	1.693	1.709	0.001	36:64	0.053	0.031

Table 21. Relation between Atomic Proportions of Al and Ca and Optical Properties of Analyzed Orthopyroxene.

S. Nos.	$2V_x$ ± 1° (max)	N_z ± 0.001	6Al/O	6Ca/O
O-23	57	1.706	0.125	0.170
O-1	56	1.707	0.118	0.180
O-6R	57	1.709	0.076	0.188
O-14	58	1.701	0.064	0.104
O-13	57	1.703	0.062	0.146
O-56	60	1.702	0.055	0.111

Zoned orthopyroxenes with iron rich rims (showing abnormally low $2V_x$) are common in the Trident andesites. Lewis (1960) attributes this phenomenon to oxidation. Separates 0-6 and 0-23 contained a few of these grains, and it is interesting to note that these samples have the highest $6Fe^3/0$ values (0.145 and 0.084 respectively). Lewis (ibid., p. 1125) has also observed that compositionally similar orthopyroxenes from oxidized rocks give smaller values for $2V_x$ and N_z than those from the unoxidized equivalents. Orthopyroxenes No.9 to 11 of Kuno (op. cit., p.34), which have similar ΣFe:Mg ratios to the Trident orthopyroxenes, contain less than 0.040 $6Fe^3/0$. With the exception of 0-14, the Trident orthopyroxenes have a higher Fe^3 content. The low $2V_x$ and N_z values of the analyzed orthopyroxenes may be partially explained by the oxidation of $Fe^2 \rightarrow Fe^3$. The zoned pyroxenes with $2V_x$ as low as 36° may be the extreme products of oxidation.

Ca Content of Orthopyroxenes

The Trident orthopyroxenes are characterized by an unusually high Ca content (CaO wt.% - 2.63-6.89). Kuno (op. cit., pp. 35-38), in discussing the thermometric significance of the Ca content of orthopyroxenes from volcanic rocks, observed a 6Ca/0 range of 0.104 to 0.057 in andesites and 0.053 to 0.045 in dacites; and the higher 6Ca/0 value of 0.104 has been associated with higher temperatures of the pigeonitic series by Kuno (ibid., p. 38).

In a representative sample of orthopyroxenes from volcanic, plutonic and even metamorphic rocks (Deer, et al, op. cit., pp. 15-22) the 6Ca/0 value rarely exceeds 0.104. (Igneous maximum = 0.106; Metamorphic = 0.162). Atlas (1952) had indicated that the maximum possible replacement of Mg by Ca in the $MgSiO_3$ molecule is 0.115 at 1100°C. This observation agreed well

with Kuno's observations, and thus fixed the upper limit of 6Ca/O at 0.115 for orthopyroxenes from volcanic rocks. High Ca-orthopyroxenes reported by Groves (1935) were considered to be contaminated by clinopyroxene. These criteria were used to define the separation between the hypersthene and pigeonite fields at 5% mol. $CaSiO_3$ in the pyroxene quadrilateral.

In the light of the above discussion, the Trident orthopyroxenes are most unusual. They do not show any microscopic evidence of exsolution lamellae; and serious clinopyroxene contamination is unlikely. X-ray diffraction runs confirmed the high purity 0-56, 14, 1 and 13. Very minor clinopyroxene contamination was revealed in 0-23, 6 and 6R, but contamination is below 5%. Calculations also showed that 5% contamination by coexistent clinopyroxene would increase the CaO content by less than 0.6 wt.% or approximately 0.025 Ca on 6-oxygens (as in the case of 0-6). The high Ca content of the analyzed orthopyroxenes is, therefore, real.

Kuno's generalization concerning a maximum 6Ca/O content of 0.115 for orthopyroxenes from volcanic rocks is also contradicted by occurrences such as the bronzite from a metamorphosed (?) ejected block of picrite basalt from Kilauea (ΣFe:Mg = 24.2:75.8; $CaSiO_3$ mol. = 8.5%; 6Ca/O = 0.162; CaO = 4.19 wt.%), as described by Muir et al (1957); and hypersthene from a hypersthene basalt, 1887 flow of Mauna Loa ($CaSiO_3$ mol. = 13.13%; 6Ca/O = 0.255; CaO = 6.65 wt.%), as discussed by Tilley and Scoon (1961, p. 63). It should be noted that the solvus curve, as determined by Atlas (op. cit.) has a precision of $\pm$ 3% (mol.) which is a fairly large error when compared to the 6-1 mol.% variation in $CaSiO_3$, seen in the solvus range between 1100°C and 700°C. Furthermore, Atlas' diagram concerns the $Mg_2Si_2O_6$ and $CaMgSi_2O_6$ end members only. The role of the Ca-Fe end members was not considered. The studies of Bowen, Schairer and Posnjak (1933) on

the CaO-FeO-SiO_2 system shows that 74 mol.% solubility of $FeSiO_3$ in monoclinc $CaSiO_3$ is possible, which would invert below 940°C to low-temperature $wollastonite_{ss}$ (monoclinc parawollastonite and triclinic wollastonite). The minimum Ca content of $ferrosilite_{ss}$ would be 26 mol.%, and a lesser content of Ca would induce the fayalite + tridymite reaction in the above sytem. These relations are important to the discussion of high Ca orthopyroxenes.

Recent studies on polymorphic transitions have challenged the ortho/clinopyroxene inversion curve for magmatic pyroxenes (Brown, 1957). Exsolution lamellae bearing plutonic orthopyroxenes and pigeonites have also been at odds with the inversion curve. Barth (1951) found support for this ortho/clino inversion in his solvus schematic of the pyroxene quadrilateral. Unfortunately, however, Barth's interpretation of the data of Bowen. et al appears to have been in error. According to the prevailing concept of pyroxene crystallization, the high temperature phase is monoclinic, which is succeeded under sub-solvus temperature by Ca-poor (< 5 mol.%) orthopyroxene and Ca-rich clinopyroxene. Under conditions of a depressed liquidus, the early phase was orthopyroxene (Ca-poor) succeeded by pigeonite (Brown, op. cit.). The high temperature clinopyroxenes at the Mg and Fe ends of the series are in fact proto-pyroxenes (Sclar,et al, 1964; Boyd and England,1965, p. 118; Lindsley, 1965b, p.149), and the following low temperature phases are all orthorhombic. Ploymophism of similar nature has been demonstrated in the compositional range of Fs_{32-36} by Akimoto et al (1966, pp. 484-485) and Lindsley (op. cit., p. 149-150). The so-called inversion curve, in the light of the above data, is actually reversed; and the question is now raised as to whether pigeonites are all inverted orthopyroxenes.

Yoder, Tilley and Schairer (1963, p. 85; 1964, pp. 121-132) had prepared working liquidus diagrams for the system $CaSiO_3$-$FeSiO_3$, accompanied

by isothermal plane projections. In fig. 14 the liquidus diagram has been recast in mol.% of the pyroxene end members, and the solvus within the Di-Hd-En-Fs field has been extrapolated (fig. 15) from Atlas (op. cit.), Boyd and Schairer (1962) and Bowen et al (op. cit.). The configuration of the solvus surface is shown by isothermal contours. In the Wo-Fs system, the solidus intersects the solvus at $\sim$ 1100°C, which indicates that the solvus (a parabolic surface at the En-Di end, with a crestal axis parallel to the En-Fs join) would flatten out considerably before reaching the Wo-Fs join. Fig. 15 attempts to reconstruct the configuration of the solvus of possible members of the Di-En_{ss}+ Wo-Fs_{ss} series. The isotherm configuration (liquidus and solvus, figs. 14 and 15) supports a wider Ca-rich orthopyroxene stability field than usually accepted in the temperature range of magmatic crystallization. A comparison of the liquidus and solvus isotherms shows that the theoretical range of Ca content in orthorhombic pyroxene is $\sim$ 25 mol.% at 1275°C,$\sim$ 9 mol.% at 1100°C and $\sim$ 7 mol.% at 700°C (Fs = 20-55 mol.%). The temperatures are those of the solvus surface, and, thus, the above are stable compositions. These inferences are independent of the variations in the solidus - solvus intersections due to varying oxygen/water pressures. Although there is a theoretical gap between the liquidus for the orthorhombic phase and the solvus surface on the Ca-rich side, the solidus is likely to obliterate the orthopyroxene field completely in this part of the diagram. All naturally occurring pyroxene compositions in this field are singularly monoclinic.

The above considerations indicate the physico-chemical stability of high Ca-orthopyroxenes, and, therefore, the high-Ca-hypersthenes are not theoretically anomalous. The analyzed pyroxenes and the two occurrences (Kilauea and Mauna Loa) referred to earlier, have been plotted on fig. 15.

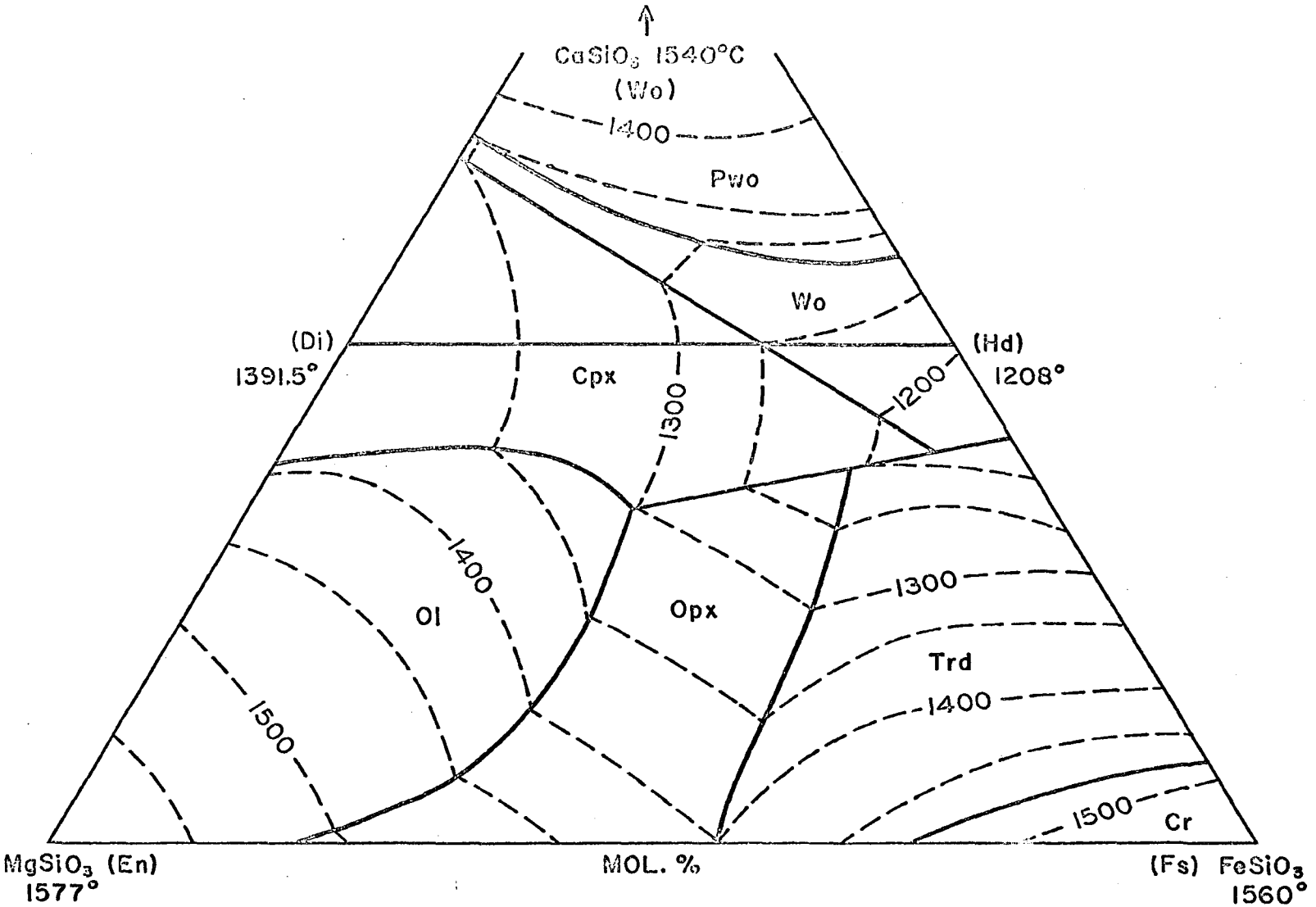

Fig. 14. Modified liquidus diagram after Yoder, Tilley and Schairer (1963, fig. 16, p.85).

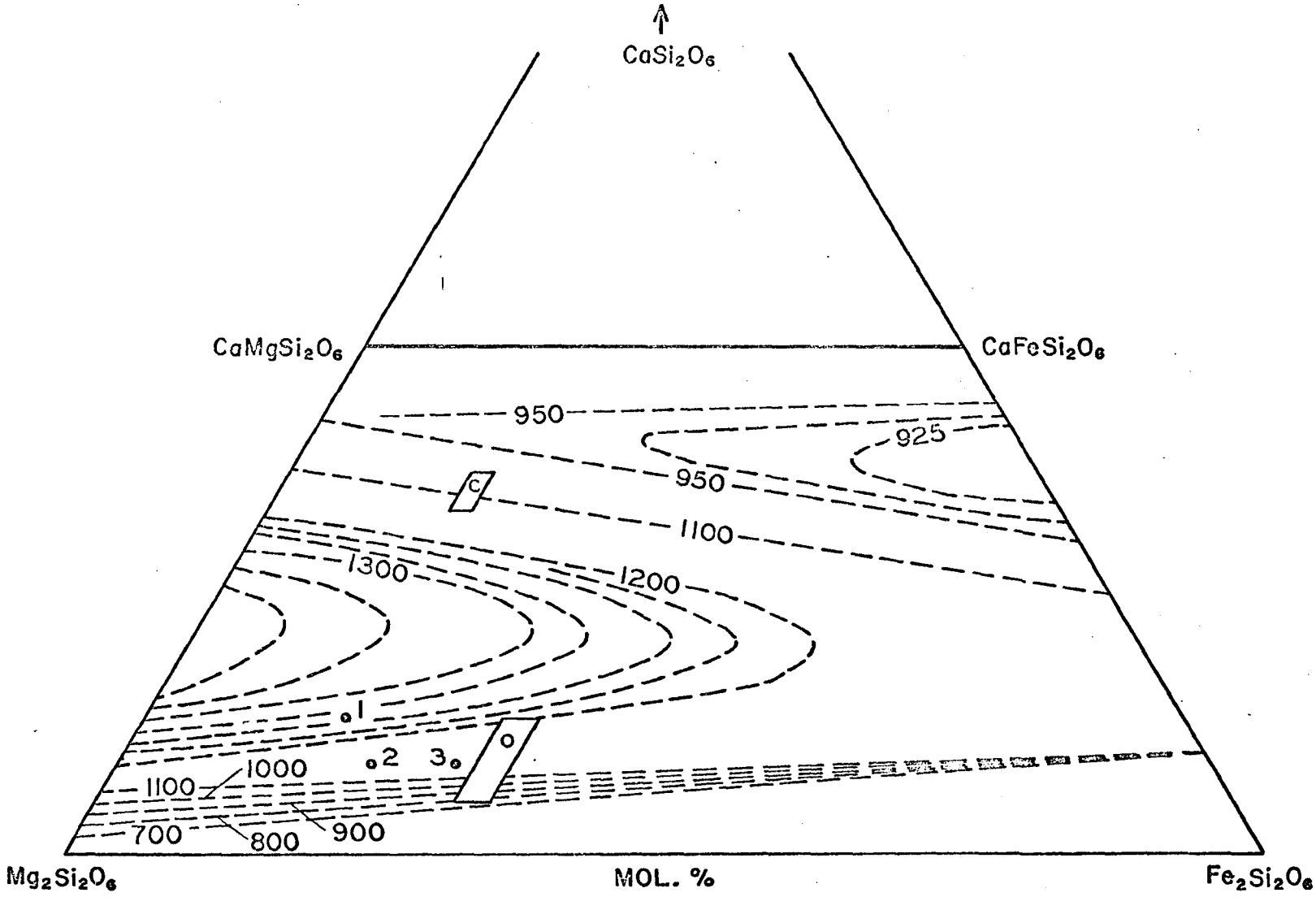

Fig. 15. Solvus projection for the $Mg_2Si_2O_6$-$CaMgSi_2O_6$ system (Atlas, 1952; Boyd and Schairer, 1962) and $CaSiO_3$-$FeSiO_3$ system (Bowen and others, 1933) with plots of Trident orthopyroxene (o), clinopyroxene (c), high-Ca orthopyroxene from hypersthene basalt, Mauna Loa (1), orthopyroxene (bronzite) from Kilauea picrite basalt (2) and pigeonite-hypersthene, Usugoya-Zawa (3). (Isothermals in degrees centigrade).

The composition of the high temperature orthorhombic polymorph of pigeonite from Usugoya-Zawa, reported by Kuno and Nagashima (1952) as cited by Akimoto et al (1966, p. 483), has also been plotted in the same diagram. The plots tend to confirm the validity of the extrapolated solvus surface configuration. The extrapolated solvus surface (fig. 15) may also explain the trends of clinopyroxene series from different igneous rock series, in terms of temperature gradients.

Unit Cell Parameters and Composition

Unit cell parameters were calculated for all seven samples using the (420), (121), (321), (621), (511), (421), (131), (202) and (430) reflections (obtained with a Norelco X-ray diffractometer, using CuKα radiation). a and b cell dimensions were calculated from the (610), (420) and (430) reflections, and the values were combined with (321) and (131) reflections to obtain the c cell dimension. The corrected 2θ values for all the reflections, cell parameters, unit cell volume, ionic volume per unit cell, and packing indices are given in tables 22 and 23 (data on ionic radii from Pauling, 1960; ionic volumes from Yamaguchi, 1964, p. 207).

Hess (1952) and Kuno (1954b) seem to have reversed the earlier conclusions of Ramberg and DeVore (1951) regarding the non-ideality of the En-Fs_{ss} series. Hess and Kuno demonstrated a linear correlation between a, b and c parameters and the Fs component in mol.%. They also showed, however, that variations could also be caused by Ca and Al content. Ramberg and DeVore had only investigated the effect produced by Al content; and Howie (1963) admitted the variations which were introduced by other cations but did not attribute these effects to a non-ideal solid solution series. The effects of varying Al, Ca, Fe^3 and Mn content on the orthopyroxene cell paramenters, as suggested by the above authors, are summarized in table 24.

Table 22. X-ray Data for Orthopyroxene (Cukα, Ni-filter, 35 kv, 15 ma).

	← 2 θ Angles in Degrees →						
S. Nos.	0-56	0-14	0-1	0-6R	0-6	0-23	0-13
hkl							
*420	28.05	28.03	28.09	27.99	28.05	27.97	28.10
121	26.65	?	?	26.80	26.83	26.73	?
*321	30.26	30.25	30.28	30.23	30.38	30.21	30.28
*610	31.03	31.03	31.07	30.97	31.01	30.96	31.07
511	31.60	31.53	31.61	31.51	31.53	?	31.60
421	32.96	32.97	32.99	32.91	32.95	32.93	32.98
*131	35.20	35.18	35.13	35.17	35.21	35.13	35.28
202	35.76	37.73	37.73	35.63	35.73	35.63	35.76
*430	36.20	36.18	36.19	36.15	36.15	36.15	36.28

*Reflections considered in calculations

Table 23. Unit Cell Data for Orthopyroxene.

S. Nos.	a (Å)	b (Å)	c (Å)	Cell Volume (Å^3)	Ionic Volume (Å^3)	Packing Index
0-56	18.2792	8.8626	5.2327	847.7039	1163.8400	13.729
0-14	18.2852	8.8702	5.2304	848.3363	1164.0689	13.720
0-1	18.2264	8.8698	5.2458	848.0598	1167.0276	13.760
0-6R	18.3291	8.8730	5.2210	849.1127	1166.9040	13.744
0-6	18.2652	8.8754	5.1836	840.3184	1170.9168	13.936
0-23	18.3944	8.8569	5.2624	857.2395	1165.7872	13.600
0-13	18.2613	8.8402	5.2352	845.1369	1165.3232	13.788

Table 24. Effects of Al, Ca, Fe^3 and Mn on Unit Cell Parameters of Orthopyroxene as Suggested in Previous Studies.

Cations and Coordinations	a(Å)	b(Å)	c(Å)	Ref.
Al(iv)	+	?	?	1
Al(vi)	-	?	?	1,4
Al(?)	n.e	-	+ or n.e	2,3,4
Fe^3(vi)	-	?	?	2
Fe^3(iv)	?	?	?	
Fe^3(?)	-	-	n.e	2,4
Ca	+	n.e	+ (small)	2,3,4
Mn	+	+	+	4

n.e. - No effect
1 - Ramberg & Devore, 1951, p. 206
2 - Hess. 1952, pp. 181 and 186
3 - Kuno, 1954b, pp. 43-44
4 - Howie, 1963, pp. 220-1.

Both Hess and Kuno agreed that the effects of minor substitutions are the least in the c cell parameter; and Howie (op. cit.), emphasizing this point, considered the c parameter to be the most reliable index for compositional extrapolations. The tabulation in table 24 reveals the paucity of data on the effects of cations, but most sources agree on the negative effect of increasing Al on b and the positive effect of increasing Ca on a and c. These effects are, in turn, superimposed on the initial parameters determined by the molecular proportions of En and Fs. The a, b and c cell parameters of the analyzed orthopyroxenes have been plotted against $(Fe^2,Fe^3,Mn)SiO_3$ (mol.%), following Hess and Kuno, in figs. 16-18. Ca and Al (atomic proportions) have been shown in parenthesis against each plot to check the relations suggested by Hess and Kuno. The variation trends corresponding to Ca content of 0.020 and 0.060 and Al content of 0.010 and 0.050 (Hess and Kuno) have also been transferred to the above plots for comparison. These plots fail to show the relations between Ca and Al content and cell parameters as indicated by Hess and Kuno. Furthermore, the correlation, between Fs (mol.%) and cell parameters is poor. Obviously, there is no simple correlation between Ca, Al,Fe^{2+} Fe^{3+} Mn and cell parameters.

There is some justification for considering orthopyroxenes as solid solutions of the Wo-En-Fs-Jd-Ac-Ca/Mg-Tsch molecules (Kushiro, 1965a, p.106; 1965b, p. 110; Clark, Schairer and Neufville, 1962, p. 61). The composition and unit cell parameters of these pyroxene end members and their polymorphs are listed in table 25.

Al, Fe^3 and Ti are capable of both 4 and 6-fold coordination, and knowledge of their distribution between the two sites is necessary to calculate the relative proportions of the different end members. Within limited, but ideal solid solutions, the resultant cell dimension of the

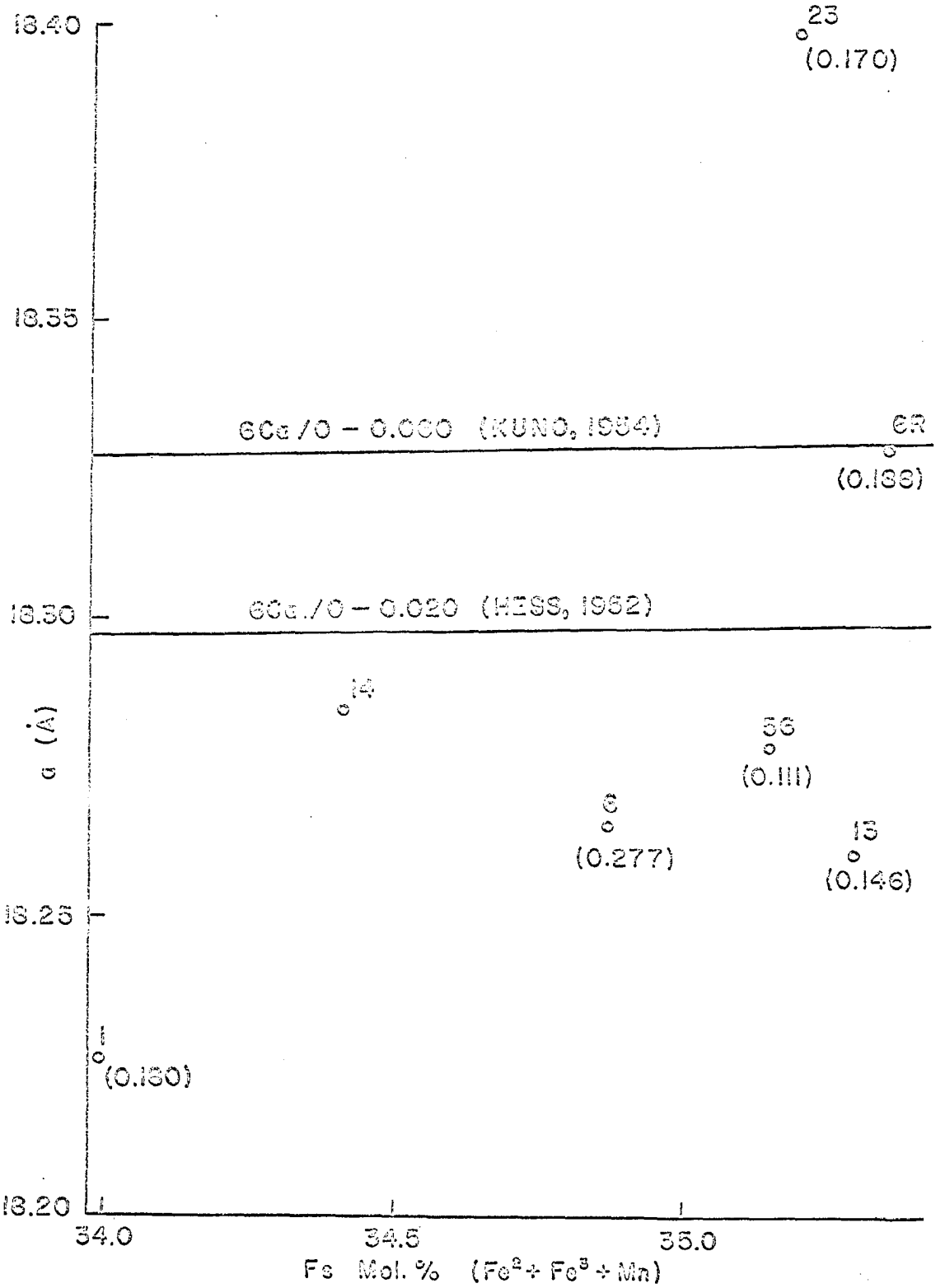

Fig. 16. Plot showing the lack of correlation between mol. % Fs and 'a' cell parameter. Figures in parentheses are 6Ca/O of the analyzed orthopyroxene. Note lack of agreement with trends suggested by Hess (1952) and Kuno (1954).

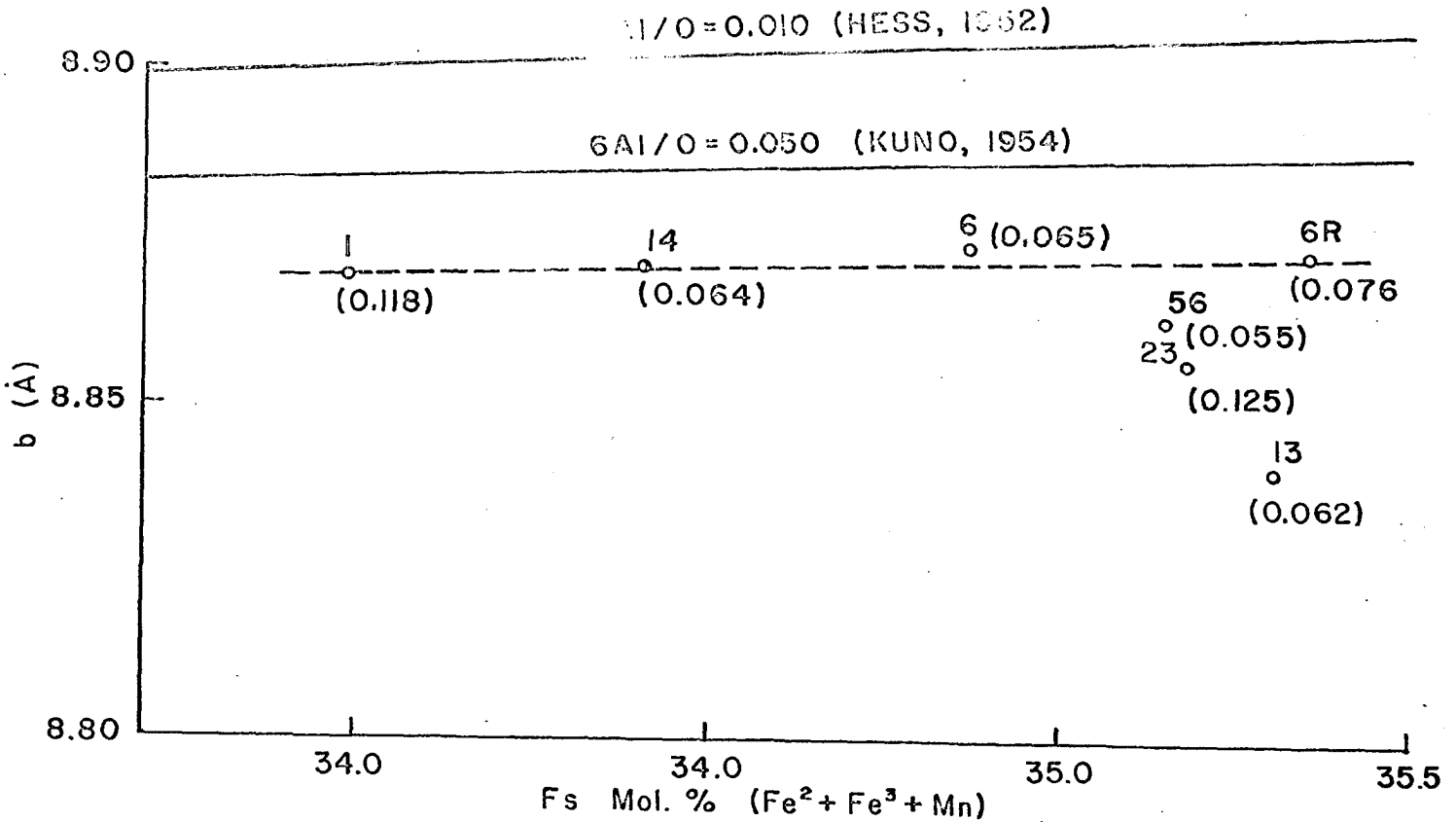

Fig. 17. Plot showing the lack of correlation between mol.% Fs and 'b' cell parameter. Figures in parentheses are 6Al/O of analyzed orthopyroxene. Note lack of agreement with trends suggested by Hess (1952) and Kuno (1954).

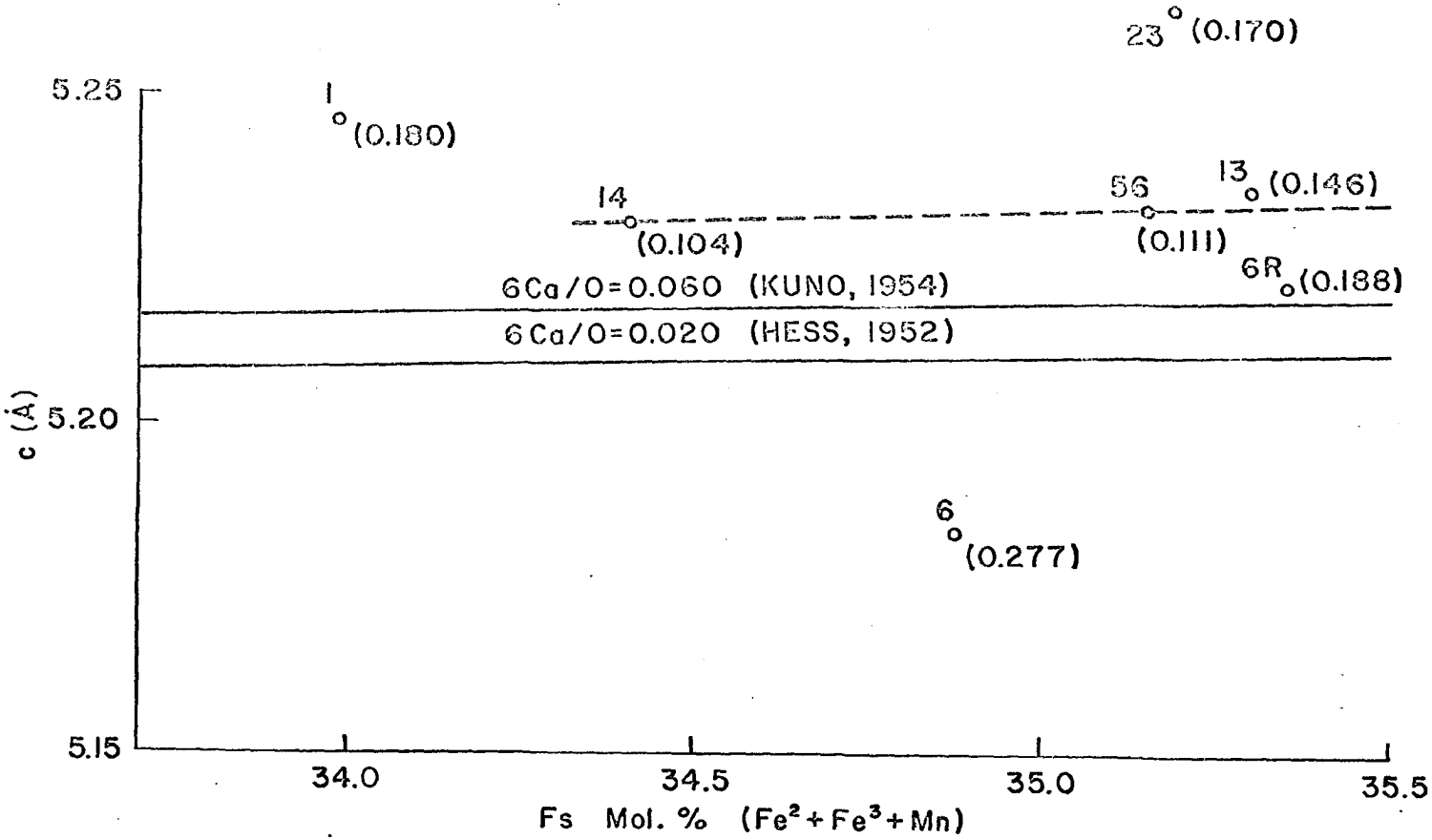

Fig. 18. Plot showing the lack of correlation between mol.% Fs and 'c' cell parameter. Figures in parentheses are 6Ca/O of analyzed orthopyroxene. Note lack of agreement with trends suggested by Hess (1952) and Kuno (1954).

Table 25. Structural

	a(Å)	b(Å)	c(Å)	α
$Ca_2Si_2O_6$				
Psendowollastonite	6.90	11.78	19.65	90°
Parawollastonite	15.42	7.32	7.07	
α Wollastonite	7.94	7.32	7.07	90°02'
$Mg_2Si_2O_6$				
Clinoenstatite	9.12	8.86	5.24	
Protoenstatite	9.25	8.74	5.32	
Orthoenstatite	18.23	8.81	5.20	
$Fe_2Si_2O_6$				
Clinoferrosilite	9.7085	9.0872	5.2284	
Ferroasilite III	6.57	7.51	22.68	115°3
Orthoferrosilite	18.431	9.080	5.238	
$CaMgSi_2O_6$				
Diopside	9.745	8.925	5.248	
$NaAlSi_2O_6$				
Jadeite	9.50	8.61	5.24	
$NaFe^3Si_2O_6$				
Acmite	9.65	8.79	5.29	
$CaAl_2SiO_6$				
Ca-Tschermak's Mol.	9.615	8.661	5.272	

1. Deer, Howie &Zussmann, 1963, Vol.2 . pp.9,80,99,169,
2. Morimoto, 1959, 3.Burnham,1965,p.203, and

Data for Pyroxene End-Members

β	γ	Space Group and Z	Unit Cell Volume (A^3)	Ref
90°48'	119°18'	$P\bar{1}$,24	-	1
95°24'		$P2_12_12$	794.50	1
95°22'	103°26'	$P\bar{1}$,6	398.58	1
92°24'		$P2_1c$,4	423.41	2
		Pbcn,8	430.10	2
		Pbca,16	838.51	1
108°432		$P2_1c$,8	438.54	3
80°5	96°5	?	-	
		Pbca,116	876.88	3
105°87		C2/c,4	439.08	4
107°26'		C2/c,4	408.89	1
107°4		C2/c,4	428.08	1
104°12		C2/c,4	421.79	4

4. Clark, Schairer & Neufville, 1962, p. 62.

complex would depend on those of the participating end members. A correlation is possible when composition can be precisely recalculated in terms of the molecular end members. In this section, orthopyroxene compositions have, so far, not been discussed in terms of pyroxene end members other than En and Fs. The structural formulae given in table 17 are based on a convention for the recalculation of clinopyroxene analyses, adopted by Kushiro (1960, 1962) and Yoder and Tilley (1962, p. 366), which is a modification of methods proposed by Yagi (1953) and Kuno (op cit).

Al, Fe^3 and Ti are typically 6 coordinated cations. Entry of (Fe^3+Ti) in the tetrahedral site can be visualized in the analogue of the 'A' site in inverse spinel structure. From this analogy, it appears that the effect of 4-coordination of (Fe^3+Ti) would be an increase in the c parameter. Similarly the entry of Al into the tetrahedral site can be compared to the analogy furnished by the body centered anorthite or primitive anorthite structures, and the c cell parameter would decrease with increasing 4-coordination of Al. Lattice distortions and non-correspondence of chains produced by the entry of Fe^3, Ti and Al into the tetrahedral site would also cause readjustments in the octahedral lattice interstices; and corresponding changes in the a and b parameters are likely.

The opposing effects of 4-coordinated Fe^3+ Ti versus Al would be evident in the relations between the c parameter and 2-Si (atomic proportions of cations, other than Si, in tetrahedral site). The c cell parameters of the analyzed orthopyroxenes have been plotted against (2-Si) in fig. 19. The two trends are due to the dominance of (Fe^3+ Ti) and Al in the tetrahedral sites as labelled in fig. 19 (or greater 6-coordination of Al and Fe^3 + Ti respectively, as indicated on the following diagram). Further confirmation of this is furnished by relations shown in fig. 20, where unit

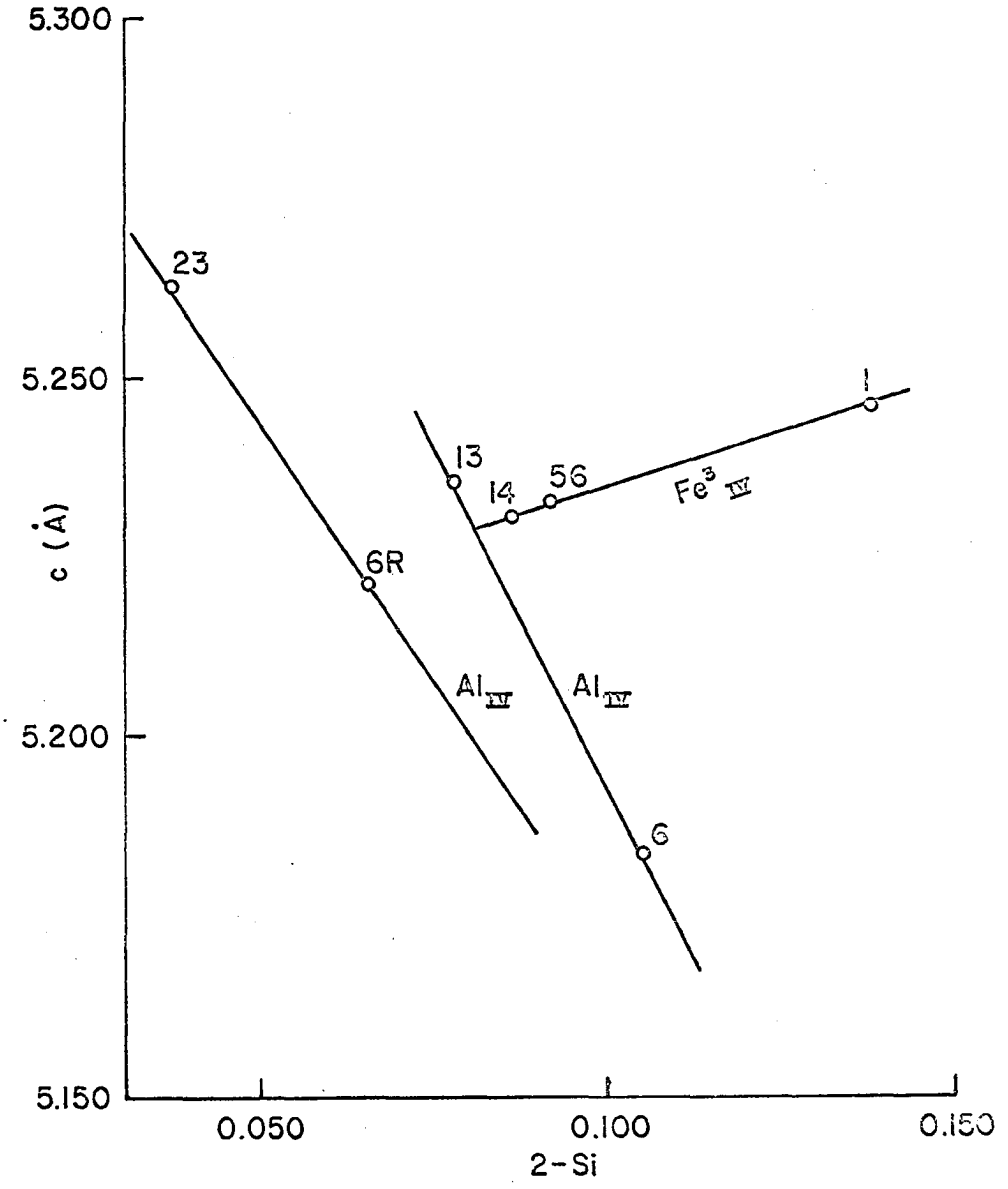

Fig. 19. Diagram showing contrasted c(Å) - (2-Si) trends of the two orthopyroxene groups.

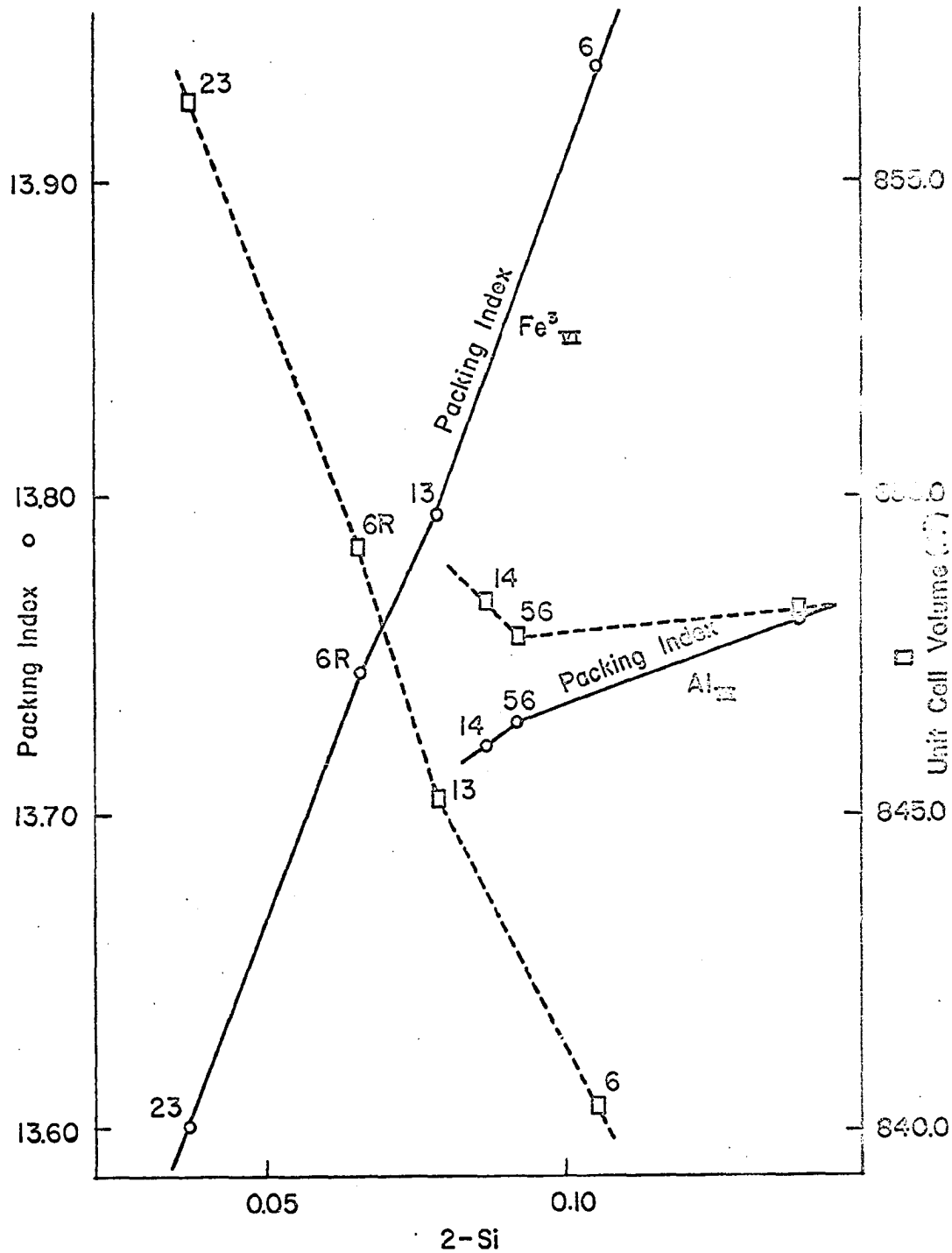

Fig. 20. Plot showing the relations of packing indices and unit cell volumes of analyzed orthopyroxene to 2-Si.

cell volumes and packing indices have been plotted against (2-Si). Considering the relative volumes of Fe^3 -O units (hematite rhombohedral structure) and Si-O units (silica tetrahedra), the effects would be minor and cause little change in packing index. In both the figures the slopes of the lines defined by the plots of O-14, 56 and 1 are characteristically gentle; whereas the lines defined by O-23, 6R, 13 and 6 are steeper, reflecting a greater volume change caused by 4-coordination of Al.

End Member Composition of Orthopyroxenes

Following the above guide lines, Al and Fe^3 + Ti were distributed in the octahedral and tetrahedral sites during recalculation of the chemical analyses. However, a limiting condition is met in the fact that 6-coordinated Fe^3 cannot exceed the atomic proportion of Na + K, as there is no end member other than acmite, which can accomodate Fe^3. Al (vi), however, can be assigned to Na (Jd) and Ca (Tschermak's mol.). Ti has been grouped with Fe^3 as there is no satisfactory method for determining Ti coordination, and the Ti content is also very low in these pyroxenes. The procedure for the distribution of Fe^3 + Ti and Al in the octahedral and tetrahedral sites, was, therefore, as follows:

Pyroxenes O-56, 14 and 1:

(1) (2-Si) was first filled by Fe^3 + Ti, and any remaining vacancy was filled by Al. Excess Al was then assigned to octahedral site.

(2) If (2-Si) < Fe^3 + Ti, then excess Fe^3 + Ti and total Al were assigned to the octahedral site.

(3) If (Fe^3 + Ti) (vi) > (Na + K), then excess (Fe^3 + Ti) (vi) was transferred back to the tetrahedral site. Equivalent Al was then returned to the octahedral site.

Pyroxenes 0-23, 6R, 13 and 6:

(1) (2-Si) was filled by Al, and excess Al and Fe^3 + Ti were assigned to the octahedral site. If (2-Si) > Al, then Fe^3 + Ti was added until balance was achieved. Excess Fe^3+Ti was then assigned to actahedral site.

(2) same as (3) above.

The above recalculation procedure resulted in cation distribution in the two sites as shown in table 26. The formulae of the analyzed samples in terms of the fundamental end members were then calculated from this distribution, as shown in table 27. Unit cell volumes were calculated based on the unit cell volumes of the fundamental end members (shown in table 25). (For 0-14, β - $Na_2Si_2O_5$ had to be calculated due to persistent Na + K excess, data for β - $Na_2Si_2O_5$ taken from Wyckoff, 1960). The calculated unit cell volumes are based on the end member composition of the orthopyroxenes, recast to 100 (shown in table 27). The calculated and observed unit cell volumes are listed in table 28 and the error gap is usually <0.25% and rarely >1%, which is presumably due to the unknown molecules containing Ni, Cr etc. The Tschermak's molecule has been assumed to be Ca-Tsch. However, it is likely that Mg-Tschermak's molecule is also present. The correlation between the measured and calculated cell volumes (table 28) supports the validity of the method outlined above.

Correlation between cell parameters and composition can now be discussed in terms of the data listed in table 27. Apparently, the cell parameters are largely determined by the dominant end members, although the minor ones may be responsible for deviations. A comparison of the cell parameters of the different end members with those of En would show that the effects of the different end members, entering in solid solution with En, are likely

Table 26 . Distribution of Cations in Octahedral and Tetrahedral Sites in Orthopyroxene.

Cations	0-56		0-14		0-1		0-6R		0-6		0-23		0-13	
	Oc	Te	Oc	Te	Oc	Te	Oc	Te	Oc	Te	Oc	Te	Oc	Te
Si		1.908		1.914		1.862		1.935		1.895		1.963		1.922
Al	0.033	0.022	0.023	0.041	0.054	0.064	0.057	0.019	0.040	0.005	0.114	0.011	0.018	0.044
(Fe^3 + Ti)	0.021	0.070	-	0.045	0.043	0.074	0.037	0.046	0.045	0.100	0.082	0.026	0.033	0.034
Ti									0.025					
(Fe^2+ Mn)	0.588		0.606		0.505		0.554		0.451		0.490		0.592	
Mg	1.212		1.218		1.169		1.121		1.113		1.057		1.173	
Ca(Wo)	0.090		0.104		0.126		0.131		0.237		0.056		.128	
Ca(Tsch)	0.021		-		0.054		0.057		0.040		0.114		.018	
(Na + k)	0.033		0.045		0.043		0.037		0.045		0.082		0.033	
Other Cations (Ni,Cr,etc.)	0.003		0.004		0.006		0.005		0.005		0.004		0.005	

Table 27 . Calculated End-member Composition (mol.%).

	0-56	0-14	0-1	0-6R	0-6	0-23	0-13
Enstatite	60.60	60.90	58.45	56.05	55.65	52.85	58.65
Ferrosilite	29.40	30.30	25.25	27.70	22.55	24.50	29.60
Wollastonite	4.50	5.20	6.30	6.60	11.85	2.80	6.40
Jadeite	1.20	12.30	-	-	-	-	-
Acmite	2.10	-	4.30	3.70	4.50	8.20	3.30
Tschermak's	2.10	-	5.40	5.70	4.00	11.40	1.80
β-$Na_2Si_2O_5$	-	1.10	-	-	-	-	-
Others	0.10	0.20	0.30	0.25	1.45	0.25	0.25

Table 28 . Calculated vs. Observed Unit-Cell Volumes.

	0-56	0-14	0-1	0-6(R)	0-6	0-23	0-13
Calc Unit Cell Vol. ($Å^3$)	848.05	839.25	846.47	847.20	843.09	848.74	847.73
Obs. Unit Cell. Vol. ($Å^3$)	847.70	848.34	848.06	849.11	840.32	857.24	845.14
Percentage Diff.	< 0.05%	< 1.2%	< 0.2%	< 0.2%	< 0.3%	< 1%	< 0.3%

to be as shown in table 29. For convenience in plotting, the end member compositions have been grouped as shown in table 30. According to the grouping given in table 30, the cell parameters have been plotted against Fs and (Ac + Jd + Ca - Tsch) mol% (for 0 - 56, 14, 1 and 13) in figs. 21 and 22; and against Wo and (Ac + Ca - Tsch) mol.% (for 0 - 6R, 6 and 23) in figs. 23 and 24. In pyroxenes 0 - 56, 14, 1 and 13 the effects of Wo and Ac + Jd + Ca - Tsch are manifest in the variations in the b and c cell parameters, and the a parameter is related to Fs content. In 0 - 6R, 6 and 23, variations in a and c parameters are caused by Wo and Ac + Ca - Tsch content while b parameter is influenced by Fs contents.

Composition and Norm

The distinction between the two pyroxene groups 0 - 56, 14, 1, 13 and 0 - 6R, 6, 23), as indicated above, is also maintained by normative compositions. The first group is characterized by normative Ol and the second by normative Qz. Normative Ol in hypersthene has been assigned to the presence of Tschermak's molecule by Yoder and Tilley (op. cit., p. 364-365), but normative Ol bearing 0 - 14 (table 18), without Tschermak's mol. (table 27), contradicts this generalization. An interpretation of the above would be that the Ol normative pyroxenes crystallized from silica undersaturated melts under low P_{O_2} (as also indicated by dominant 4-coordinated Fe^3); and the Qz normative pyroxenes crystallized from silica saturated melts and under higher P_{O_2} (as reinforced by dominance of 6-coordinated Fe^3).

Petrogenetic Significance

The petrogenetic significance of Jd and Tschermak's mol. in orthopyroxene is not well understood. However, the range of Jd and Tsch mol.% of the analyzed orthopyroxenes indicates that the crystallization took place

Table 29. Probable Nature of Changes in Unit Cell Parameters of Enstatite due to Solid Solution with Other Pyroxene End-members.

Pyroxene End-members	a(Å)	b(Å)	c(Å)
Fs	+	+	+
Wo	-(large)	-(small)	+ (small)
Ac	+	-(small)	+ (?)
Jd	+	-(small)	+ (?)
Ca-Tsch	+	-(small)	+ (?)

Table 30. Grouping of End-member Compositions of Analyzed Orthopyroxene.

S. Nos.	Mol. %			En:Wo
	En + Wo	Fs	Ac + Jd + Ca-Tscn	
0-56	65.1	29.4	5.4	93.1:6.9
0-14	66.2	30.3	2.3 (Jd only) 3.4 (including $\beta Na_2Si_2O_5$)	92.1:7.9
0-1	64.75	25.25	9.7	90.3:9.7
0-13	65.05	29.6	5.1	90.2:9.8
	En + Fs	Wo	Ac + Ca - Tsch	En:Fs
0-6R	83.7	6.6	9.4	66.9:33.1
0-6	78.2	11.85	8.5	71.2:28.8
0-23	77.35	2.8	19.6	68.3:31.7

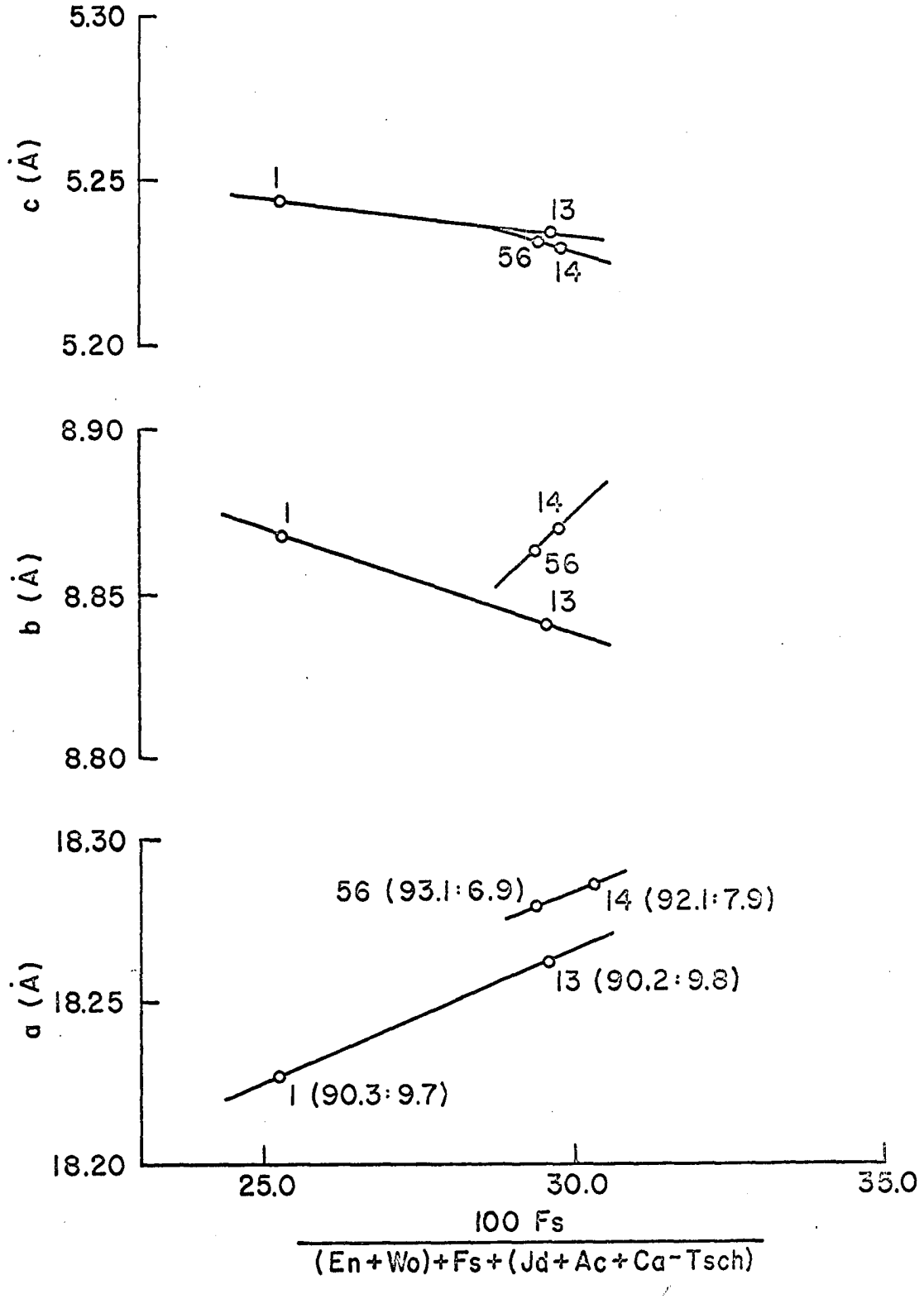

Fig. 21. Fs (mol%) - cell parameter variation diagram. (En:Wo ratio in parenthesis).

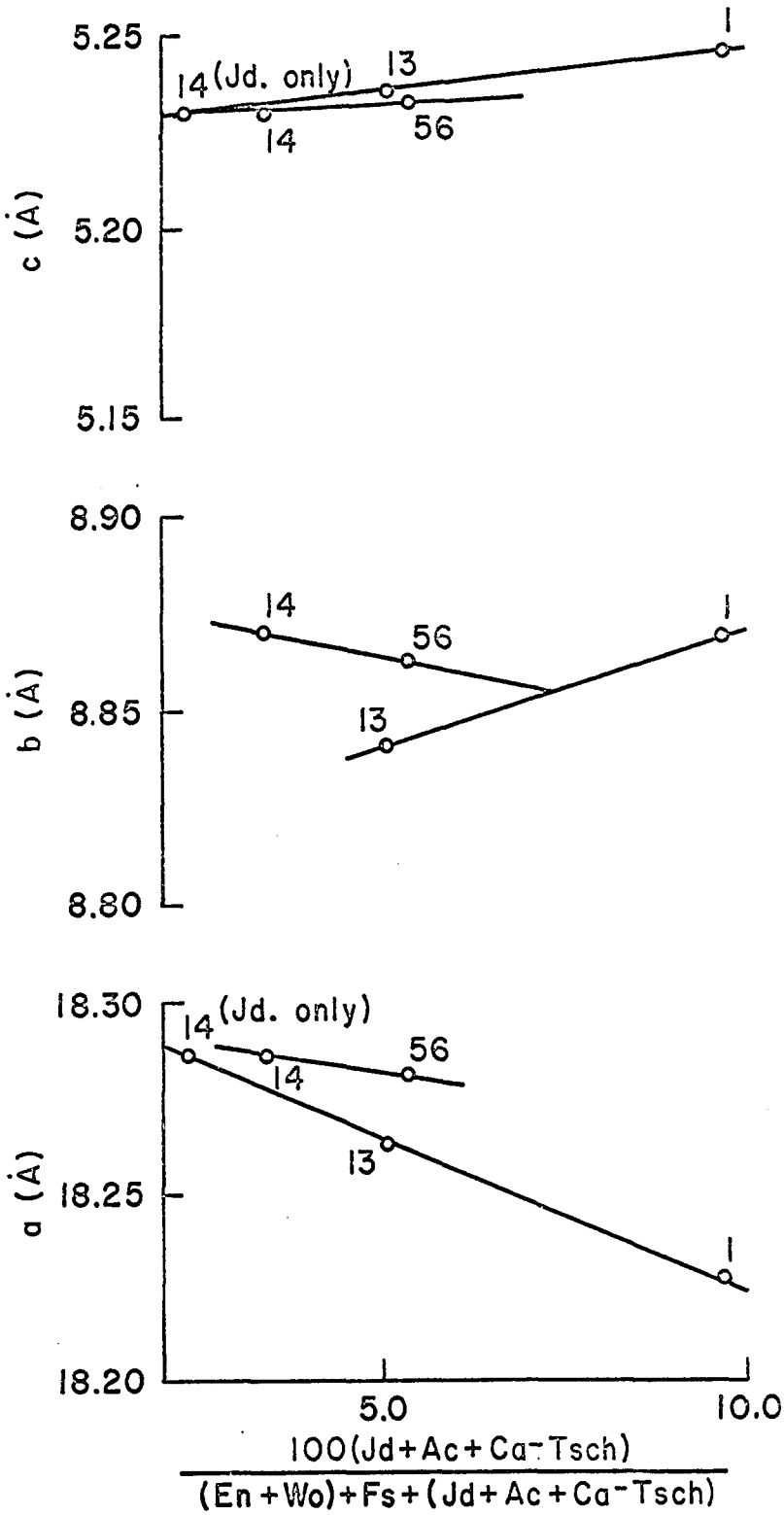

Fig. 22. Jd + Ac + Ca-Tsch (mol.%) - cell parameter variation diagram.

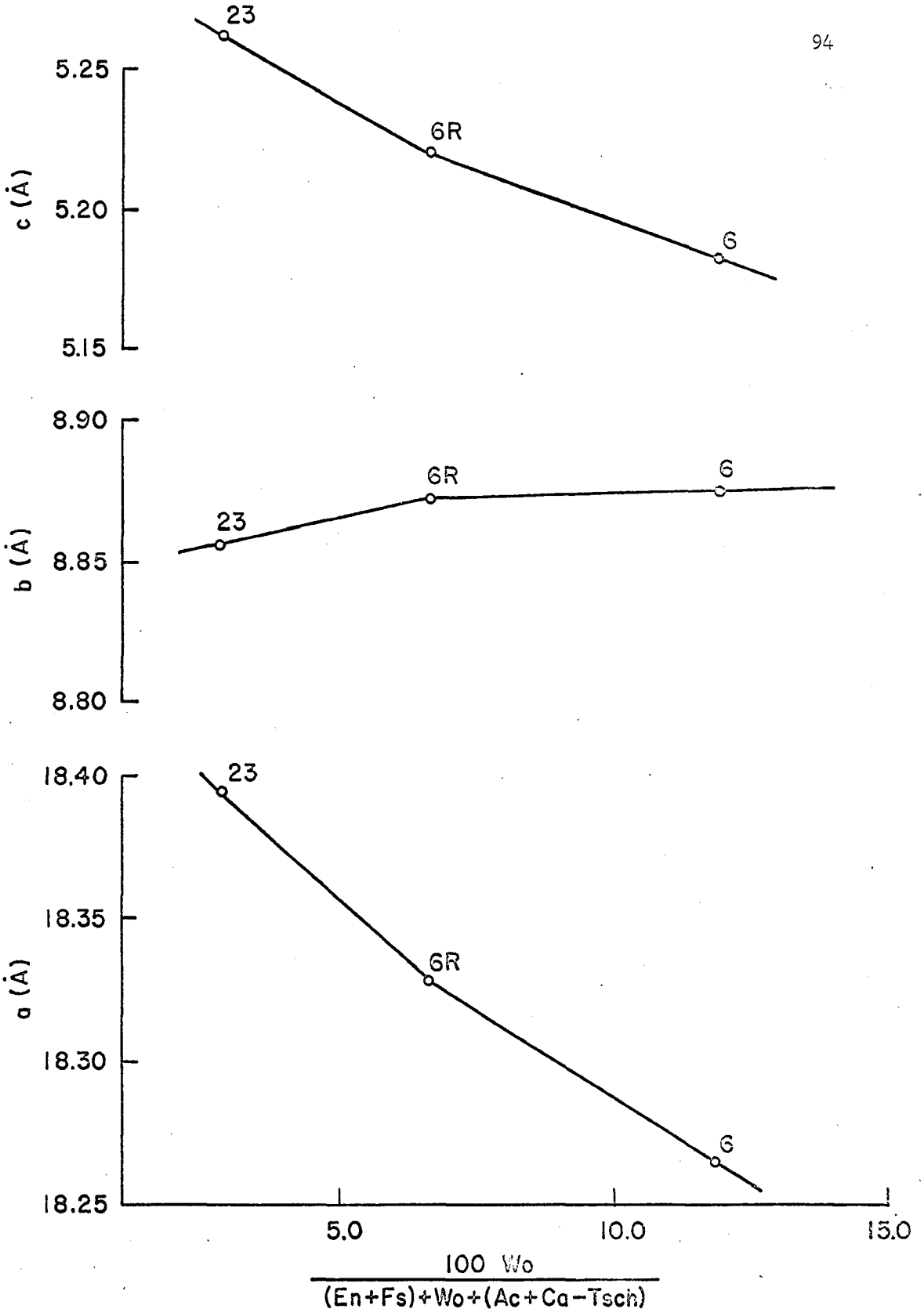

Fig. 23. Wo (mol.%) - cell parameter variation diagram.

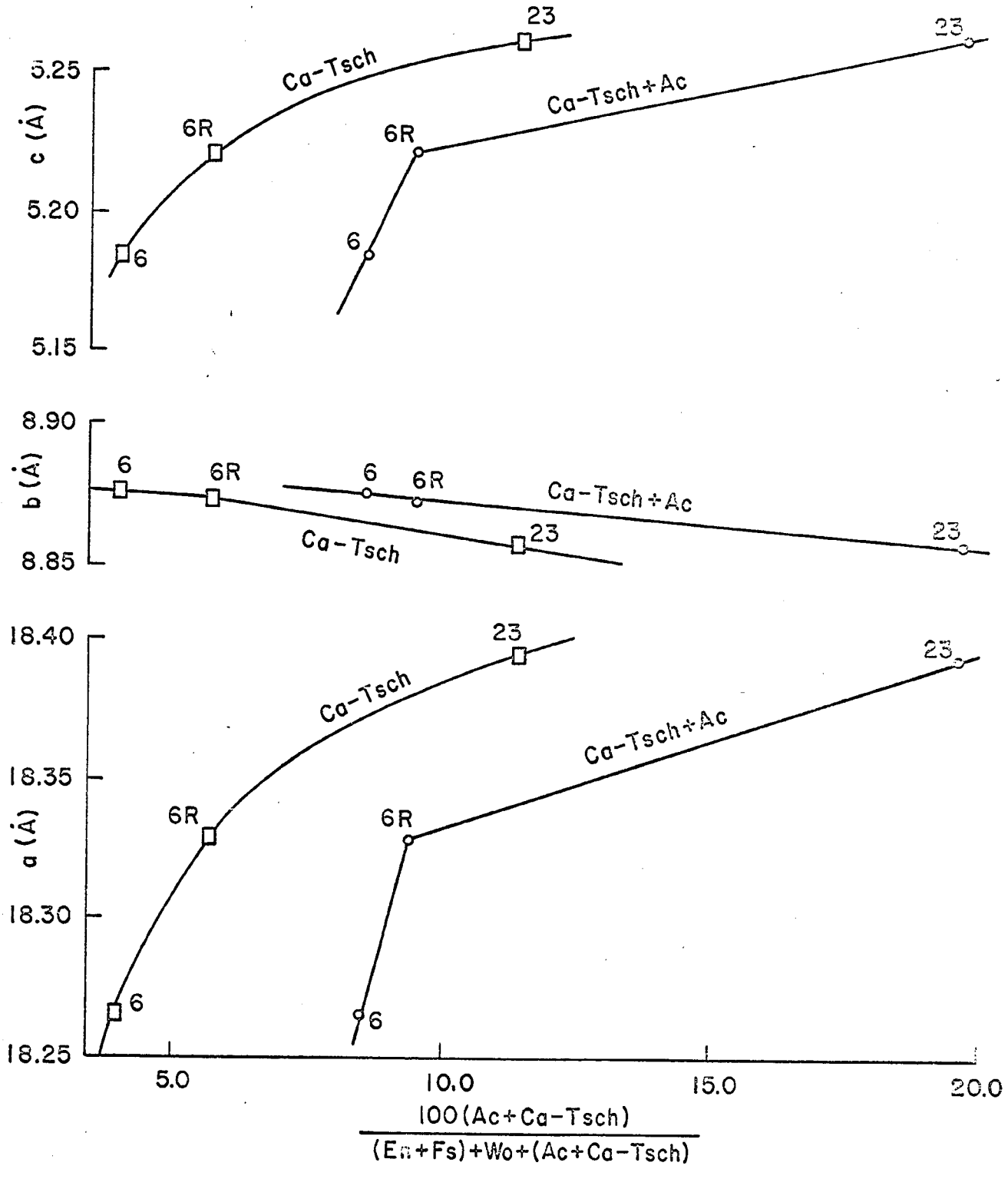

Fig. 24. Ac + Ca-Tsch (mol.%) - cell parameter variation diagram.

at pressures (total) less than 10 kb, as can be deduced from the data on En-Jd and En-Tsch systems, obtained by Kushiro (1965a, pp. 104, 106). From the compositional point of view, the introduction of Jd and Ca-Tsch in orthopyroxene would cause Na-Al and Ca-Al depletion of the residual liquid. These effects would be complicated by co-crystallizing plagioclase.

The correlation between the presence of Jd mol. and normative Ol in orthopyroxene composition, as indicated above, indicates that Jd mol. may be introduced under low oxygen/high water pressures, while the presence of Ca-Tsch mol. and normative Qz may be indicative of crystallization under higher oxygen/low water pressures.

CLINOPYROXENE

Calcic augite (C-56, 14, 1, 6, 23 and 13) coexistent with the orthopyroxene discussed in the preceding section was separated and analyzed. X-ray diffraction analyses confirmed the purity of the samples. Cell parameters and unit cell volumes were also calculated. The chemical composition, structural formulae and molecular norms of the clinopyroxenes are given in tables 31 to 34 inclusive.

Optical Properties and Chemical Composition

Hess (1949) and Muir (1951) demonstrated the correlation between $2V_Z$ and mol.% of Wo (wollastonite), and between N_y and mol % of CFs (clinoferrosilite). Minor effects are produced by the coordination level of Al, Fe^3 and Ti (Hori, 1954). 4-coordinated Al, Fe^3 and Ti tend to increase the $2V_Z$, and reduce the N_y; while 6-coordination tends to reverse these effects. Optical properties and chemical parameters including Wo ($CaSiO_3$) mol.% and (Fe^2,Fe^3,Mn) SiO_3 mol.% are given in table 35. There is some correlation between $2V_Z$ and the Wo content, but other correlations are not present.

Table 31. Chemical Composition and Structural Formulae (6-oxygens) of Clinopyroxene.

Wt.%	C-56	C-14	C-1	C-6	C-23	C-13
SiO_2	49.70	51.57	49.20	51.13	49.45	51.72
TiO_2	0.68	0.40	0.72	0.52	0.74	0.64
Al_2O_3	2.52	2.68	3.02	2.83	3.61	2.13
Fe_2O_3	2.49	1.38	2.48	2.72	2.58	1.27
FeO	7.43	8.04	7.09	6.76	7.58	8.78
MnO	0.32	0.37	0.34	0.35	0.33	0.44
MgO	15.84	14.49	15.66	15.03	15.72	14.71
CaO	19.77	20.31	20.72	19.59	19.42	19.83
Na_2O	0.49	0.81	0.51	0.62	0.71	0.61
K_2O	0.09	0.15	0.11	0.09	0.03	0.10
H_2O^-	0.02	0.00	0.03	0.00	0.00	0.00
H_2O^+	0.06	0.00	0.06	0.22	0.05	0.00
P_2O_5	0.07	0.18	0.12	0.15	0.26	0.12
Total	99.62	100.38	100.16	100.01	100.52	100.35
Ni	0.009	0.015	0.028	0.013	0.015	0.024
Cr	0.019	0.012	0.021	0.024	0.017	0.010
				Analyst: H. Haramura		
Cations						
Si	1.865	1.911	1.840	1.897	1.835	1.919
Al	0.112	0.089	0.133	0.088	0.145	0.081
		0.028		0.036	0.013	0.012
Ti	0.019	0.011	0.020	0.015	0.020	0.018
Fe^{3+}	0.004	0.039	0.007	0.076	0.072	0.036
	0.067		0.063			
Fe^{2+}	0.234	0.250	0.223	0.211	0.236	0.273
Mn	0.010	0.012	0.011	0.011	0.010	0.014
Mg	0.889	0.803	0.876	0.834	0.873	0.816
Ca	0.798	0.809	0.833	0.782	0.775	0.791
Na	0.036	0.058	0.037	0.045	0.051	0.044
K	0.004	0.007	0.005	0.004	0.001	0.005
P	0.002	0.006	0.004	0.005	0.008	0.004
Ni	0.0003	0.001	0.001	0.0004	0.0006	0.0009
Cr	0.0008	0.001	0.0009	0.001	0.0007	0.0004
Z	2.000	2.000	2.000	2.000	2.000	2.000
XY	2.041	2.025	2.054	2.005	2.040	2.014

Table 32. Clinopyroxene Composition Expressed as Metasilicate End-Members (Mol. %).

Mol.%	C-56	C-14	C-1	C-6	C-23	C-13
Ca	39.86	42.29	41.38	40.86	39.42	40.78
Mg	44.41	41.98	43.52	43.57	44.40	42.28
$(Fe^{2}+Fe^{3}-Mn)$	15.73	15.73	15.10	15.57	16.17	16.74
Ca	41.53	43.45	43.10	42.80	41.12	40.07
Mg	46.27	43.14	45.35	45.64	46.33	43.41
Fe^{2+}	12.20	13.41	11.55	11.56	12.55	14.52
$100Fe^{2+}/(Fe^{2+}+Mg)$	20.86	23.71	20.30	20.21	21.31	25.07
$100\Sigma Fe/(\Sigma Fe+Mg)$	26.14	27.21	25.72	26.30	26.75	28.33

Table 33. Cation Proportions Recalculated to 4.

Cations	C-56	C-14	C-1	C-6	C-23	C-13
Si	1.846	1.899	1.816	1.895	1.817	1.912
Al	0.111	0.116	0.131	0.124	0.156	0.093
Ti	0.019	0.011	0.020	0.015	0.020	0.018
Fe^{3+}	0.070	0.039	0.069	0.076	0.071	0.036
Fe^{2+}	0.232	0.248	0.220	0.211	0.234	0.272
Mn	0.010	0.012	0.011	0.011	0.010	0.014
Mg	0.880	0.798	0.864	0.833	0.864	0.813
Ca	0.790	0.804	0.821	0.781	0.767	0.788
Na	0.036	0.058	0.037	0.045	0.050	0.044
K	0.004	0.007	0.005	0.004	0.001	0.005
P	0.002	0.006	0.004	0.005	0.008	0.004
Ni	0.0003	0.001	0.001	0.0004	0.0006	0.001
Cr	0.0008	0.001	0.0009	0.001	0.0007	0.0004

Table 34 . Molecular Norm of Clinopyroxene

Qz	0.00	0.00	0.00	0.00	0.00	0.00
Or	0.53	0.88	0.64	0.53	0.17	0.59
Ab	4.42	6.71	0.21	5.58	5.35	5.47
An	4.43	3.22	5.61	4.68	6.53	2.77
Ne	0.00	0.32	2.61	0.00	0.58	0.00
Di	74.93	76.79	76.98	73.42	69.99	75.86
Hy	0.30	0.00	0.00	7.57	0.00	5.67
En	0.24			6.29		4.34
Fs	0.05			1.27		1.33
Ol	11.66	9.69	10.08	4.30	13.11	7.14
Fo	9.61	7.53	8.37	3.58	10.77	5.45
Fa	2.05	2.16	1.70	0.72	2.34	1.68
Mt	2.61	1.43	2.58	2.85	2.67	1.32
Il	0.95	0.55	1.00	0.72	1.02	0.89
Ap	0.14	0.37	0.25	0.31	0.54	0.25

Table 35 . Composition and Optical Properties of Clinopyroxene.

S. Nos.	$Ca_2Si_2O_6$ (Mol.%)	$\frac{Fe \times 100}{(Fe+Mg)}$	$N_y \pm .001$	$2V_z \pm 1°$
C-56	39.86	26.14	1.690	59-56°
C-14	42.29	27.21	1.688	58°
C-1	41.38	25.72	1.694	58°
C-6	40.86	26.30	1.693	54-52°
C-23	39.42	26.75	1.691	55-53°
C-13	40.98	28.33	1.688	55-54°

Table 36. X-ray Diffraction Data for Clinopyroxene (Cuk α, Ni-filter, 35 kv, 15 ma).

← 2 θ angles in degrees →

S. Nos.	C-56	C-56R+	C-14	C-1	C-6	C-23	C-13
hkl							
220	27.79	27.75	27.71	27.76	27.72	27.72	27.73
22$\bar{1}$	29.99	29.96	29.95	29.97	29.95	29.96	29.92
310	30.48	30.47	30.44	30.48	30.46	30.46	30.42
31$\bar{1}$	31.01	31.00	30.96	30.98	30.96	30.97	30.95
13$\bar{1}$	35.14	35.11	35.06	35.10	35.09	35.09	35.04
11$\bar{2}$, 221	35.91	35.92	35.86	35.89	35.88	35.89	35.82
022, 22$\bar{2}$	41.14	41.18	41.14	41.03?	41.12	41.05	41.09
*330	42.01	42.08	41.95	42.08	42.03	41.99	41.90
*33$\bar{1}$	42.41	42.48	42.34	42.44	42.40	42.31	42.32
*42$\bar{1}$	42.96	43.00	42.89	42.97	42.95	42.87	42.87
420	?	43.70	?	?	?	?	43.69
*041	44.48	44.55	44.37	44.47	44.46	44.41	44.38
?40$\bar{2}$,240	49.45	49.69	49.69	49.79	49.75	49.69	49.68
222	49.78	49.91	49.80	49.93	49.99	49.88	49.79
*150	52.20	52.35	52.13	52.19	52.19	52.10	52.10
*53$\bar{1}$,22$\bar{3}$	56.68	56.69	56.57	56.70	56.67	56.59	56.55
440	57.01	56.93	57.00	57.18	57.10	57.00	56.96

+ C-56R is a second sample prepared for redetermination of manganese.

* Reflections used for cell parameter calculations.

Chemical Composition

The chemical analyses of the clinopyroxenes have been recalculated, following the convention given by Yoder and Tilley (1962, pp. 366-367), and given in table 40 (in comparison with recalculations based on X-ray data).

The chemical composition recast as mol.% $CaSiO_3$-$MgSiO_3$ - (Fe^2,Fe^3,Mn) SiO_3 and (Ac + Jd), Di, Hd (table 40) have been plotted in figs. 25 and 26. Distinct trends or correlations are not discernible in either of the two diagrams.

The triangles of closure in the (Ac + Jd) -Di -Hd diagram (fig. 26) represent the Tschermak's molecule. Fig. 26 is noteworthy in that it illustrates the chemical similarity of the Trident clinopyroxenes to those from alkalic rocks as reported by Yagi (1953) and Yoder and Tilley (op. cit., p. 368, fig. 5).

Unit Cell Parameters

The cell parameters of the analyzed clinopyroxenes were calculated from the (220), (22$\bar{1}$), (310), (31$\bar{1}$), (13$\bar{1}$), (11$\bar{2}$),(221), (022, 22$\bar{2}$), (330), (33$\bar{1}$), (42$\bar{1}$),(?)(420) (041),(?) (40$\bar{2}$, 240), (42$\bar{2}$, 510), (222), (150), (53$\bar{1}$, 22$\bar{3}$) and (?)(440) reflections. The corrected 2θ angles are listed in table 36. The best reflections in the high angle range were used in the final unit cell parameter calculations. Cell parameters, unit cell volume, ionic volume per unit cell and packing indices are also given in table 37.

The a, a sin β, b and c cell parameters have been correlated to the relative molecular proportions of the Wo, CEn and CFs molecules by Kuno and Hess (1953), Kuno (1955) and Brown (1960). Their observations on the variations of a sin β, b and c parameters are summarized below:

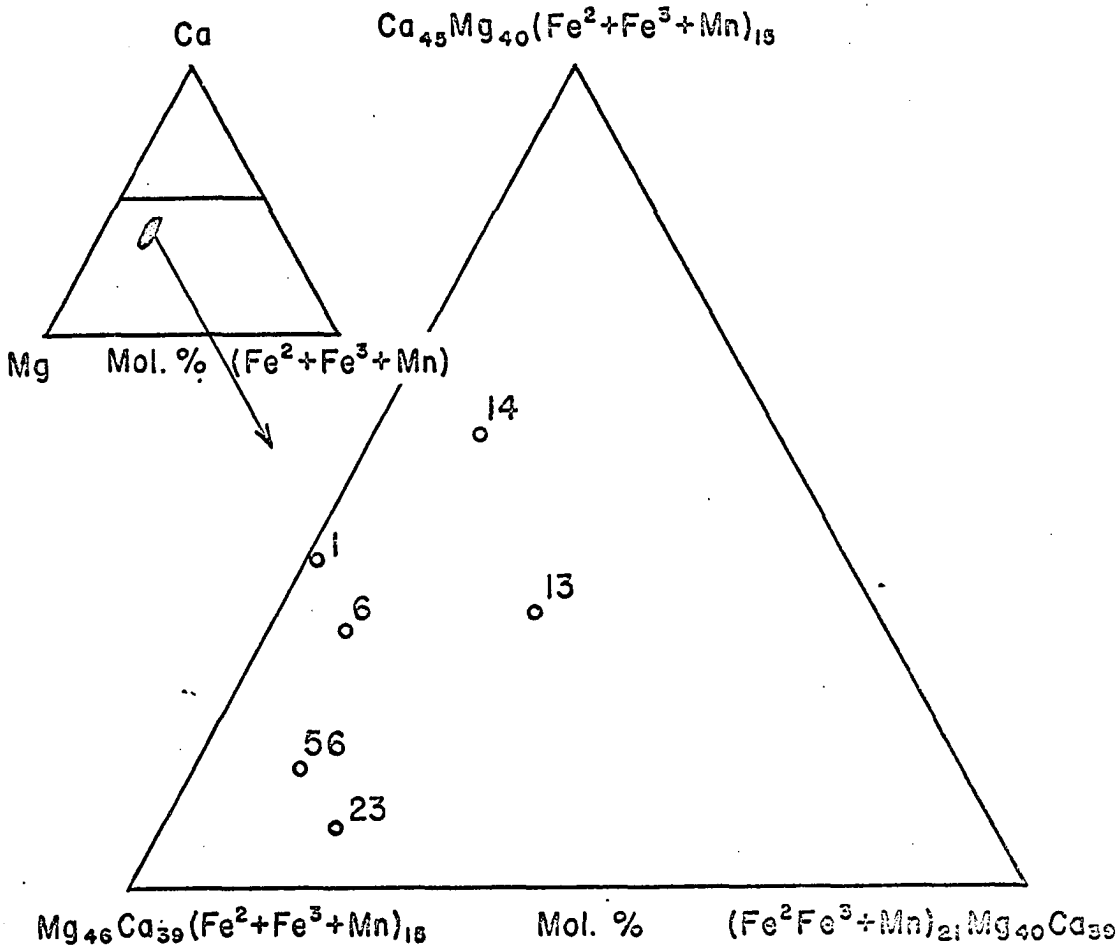

Fig. 25. Mg-Ca- ΣFe plot of clinopyroxene.

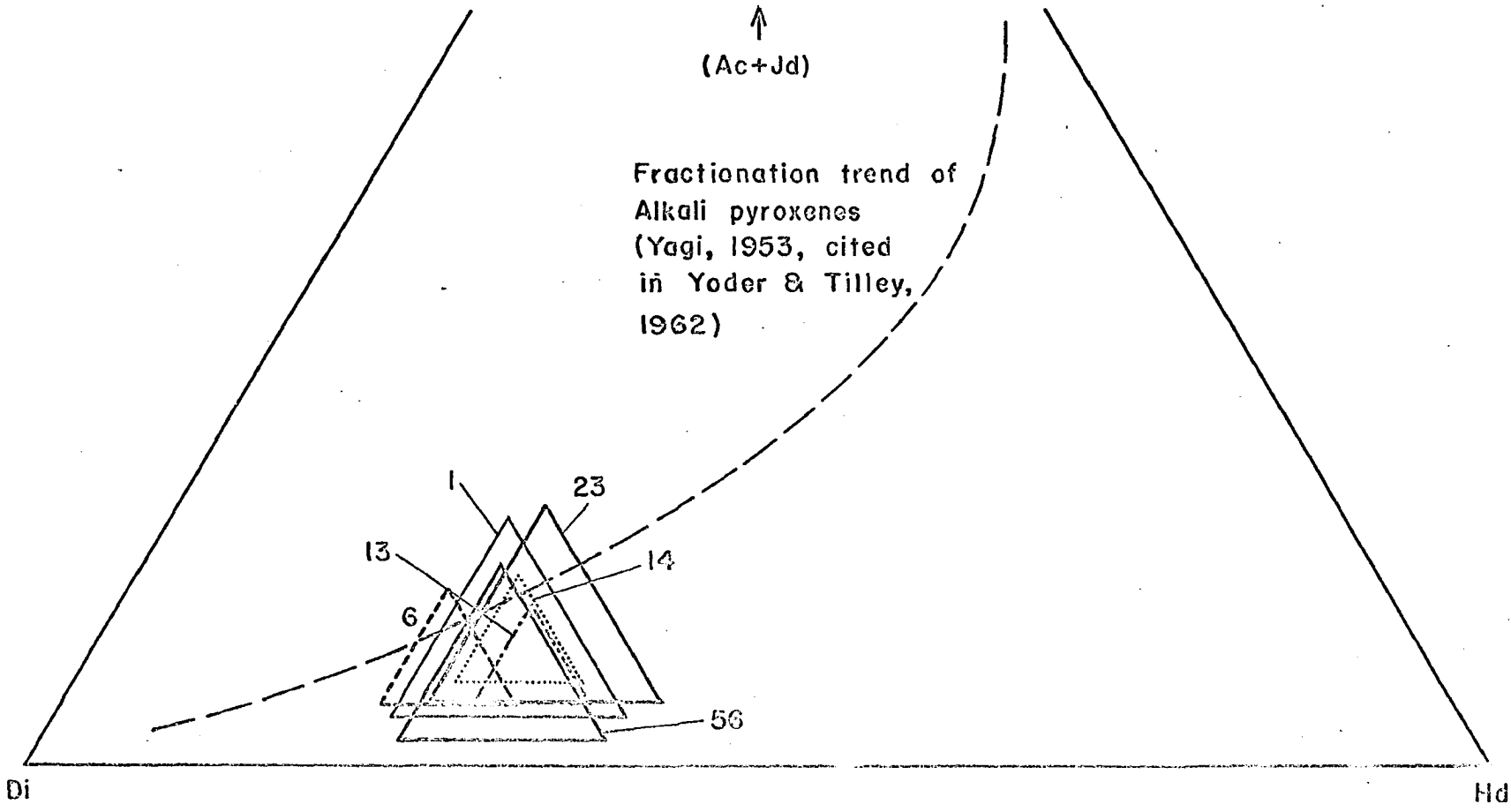

Fig. 26. Di - (Ac+Jd) -Hd plot of clinopyroxene showing the overlap in the clinopyroxene compositions of alkali basalts and the Trident andesites. (The area of the triangle represents the proportion of Tschermak's molecule).

Table 37. Unit Cell Data for Clinopyroxene.

S. Nos.	Cell Parameters (Å) a	b	c	β°	a Sinβ(Å)	Cell Vol Å^3	Ionic Vol. Å^3	Packing Index
C-56	9.7401	8.91941	5.2112	106°12'	9.3534	434.75	297.99	6.854
C-14	9.7431	8.93341	5.2433	106°14'	9.3543	438.16	298.32	6.808
C-1	9.7400	8.9206	5.2071	105°56'	9.3660	435.05	298.41	6.859
C-6	9.7420	8.9209	5.2185	106°11'	9.3562	435.57	297.71	6.835
C-23	9.7469	8.9362	5.2182	106°34'	9.3424	435.64	297.72	6.834
C-13	9.7635	8.9349	5.2304	106°08'	9.3798	438.35	298.02	6.799

Table 38. Distribution of Cations in Tetrahedral and Octahedral Sites in Clinopyroxene.

	Octahedral Site							Tetrahedral Site		
S.Nos.	Mg	Fe^{2+}+Mn	$Ca_{(Wo)}$ + $Ca_{(Tsch)}$	Na+K	Fe^{3}+Ti	Al	Other Cations (Ni,Cr,etc.)	Fe^{3}+i	Al	Si
C-56	0.880	0.242	0.784+0.006	0.040	0.040	0.006	0.003	0.049	0.105	1.846
C-14	0.798	0.260	0.804	0.065	0.050	0.015	0.008	-	0.101	1.899
C-1	0.864	0.231	0.821	0.042	0.036	0.006	0.006	0.053	0.125	1.816
C-6	0.833	0.222	0.720+0.061	0.049	0.049	0.061	0.006	0.042	0.063	1.895
C-23	0.864	0.244	0.754+0.013	0.051	0.051	0.013	0.009	0.040	0.143	1.817
C-13	0.813	0.286	0.778+0.010	0.049	0.049	0.010	0.005	0.005	0.083	1.912

Table 39. Calculated Composition in Terms of Pyroxene End-Members.

	Mol.%							
S.Nos.	CEn	CFs	Wo	Equiv. Di.	Jd	Ac	Ca-Tsch	Others (with Ni, Cr. etc)
C-56	44.0	12.1	39.2	78.4	-	4.0	0.6	0.1
C-14	39.9	13.0	40.2	79.8	1.5	5.0	-	0.4
C-1	43.2	11.6	41.1	82.2	0.6	3.6	-	-
C-6	41.7	11.1	36.0	72.0	-	4.9	6.1	0.2
C-23	43.2	12.2	37.7	75.4	-	5.1	1.3	0.5
C-13	40.7	14.3	38.9	77.8	-	4.9	1.0	0.2

Increasing Fe^2	:	Increasing b (Brown)
Increasing Ca	:	(a) rapid increase in a sin β (Brown)
		(b) slight increase in b or decrease in b (Kuno, 1955, p. 81)
		(c) no effect on c (Brown).
Increasing Al(vi)	:	decreasing b (Kuno and Hess, 1953), fig. 4; Kuno, 1955, fig. 4; Brown, 1960, fig.2)
Increasing Al(iv)	:	minor increase in c (Kuno, 1955, fig. 2)

The above realtions are caused by ionic substitutions, and according to Brown (op. cit.) the c parameter changes are of uncertain validity.

On the basis of the arguments offered regarding the composition of the orthopyroxenes, there is enough justification for considering the clinopyroxenes as solid solutions of Wo-CEn-Cfs-Jd-Ac-Tsch (wollastonite - clinoenstatite - clinoferrosilite - jadeite - acmite - Tschermak's mol.).

The relations between the c cell parameter and (2 Si) as shown in fig. 27 indicate dominant 4-coordination of Al, and the same is also confirmed by the curve defined by the packing index (2-Si) variation curve in fig. 28. It is further observed that the plots split into two parallel trends, each corresponding to predominant 4-coordination of Al. Considering the petrogenetic significance of the packing index (Yamaguchi, 1964) the sequence of crystallization shown by the packing index is C-1, 56, 6, 23, 14, 13.

Cation distribution between two sites and chemical compositions recast in terms of the pyroxene end members are shown in tables 38 and 39. The composition in terms of end members following the method suggested by Kushiro (1960, 1962) and Yoder and Tilley (op. cit.) is shown in table 40 for comparison.

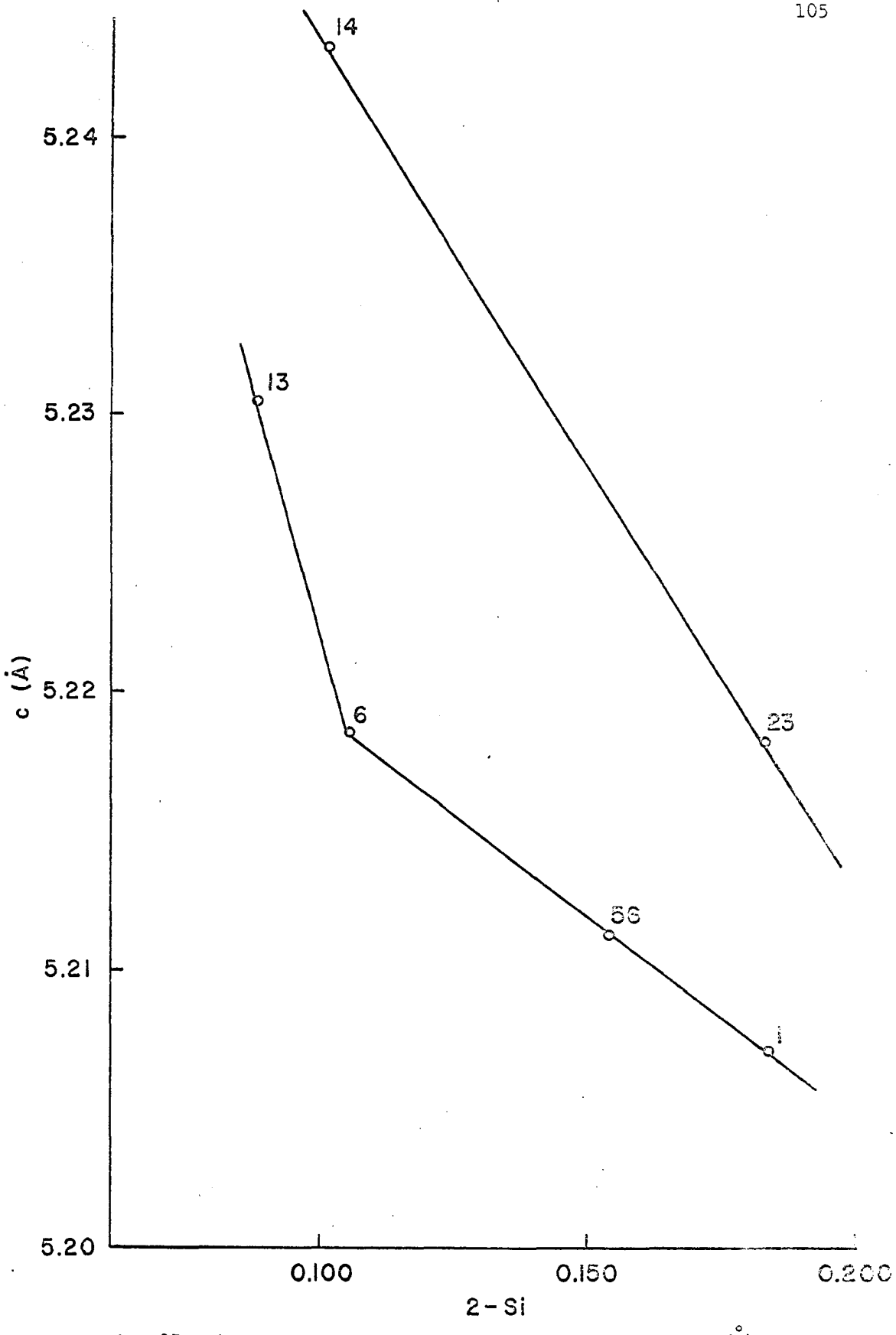

Fig. 27. Diagram showing the inverse relation between c(Å) and (2-Si) of clinopyroxene.

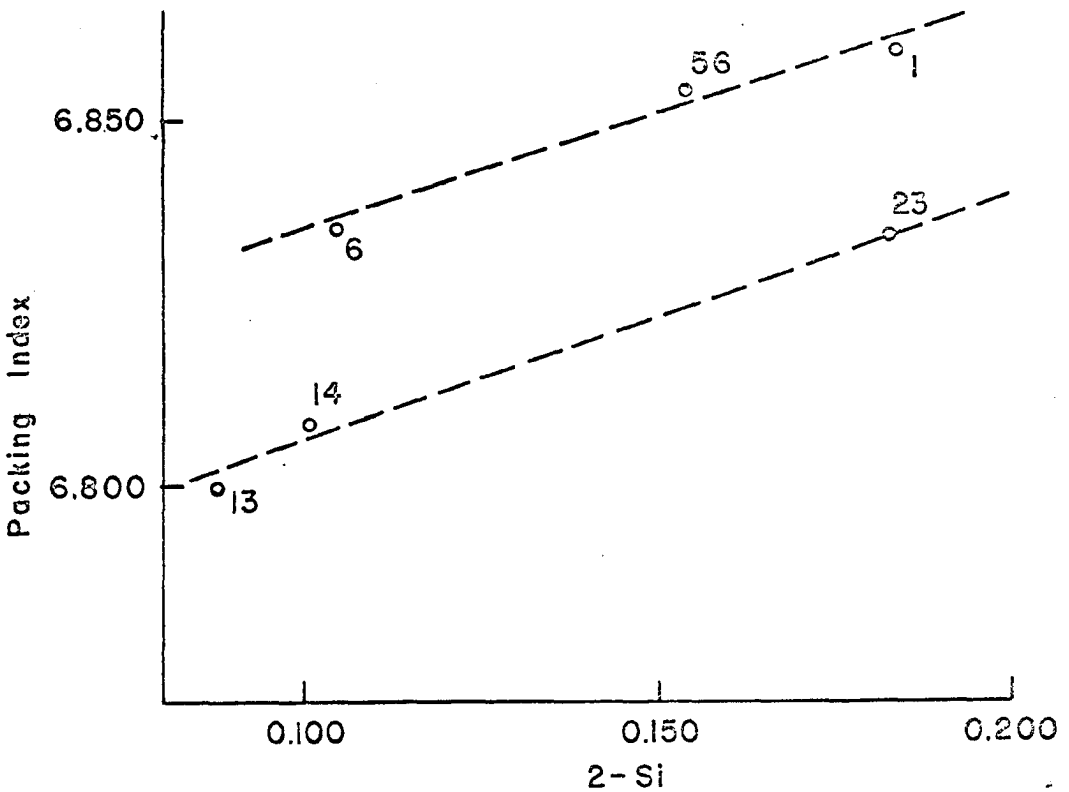

Fig. 28. Diagram showing the relation between packing index and (2-Si) of analyzed clinopyroxene.

The unit cell volumes were derived from the calculated molecular ratios and structural formulae using the cell volumes of the end members (table 25). Since there is a possibility of both pseudowollastonite and parawollastonite, the cell volume of diopside was used rather than equivalent (En,Wo). The close agreement between the calculated and observed unit cell volumes as shown in table 41 (error < 0.70%) confirms the solid solution relations.

The probable nature of variations in cell parameters of clinoenstatite due to solid solutions with the other pyroxene end members are shown in table 42. These approximations are based on the cell parameters of the different end members given in table 25. For convenience in plotting, the end member composition, given in table 39, have been grouped as shown in table 43.

The a sin β, b and c parameters have been plotted against the Wo and (Jd + Ac + Ca - Tsch) mol.% in figs. 29 and 30 respectively. In the Trident clinopyroxenes the effects of changing Jd + Ac + Ca - Tsch concentrations are seen in the b and c parameters while the effect of changing Wo concentration is seen in all of the cell parameters (figs. 27 and 28). The small differences in the CEn:CFs ratios, as shown in table 43, do not account for the variation in the observed cell parameters, and particularly the b parameter. This phenomenon contradicts the conclusions of Hess, Kuno and Brown (op. cit.).

Structural Formulae, Norms and their Petrogenetic Significance

Clinopyroxenes, C-23, 1 and 14 are characterized by normative nepheline while C-56, 6 and 13 contain normative hypersthene. All clinopyroxenes contain normative olivine (table 34). This indicates the undersaturated

Table 40 . End-Member Composition (according to the method of Yoder and Tilley, 1962).

S.Nos	Mol.% Di	Hd	Tsch	Ac + Jd
C-56	56.4	24.2	15.4	4.0
C-14	57.4	26.0	10.1	6.5
C-1	54.3	23.1	18.4	4.2
C-6	62.3	22.2	10.5	4.9
C-23	52.2	24.4	18.3	5.1
C-13	57.7	28.6	8.8	4.9

Table 41. Calculated vs. Observed Unit Cell Volumes ($\mathring{A}^3$).

	C-56	C-14	C-1	C-6	C-23	C-13
Calc. unit cell vol.	437.71	436.63	438.09	436.53	437.34	438.00
Obs. unit cell vol.	434.75	438.16	435.05	435.57	435.64	438.35
% difference	<0.7	<0.5	<0.7	<0.4	<0.5	<0.1

Table 42. Probable Nature of Changes in Unit Cell Parameters of Clinoenstahite due to solid solution with other Pyroxene end-members.

Cell parameters End-members	a/a sin β(Å)	b(Å)	c(Å)
CFs	-	+	-
PWo/Wo	+/-	-	+
Jd	+	-	Small
Ac	+	-	+ (?)
Ca-Tsch	+	-	+ (?)

Table 43. Grouping of End member Composition of Analyzed Clinopyroxene.

S. Nos.	Mol. % (CEn+CFs)	(Wo+Ca-Tsch)	(Jd+Ac)	CEn:CFs
C-56	56.1	39.8	4.6	78.4:21.6
C-14	52.9	40.2	6.5	75.4:24.6
C-1	54.75	41.05	4.2	78.9:21.1
C-6	52.8	42.1	11.0	79.0:21.0
C-23	55.4	39.0	6.4	77.98:22.02
C-13	55.0	39.9	5.9	74.0:26.0

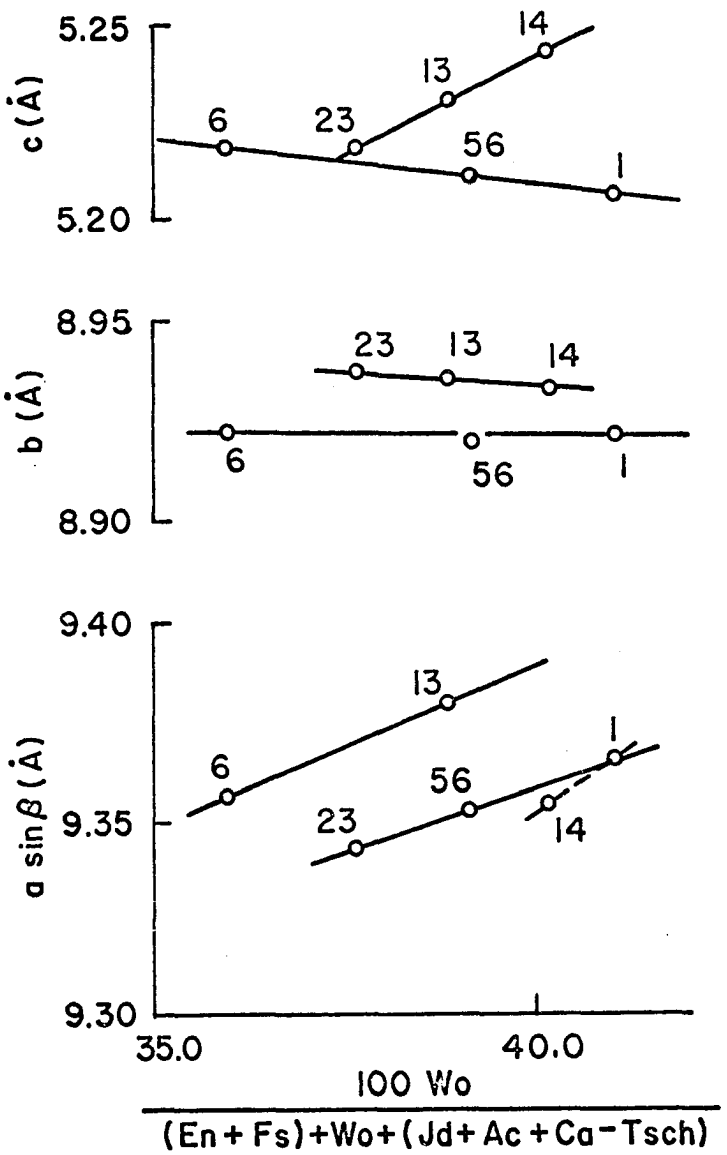

Fig. 29. Diagram showing relations between mol.% Wo and cell parameters of analyzed clinopyroxene.

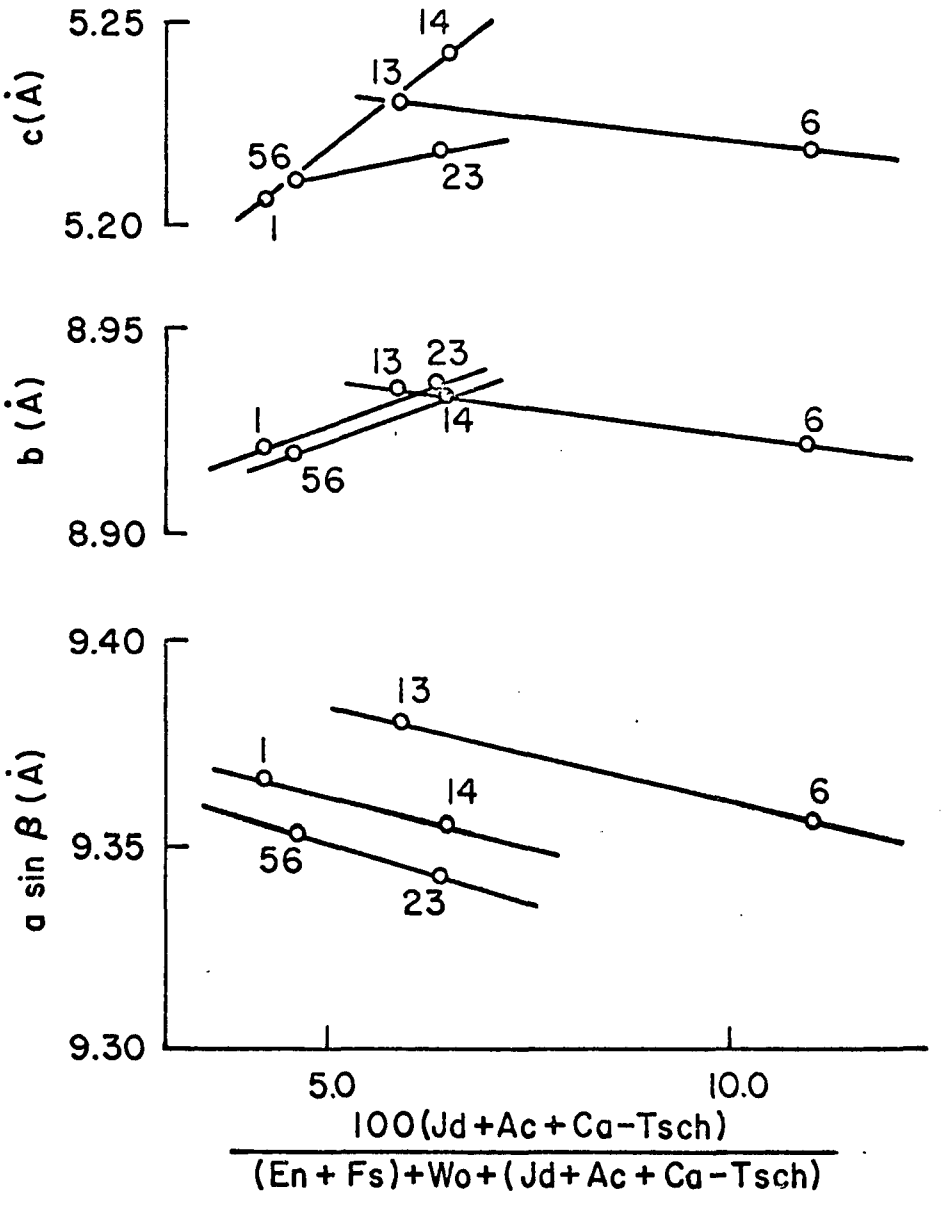

Fig. 30. Diagram showing relations between mol.% (Jd + Ac + Ca-Tsch) and cell parameters of analyzed clinopyroxene.

nature of the parent melt from which they crystallized. Furthermore, the nepheline bearing clinopyroxenes (C-23,1 and 14) must have crystallized from critically undersaturated melts, similar to the pyroxenes from alkali basalts and hawaiites, as reported by Yoder and Tilley (op. cit., p. 365). Clinopyroxenes 1 and 14 contain the jadeite molecule and remaining clinopyroxenes contain Ca-Tschermak's molecule (table 39).

The crystallization of clinopyroxenes C-56, 6, 23 and 13 did not enrich the residual melt in silica while the jadeite bearing clinopyroxenes C-1 and C-14 may have (Yoder and Tilley, op. cit., p. 413). A consistent range in the acmite content or 6-coordinated Fe^3 indicates a high and near constant P_{O_2} during the crystallization of these particular clinopyroxenes. The entry of Jd molecule was facilitated by increasing P_{O_2} or accelerated H_2 escape, or conditions which would accelerate crystallization of An - rich plagioclase; while the entry of Ca-Tsch molecule was initiated by P_{H_2O} buildup decrease of P_{O_2} leading to suppression of plagioclase crystallization. C-1 and 14 crystallized under increasing P_{O_2}, while C-56, 23, 13 and 6 crystallized under conditions of decreasing P_{O_2}/P_{H_2O} build-up.

Further discussions of the sequence of crystallization of the clinopyroxene are discussed in a later section on coexistent pyroxene relations.

CHEMICAL RELATIONS OF COEXISTING PYROXENES

Si-Al Ratio

The Al content of clinopyroxenes has been considered to be a critical petrogenetic index (Kushiro, 1960). Si-Al plots of the analyzed ortho - and clinopyroxenes are shown in fig. 31. The compositional fields of clinopyroxenes from the tholeiitic and alkali basalt series have also been transferred to the diagram (as taken from Kushiro, op. cit., p. 549, fig. 1).

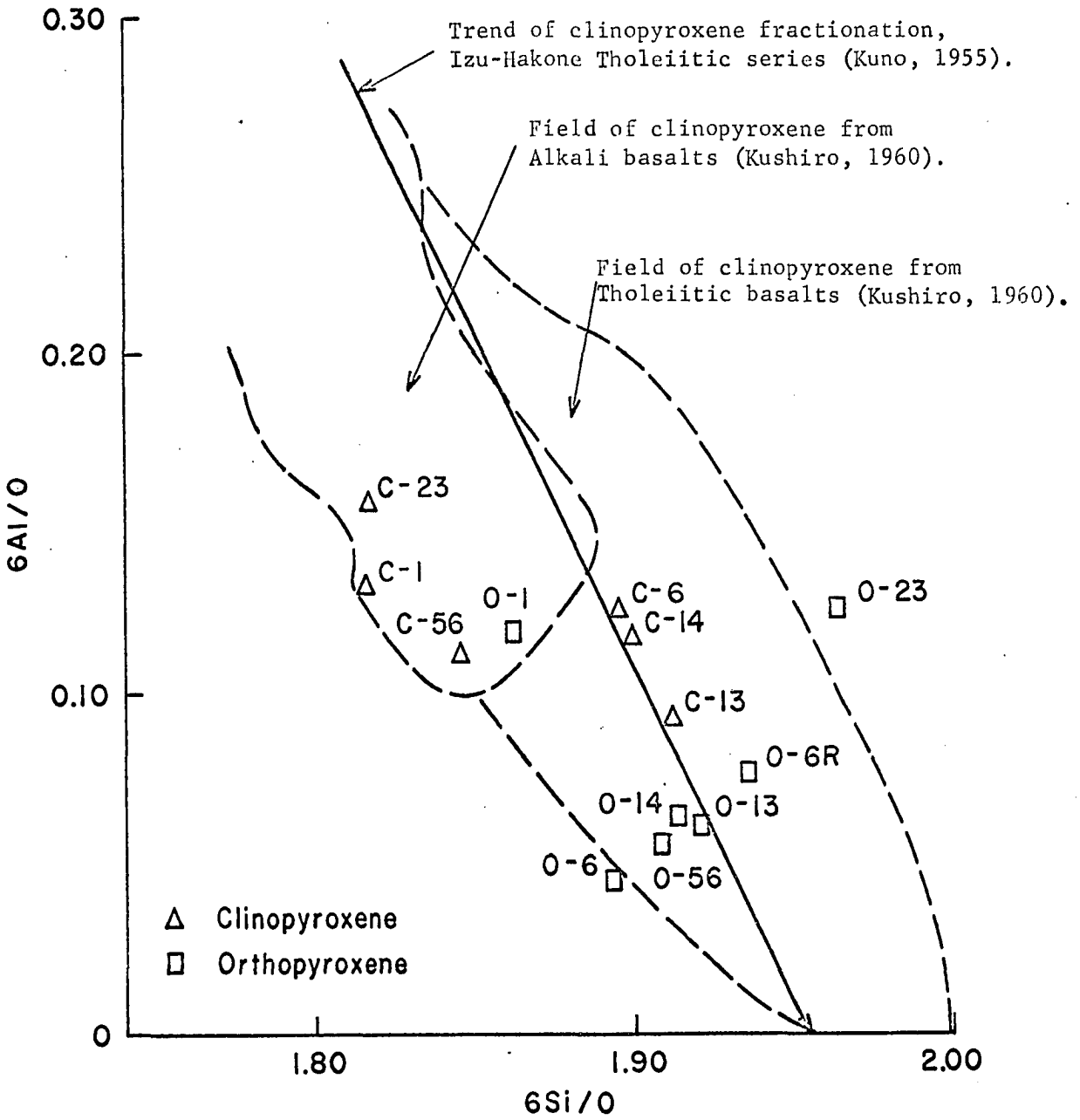

Fig. 31. Si-Al plot showing comparative compositions of Trident clino- and orthopyroxenes and those from tholeiitic and alkali basalts.

Fractionation trends of the Izu-Hakone tholeiitic (high-alumina) clinopyroxenes are shown on the same diagram by an arrow (after Kuno, 1955). This Izu-Hakone trend partially coincides with the clinopyroxene trend from the Skaergaard complex (Brown, (1957), which was believed to have been derived from an undersaturated high-alumina basalt magma by Yoder and Tilley (1957) and Kuno (1960). Plots for clinopyroxenes C-6, 14 and 13 are remarkably similar to those from the Skaergaard complex (Kushiro, op. cit., p. 543). Fig. 31 reveals that clinopyroxenes C-23, 1 and 56 plot in the field of clinopyroxenes from alkali basalts, and the trends are approximately parallel to those for clinopyroxenes from Black Jack (Wilkinson, 1957) and Atumi Sills (Kushiro, 1959), belonging to typical alkali basalt Series. Clinopyroxenes C-6, 14 and 13 form a distinct group which occupies the center of the tholeiitic field, paralleling the trends defined by the clinopyroxenes of the Izu-Hakone (tholeiitic) and Skaergaard complex (high-alumina series). Generally there is an inverse relation between Si and Al in the analyzed clinopyroxenes, while the coexistent orthopyroxenes show a covariance between Si and Al proportions. Obviously, C-23, 1, 56 and (?) 14 crystallized from an undersaturated melt (or critically undersaturated melt, as suggested by the normative nepheline content of C-23, 1 and 14) which shifted the composition of the coexisting melt toward the tholeiitic - high-alumina basalt field.

Distribution Coefficients

Distribution coefficients of cations between coexisting equilibrium ortho - and clinopyroxene phases have been hailed as thermometric indices (McIntyre, 1963, p. 1209). However, Kretz (1961, p. 374) concluded that the $K_{D\ Mg}$ of igneous pyroxene pairs is greater than metamorphic pairs, and attributed this effect primarily to temperature differences (ibid., p.378).

During intrusive igneous and metamorphic crystallization equilibrium is often attained provided pressure-temperature conditions are suitable, but in extrusive systems disequilibrium relations characterize the course of crystallization. Thus, coexisting assemblages in solidified lavas may not have been in equilibrium with a liquid equivalent to the bulk composition, or the mineral phases may themselves constitute disequilibrium assemblages. This means, for example, that coexistent pyroxenes may not be co-crystallized phases in volcanic rocks. An interpretation of the distribution coefficients of the analyzed pyroxene pairs should be tempered by this fact. The distribution of minor elements between coexistent phases may not reveal these anomalies within a limited period of crystallization, but the partition of major components may not be as systematic as that of equilibrium assemblages.

The distribution of the major cations Mg, Fe and Ca and the minor cation Mn has been calculated for analyzed coexistent pyroxenes. The following distribution coefficents have been listed in table 44:

$K_{D\ Mg}$; with reference to Ca, $(Fe^{2+} + Mn)$, Fe^{2} and $(Fe^{2} + Ca)$,

$K_{D\ Fe}$; with reference to Mg and Ca,

$K_{D\ Ca}$; with reference to $(Fe^{2+} + Mg)$ and $<Fe^{2+} + Mn + Mg)$,

$K_{D\ Mn}$; with reference to $(Fe^{2+} + Mg + Ca)$.

Since the solid solution end members are also multicomponent systems, the study becomes more difficult. An example of this is furnished by the distribution of Mn between coexistent pyroxenes. The approximate parallelism between the tie lines (fig. 32) indicates fairly constant values of $K_{D\ Mn\ (Fe^{2},Mg)}$ (cf. Carstens, 1958). However, when Ca is considered, $K_{D\ Mn}$ values show a greater dispersion (table 44). Mutual solid solutions between the Ca, Mg and Fe end members are possible, and unless the molecular

Table 44 . Distribution Coefficients of Cations in Coexistent Ortho - and Clinopyroxenes.

S.Nos.	K_D Mg[Ca]	K_D Mg[Fe+Mn]	K_D Mg[Fe]	K_D Mg[Fe+Ca]	K_D Fe[Mg]	K_D Fe[Ca]	K_D Ca[Fe+Mg]	K_D Ca[Fe+Mg+Mn]	K_D Mn[Fe+Mg+Ca]
O&C-56	9.8042	0.5667	0.5664	2.0851	1.7657	17.270	0.0880	0.0876	2.4175
O&C-14	11.7955	0.6546	0.6493	2.3371	1.5399	18.169	0.0751	0.0750	1.8607
O&C-1	6.1721	0.6190	0.6167	2.1248	1.6215	10.022	0.1439	0.1434	2.0782
O-6R&C-6	5.5917	0.5394	0.5360	1.8622	1.8658	10.416	0.1523	0.1516	2.2565
O&C-6	3.7669	0.6575	0.6542	1.8724	1.5287	5.766	0.2398	0.2392	1.8218
O&C-23	5.5229	0.6093	0.6078	1.8892	1.6450	9.106	0.1658	0.1588	2.0852
O&C-13	7.7860	0.6968	0.6921	2.1451	1.4451	11.273	0.1158	0.1153	1.7727

Table 45 . Concentrations of Major Cations in Coexistent Ortho - and Clinopyroxenes.

S. Nos.	Major Cation Concentrations					
	Orthopyroxenes			Clinopyroxenes		
	X Mg[Fe+Ca]	X Fe[Mg+Ca]	X Ca[Fe+Mg]	X Mg[Fe+Ca]	X Fe[Mf+Ca]	X Ca[Fe+Mg]
O&C-56	0.6423	0.299	0.0588	0.4627	0.122	0.4154
O&C-14	0.6394	0.306	0.0546	0.4314	0.134	0.4346
O&C-1	0.6381	0.264	0.0983	0.4535	0.115	0.4310
O-6R&C-6	0.6099	0.288	0.1023	-	-	-
O&C-6	0.6112	0.237	0.1521	0.4564	0.116	0.4280
O&C-23	0.6199	0.276	0.1038	0.4633	0.126	0.4113
O&C-13	0.6220	0.301	0.0774	0.4341	0.145	0.4207

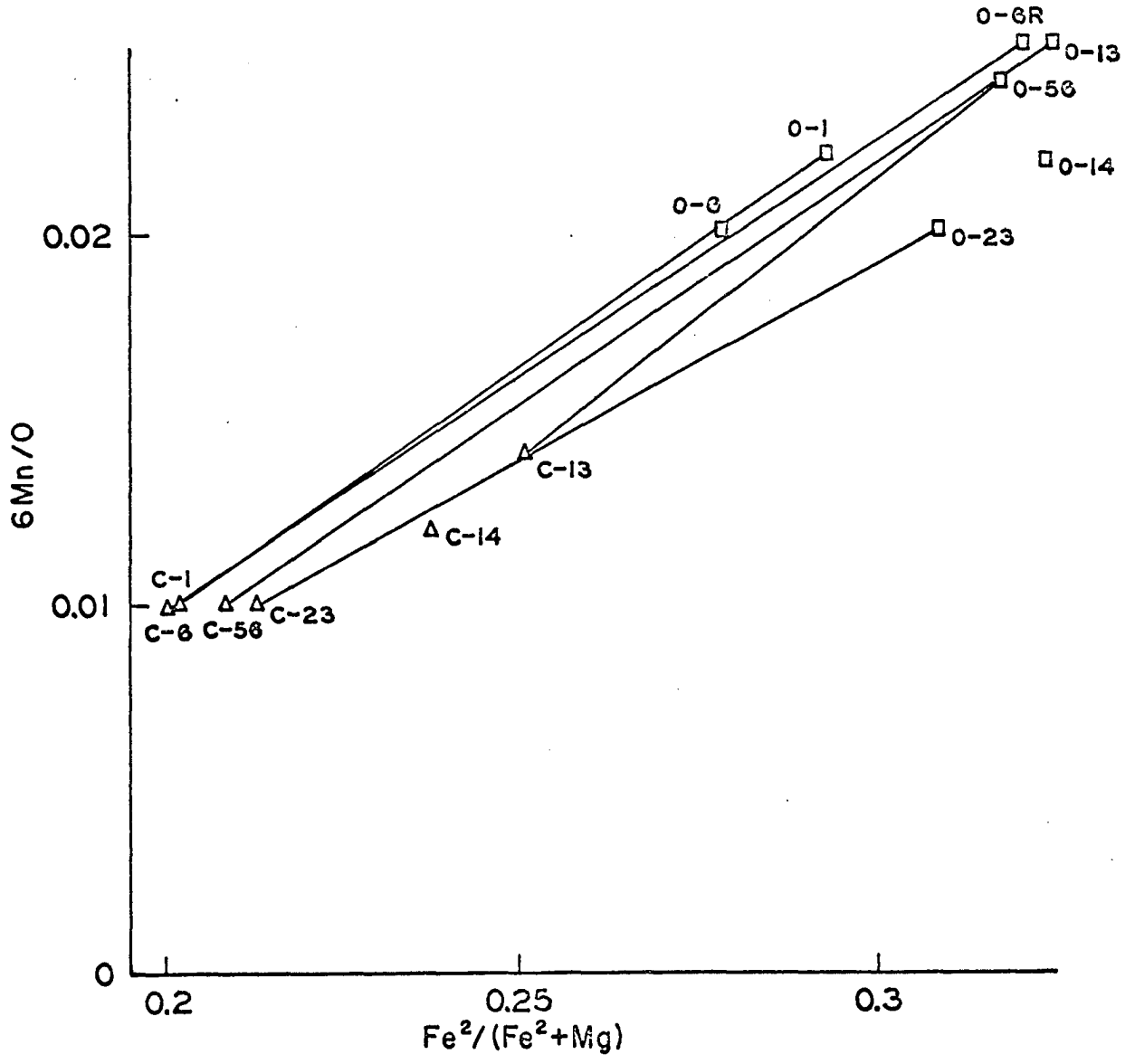

Fig. 32. Plot showing the distribution of Mn between coexistent clino- and orthopyroxenes.

proportions of end members within the binary systems are known, the distribution coefficients would be insignificant. The limitations introduced by the above discussion, are as follows:

(1) In the absence of definite evidence, mineral phases cannot be strictly considered as products of synchronous crystallization,

(2) One or both of the co-crystallized phases may have reacted differently with coexisting liquids in the course of fractionation,

(3) In the entire spectrum of magmatic crystallization coexistent phenocrystal phases may not be the equilibrium phases corresponding to the bulk composition of the source rock or the coexisting glass.

The variations of the calculated distribution coefficients (table 44) reflects the above limitations. However, $K_{D\ Mg}$ (Fe^2, Fe^{2+} Mn, Fe^{2+} Ca), $K_{D\ Fe(Ca)}$ and $K_{D\ Mn\ (Mg\ +\ Fe^{2+}\ Ca)}$ appear to be reasonably consistent. A general interpretation of these coefficients would indicate that the phases were comagmatic and that deviations are related to some of the variables discussed above.

The most useful clue derived from the above studies indicates that pyroxene pairs 1 and 13 are simultaneous phases, or nearly so; and thus useful as a base for extrapolation . The simultaneity of pyroxene pairs 1 and 13 are also supported in part by the Si-Al relations shown in fig. 31, where the disequilibrium between the pyroxene pair 23 is also distinctly revealed. In the same diagram clino- and orthopyroxenes C-1 and O-1 are very basic, high-alumina, low silica and densely packed phses. Plots of the ortho- and clinopyroxenes O-13 and C-13 lie very close to the high alumina fractionation trend. It is significant that the source rock (KT-13) was obtained from a block which was in solid state before ejection (a plug or solidified crust (?)).

Following the lead mentioned in the above paragraph, the distribution of the major components Mg,Fe and Ca (with reference to total Mg + Fe + Ca - table 45) in the coexistent pyroxenes has been plotted in fig. 33. The trend determined by the plots of pyroxene pairs 1 and 13 has been used as a base line for the projection of the other pairs (in each case). Plot of pyroxene pair 23 on Fe distribution curve (fig. 33) fall on the trend defined by the pyroxene pairs 1 and 13. These projections reveal the concentrations of the major components, which would have existed in equilibrium orth- and clinopyroxene phases. The projections also reveal the theoretical sequence of crystallization of the orthopyroxenes and clinopyroxenes in regard to the variation in the molar concentration of Mg, Fe and Ca metasilicates. The gradients of major cation distribution as determined by pyroxene pairs 1 and 13 correspond to:

$$K_D^{O-C}\ Mg\ (Fe + Ca) \sim 2.0$$

$$K_D^{O-C}\ Fe\ (Mg + Ca) \sim 2.4$$

$$K_D^{O-C}\ Ca\ (Fe + Mg) \sim 0.2$$

These are acceptable values. Variations in Mg and Fe are of value in tracing the trend of fractionation, but Ca is of doubtful value due to competition for Ca by co-crystallizing plagioclase.

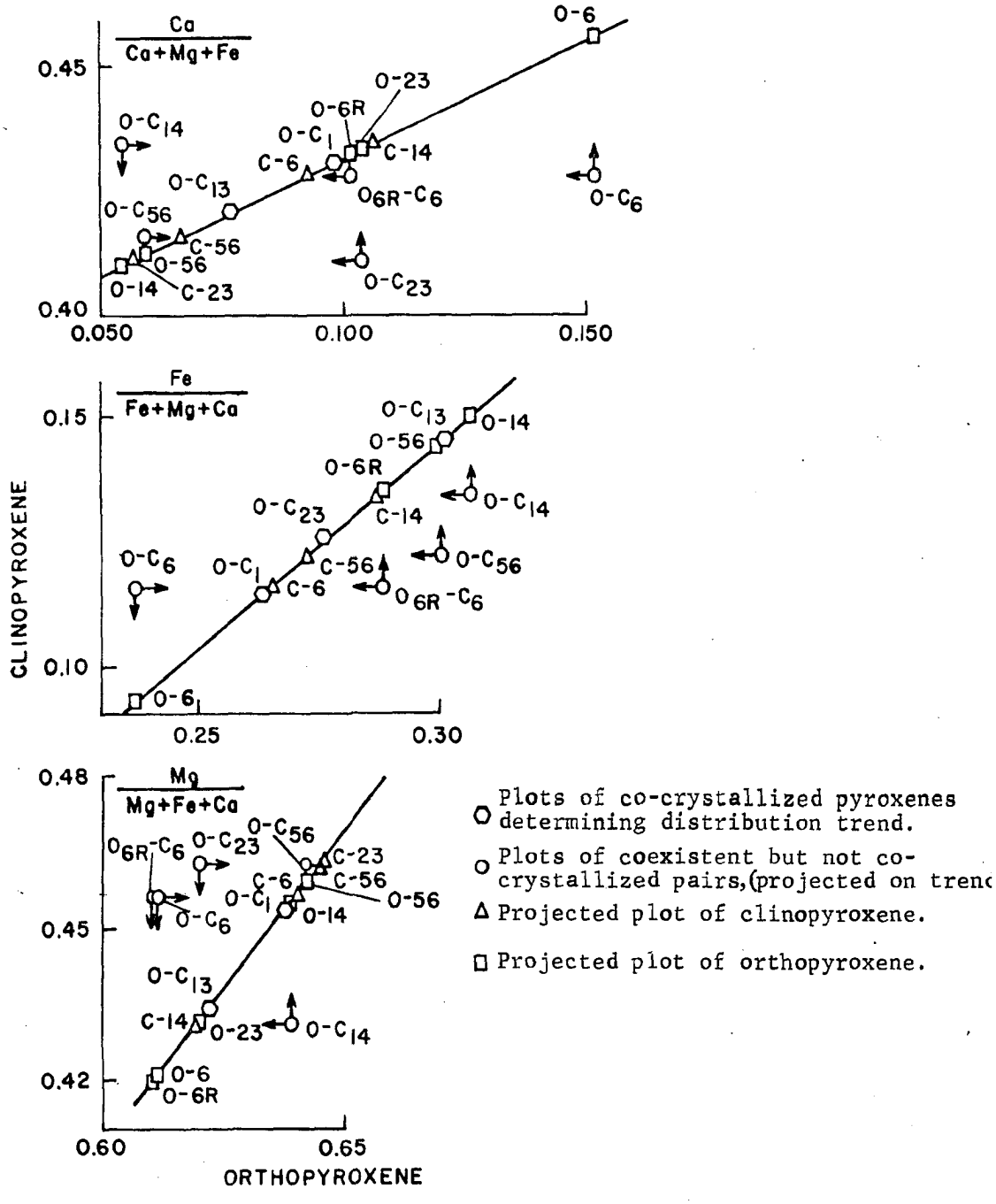

Fig. 33. Distribution of major cations in analyzed coexistent pyroxenes and trends determined by the plots of co-crystallized pairs 1 and 13; projected plots of other pairs are also shown.

Normative versus Crystalline Pyroxene Phases

Bulk normative pyroxene:

Normative pyroxene compositions calculated (Table 53) from each of seventeen analyzed andesite specimens are plotted in the pyroxene diagram shown as fig. 34. Analyses 18 and 27 are of the prehistoric lavas. Plots of specimens belonging to the same flow units have been linked by solid lines. The distribution of the plots defines three different trends- (5-6), (18-11) and (27-14-TC), and these trends are shown by broken lines. Significantly, two of the trends coincide with the plots of the normative pyroxenes of the prehistoric lavas. This coincidence expresses the general magmatic consanguinity of the Trident lavas. In addition, all of these plots define the successive pyroxene fractions which would have crystallized from melts equivalent to the bulk rock compositions, if equilibrium conditions prevailed. Recalling the analogy with the diopside-forsterite-(enstatite)-silica system, all of these plots belong to the two-pyroxene field, and the trend lines seem to shift the liquid phase towards general silica enrichment or saturation. Trend of normative pyroxene composition from one flow unit is, however, different (particularly the portion defined by 1-2-3-10), which incidentally intersects the previously mentioned trends (a, b and c -fig. 34). Both trends show Fe enrichment, and Mg depletion in the case of a, b and c, and Ca depletion in the case of 1-2-3-10 trends are evident too. A check against the solvus diagram (fig. 15) reveals that the trends a, b and c are attributable to gentle cooling gradients, and the other trend (1-2-3-10) to steep cooling gradients. The latter can be correlated to the post-eruptional environment, with particular emphasis on the control of bulk compositions by the ratio of glass to crystalline plagioclase. The trend of bulk compositional variation in an individual flow is related to the crystallization of plagioclase under high P_{O_2} of an

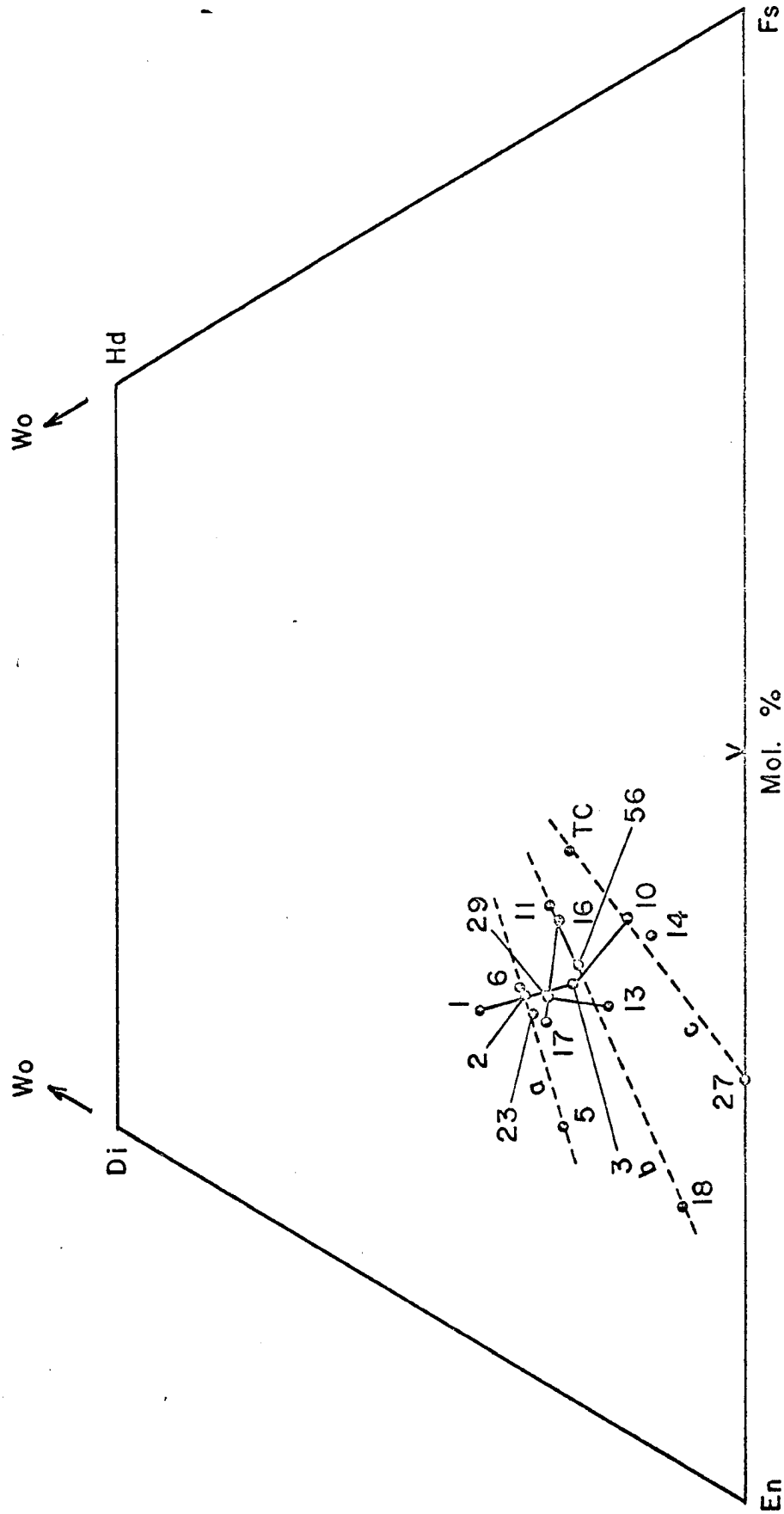

Fig. 34. Normative pyroxenes from molecular norms of the Trident andesites. Plots of normative pyroxenes from same lava units are joined by solid lines.

atmospheric environment; whereas the stable Ca:Fe ratio defined by trends a, b and c reflect sub-crustal fractionation effects under lower P_{O_2}. Conceivably, fractionation at sub-crustal levels may have brought the residual liquid compositions to some stage along the trends a, b and c before eruption. During subsequent crystallization under at mospheric pressure, trends had followed courses parallel or similar to that defined by (1-2-3-10) in fig.34.

Extensions of trends a and b to En-Fs join (fig. 34) indicates primary olivine fractions; and the first pyroxene phase would be monoclinic. Crystallization along c trend would encourage orthorhombic pyroxenes.

Chemical relations of the normative pyroxenes of the Trident andesites and composition of the analyzed coexistent pyroxenes are shown in fig. 35, a Wo-En-Fs diagram. The triangles formed by the three plots corresponding to the normative and the coexistent pyroxenes express the disequilibrium between the actual vs normative pyroxenes calculated from the bulk compositions. The absence of a triangle in case of 0, C and KT-23 and the near linear curves in 0,C and KT-1 and 13 confirm the phase equilibrium in these three cases; a conclusion which was in part deduced from earlier data. The plot of the normative pyroxene composition on the pyroxene tie line is also an expression of the relative proportions of the two phases in the rock.

Normative Pyroxene Composition of Groundmass Glass:

The normative pyroxene compositions of groundmass glass and compositions of the analyzed crystalline phases are graphically compared in fig. 36 on a standard pyroxene triangle. Evidently the normative pyroxene compositions of the residual liquids (glass from KT-23, 6 and 13) were derived during crystallization of clino- and orthopyroxene 23, 6 and 13: while in case of 1, 14 and 56, orthopyroxenes crystallized later than the clinopyroxenes.

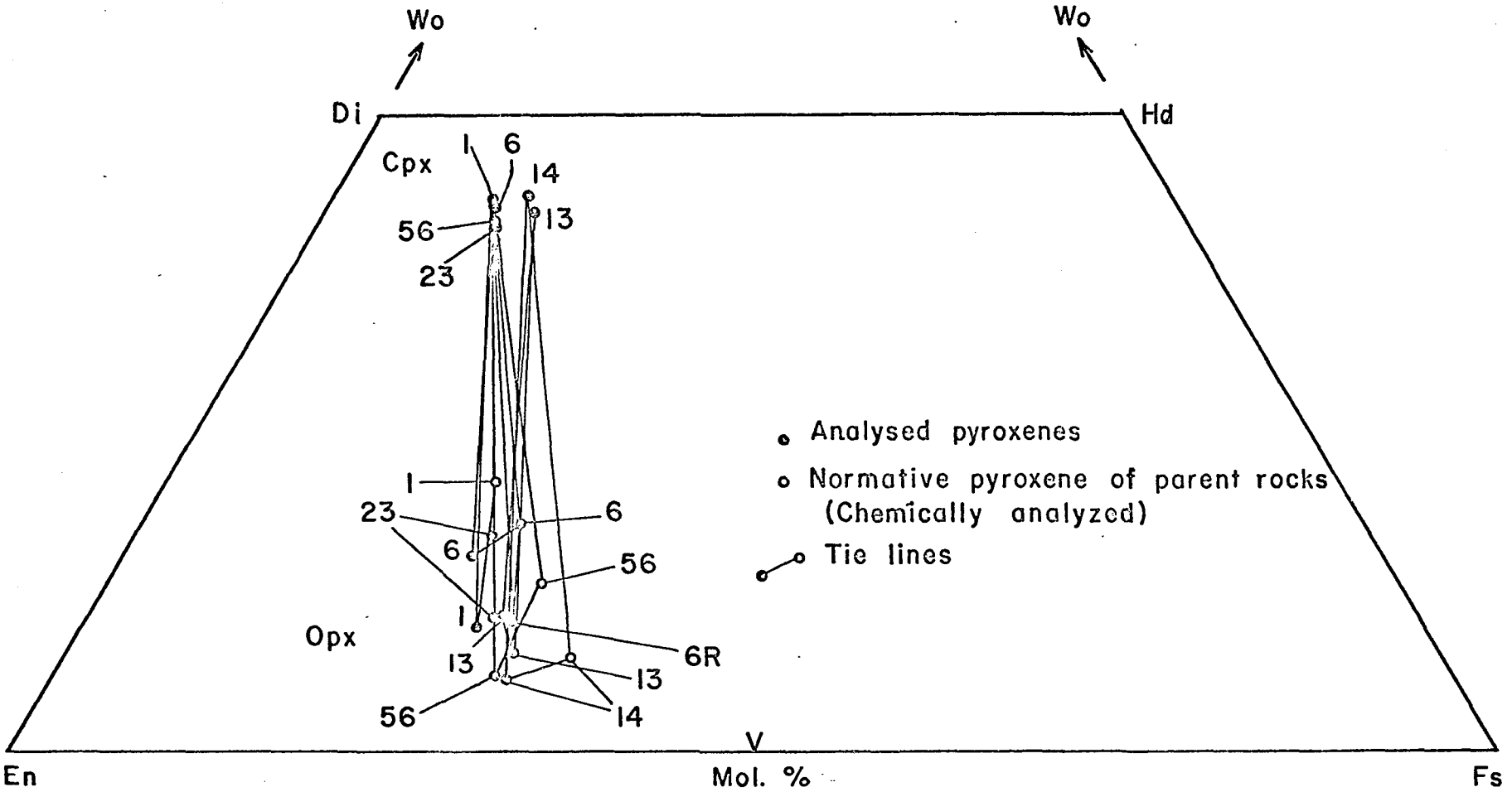

Fig. 35. Wo-En-Fs plot of coexistent orthopyroxene, clinopyroxene and normative pyroxenes from the parent rock.

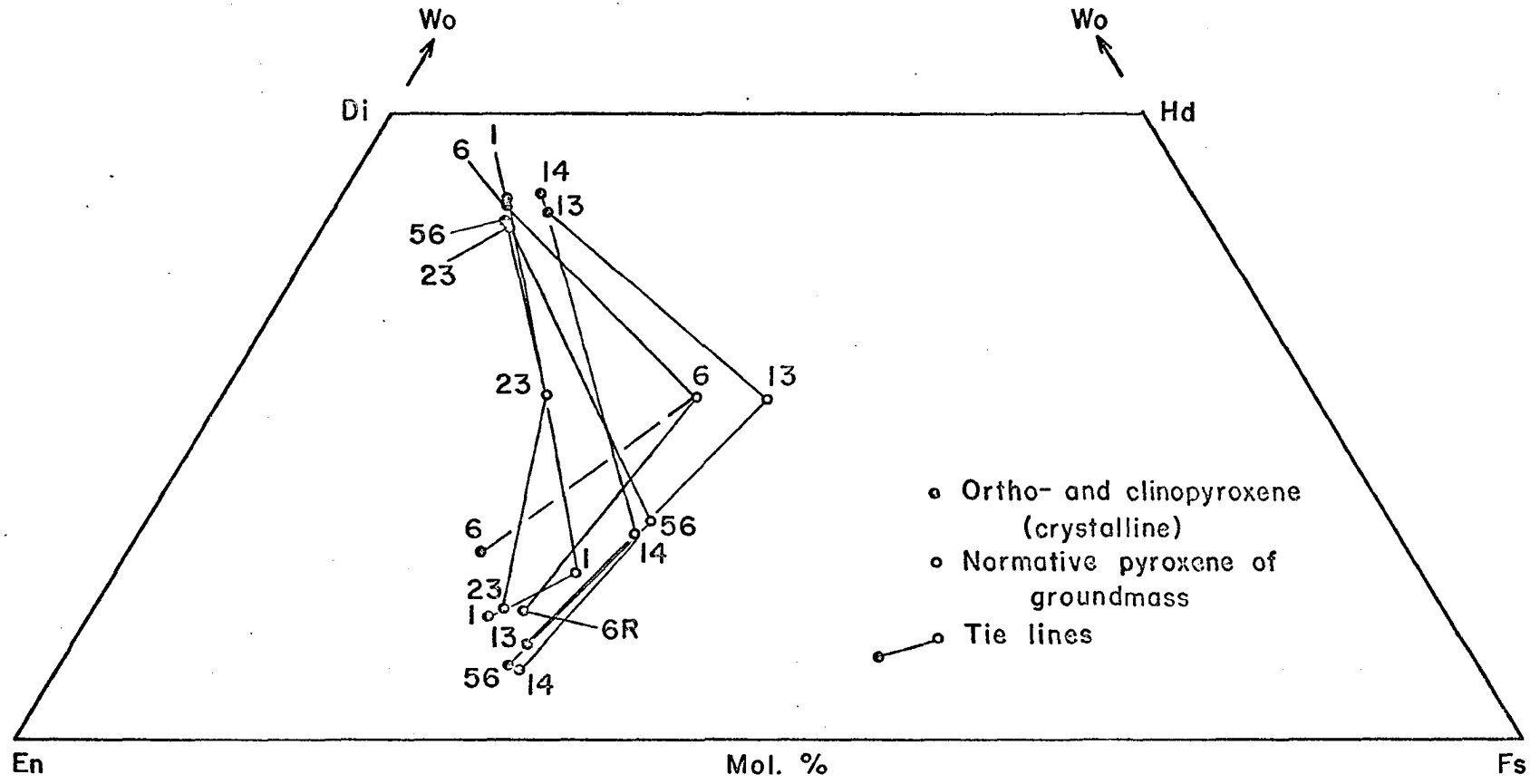

Fig. 36. Wo-En-Fs plot of coexistent orthopyroxene, clinopyroxene and normative pyroxenes from the groundmass.

Crystallization of clinopyroxene 23, followed by orthopyroxene 1, would cause the normative pyroxene composition of the residual liquid to shift to 1 (fig. 36); and later, clinopyroxene 23, in contact with residual liquid, would induce the crystallization of a modified clinopyroxene 23 and orthopyroxene 23. At this stage the normative pyroxene composition of the residual liquid would move to 23 (fig. 36).

Two distinct trends, revealed by the normative pyroxene compositions (1-14-56-13 and 23-6-13, fig. 36) converge at 13. It is probable that this is an expression of the variation trends in the composition of the residual liquid under different rates of cooling; the trend defined by normative pyroxene composition (1-14-56-13) reflecting liquid descent under a lower rate of cooling, while the trend defined by (23-6-13) appear to have been caused by a higher rate of cooling. It is also suggested that plots of normative pyroxene composition 23 and 6 and those of analyzed pyroxene pairs 23 and 6 define small sectors of the pyroxene liquidus and solidus, respectively, in the Wo-En-Fs system.

Sequence of Pyroxene Crystallization

From previous discussions, it appears that the following criteria are useful in the derivation of the relative order of crystallization:

(1) Phase relations of molecular end members (Fs and Wo mol.%),

(2) Packing indices and (2-Si) relations,

(3) Distribution coefficients of major cations in coexistent phases.

The relative order of crystallization (if the analyzed pyroxenes are assumed to have originated from the same magma), as indicated by parameters 1, 2 and 3 above, are compared in table 46. During the fractional crystallization of a basic or intermediate magma, pyroxene and plagioclase crystallize simultaneously, and any suggested sequence of crystallization involving the

fractionation of Ca must consider the composition of the coexistent plagioclase phenocrysts. These relations are extremely complex, and further comment is made on this problem in the section on mineral paragenesis in the final chapter.

Pyroxene Data from Other Sources

Published studies on coexistent pyroxene phases in andesites are rare and few comparative data are available.

Coexistent hypersthene and diopside from the Sheep Mountain andesite were studied by Larsen et al (1936, pp. 695-696). The alkali content of the hypersthene was not determined. Comments on the chemistry of the two phases were not offered, and the purity of the samples was not optimum (ibid. p. 696). According to Larsen et al, the clinopyroxene contained the acmite molecule. The Al and Si content was higher than in pyroxenes from typical tholeiitic basalts. The main objective was a comparison of the Fe/Mg ratios of these particular pyroxenes with those from basalt. Kuno (1950, p. 964) mentions the chemical composition of three hypersthenes from Hakone andesites, and these have a compositional range of Wo_3 En_{54-61} Fs_{36-43}. The alkali content was not determined, nor were the coexistent clinopyroxenes analyzed. An allegedly coexistent (ibid. p. 973) clinopyroxene, (augite), discussed by Kuno, appears to be co-crystallized clinopyroxene, coexistent with pigeonite. Another chemical analysis of an augite from a Hakone andesite (Kuno, 1955, p. 74) is characterized by lower Al_2O_3 and Na_2O and higher K_2O than the Trident augites. Recalculation of this analysis to the pyroxene end member composition revealed the presence of acmite and Tschermak's molecules, but no jadeite.

Table 46 . Relative Order of Pyroxene Crystallization as Shown by Different Parameters.

	Phase Relations En:Wo and En:Fs ratios	Concentrations of major cations			Packing Index	Suggested Sequence
		X Fe	X Mg	X Ca		
Orthropyroxene						
	6R	6	6R	14	23	GR/6
	23	23	6	56	14	23
	6	6R	23	13	56	6/6R
	13	14	13	1	6R	13
	1	13	1	6R	1	1
	14	56	14	23	13	14
	56	1	56	6	6	56
Clinopyroxene						
	13	6	14	23	13	13
	14	13	13	56	14	14
	23	14	1	13	23	1/23
	56	1	6	6	6	6
	1	56	56	1	56	56
	6	23	23	14	1	23/1

Table 47 . Chemical Composition of Plagioclase Phenocrysts.

Component	PP-56	PP-14	PP-1	PP-6	PP-23	PP-13
SiO_2	55.63	55.20	53.85	54.98	55.26	55.75
Al_2O_3	27.97	27.93	28.60	28.53	27.64	28.38
TiO_2	tr	tr	tr	tr	tr	tr
Fe_2O_3	0.22	0.24	0.25	0.38	0.22	0.33
FeO	0.25	0.26	0.36	0.26	0.30	0.29
MnO	tr	tr	tr	tr	tr	tr
MgO	0.09	0.07	0.21	0.11	0.13	0.09
CaO	10.05	9.71	11.38	9.80	10.41	9.66
Na_2O	5.42	5.91	5.27	5.26	5.49	5.54
K_2O	0.16	0.32	0.06	0.29	0.17	0.42
H_2O	0.02	0.00	0.00	0.12	0.10	01.00
H_2O^+	0.00	0.10	0.00	0.00	0.10	0.10
P_2O5	tr	tr	tr	tr	tr	tr
Total	99.81	99.74	99.98	99.73	99.82	100.46

Analyst - H. Haramura

PLAGIOCLASE FELDSPAR

Coexistent phenocrystal and groundmass plagioclase were separated and chemically analyzed. Chemical analyses and molecular compositions of plagioclase recalculated to 32 oxygens are given in tables 47-50.

Chemical Composition

In the recalculation of chemical analyses in mol.% of the end members anorthite ($CaAl_2Si_2O_8$)-albite ($NaAlSi_3O_8$)-orthoclase ($KAlSi_3O_8$), Fe^2 and Mg have been added to Ca (Deer et al, 1963, vol. 4, p. 107). Fe^3 has been considered to be in 4-coordination. Fe^2 is generally treated as an impurity in plagioclase, but there is some evidence of covariance of Fe^2 and Mg (tables 47-50), and Fe^2 cation may occupy a site in the lattice.

As previously mentioned, there is a considerable variation in the composition of both phenocrystal and groundmass plagioclase (zoned and homogeneous). The compositional range is much less in the groundmass plagioclase. The chemical analyses listed in tables 47-50 must be treated as average compositions. The compositional ranges determined in thin sections by optical methods have been mentioned earlier (table 8). Chemical and optical determinations show a fair agreement for homogeneous phenocrysts. The systematic error observed between the chemical and optical determinations of groundmass plagioclase composition (tables 8 and 49-50) may be related to the use of Tröger's (1956) high temperature plagioclase extinction angle curves. Groundmass plagioclase may actually be of the intermediate type. If extinction angle curves for low temperature plagioclase are used the An (anorthite) content would increase by $\sim$ 10%, and the disparity between optical and chemical determinations would be minor.

Considering plagioclase as a continuous reaction series, compositional trends in modal plagioclase should be related to equilibrium states with

Table 48. Structural Formulae of Plagioclase Phenocrysts (based on 32 oxygens).

S.Nos	PP-56	PP-14	PP-1	PP-6	PP-23	PP-13
Cations						
Si	10.027	9.990	9.756	9.934	10.003	9.992
Al	5.949	5.965	6.071	6.083	5.904	6.003
Fe^{3+}	0.029	0.032	0.034	0.051	0.030	0.044
Total	16.005	15.987	15.861	16.068	15.937	16.037
Fe^{2+}	0.039	0.039	0.054	0.039	0.046	0.043
Mg	0.024	0.019	0.056	0.029	0.035	0.024
Ca	1.947	1.889	2.217	1.903	2.025	1.861
Na	1.900	2.080	1.857	1.849	1.933	1.931
K	0.037	0.074	0.014	0.067	0.039	0.096
Total	3.947	4.101	4.198	3.887	4.078	3.96
Mol.%						
An	50.9	47.5	55.4	50.7	51.6	48.7
Ab	48.1	50.7	44.2	47.6	47.4	48.8
Or	1.0	1.8	0.4	1.7	1.0	2.5

Table 49. Chemical Composition of Groundmass Plagioclase.

Component	GP-56	GP014	GP-1	GP-6	GP-23	GP-13
SiO_2	54.57	54.78	52.70	54.95	53.58	54.83
Al_2O_3	27.59	28.39	29.04	27.71	28.00	28.13
TiO_2	tr	tr	tr	tr	tr	tr
Fe_2O_3	0.35	0.27	0.33	0.34	0.35	0.34
FeO	0.33	0.29	0.39	0.36	0.38	0.36
MnO	tr	tr	tr	tr	tr	tr
MgO	0.09	0.06	0.24	0.07	0.12	0.13
CaO	11.45	11.11	12.45	11.05	12.06	10.66
Na_2O	4.96	5.13	5.02	5.04	4.99	5.32
K_2O	0.34	0.29	0.07	0.35	0.14	0.54
H_2O	0.02	0.05	0.05	0.00	0.10	0.00
H_2O^+	0.00	0.05	0.00	0.06	0.00	0.05
P_2O_5	tr	tr	tr	tr	tr	tr
Total	99.70	100.42	100.29	99.93	99.72	100.36

Analyst: H. Haramura

Table 50 . Structural Formulae of Groundmass Plagioclase (based on 32 oxygens).

S. Nos.	GP-56	GP-14	GP-1	GP-6	GP-23	GP-13
Cations						
Si	9.914	9.872	9.589	9.948	9.768	9.895
Al	5.915	6.037	6.235	5.920	6.024	5.990
Fe^3	0.048	0.035	0.045	0.046	0.048	0.046
Total	15.877	15.944	15.869	15.914	15.840	15.931
Fe^2	0.050	0.043	0.060	0.055	0.058	0.054
Mg	0.024	0.016	0.065	0.019	0.032	0.035
Ca	2.236	2.152	2.435	2.151	2.364	2.068
Na	1.753	1.798	1.777	1.775	1.770	1.869
K	0.079	0.067	0.016	0.081	0.033	0.125
Total	4.124	4.076	4.353	4.081	4.257	4.151
Mol. %						
An.	56.0	54.2	58.8	54.5	57.6	52.0
Ab.	42.5	44.1	40.8	43.5	41.6	45.0
Or.	1.5	1.7	0.4	2.0	0.8	3.0

Table 51 . Normative and Determined An - Ab - Or Composition of Whole Rocks, Groundmass Glass and Plagioclase.

	Mol. % (Norm)				Mol. %		
S. Nos.	An	Ab	Or	S. Nos.	An	Ab	Or
	Bulk Rock			Phenocrystal Plagioclase			
KT-56	38.38	49.36	12.25	PP-56	50.90	48.10	1.00
Kt-14	36.00	50.56	13.42	PP-14	47.48	50.72	1.80
KT-1	35.15	52.42	12.41	PP-1	55.40	44.20	0.40
KT-6	33.62	52.25	14.12	PP-6	50.70	47.60	1.70
KT-23	35.76	51.81	12.41	PP-23	51.64	47.40	0.96
KT-13	32.48	53.19	14.32	PP-13	48.70	48.80	2.50
	Groundmass Glass				Groundmass Plagioclase		
GM-56	24.80	55.83	19.36	GP-56	56.0	42.5	1.5
GM-14	20.25	55.73	24.00	GP-14	54.24	44.1	1.65
GM-1	23.66	56.83	19.50	GP-1	58.80	40.80	0.40
GM-6	25.23	54.97	19.78	GP-6	54.50	43.50	2.00
GM-23	22.91	57.91	19.16	GP-23	57.65	41.58	0.77
GM-13	20.31	54.99	24.68	GP-13	51.96	45.02	3.02

coexistent melts during progressive crystallization. The chemical composition of coexistent phenocrystal and groundmass plagioclase have been plotted on the standard An(anorthite)-Ab(albite)-Or(orthoclase) diagram (fig. 37), and the parallelism of the tie lines indicates that the phenocrystal and groundmass phases were derived from the same parent melt during progressive crystallization. Presumably, the groundmass phase was the last to crystallize, and was in approximate equilibrium with a coexisting liquid phase which was compositionally similar to the glassy groundmass. The plots of the groundmass plagioclase compositions (GP-1, 56, 14 and 13) and (GP-23 and 6), as seen in fig. 37 are accompanied by parallel compositional trends of phenocrystal plagioclase. If both modes of plagioclase are treated of successive generation from a common melt, the sequence of crystallization would be 1-23-56-6-13-14 in the phenocrystal mode and 1-23-56-6-14-13 in the groundmass plagioclase, and it is interesting to note that the variations in Fe^2 and Mg (tables 48 and 50) indicate the same order of crystallization.

Plagioclase phenocrysts from andesitic rocks have not been studied from this point of view by previous authors. The cumulative literature, to date, deals with relations based on optical rather than chemical data. Kuno distinguished plagioclase phenocrysts vs xenocrysts in the Izu-Hakone suites (1950, pp. 967-968), while Larsen et al (1938, p. 252) were convinced that many so-called phenocrysts were xenocrysts rather than phenocrysts, based on a statistical study of plagioclase in the San Juan volcanics (optical data). Two analyzed phenocrystal phases from Sheep Mountain andesite and Los Pinos latite-andesite, reported by Larsen et al (ibid., p.235) appear to be unusually rich in K (Or = 5.5-6%). Wilcox (1954, pp. 323, 325) also discussed the possibilities of equilibrium between plagioclase phenocrysts and microphenocrysts from the Paricutin lavas, based on optical data. The

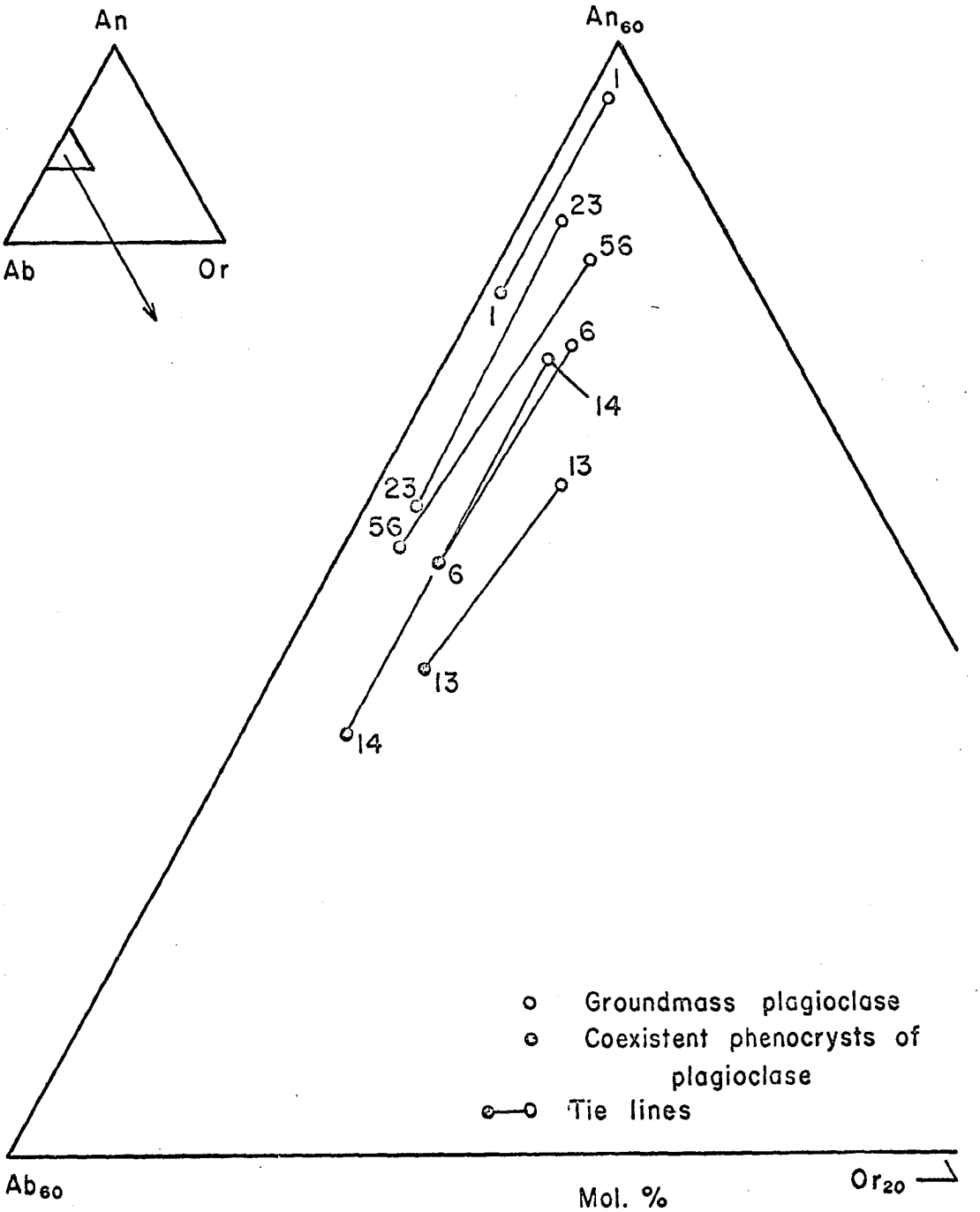

Fig. 37. An-Ab-Or (mol.%) plot of analyzed coexistent phenocrystal and groundmass plagioclase.

parallelism of the tie lines (fig. 37) plus petrographic evidence argues against major xenocryst contamination of phenocrystal plagioclase.

The average composition of the phenocrystal fraction is less calcic than the coexistent groundmass plagioclase (fig. 37). A similar relationship was attributed to a xenocrystal origin (Ab- rich phenocrysts in the San Juan Lavas) by Larsen et al (op. cit., p. 254). Phase equilibrium relations in the Di-An-Ab system (Bowen, 1915, 1928, as cited in Turner and Verhoogen, 1960, p. 103-104) indicate that the crystallization of the diopside phase depresses the An content of the co-crystallizing plagioclase, and this condition may apply to the phenocrystal plagioclase. Crystallization of the groundmass plagioclase was probably accompanied by a lower molar concentration of Di in the melt and a resultant increase in the An content.

The composition (average) of the plagioclase should be related to that of the groundmass and bulk rock composition, if the reactive components formed a closed system, and the phenocrysts are truly cognate. Normative feldspar compositions (mol.% An, Ab, Or) calculated from the chemical analyses of the host rock and its glassy groundmass (tables 52 and 53) as compared to the composition of the crystalline plagioclase are given in table 51, and plotted on An-Ab-Or diagram (fig. 38). The tie lines indicate the near-equilibrium relations. From the same diagram it is clear that the An-Ab-Or compositions of the whole rock are well within the single feldspar field (Turner and Verhoogen, op. cit., p. 112). Plots of the normative feldspar composition of the groundmass glass are in the two feldspar field. Such liquids would yield anorthoclase-sanidine if crystallization were to continue, rather than quenching to glass.

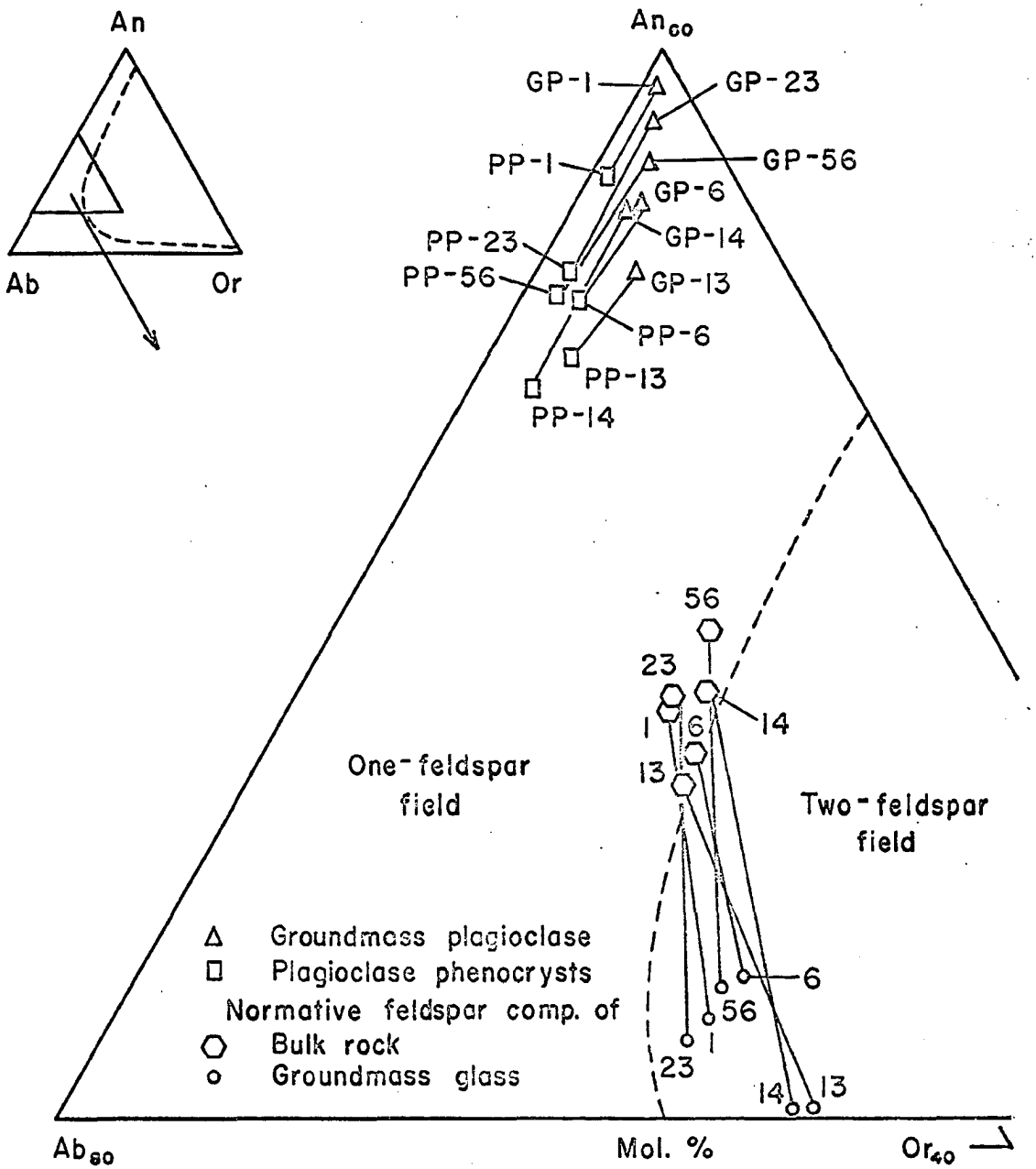

Fig. 38. An-Ab-Or plot of normative and constituent feldspar, Trident andesites (feldspar fields taken from Turner and Verhoogen, 1960, p. 112).

GROUNDMASS GLASS

Chemical analyses and molecular norms of glassy groundmass phases (coexistent with the analyzed crystalline phases) are given in table 52. Glass GM-23 appeared to be unusually rich in iron (disseminated magnetite in dark brown glass). The volumetric percentage (13.7%) of included magnetite was calculated by the point count method, and the chemical analysis was corrected.

The chemical composition of the groundmass glasses have been plotted on SiO_2, F-M-A and C-N-K diagrams (figs. 39 and 40). The distribution of the plots in all three diagrams is analogous to differentiation trend within a small compositional range.

Assuming that all flows represent eruptive fractions derived from a parent magma, it appears promising to investigate whether the variation trends in the composition of the glass agreed with the nature and sequence of the crystallizing phases. Considering the protracted crystallization of plagioclase, which coincides with and extends beyond the span of pyroxene crystallization it could be expected that the effects of plagioclase crystallization would be dominant in the composition of the glassy residuum, particularly in respect of the variations in CaO, Na_2O, K_2O and Al_2O_3 content. Fluctuations in the rate of plagioclase crystallization (caused by variations in water pressure) would also be reflected in the variations of the above components of the glass composition. Variation trends of FeO, Fe_2O_3, MgO and CaO in the composition of groundmass glass may retain the effects of pyroxene fractionation, which may be a dominating factor when the rate of plagioclase crystallization slows down due to an increase in the pressure of water in the system. The two trends shown by full and

Table 52 . Chemical Composition and Molecular Norms of Groundmass Glass.

Component	GM-56	GM-14	GM-1	GM-6	GM-23	GM-23*	GM-23 Average	GM-13
SiO_2	66.78	69.80	66.56	68.83	59.22	68.58	64.10	70.63
TiO_2	0.67	0.47	0.74	0.47	2.22	1.02	1.62	0.48
Al_2O_3	14.93	14.80	14.89	15.14	11.59	13.42	12.54	14.61
Fe_2O_3	1.75	0.97	2.04	1.56	7.78	0.28	4.04	0.47
FeO	2.96	2.03	3.02	1.86	5.71	1.42	3.58	1.94
MnO	0.09	0.09	0.10	0.09	0.18	0.15	0.17	0.08
MgO	1.71	1.28	1.88	1.05	3.42	3.96	3.66	0.95
CaO	4.21	3.36	3.87	4.28	4.53	5.25	4.91	3.54
Na_2O	4.06	4.17	4.16	4.04	3.32	3.84	3.59	4.06
K_2O	2.14	2.73	2.17	2.21	1.67	1.93	1.81	2.77
H_2O^-	0.12	0.00	0.00	0.00	0.00	0.00	-	0.10
H_2O^+	0.05	0.12	0.12	0.02	0.35	0.41	-	0.10
P_2O_5	0.12	0.06	0.12	0.09	0.16	0.19	0.18	0.06
Total	99.59	99.88	99.67	99.64	100.15	100.00		99.79

Analyst: H. Haramura

Mol. Norm.								
Qz	21.77	23.94	21.21	24.89	20.11	22.66	21.39	25.46
Or	12.81	16.23	12.97	13.20	10.24			16.52
Ab	36.95	37.70	37.79	36.70	30.95			36.81
An	16.41	13.69	15.73	16.84	12.24			13.59
Di	3.16	2.15	2.32	3.23	8.00			2.99
Hy	5.81	4.45	6.50	2.61	6.43			3.30
En	3.76	2.86	4.45	1.81	6.04			1.82
Fs	2.04	1.58	2.04	0.80	0.39			1.48
Mt	1.85	1.02	2.15	1.65	8.44			0.49
Il	0.94	0.65	1.04	0.66	3.21			0.67
Ap	0.25	0.12	0.25	0.19	0.34			0.12
Na_2O+k_2O	6.20	6.90	6.33	6.25	4.99	5.77		6.83
$K_2O/(Na_2O+k_2O)$	0.34	0.39	0.34	0.35	0.33	0.33		0.40
$\Sigma Fe/\ \Sigma Fe+Mg$	0.60	0.57	0.60	0.64	0.68	-		0.59

* Calculated composition of GM-23 after subtraction of 13.7% modal magnetite.

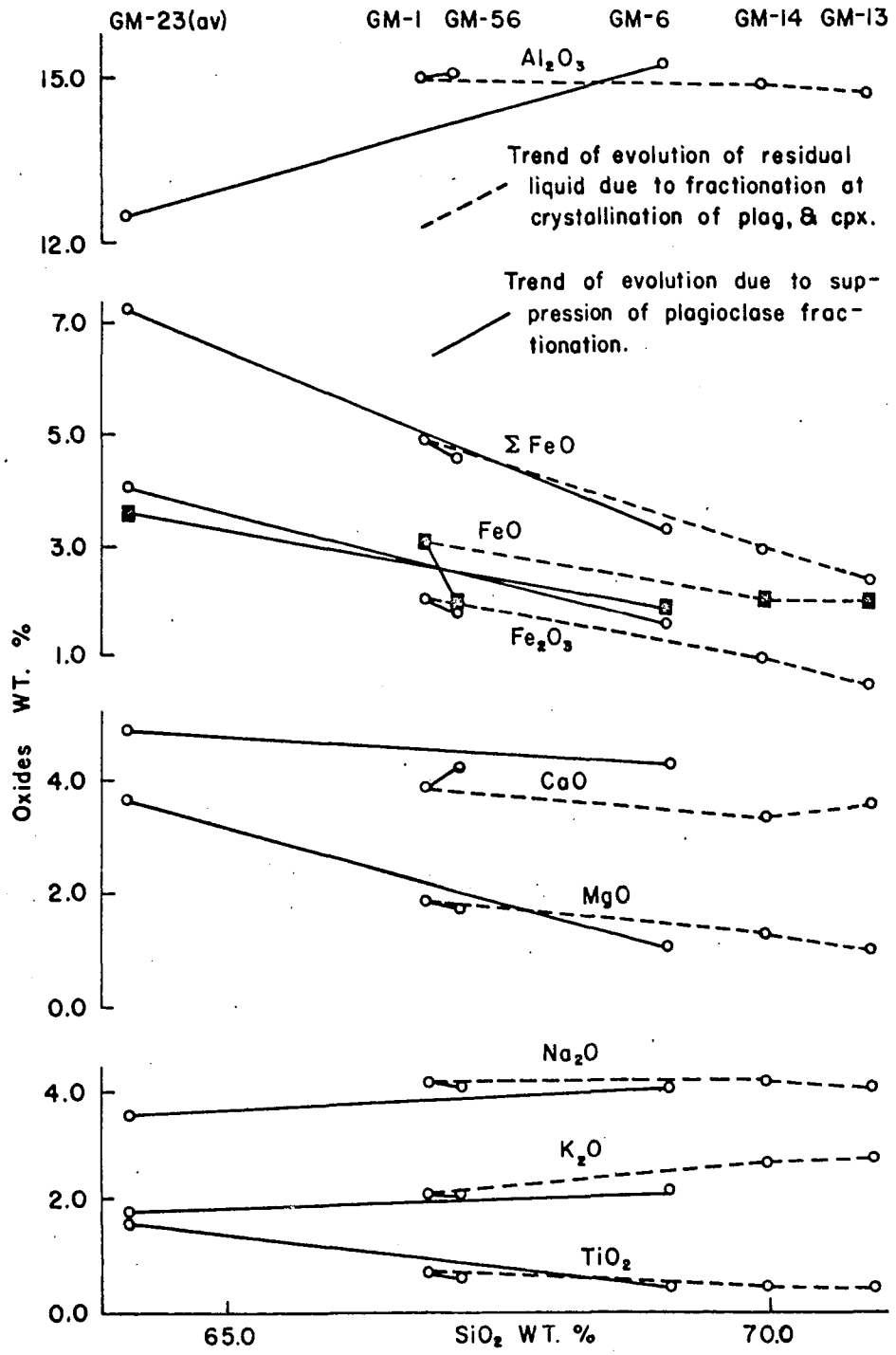

Fig. 39. Silica variation diagram of chemically analyzed groundmass glass.

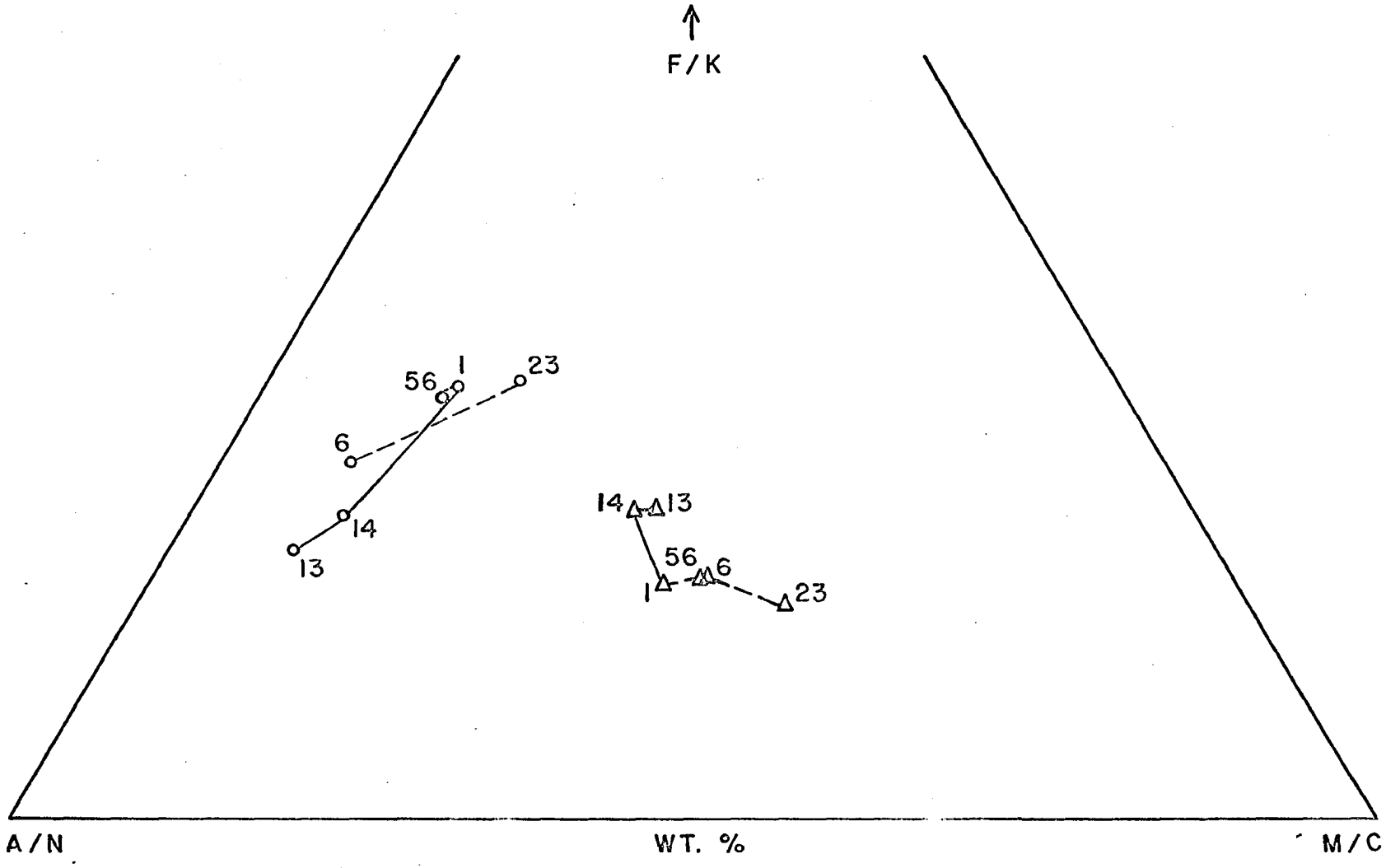

Fig. 40. FMA (circles) and CNK (triangles) plots of analyzed groundmass glass (for explanations of tie lines, see fig. 39).

broken lines in figs. 39 and 40 can be considered to be due to rapid and slow rates of plagioclase fractionation respectively. The effects of pyroxene fractionation appear to be steady.

The course of fractionation suggested by the plots in FMA and CNK diagram (fig. 40) are as follows:

FMA : 23 - 1 - 56 - 6 - 14 - 13

CNK : 23 - 6 - 56 - 1 - 14 - 13

The SiO_2 variation diagram (fig. 39) also supports this. The variation in normative Qz (as a measure of saturation in silica), given in table 52, indicate a course of evolution as 1-23-56-14-6-13, which differs from the above, only in respect of the relative position of compositions of GM-1 and 6. Further comment on this problem has been made in the section on mineral paragenesis in the final chapter.

Wilcox (1954) studied the groundmass compositions (extrapolations from bulk compositions) of the Paricutin andesites; and deduced that the glassy mesostases represented quenched residual liquid in equilibrium with co-crystallizing hypersthene and plagioclase (ibid., pp. 306, 325). From refractive indices of the glass, he concluded that the glass was progressively enriched in silica in successively younger flows. No other chemical data on groundmass glass appears to be present in the literature.

CHAPTER IV

COMPARATIVE BULK CHEMICAL COMPOSITION OF THE TRIDENT ANDESITES

Representative bulk specimens from each flow were chemically analyzed. Fresh, unaltered and inclusion-free samples were prepared from thin slices sawn from the various andesites. The 1958 flow was selected for the study of the compositional variation within a single flow unit. Six specimens were collected from localities designed to sample the lateral and vertical variations. Two samples from the pre-historic lavas and a block from the rim of the crater were also analyzed. Analyzed specimens and their parent flows are listed below (bulk specimens from which constituent mineral fractions were also separated and chemically analyzed are also identified):

Pre-historic lavas - KT-18 and 27

1953 flow - KT-11^{+} and 56^{++}

1957 flow - KT-14^{++}

1958 flow - KT - 1^{++}, 2, 3, 10, 16 and 17.

1959 flow - KT - 5^{+} and 6^{++}

1960 flow - KT -23^{++}

1954 block avalanche - KT - 13^{++}

1963 block avalanche - KT - 29

Trident Crater rim - TC

(+ - magnetite only; ++ - all phases)

The precision of analytical techniques was checked by repeat analyses on KT-11, 13 and 17, at the conclusion of the study. The bulk chemical analyses, molecular norms, range of bulk chemical composition and related data are shown in tables 53 to 55. Analytical error for major components in the analyses is detailed in table 54.

Table 53. Bulk Chemical Composition and Molecular Norms of the Trident Andesites

Age	Prehistoric Lavas				1953 Flow					
S.Nos. / Components	18	18(w.f.)	27	27(w.f.)	11	11(w.f.)	11R	11R(w.f.)	56	56(w.f.)
SiO_2	61.02	61.55	62.57	62.99	60.11	60.77	60.48	61.01	61.07	61.29
TiO_2	0.52	0.52	0.60	0.60	0.56	0.57	0.55	0.55	0.71	0.71
Al_2O_3	17.29	17.44	16.98	17.09	16.96	17.15	16.84	16.99	17.11	17.17
Fe_2O_3	3.59	3.62	2.56	2.58	1.99	2.01	2.05	2.07	2.43	2.44
FeO	2.89	2.92	3.43	3.45	4.21	4.32	4.22	4.26	3.86	3.87
MnO	0.13	0.13	0.13	0.13	0.13	0.13	0.13	0.13	0.13	0.13
MgO	2.73	2.75	2.68	2.70	3.14	3.17	3.14	3.17	2.95	2.96
CaO	5.75	5.80	5.02	5.05	6.36	6.43	6.52	6.58	6.20	6.22
Na_2O	3.74	3.77	3.85	3.86	3.89	3.93	3.60	3.63	3.71	3.72
K_2O	1.34	1.35	1.41	1.42	1.39	1.41	1.38	1.39	1.40	1.41
H_2O^-	0.33		0.12		0.11		0.14		0.04	
H_2O^+	0.68		0.28		0.58		0.59		0.18	
P_2O_5	0.14	0.14	0.12	0.12	0.12	0.12	0.12	0.12	0.07	0.07
Total	100.15	100.01	99.73	100.01	99.61	100.01	99.76	100.00	99.86	100.01
Ni	0.0005		0.001		0.001					
Cr	0.004		0.003		0.004					
Mol. Norm.										
Qz	16.56		17.74		12.18				14.67	
Or	8.03		8.43		8.31				8.34	
Ab	34.09		34.81		35.37				33.60	
An	26.84		24.42		25.02				26.13	
Co	-		0.34		-					
Di	0.95		-		4.90				3.55	
En	7.25		7.49		7.18				6.97	
Fs	1.39		2.93		3.85				2.99	
Hy(En+Fs)	8.65		10.42		11.03				9.97	
Mt	3.81		2.70		2.10				2.56	
Il	6.73		0.84		0.79				0.99	
Ap	0.29		0.25		0.25				0.14	
Total Fels	85.54		85.76		80.10				82.76	
Total Mafic	14.45		14.23		19.09				17.23	

N.B.- w.f. Water free
R - Repeated analyses

Analyst: H. Matsumoto
T. Katsura

←1957 Flow		←1958 Flow→								
14	14(w.f.)	1	1(w.f.)	2	2(w.f.)	3	3(w.f.)	10	10(w.f.)	S. Nos. Compo-nents
62.30	62.86	60.93	61.26	60.99	61.36	62.48	62.61	61.29	61.68	SiO_2
0.58	0.58	0.64	0.64	0.54	0.54	0.55	0.55	0.51	0.51	TiO_2
16.99	17.14	16.03	16.12	16.58	16.68	16.39	16.42	17.54	17.65	Al_2O_3
2.08	2.10	3.23	3.25	2.94	2.96	2.69	2.70	1.95	1.96	Fe_2O_3
3.64	3.67	3.43	3.45	3.55	3.57	3.53	3.54	3.88	3.90	FeO
0.12	0.12	0.13	0.13	0.13	0.13	0.13	0.13	0.11	0.11	MnO
2.38	2.40	3.45	3.47	3.06	3.08	2.83	2.84	2.65	2.67	MgO
5.51	5.56	6.35	6.38	6.18	6.22	5.61	5.62	6.05	6.09	CaO
3.84	3.87	3.78	3.80	3.89	3.91	3.84	3.85	3.91	3.94	Na_2O
1.55	1.56	1.36	1.37	1.40	1.41	1.62	1.62	1.35	1.36	K_2O
0.13		0.05		0.11		0.10		0.12		H_2O^-
0.29		0.51		0.04		0.16		0.03		H_2O^+
0.12	0.12	0.13	0.13	0.13	0.13	0.13	0.13	0.12	0.12	P_2O_5
		100.02	100.01	99.54	100.01	100.06	100.01	99.51	100.01	Total
0.001		0.001		0.001		0.0005		0.001		Ni
0.005		0.005		0.006		0.005		0.004		Cr
										Mol. Norm.
16.46		14.77		14.35		16.20		14.21		Qz
9.28		8.11		8.35		9.64		8.04		Or
34.97		34.30		35.29		34.74		35.42		Ab
24.89		23.00		23.89		22.87		26.56		An
		-		-		-		-		Co
1.62		6.38		4.98		3.45		2.34		Di
6.13		7.07		6.68		6.63		6.63		En
3.33		1.76		2.29		2.57		3.72		Fs
1.47		8.83		8.97		9.20		10.36		Hy(En+Fs)
2.20		3.41		3.10		2.83		2.05		Mt
0.81		0.90		0.76		0.77		0.71		Il
0.25		0.27		0.27		0.27		0.25		Ap
85.12		80.19		81.89		83.46		84.26		Total Fels
14.37		19.80		18.10		16.53		15.73		Total Mafic

N.B. - w.f. Water free
R - Repeated analyses

Analyst: H. Matsumoto
T. Katsura

Table 53. Bulk Chemical Composition and Molecular Norms of the Trident Andesites

Age	←						1959 Flow			→
S.Nos. / Components	16	16(w.f.)	17	17(w.f.)	17R	17R(w.f.)	5	5(w.f.)	6	6(w.f.)
SiO_2	60.81	61.60	61.75	62.66	61.76	62.43	60.88	61.51	62.33	62.52
TiO_2	0.60	0.61	0.55	0.56	0.55	0.56	0.54	0.55	0.60	0.60
Al_2O_3	16.31	16.52	16.04	16.28	16.20	16.38	16.69	16.86	16.28	16.33
Fe_2O_3	2.27	2.30	2.92	2.96	2.88	2.91	3.65	3.69	2.95	2.96
FeO	4.18	4.23	3.22	3.27	3.30	3.34	2.91	2.94	3.26	3.27
MnO	0.13	0.13	0.13	0.13	0.13	0.13	0.12	0.12	0.12	0.12
MgO	3.10	3.14	2.89	2.93	2.90	2.93	2.97	3.00	2.80	2.81
CaO	5.99	6.07	5.74	5.83	5.89	5.95	5.78	5.84	5.77	5.79
Na_2O	3.75	3.80	3.73	3.79	3.72	3.76	3.87	3.91	3.87	3.88
K_2O	1.45	1.47	1.44	1.46	1.47	1.49	1.44	1.45	1.59	1.59
H_2O^-	0.16		0.20		0.08		0.09		0.12	
H_2O^+	1.13		1.16		1.08		0.58		0.15	
P_2O_5	0.12	0.12	0.13	0.13	0.12	0.12	0.12	0.12	0.13	0.13
Total	100.00	100.01	99.90	100.01	100.08	100.00	99.64	100.01	99.97	100.01
Ni	0.0005		0.001				0.0005		0.001	
Cr	0.005		0.004				0.003		0.004	
Mol. Norm.										
Qz	14.35		17.08				15.51		16.32	
Or	8.72		8.68				8.64		9.47	
Ab	34.27		34.20				35.29		35.05	
An	23.81		23.26				24.29		22.55	
Co	-		-				-		-	
Di	4.51		3.96				3.22		4.37	
En	7.20		6.62				6.95		6.12	
Fs	3.58		1.98				1.18		1.85	
Hy(En+Fs)	10.79		8.60				8.13		7.97	
Mt	2.41		3.11				3.87		3.11	
Il	0.85		0.78				0.76		0.84	
Ap	0.25		0.27				0.25		0.27	
Total Fels	81.16		83.24				83.73		83.41	
Total Mafic	18.85		16.75				16.26		16.58	

N.B. - w.f. Water free
R - Repeated analyses

Analyst: H. Matsumoto
T. Katsura

1960 Flow ⟵		1954 Block Avalanche ⟶				1963 Block Avalanche				
23	23(w.f.)	13	13(w.f.)	13R	13R(w.f.)	29	29(w.f.)	TC	TC(w.f.)	S. Nos. Components
61.22	61.70	63.15	63.86	63.66	63.72	59.84	59.99	61.65	61.97	SiO_2
0.52	0.52	0.53	0.54	0.52	0.52	0.73	0.73	0.63	0.63	TiO_2
16.81	16.94	16.02	16.01	16.03	16.03	16.95	16.99	16.88	16.97	Al_2O_3
2.99	3.01	2.51	2.54	2.49	2.49	2.77	2.78	2.20	2.21	Fe_2O_3
3.17	3.19	3.29	3.33	3.34	3.34	4.03	4.04	4.23	4.25	FeO
0.12	0.12	0.11	0.11	0.01	0.11	0.14	0.14	0.12	0.12	MnO
2.86	2.88	2.60	2.63	2.42	2.42	3.62	3.63	2.42	2.43	MgO
6.09	6.14	5.06	5.12	5.72	5.73	6.79	6.81	6.25	6.28	CaO
3.90	3.93	3.91	3.95	3.90	3.90	3.44	3.45	3.67	3.69	Na_2O
1.42	1.43	1.60	1.62	1.61	1.61	1.34	1.34	1.31	1.32	K_2O
0.20		0.09		0.04		0.00		0.08		H_2O^-
0.63		0.39		0.48		0.09				H_2O^+
0.13	0.13	0.11	0.11	0.12	0.12	0.10	0.10	0.13	0.13	P_2O_5
100.06	100.01	99.37	100.01	100.42	100.00	99.84	100.01	99.83	100.01	Total
0.0005		0.0005						0.003		Ni
0.005		0.005						0.006		Cr
										Mol. Norm.
15.03		17.90				13.52		16.22		Qz
8.48		9.61				7.98		7.84		Or
35.43		35.70				31.14		33.40		Ab
24.46		21.80				27.07		26.07		An
-		-				-		-		Co
4.20		2.39				4.98		3.60		Di
6.36		6.43				8.23		5.68		En
1.84		2.49				2.89		3.68		Fs
8.20		8.92				11.13		9.36		Hy(En+Fs)
3.16		2.66				2.91		2.33		Mt
0.73		0.75				1.02		0.88		Il
0.27		0.23				0.21		0.27		Ap
83.41		85.01				79.72		83.54		Total Fels
16.58		14.98				20.27		16.45		Total Mafic

N.B. - w.f. water free
R - Repeated analyses

Analyst: H. Matsumoto
T. Katsure

Table 54. Range in Bulk Chemical Composition of Trident Andesites.

Whole Suite

Wt.%	Low	High	Range	Accuracy of Chemical Analysis (± wt.%)
SiO_2	59.84	63.66	3.82	0.50
TiO_2	0.51	0.73	0.22	0.03
Al_2O_3	16.01	17.54	1.53	0.20
Fe_2O_3	1.95	3.65	1.70	0.20
FeO	2.91	4.23	1.32	0.20
MnO	0.11	0.14	0.03	0.01
MgO	2.38	3.45	1.07	0.20
CaO	5.51	6.79	1.28	0.20
Na_2O	3.44	3.91	0.47	0.06
K_2O	1.31	1.62	0.31	0.06
P_2O_5	0.07	0.14	0.07	0.02

Single lava (1958 Flow)

wt.%	Low	High	Range	Accuracy of Chemical Analysis (± wt.%)
SiO_2	60.93	62.48	1.55	0.50
TiO_2	0.51	0.64	0.13	0.03
Al_2O_3	16.03	17.54	1.51	0.20
Fe_2O_3	1.95	3.23	1.28	0.20
FeO	3.22	4.18	0.96	0.20
MnO	0.11	0.13	0.02	0.01
MgO	2.65	3.45	0.80	0.20
CaO	5.61	6.35	0.74	0.20
Na_2O	3.72	3.91	0.19	0.06
K_2O	1.35	1.47	0.12	0.06
P_2O_5	0.12	0.13	0.01	0.02

Table 55. Petrochemical Calculations, Indices and Ratios

	S. Nos.	1	2	3	4	5	6
Prehistoric Lavas							
	18	58.68	70.36	56.23	0.26	61.08	55.95
	27	60.98	69.09	55.11	0.26	63.91	58.77
1953 Flow							
	11	55.86	66.60	52.52	0.26	63.58	58.57
	56	56.61	68.07	54.02	0.27	61.62	56.25
1957 Flow							
	14	60.71	70.62	57.04	0.28	64.00	58.42
1958 Flow							
	1	57.18	65.88	51.26	0.26	64.84	59.86
	2	57.99	67.96	53.70	0.26	64.62	59.63
	3	60.58	68.73	54.66	0.29	65.99	60.30
	10	57.67	68.75	54.88	0.25	62.07	57.15
	16	57.34	67.54	53.48	0.27	64.36	59.00
	17	59.96	68.00	53.71	0.27	64.84	59.52
1959 Flow							
	5	59.44	68.84	54.40	0.27	64.39	59.23
	6	60.84	68.92	54.73	0.29	66.38	60.85
1960 Flow							
	23	58.94	68.29	53.99	0.26	64.23	59.16
1954 Block Avalanche	13	63.21	69.05	54.98	0.29	67.52	62.09
1963 Block Avalanche	29	52.64	65.26	50.80	0.28	59.10	53.50
Trident Crater		57.46	72.66	59.47	0.26	61.27	56.16

Col. 1 - Differentiation Index (Norm. Qz + Or + Ab + Ne + Lc) (Thornton and Tuttle, 1960).

Col. 2 - $100\ (FeO + Fe_2O_3)/(FeO + Fe_2O_3 + MgO)$.

Col. 3 - $100\ (Fe^2 + Fe^3 + Mn)/(Fe^2 + Fe^3 + Mn + Mg)$.

Col. 4 - $K_2O/(Na_2O + K_2O)$.

Col. 5 - $100\ (Or + Ab)/(Or + Ab + An)$.

Col. 6 - $100\ Ab/(Ab + An)$.

Bulk chemical data were evaluated in terms of the following chemical parameters:

(1) Alkali - lime index (Peacock),

(2) Variation diagrams

(a) SiO_2/major oxides,

(b) $\Sigma FeO-MgO-(Na_2O+K_2O)$, and

(c) $CaO-Na_2O-K_2O$

(3) $(FeO+Fe_2O_3)/(FeO+Fe_2O_3+MgO)$ - SiO_2, and

(4) $(Fe^2+Fe^3+Mn)/(Fe^2+Fe^3+Mn+Mg)$ - Ab/(An+Ab).

Alkali-Lime Index

According to Peacock's alkali-lime index (Barth, 1962, p. 170) the Trident andesites are calcic rather than calc-alkalic (Pre-historic flows = 62.18; Post-1953 flows = 62.50 - see fig. 41). It is doubtful whether such high alkali-lime indices are necessarily caused by contamination as suggested by Barth (ibid., p. 173). In case of the Trident andesites, these high values are caused by the relatively high SiO_2 content. However, the comparative indices of pre-historic and recent lavas indicate that the index has increased with time, and further substantiate the genetic relationship between the two groups of lavas (relationship which is also indicated by the normative pyroxene compositions).

Variation Trends

Variation diagrams are alleged to show the progressive concentration of silica and alkalis in differentiates derived from a parent melt, and the consanguinity of genetically related members of a suite.

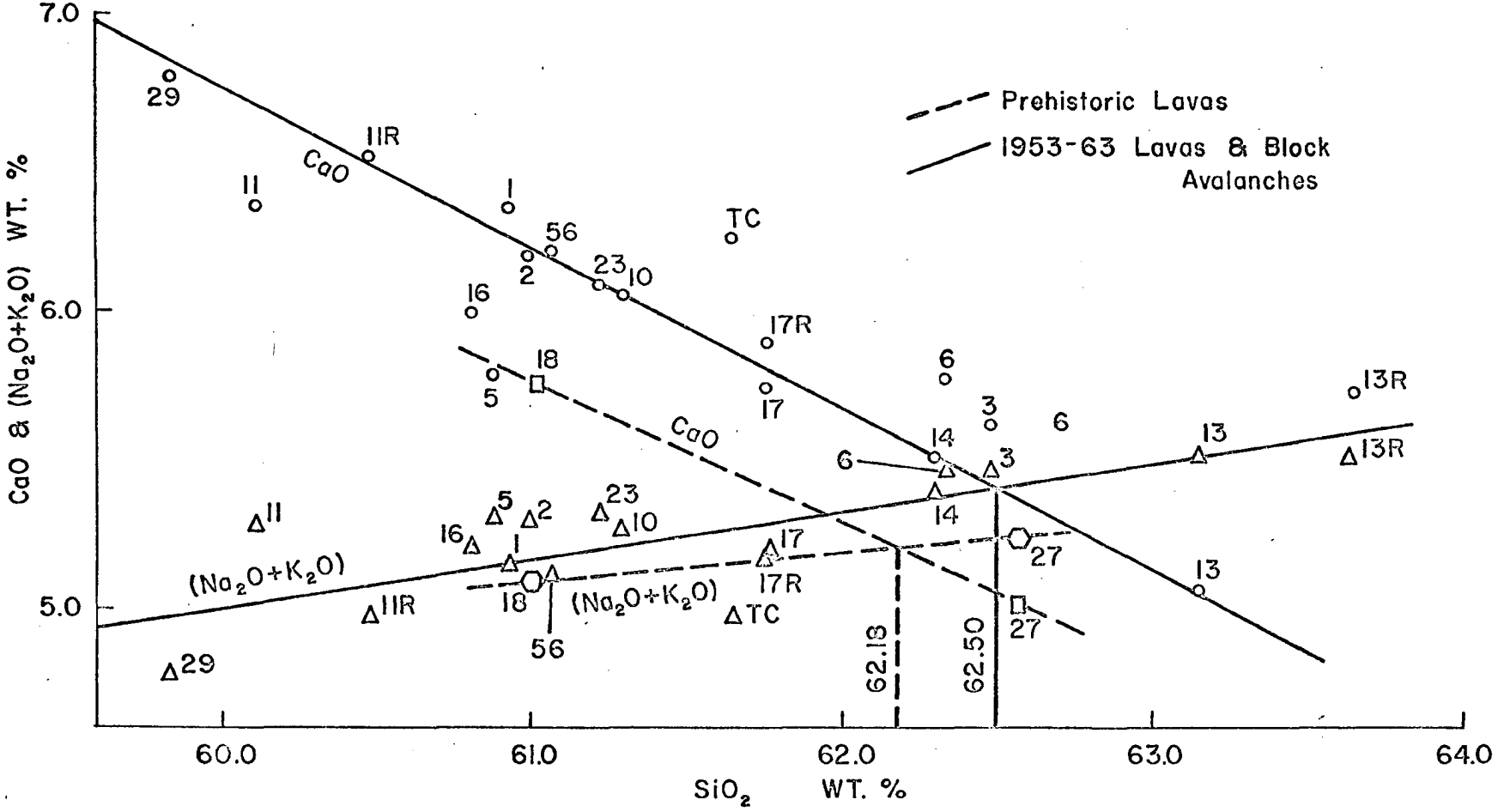

Fig. 41. Variation diagram showing Peacock's alkali-lime indices of prehistoric and 1953-1963 lavas and avalanches.

Silica variation diagrams (water free): Diagrams illustrating variation within a single flow unit (1958) and the whole suite (including the pre-historic lavas) are shown as figs. 42 and 43. Within the 1958 flow (fig. 42) only ΣFeO, MgO and CaO show a general tendency to decrease, while K_2O tends to increase with increasing silica. Fe shows an initial reducing trend which is sharply reversed to an oxidizing trend with increasing silica content. The variation of MgO, ΣFeO, CaO, Al_2O_3 is likely to be irregular due to possible disequilibrium relations between the coexistent crystalline phases. However, Na_2O, K_2O vs SiO_2 variations are probably significant in view of the apparent equilibrium relations between the late plagioclase and quenched glass of the groundmass.

A composite silica variation diagram (fig. 34) demonstrates the general consangunity of the suite, as shown by the coherent curves defined by the plots of ΣFeO, MgO, CaO, Na_2O, K_2O and TiO_2. Variation of Al_2O_3, FeO and Fe_2O_3 appears to be unsystematic. The chemical composition of the sequentially erupted flows does not appear to have changed sharply during the eruptive cycle of 1953-1963. It is interesting that the andesite blocks ejected in 1963 (KT-29) and 1954 (KT-13) represent end members of the entire compositional range.

FMA and CNK variation diagrams: The chemical compositions of the andesites have been plotted on standard FMA and CNK diagrams in figs. 44 and 45 respectively. A curve similar to differentiation trend is defined by the distribution of the plots in both diagrams, but the range in composition is very small. The compositional field of the Trident andesites is intermediate between the trends of differentiation reported for the Hawaiian alkali basalt series (Yoder and Tilley, 1962, p. 424) and alkali basalt

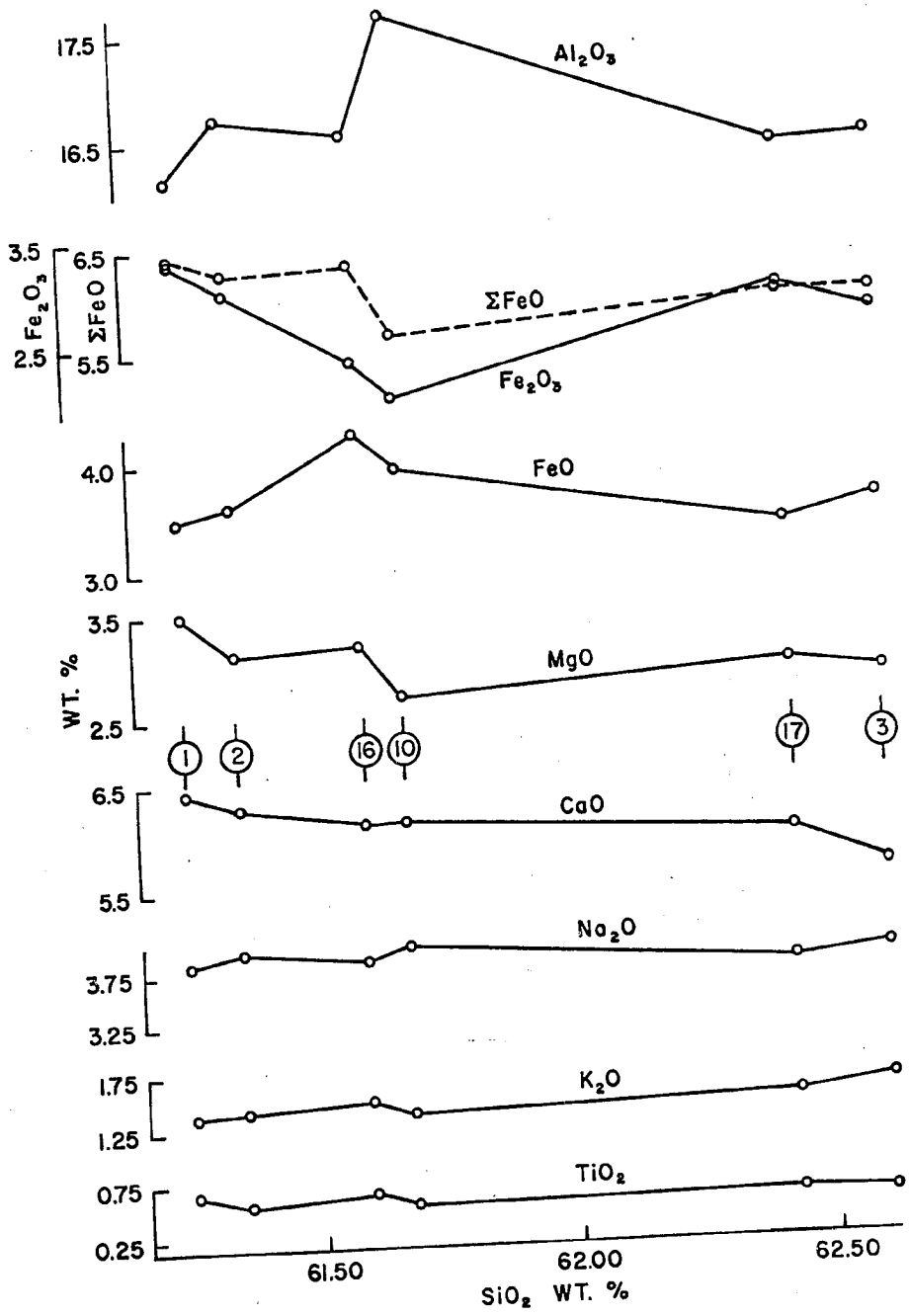

Fig. 42. Silica variation diagram - 1958 flow.

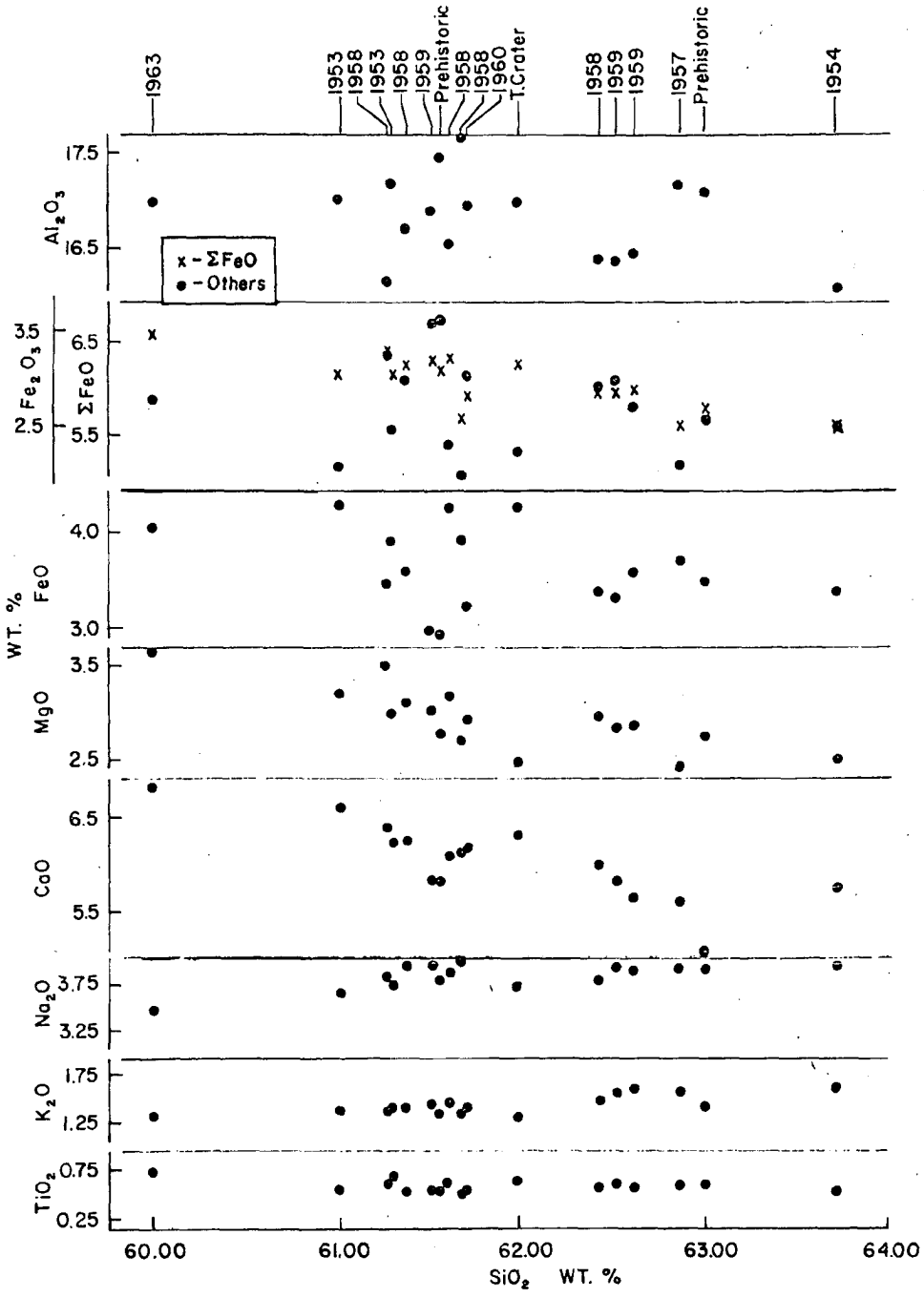

Fig. 43. Silica variation diagram - Trident andesites.

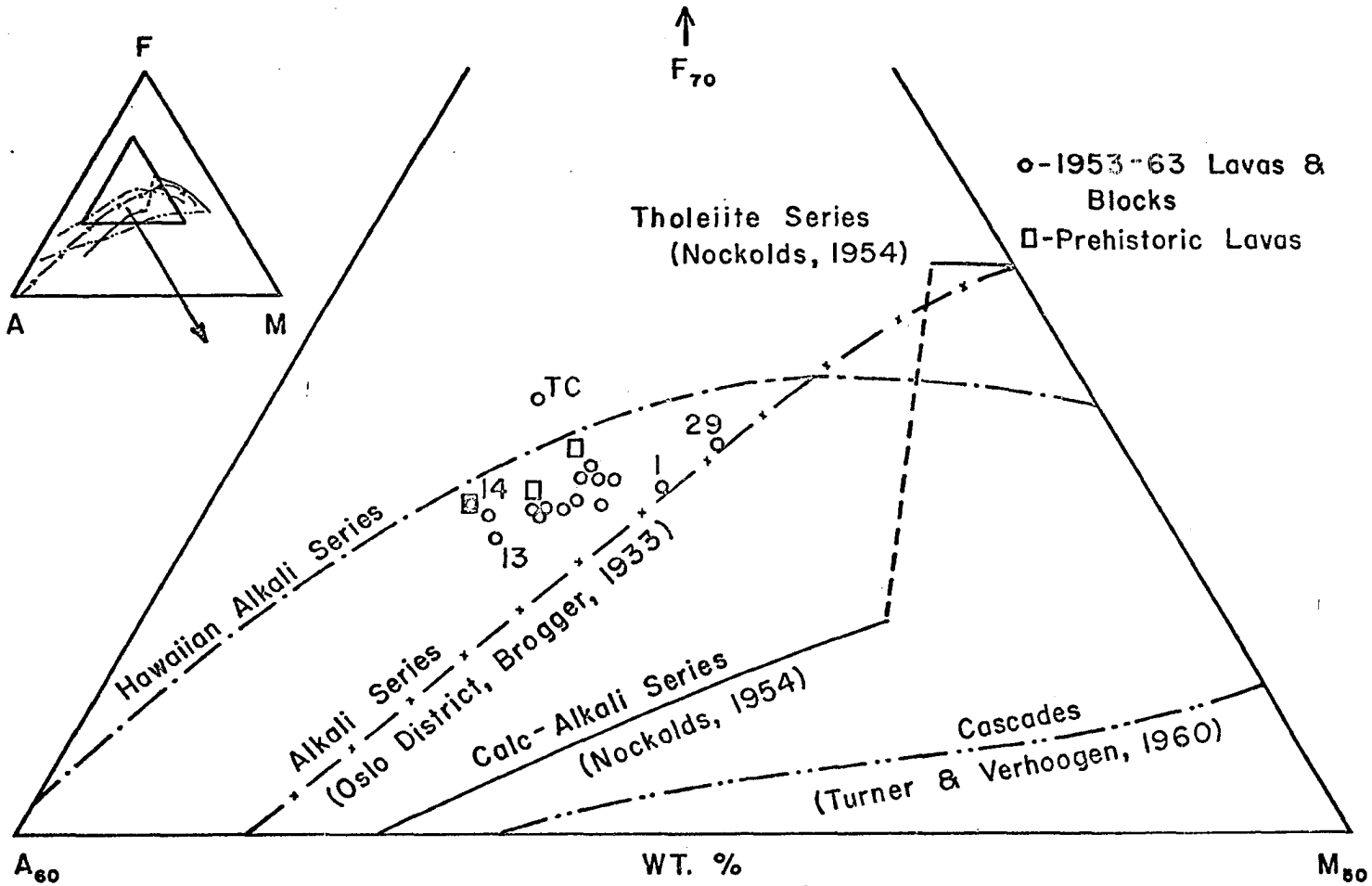

Fig. 44. FMA plot of Trident andesites. Trends for tholeiite, alkali and calc-alkali series taken from Yoder and Tilley (1962, fig. 18, p. 424).

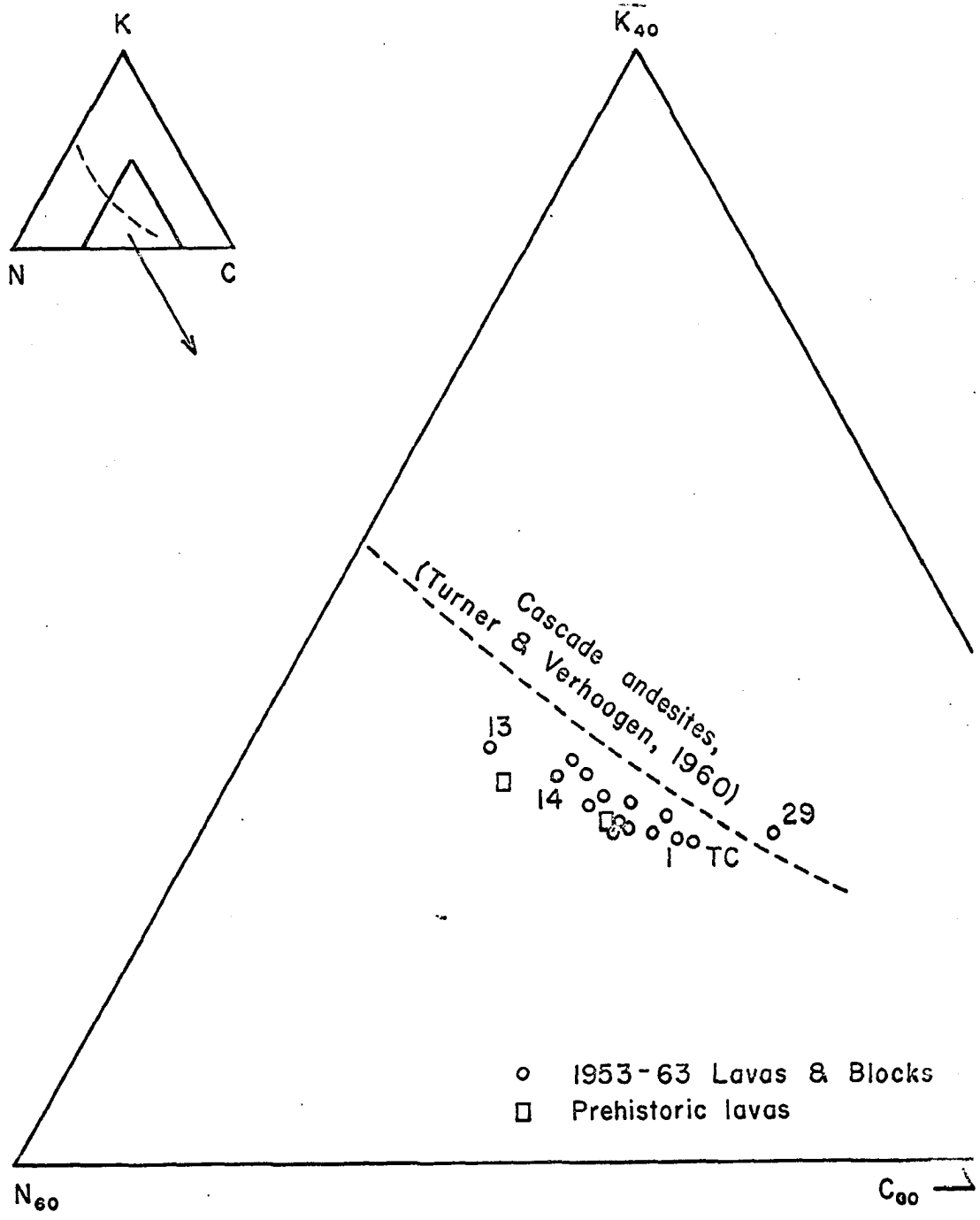

Fig. 45. CNK plot of Trident andesites.

series (Oslo, Brogger, 1933, as cited by Yoder and Tilley, op. cit.). The lack of coincidence between the Trident suite and typical calc-alkali trend is immediately apparent (fig. 44). Furthermore, as seen in both the diagrams, KT-29 and KT-1 have more basic compositions (Fe, Mg and Ca), which may lie more toward the composition of the parent magma, while Kt-14, 13 and TC are thought to represent variants which were crystallized under somewhat different thermodynamic conditions. There is a suggestion of an iron enrichment trend in the plots of KT-29 and TC, as compared to the compositional field defined by KT-29-14-13 on both diagrams (the latter group is apparently characterized by alkali enrichment). KT-29 is from a block which was presumably ejected from the vent in 1963; and the site from which it was obtained was degassing violently. Sample TC was obtained from a small plug like mass on the rim of the crater. Sub-crustal crystallization where the role of partial oxygen pressure was less important, would encourage a trend toward a composition similar to TC (iron enrichment as suggested by Osborn, 1959); while constant and/or increasing partial pressure of oxygen would displace the composition along a trend of silica/alkali enrichment, similar to that defined by KT-29-1-14-13.

Fe Ratio - Silica Relations

The $(FeO+Fe_2O_3)/(FeO+Fe_2O_3+MgO)$ - SiO_2 variation in bulk composition of lava series derived from a common parent melt should reflect the role of partial oxygen pressure during these crystallization events (Osborn, 1959. In fig. 46, Trident andesite field occupy a field bounded by two boundary curves (full lines), defined by plots 29-11-56-5-TC (close to the $FeO+Fe_2O_3$ enrichment trend under low partial pressure of oxygen as determined by Osborn, op. cit.) and plots 29-1-13 (corresponding to the silica enrichment trend encouraged by constant/increasing partial pressure

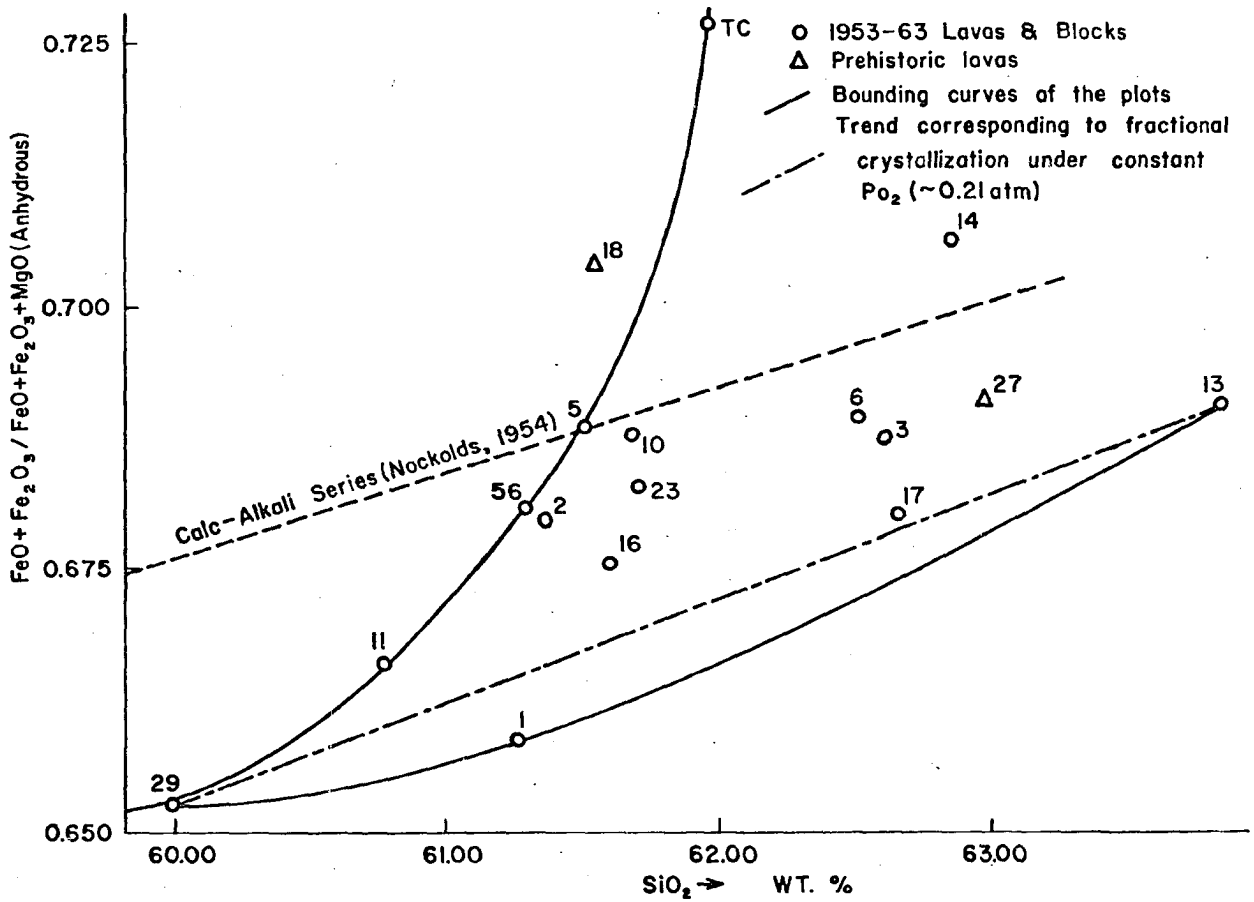

Fig. 46. (FeO + Fe_2O_3)/(FeO + Fe_2O_3 + MgO) - SiO_2 plot of Trident andesites.

of oxygen, based on experimentally determined trends by Osborn, ibid., p. 629). Furthermore, it is evident that the plots do not show any relation to the type calc-alkali trend (as extrapolated from Yoder and Tilley, op. cit., p. 423, fig. 17). The entire compositional field of the Trident andesites has been shifted to a more silica enriched field than that outlined in the systems discussed by Osborn, and the compositional trends of naturally occurring tholeiites, the high-alumina and alkali basalt series (Yoder and Tilley, op. cit.). The deviation from the silica enrichment trend, represented by the trend 29-11-56-5-TC or those paralleling it, indicates a decline in partial pressure of oxygen, which could be attributed to increasing water pressure with little or no diffusion of hydrogen. This condition could be induced during the period immediately preceding a violent eruption, when the vent is closed by a carapace or plug.

Fe and Ab Ratios

In respect to the above, the liquidus temperatures corresponding to the various bulk compositions are thought to be important. $(Fe^2+Mn)/(Fe^2+Mn+Mg)$ - Ab/(Ab+An) variation has been cited by Wager (1956) as an index of the liquidus temperature. Yoder and Tilley (op. cit., p. 386-387) pointed out the inadequacies of such an index after including Fe^3; and found a better correlation on an FMA diagram for compositions having a major phase on the liquidus. The FMA diagram of the Trident andesites (fig. 44) reveals only minor variations in the corresponding liquidus temperatures (decreasing toward the iron end of the diagram). This relationship is also reflected to some extent in the $(\Sigma Fe+Mn)/(\Sigma Fe+Mn+Mg)$ - Ab/(Ab+An) plot of the Trident andesites (fig. 47). However, in Yoder and Tilley's criticism, the roles of CaO and SiO_2 were ignored. Wager had attempted to derive an index which considered the roles of both femic and

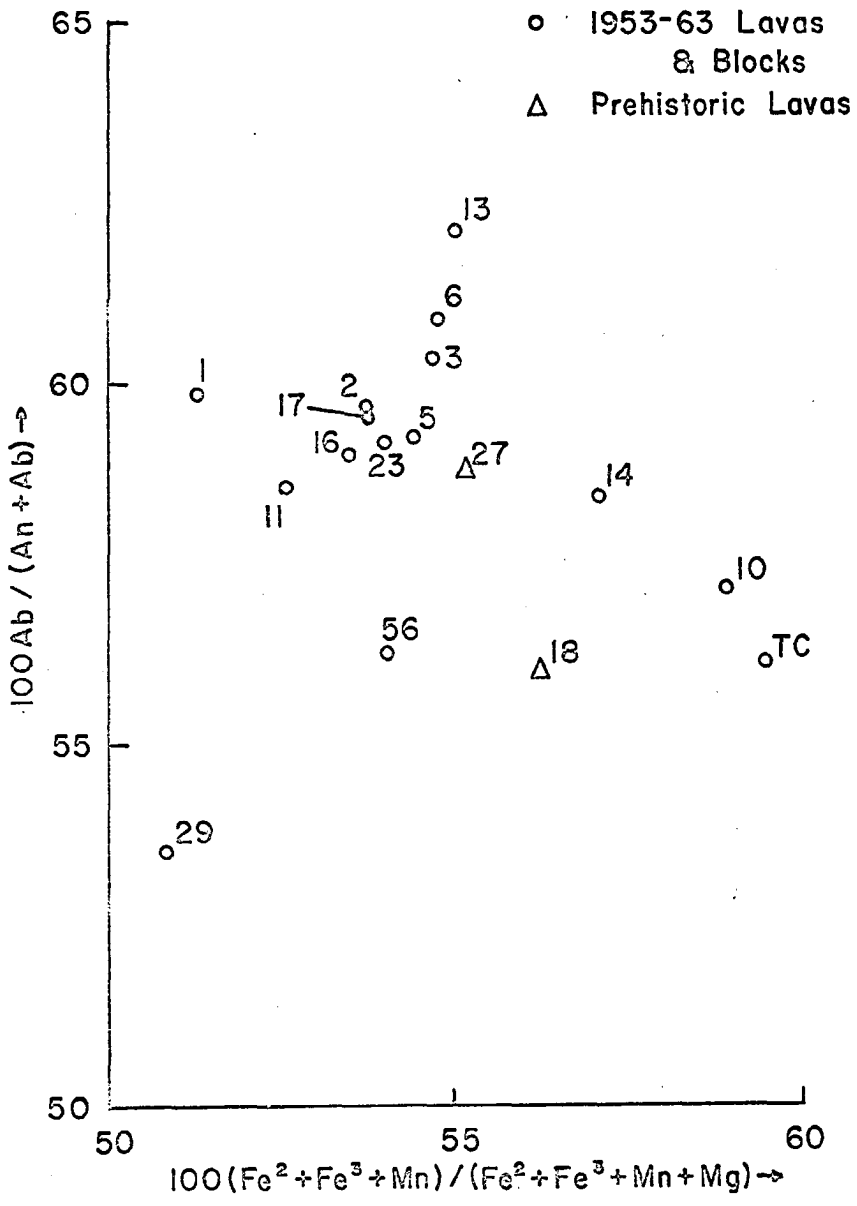

Fig. 47. Modified Wager plot of Trident andesites.

salic components, and liquidus temperatures are related to all of these components. In fig. 47 the majority of the Trident andesite plots define an arcuate trend (1-TC) and the remaining plots tend to follow a diagonal traced from plots of 29 to 13. A basic composition and higher liquidus temperature is indicated by the plot of 29, and the lowest liquidus temperature is indicated by the plot of 13. Liquidus temperatures for compositions between 1 and TC would be nearly the same. The trend from 29 to 13 indicate little increase in iron as compared to alkali enrichment; while between 1 and TC iron enrichment was dominant. Based on the significance of the two trends identified in fig. 46 in regard to partial oxygen/water pressure conditions, the compositional range within a single lava flow (KT-1, 2, 3, 16, 17 and 10, in fig. 47) sees to reflect the dominant effect of low partial pressure of oxygen/increasing water pressure with little or no diffusion of hydrogen with similar liquidus temperatures. On the other hand, the range of variation between different flow units, as reflected in the trend defined by the plots of 29, 56, 5 and 13, may have been caused by higher partial oxygen pressures.

CHAPTER V

CONCLUSIONS

PETROGENESIS OF THE TRIDENT ANDESITES

Five successive flows were erupted by the new vent of Mt. Trident during the period 1953-1960. With the possible exception of Paricutin volcano (Wilcox, 1954), the recent eruptive activity of Trident volcano has provided a unique opportunity for the study of contemporary andesites erupted along the North American segment of the Pacific rim. Of special interest, are the five sequential flows erupted in a very short period of time (seven years), the transitional tectonic location of the vent, and the classic question of whether or not each flow was derived from a separate magma batch or a common reservoir of magma.

In the previous sections, the petrography, chemical mineralogy and bulk chemistry of the andesite flows have been discussed in detail, and various physicochemical parameters have been expressed, in an attempt to answer these question.

Discussions of differentiation and fractionation trends in the previous sections have a somewhat different orientation than those in most petrological studies in that this investigation marks an attempt to determine whether fractionation and/or differentiation processes have played a role in the genesis of the Trident andesites, over a geologically insignificant period of time; a difficult and more elusive problem than the differentiation of compositionally distinct variants from a basic parent magma.

The genesis of the Trident andesites is clouded by the inherent enigma of the andesite problem, and the restricted range of bulk chemical and mineral composition which marks this sequence of flows.

The mineralogical and geochemical evidence provided by the constituent phases and bulk composition of the individual flow units indicates a general tendency toward increasing alkalis and silica in progressively younger flows, but the record also reveals at least one reversal in this trend.

The chemistry of coexistent plagioclase, pyroxene, magnetite and groundmass phases strongly support the existence of crystallization fractionation in a reservoir of parent magma which was periodically interrupted by the removal of erupted lavas. Each of these events was associated with cyclic changes in oxygen partial pressure and water pressure, and extraction of magma from the reservoir also influenced the fractionation of major and minor components in the crystalline phases of succeeding flows.

It is difficult, if not impossible, to reconstruct the crystallization history of each flow, in terms of the progressive crystallization of each batch of magma from the reservoir to emergence at the vent, and final solidification under atmospheric conditions.

Based on the viscous and blocky character of the Trident andesites when they were erupted from the vent, and the relative volume of quenched glass in the matrices, we can assume that $\sim$ 35% of the melt had crystallized before it emerged from the vent.

Interpretation of the evidence is handicapped by a lack of knowledge concerning the actual velocity at which each batch of melt ascended the conduit system, possible still-stand periods and the effect which these variations may have had on the course of crystallization. The discontinuous eruption of andesitic lavas by the Trident vent during 1953-1960 was probably caused by vent blocking and the periodic decrease of gas pressure rather than the cyclic generation of magma in separate batches based on the chemical evidence presented in the preceding sections.

In spite of these difficulties, chemical evidence provided by the constituent phases and bulk composition, indicates that the successive andesite flows were probably derived from a common parent magma and that fractional crystallization under changing oxygen partial pressures and water pressures have been responsible for the compositional variations displayed by the Trident andesites.

The evidence supporting these conclusions and the application of these findings to the andesite problem are summarized in the concluding remarks to follow.

Paragenesis of Constituent Minerals

The sequence of crystallization of the different phases in each flow, as traced from depth to final consolidation at the surface, are summarized in table 56. The interpretation of the physical conditions, which accompanied crystallization and the sympathetic variation trends of the groundmass glass compositions, are also included in the table. The sequence of crystallization, as reconstructed in table 56, shows that, (1) the earliest crystallizing phases were clinopyroxenes, plagioclase and magnetite; and (2) the coexistent phenocrystal phases and the glassy residuum were in most cases of non-simultaneous origin.

The glomeroporphyritic aggregates of plagioclase-clinopyroxene, clinopyroxene-magnetite; and monomineralic aggregates of plagioclase and clinopyroxene, as discussed in the section on petrography, lend support to the above interpretations. Petrographic analyses have included a much larger suite of samples than those included in the petrochemical studies, and could be more representative of the entire suite, in a qualitative sense. Additional examples of correlation between petrographic data and

Table 56. Tentative Reconstruction of the Sequence of Crystallization, Genesis of Coexistent Liquid Phases and Sequence of Eruption.

	P_{O_2} P_{H_2O} conditions	Crystallizing phases*	Genesis of coexistent liquid phases*	Nature of enrichment in coexistent liquid phases
Stage 1 (?1951-1953)				
	P_{O_2} increasing	M-6,23 C-23 PP-1	GM-23→6	Alkali + silica
	P_{O_2} constant/ decreasing	M-1,56 PP-56		
	P_{H_2O} increasing	C-56 O-56	GM-6→56	Iron and alumina
1953 eruption of all (56) phases.				
Stage 2 (1954-1958)	(Crystal and liquid composition in reservoir - M-6, 23; C-23; PP-1; GM-23, 6)			
	P_{O_2} increasing/ constant	M-14,13 C-6,1,14,(?)13 PP-14,13 O-14,1,13	GM-6→1 1→14→13	Iron followed by silica.
	P_{H_2O} increasing	C-13 (cont'd)		
Consolidation of all (13) phases as (?) carapace (1954-1957)				
1957 eruption of all (14) phases				
1958 eruption of all (1) phases				
Stage 3 (1959-1960)	(Crystal and liquid composition in reservoir - M-6, 23; C-23, 6; GM-23, 6)			
	P_{O_2} increasing/ constant	O-23,6R PP-23,6 M-6(cont'd)	minor changes, resorption effects.	
	P_{H_2O} increasing	O-6		
1959 eruption of all (6) phases				
1960 eruption of all (23) phases.				

*M - Magnetite; C - clinopyroxene; O - orthopyroxene; PP - plagioclase; GM - groundmass glass;
Numbers indicate sample numbers of analyzed fractions;
Chemical characteristics of the phases have been discussed in a subsequent section.

chemical trends have been observed, including the progressive genesis of the groundmass glass compositions and the actual dates of eruption, as listed below:

GM-13 - (?) 1954 (block avalanche),
14 - 1957
1 - 1958
56 - 1953
6 - 1959
23 - 1960

The lower compositional limits of phenocrystal clinopyroxene (mol. percent clinoferrosilite), orthopyroxene (mol. percent ferrosilite) and homogeneous plagioclase grains (mol. percent anorthite), as given in tables 6, 7 and 8, can be considered to be representative of equilibrium molar concentrations of the different phases in the immediate pre-eruptional stage. The compositional variation in groundmass glasses from GM-23 to 13, as shown in table 56, correlates with the variation in mol. percent of ferrosilite and anorthite (as determined from optical determinations), in the pyroxenes and plagioclase respectively, coexistent with the above groundmass glasses.

Bulk Composition

The Trident lavas, which contain 12-18% normative quartz, have been termed andesites all though this work, even though there is a large devia-

tion in their bulk composition from the average andesite as given by Nockolds (1954, p. 1019). Chayes (1965, p. 158), in his statistical study of 1526 Cenozoic andesites, found that the maximum frequency of normative quartz ranges between 12 and 18%, and favored this as a taxonomic criterion in redefining the term "andesite". The Trident lavas, are, therefore, "andesites" in a most recent sense, even though they are more siliceous and calcic than most Pacific rim andesites.

Bulk rock compositions in various igneous rock series have been equated to residual liquid compositions during progressive stages of differentiation. As indicated earlier, the bulk chemical composition of the Trident andesites is chiefly controlled by the modal ratio of glass vs plagioclase as these fractions constitute more than 90% of the bulk rock (average glass content = 60 vol.%). It is clear that the groundmass glass exerts the most dominant effect on bulk composition, but it is doubtful whether modal and/or compositional variations in the pyroxenes can be correlated with the comparative bulk composition in this particular series of andesites. The possible effect of early olivine crystallization in the parent melt may be largely concealed by those of pyroxenes and plagioclase, but it was thought that some evidence of this might have been retained in the earlier lavas and their constituent phases.

The chemical composition of the pyroxenes, plagioclase, glassy mesostases and the bulk rocks have been plotted on MgO- Al_2O_3/SiO_2 (fig. 48) and CaO- Al_2O_3/SiO_2 (fig. 49) diagrams. MgO-Al_2O_3/SiO_2 variation (fig. 48)

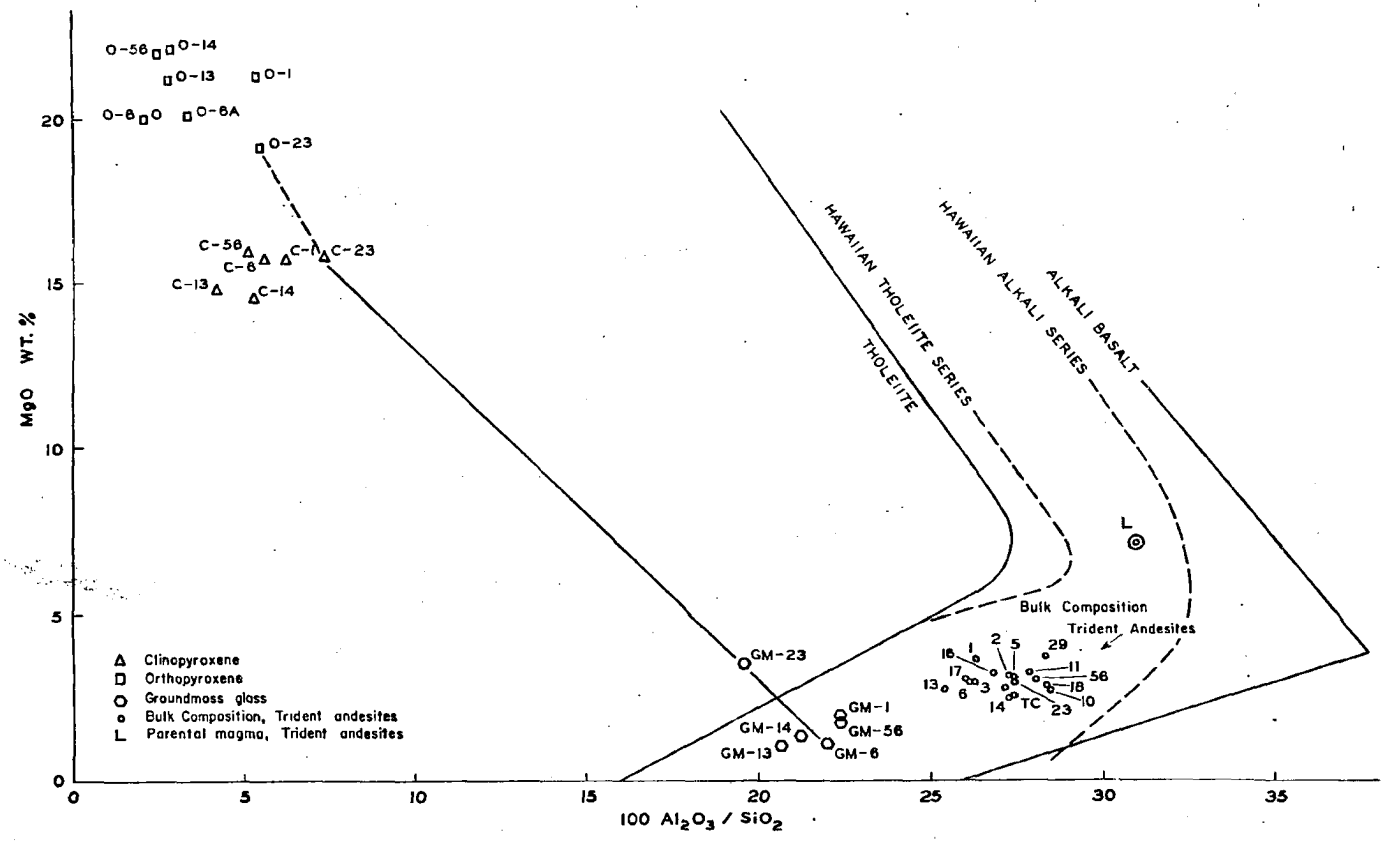

Fig. 48. MgO - Al_2O_3/SiO_2 plot of analyzed clinopyroxene, orthopyroxene, groundmass glass and bulk compositions. (Tholeiite and alkali series trends taken from Eaton and Murata, 1960, cited in Yoder and Tilley, 1962).

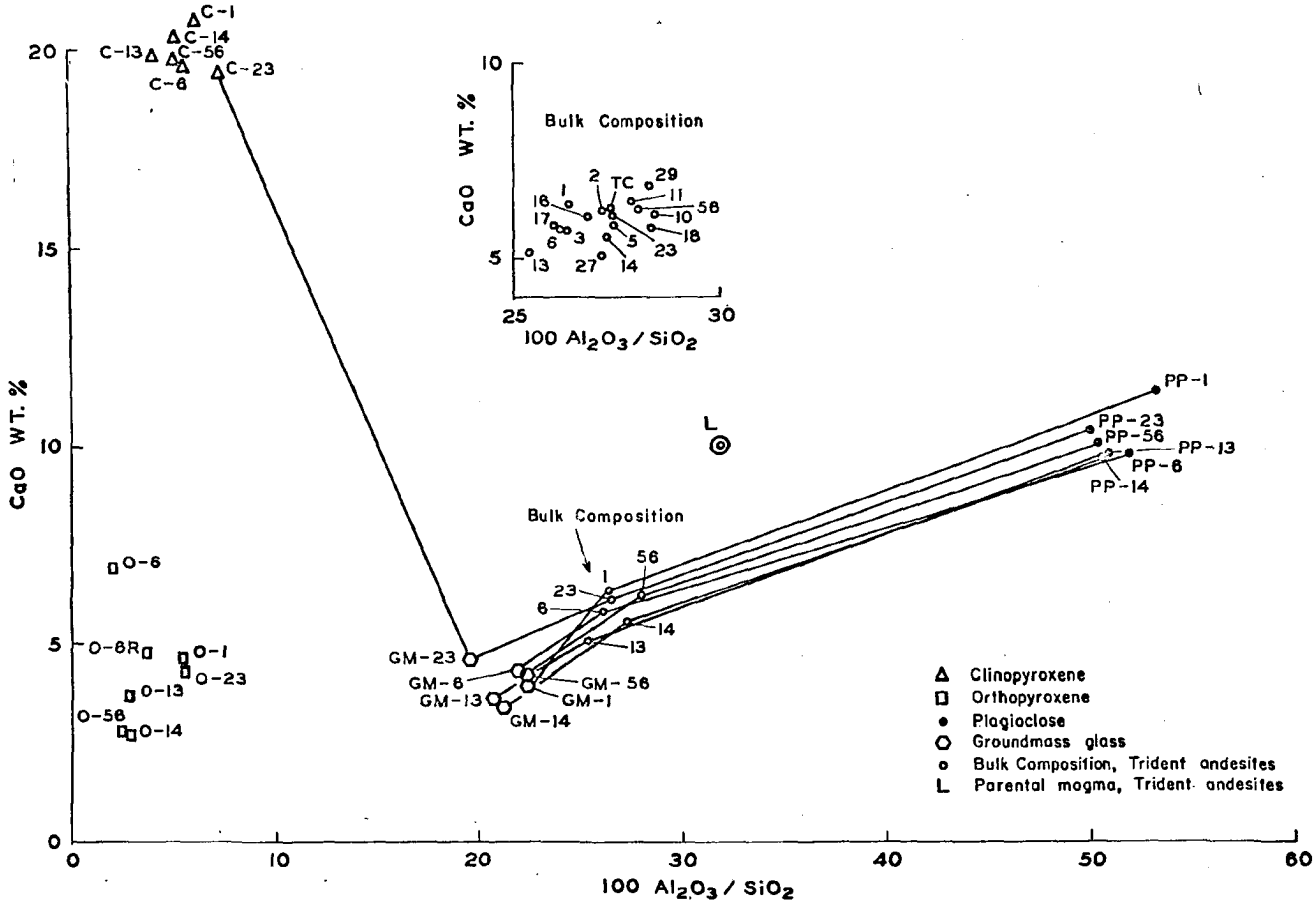

Fig. 49. CaO - Al_2O_3/SiO_2 plot of analyzed clinopyroxene, orthopyroxene, plagioclase phenocrysts, groundmass glass and parent rocks. Bulk compositions of the analyzed andesites are shown in the inset. Tie lines indicate the effect of plagioclase fractionation and resorption of C-23.

reflects the effect of pyroxene fractionation, while CaO- Al_2O_3/SiO_2 ratios (fig. 49) should be related mainly to plagioclase crystallization effects. Fig. 48 includes the trends of average tholeiite and alkali series and Hawaiian tholeiitic and alkali series, as extrapolated from Yoder and Tilley (1962, p. 414) and Eaton and Murata (1960). Plots of the bulk compositions of the Trident andesites occupy an intermediate field between the tholeiites and alkali basalts. On a (Na_2O+K_2O) -SiO_2 plot (fig. 50), the bulk compositions occupy the margin of the high-alumina basalt field (Kuno, 1965, p.310). A comparison of this plot with similar plots for the Hawaiian tholeiitic and alkalic series (Kuno, op. cit., p. 311; MacDonald and Katsura, 1964) discloses distinct difference in SiO_2 content. High-alumina basalts were not proposed for the Hawaiian volcanic series (Kuno, ibid.), but Yoder and Tilley presented rather convincing arguments for their presence (op. cit., p. 419). The Trident andesites show high alumina affinities, and differ from mugearite - hawaiite of the alkali basalt series in silica content. From figs. 48 and 49 it is clear that the andesite bulk compositions are not in the olivine fractionation field; but fall in the field characterized by pyroxene-plagioclase fractionation (also indicated by other evidence). The groundmass glasses are more highly differentiated, but belong to the same compositional field. The collinearity of the plots for clinopyroxene 23, orthopyroxene 23 and groundmass glasses 23 and 6 (as shown by tie line in fig. 48) indicate that the composition of GM-6 could be derived from that of GM-23 by crystallization of C-23 and O-23 (cf. Eaton and Murata, op. cit.). However, the distribution of the plots for the glass compositions indicates that both plagioclase and pyroxene fractionation effects are important in determining the composition of the glassy residuum; and these relations are evident in fig. 49. The parallelism of the tie lines between the plots of

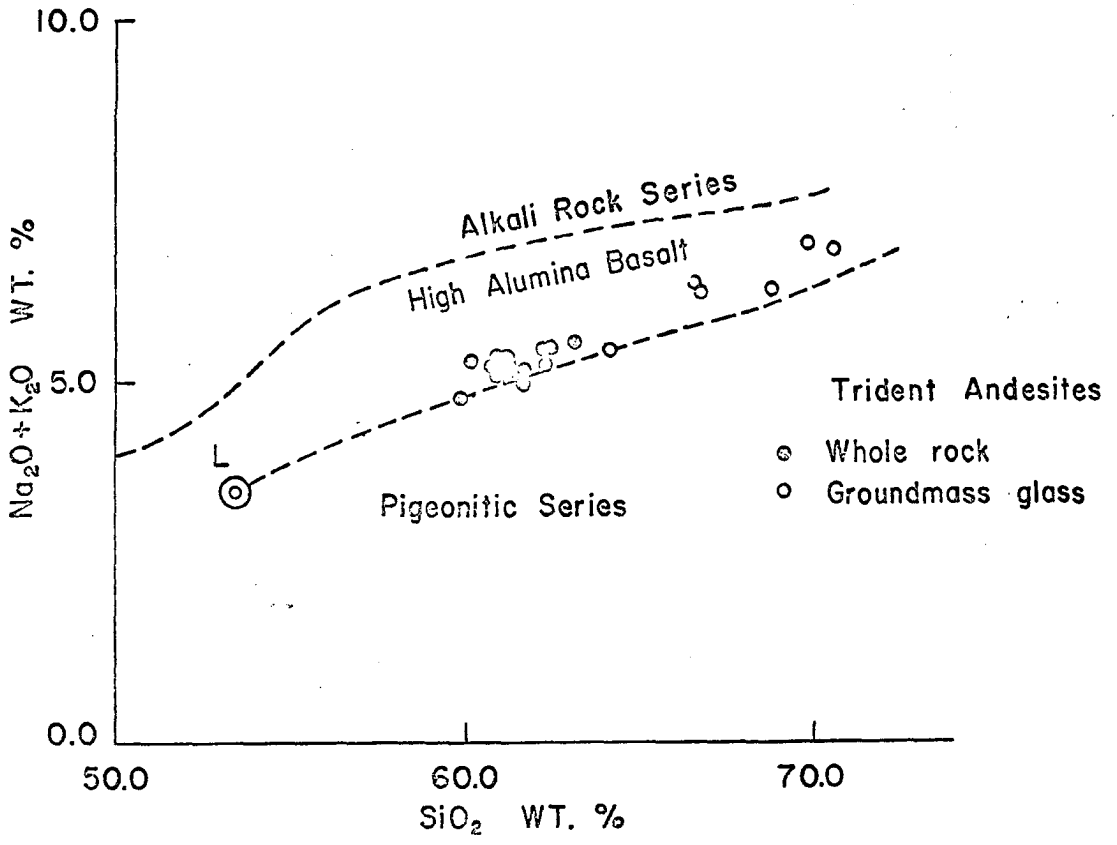

Fig. 50. $(Na_2O + K_2O)$ - SiO_2 diagram showing the plots of Trident andesites, analyzed groundmass glass and proposed parental magma composition ('L'). Field boundaries taken from Kuno (1965).

plagioclase, bulk and glass compositions indicate the dominating effect of plagioclase crystallization on the composition of the glass; with bulk composition chiefly dependent on the relative proportion of glass vs. plagioclase and pyroxene phenocrysts. However, the gentle slope of the zone defined by the tie lines between the bulk composition and the composition of the glass can be attributed to the effect of co-crystallizing clinopyroxene. The effect of orthopyroxene is not evident in fig. 49 (chemical parameters). From the same diagram it is also evident that the suppression of plagioclase displaces the liquid phase composition toward Al_2O_3 enrichment, while plagioclase fractionation encourages SiO_2 enrichment. The range in bulk composition from KT 1 to 10 and 29 to 13 (inset in fig. 49) - compositional end members of the Trident andesite suite, represent the extremes of the above mentioned trends of fractional crystallization. However, the persistent effect of late coexistent orthopyroxene crystallization moderates this tendency.

Composition of the Magma

In andesite samples KT-1 and 13, and in part in KT - 14 and 23 all or majority of the coexistent mineral phases were crystallized simultaneously or nearly so. Thus, these samples provide more reliable data for a variation diagram which may be used to estimate the composition of the parental magma. Six analyses (specimens from which constituent minerals were separated and analyzed) have been plotted on a silica variation diagram (water free basis) in fig. 51. Trend lines of CaO, ΣFeO, MgO, Na_2O and K_2O defined by the bulk compositions of 1, 13 and/or 23 and 14 have been drawn. Al_2O_3 plots are scattered (plagioclase effect). Lines have been drawn using plots of KT-1 and 13 only. A perpendicular has been drawn from the point where K_2O trend

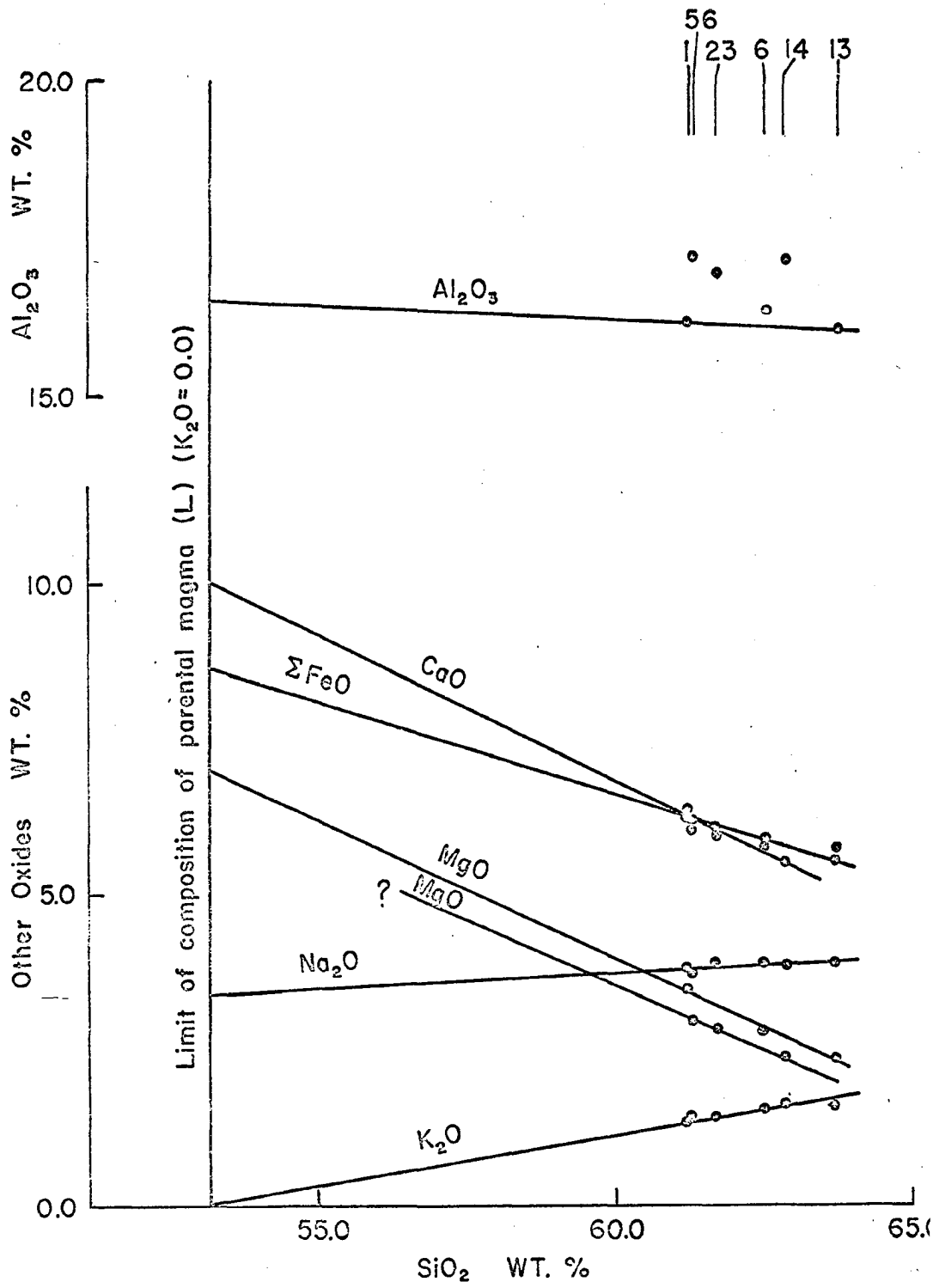

Fig. 51. Extrapolated composition of parental magma of the Trident andesites.

intersects the abscissa (wt.% SiO_2)as a boundary marking the limiting composition of the parent melt (K_2O = 0.0%, SiO_2 = 53.2%, fig. 51). Theoretically, a melt in this series could not be less undersaturated in silica. However, the K_2O variation trend used in this extrapolation is not in agreement with that which would be defined by a line drawn on plots of 56 and 13. If these plots were used, the SiO_2 content corresponding to 0.0% K_2O becomes ∿ 49.0%. The composition of the parent melt as interpreted from this diagram would be:

			Norm	
SiO_2	53.2 wt.%	Ab	-	28.8
Al_2O_3	16.5 "	An	-	29.7
MgO	7.0 "	Wo	-	8.4
ΣFeO	8.6 "	En	-	16.3
CaO	10.0 "	Fs	-	9.7
Na_2O	3.4 "	Fo	-	3.7
Others	1.3 "	Fa	-	2.4
	100.0	Others	-	1.0
				100.0

Such a composition is not andesitic, but closely resembles the composition of the parental calc-alkali magmas proposed by Nockolds and Allen (1953, p. 139, table 8). Significantly, this composition is similar to that of Paricutin parent magma, as given by Nockolds and Allen (op. cit.; Fe:Mg ratio: Paricutin - 58:42, Trident - 55:45). This magma would be undersaturated, and olivine normative. The composition of this hypothetical melt has also been plotted on figs. 48-51 ('L').

If the Trident andesites were derived from a parent magma with the composition 'L', olivine fractionation must have been minor (fig. 48). The

dominant fractionate was plagioclase with one or both pyroxenes. The dominant role of clinopyroxene rather than orthopyroxene fractionation is clarified in fig. 49.

In fig. 49 (inset), the bulk compositions of the Trident andesites have been plotted. The extreme range in bulk composition is shown along trends KT-29-13 and KT 1-10. Specimens KT-29 and 13 were obtained from the ejected blocks. Specimens KT 1 and 10 were obtained from the same lava flow (1948). Paralleling the trend defined by KT 1-10 are those of 11-56 (1953 flow) and 6-5 (1959 flow). The trend defined by KT-29 and 13 shows the effect of prolonged plagioclase fractionation, while trend KT 1-10 and those parallel are believed to be characterized by conditions of suppressed plagioclase crystallization. This could mean tha, prior to the eruptions, a period of increased water pressure brought about a retardation of plagiclase crystallization and a relative acceleration of clinopyroxene crystallization. Such a process would deplete the molar concentration of diopside vs. Ca-Tschermak's molecule; but immediately after the eruption, the groundmass plagioclase would be richer in anorthite than the last plagioclase phase which crystallized before lava was erupted from the vent. With the exception of KT -23, the composition of groundmass glasses, as plotted the same diagram (fig. 49), reflects the dominant role of plagioclase in controlling the composition of the residual liquids represented by the glasses.

In the light of the sequence of crystallization under different conditions of oxygen and water pressures as shown in table 56, it is evident that other crystallizing phases (clinopyroxene, magnetite and orthopyroxene) show distinct compositional characteristics under varying oxygen and water pressures. These characteristics, as revealed in the end member compositions of the pyroxenes and magnetite, have been discussed in Chapter III

Table 57. Compositional Characteristics and Rate of Crystallization of Phases; and Composition of Residual Liquids under Varying Conditions of Partial Oxygen Pressure and Water Pressure (in time) with Respect to Eruptions.

Time →

Crystallizing phases	Increasing P_{O_2} due to H_2 escape/decreasing P_{H_2O}.	Increasing P_{H_2O} due to closure of vent by plug and crust.
Plagioclase	Rapid	Suppressed
Clinopyroxene	Tsch Mol. % low, presence of Jd. mol., normative Ne.	Tsch Mol.% high, no Jd. mol., normative Hy.
Orthopyroxene	Later than cpx in sequency, Tsch Mol.% high, normative Qz.	Later than cpx in sequence, Tsch Mol.% low, presence of Jd and/or β-$Na_2Si_2O_5$ Mol. normative Ol.
Magnetite	Early to late in crystallization Usp-Mt-Mht_{ss}, Mt → Mht subsolidus oxidation.	Late in crystallization, Usp-Mt_{ss}, minor Mht, Usp → Mt subsolidus oxidation.
Residual Liquid	Enriched in SiO_2, depleted in FeO, MgO, CaO etc.	Enriched in Al_2O_3 and (?) FeO + Fe_2O_3

E R U P T I O N

(Chemical Mineralogy). In table 57, the compositional characteristics of pyroxenes and magnetite,rates of plagioclase crystallization, and composition of the coexistent liquid phases have been correlated to varying oxygen and water pressures preceding eruptions.

Origin of Magma 'L'

Evidently the information at hand is inadequate for a discussion on this subject (whether 'L' is primary). There is some suggestion in the discussion of Nockolds and Allen (op. cit.) of the possible existence of such primary magmas. Comparison with data from Tilley, Yoder and Schairer (1965 figs. 3-5, pp. 75-77), on the melting relations show that the composition 'L' does not lie on either the tholeiitic or alkali series. High-alumina variants of tholeiites (Warner basalt, Yoder and Tilley, op. cit., p. 362) are compositionally similar to 'L' in respect to ΣFeO and alumina, but lower in alkali content. High-alumina variants with alkalic affinities, would resemble 'L' in respect to alkali content, but not in ΣFeO and MgO. There is no direct evidence for the differentiation of 'L' from a tholeiitic or alkali basalt parent magma.

The lowest temperature at which such a melt can exist at one atmosphere is around 1080°C (analogous to the liquidus temperature of Kilauea tholeiites, Tilley et al, op. cit., p. 78) under anhydrous conditions. This estimate is based on alkali and silica contents. With increasing water pressure the solidus would be lowered, and at 5 kb of water pressure the solidus would be around 800°C (for high-alumina basalts and alkali basalts, Yoder and Tilley, 1962) with little depression of the liquidus.

It is difficult to reconstruct the exact sub-crustal or crustal environments approaching these conditions. There are several possibilities. Data for Japan presented by Shimozuru (1963, p. 520), involving a shallow M

discontinuity (∿ 20 km) and the coincidence of the low velocity layer, does not apply to the Trident problem, as recent data by Berg et al (1966) show that the M discontinuity underlying the Alaska Peninsula ranges between 32 and 38 km. However, according to Berg et al (op. cit.), immediate subcrustal zone has a Poisson's ratio of ∿ 0.3, a significant figure. Shallow seismic activity under the Alaska Peninsula, with accompanying aftershock energy release by creep (Benioff, 1951, p. 61) would supply additional thermal energy within the base of the crust to produce a significant reduction in rigidity. In this case there is no necessity to invoke heat from radiogenic sources.

TRIDENT ANDESITES AND THE ANDESITE PROBLEM

In an earlier section it was proposed that the Trident andesites were derived from a slightly undersaturated parental magma with high-alumina or alkali basalt affinities. Andesites of the calc-alkali series of the orogenic volcanoes are more classically considered to be derived from magmas of tholeiitic parentage by assimilation of sialic material or differentiation.

The basic question is what characterizes andesites - association or composition? Compositionally rocks of andesitic character can be subdivided into three groups, including those with, (a) normative quartz and hypersthene (calc-alkali andesite) (b) normative hypersthene and olivine (hawaiite) and (c) normative olivine and nepheline (mugearite). Type (a) appears to occur within the Andesite Line, type (b) tends to be restricted to the oceanic domain, while type (c) occurs in both domains. According to the prevailing concept, true andesites are of the (a) type, belonging to the calc-alkali series, as distinguished from types (b) and (c). The

proposed composition of the parent magmas of the Trident andesites, however, exhibit compositional and petrogenetic affinities toward high-alumina and alkali basalts - an important aspect of the studies of the Trident andesites and the Andesite problem.

Melts in the proposed compositional range of the Trident parent magma could be theoretically derived from partial melting of basaltic material in the basal crust. Silica saturation of the melt would be related to the temperature at which fusion takes place. The temperature gradient along the M discontinuity in the transitional zone between the oceanic and continental stable areas is likely to be higher than those of the adjacent areas. Pressure-release effects and additional supply of thermal energy from aftershock strain release are likely to create conditions suitable for partial fusion of basalt layer. Thickening and downwarps of the basalt layer would also be an additional factor in the process. The Andesite Line may be an expression of all these relationships.

SUMMARY

(1). The lavas erupted by Trident Volcano during the period 1953-60 were andesites, as defined by composition and orogenic association.

(2). The Trident andesites have dacitic affinities, and they are more siliceous than average andesites erupted by circum-Pacific volcanoes. The high silica content shows the alkali-lime index of the Trident andesites toward calcic rather than calc-alkalic, but the CaO/Σ alkali ratio is typical for that of a Pacific rim andesite.

(3). These andesites contain olivine, and the clinopyroxene displays alkalic affinities, in contrast to the high bulk silica content; and it is proposed that the andesites were differentiated from a slightly undersaturated olivine normative parent magma with alkalic affinities and a bulk composition similar to high-alumina basalt.

(4). The 1953-1960 eruptive history can be subdivided into the 1953-1954 and 1957-1960 cycles, in which each initially erupted flow appears to be intermediate in the differentiation sequence. The andesites extruded during the repetitive eruptions of 1957, 1958, 1959 and 1960 showed little evidence of progressive differentiation.

(5). Fractionation processes were mainly confined to two periods prior to the onset of the 1953 and 1957 eruptions. Fractional crystallization during these periods apparently occurred in a shallow reservoir, with initially high oxygen partial pressure which was replaced by high water pressure/low oxygen pressure prior to the eruptions.

(6). Plagioclase crystallization was accelerated during the period of higher partial oxygen pressures, but retarded by increasing water pressure.

(7). Clinopyroxenes which crystallized under high partial pressure of oxygen were poor in Ca-Tschermak's molecule, nepheline normative and contained 0.6 to 1.5% of the jadeite molecule. With increasing water pressure crystallizing clinopyroxene became richer in Ca-Tschermak's molecule. These clinopyroxenes are hypersthene normative.

(8). Orthopyroxenes, joining clinopyroxenes later in the sequence of crystallization, contain Ca-Tschermak's molecule and normative quartz (crystallizing under higher partial oxygen pressures). Increasing water pressure encouraged the entry of the jadeite component, and a reduction of the Ca-Tschermak's in the orthopyroxenes; and these orthopyroxenes are olivine normative.

(9). Under conditions of increasing partial oxygen pressure, magnetite crystallized as an early phase in the magma reservoir. Such magnetites were essentially ulvöspinel-magnetite-maghemite solid solutions, and the sub-solidus oxidation was from magnetite to maghemite. Under increasing water pressure, magnetite crystallized as an intermediate to late phase. The later magnetites were ulvöspinel-magnetite solid solutions with minor maghemite. Sub-solidus oxidation was from ulvöspinel to magnetite.

(10). Coexistent liquid phases formed during the period of fractional crystallization under high partial oxygen pressure were enriched in silica vs. alumina and depleted in the femic constituents. Under increasing water pressure the tendency was toward enrichment in alumina over silica.

(11). During the last lava eruption (1960 flow) some of the earliest density stratified phases were ejected. Since the eruption of this last flow, blocks have been ejected some of which are compositionally very basic.

(12). Melts in the proposed compositional range of the Trident parent magma could be theoretically derived from partial melting of basaltic material in the basal crust. Geothermal heat coupled with heat from aftershock strain release could provide temperatures high enough for such partial fusion. Thickening and downwarps of the crustal basalt layer would be conducive to partial fusion. These factors would impart compositional differences in the melts. Silica saturation would be related to temperature decrease along the base of the crust toward the continental areas; and the Andesite Line may be an expression of these relationships.

APPENDIX I

ERUPTIVE HISTORY OF MT. TRIDENT

Reliable records are not available for the volcanic activity of Mt. Trident prior to 1953. However, Eicher and Rounsefell (1957, p. 70) claim to have observed violent activity on Novarupta for two hours on May 19, 1949, comprising a heavy outfall of ash, drifting toward the Shelikof Strait. They further mention that a few days later Mt. Trident also erupted. Mr. W. J. Nancarrow, Park Ranger at Brooks River Station in 1950, reported three explosions during July-August, 1950 which might have been from Mt. Trident (Decker, 1963, pp. 37-38). Decker also cites reports by Mr. Al Kropf, pilot with U.S. Fish and Wild Life Service, regarding ash eruptions from a fissure on the side of Mt. Trident during July, 1951. Aerial photographs (U.S. Park Service Records, July 7, 1951) clearly show a radial fissure (over 3,000 ft long) extending down the southwest flank of Mt. Trident and an ash fall zone surrounding a burning vent located on the fissure. These aerial photographs did not show any lavas (Decker, op. cit. p. 38).

1953:

The violent activity and lava eruption of 1953 have been well documented by Snyder (1954, pp 3-4). Summarized observations are as follows:

February 15, 1953 - LCDR Frank Chase, flying at 15,000 ft over Port Heiden, observed a huge tower of smoke mushroom about 150 miles away (4-00 p.m.). The centre of activity was determined to be somewhere in the vicinity of Mt. Katmai. The height of smoke cloud was estimated at 30,000 ft. Subsequent observations correlated this smoke cloud with Mt. Trident. Northern Consolidated Airlines, King Salmon, also reported this initial explosion.

February 16, 1953 - 7:00 a.m. - Naval reconnaissance under LCDR G. H. Webster observed thick smoke layer stretching over 100 miles.
8:40 a.m. - A Navy crew of Grumman Albatross, Naval Station Kodiak, sighted a second eruption. 'Huge ball cloud rose about 7,000 ft.'...
8:50 a.m. - 'Cloud mushroomed to 30,000 ft. Top fanned out to 10-mile diameter.'
8:55 a.m. - 'Top spread like sunflower to 25-mile diameter at height of 35,000 ft.' Photocrew chief Frank O. Brink reported the cloud to be light grey and presumably mostly steam and little ash.

LCDR Glenn Thompson, U.S. Coastguard, was patrolling at lower heights and closer to the area. The smoke cloud was thick between Mr. Mageik and Mt. Katmai and Thompson erroneously thought Knife Peak to be the source.

The summary of the Navy dispatch was that a second and possibly a third column were rising approximately 10 miles southwest of Mt. Katmai.

February 17, 1953 - Navy dispatch - Mass eruption and the most spectacular event were observed.
10:55 a.m. - Plane flying at 8,000 ft observed huge black smoke ball rising to 15,000 ft. In two minutes a second cloud followed. The black cloud rose to 30,000 ft. Ash and debris were falling all around. The cloud drifted towards northwest. Sulphurous fumes were strong even within the aircraft. It appeared from the photographs that besides Trident there was one more which had joined the fray. Principal suspects were Mts. Martin and Mageik. However, another photograph, dated February 17, showed Mt. Martin steaming quietly. This narrows down the possibility to Mt. Mageik.

February 18, 1953 - Reports by the Navy patrols: Clear weather permitted better and precise observations. The vent on Mt. Trident was situated at about 3,600 ft on the southwest flank. Ash and steam were issuing out as a grey column. A blocky lava flow had spread over an area - 800 x 700 ft (plate 10a). The lava flow was very slow and viscous, and showed 'a surface of large blocks of lava formed as the stiffening material reached the surface'. Earlier dispatches had mentioned 'long streams of molten lava' but they were probably mud flows.

February 21, 1953 - Naval report: Ash column was grey and steam laden. The lava had advanced half a mile southward down the slope.

February 27, 1953 - Naval report: The eruptive column was light grey. The lava front had extended several hundred feet further down the slope.

Plate 10a. Oblique aerial photograph of the new cone of Mt. Trident shortly after the February, 1953-eruption (Photo - Mr. Peterson; courtesy of U.S. National Park Service).

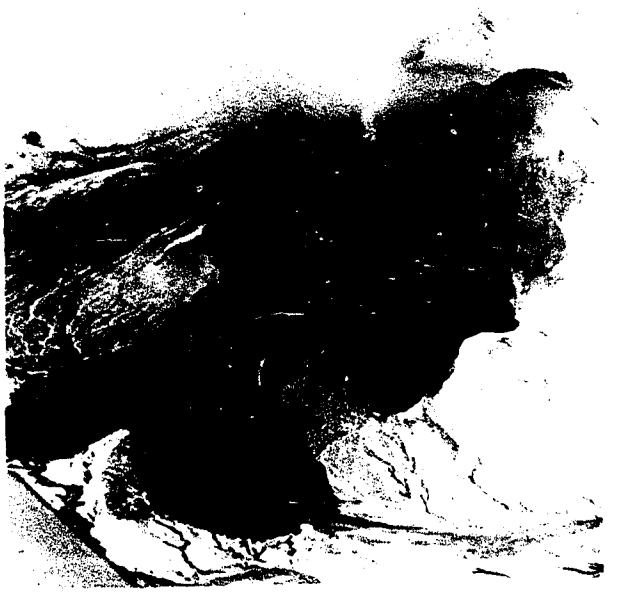

Plate 10b. Oblique aerial photograph of Mt. Trident, August, 1957, showing the disposition of 1953-54 and the subsequent 1957 flow (Photo - Mr. Steenburgh; courtesy of U.S. National Park Service).

March 4, 1953 - Naval report: Low clouds. Slight widening of the lava flow on the eastern side of the toe was observed. The eastern lobe expanded until March 9. From March 4 to 11 the central portion of the flow expanded from internal additions. Between March 9 and 11 further overflow had produced a northwestern lobe. Eruptive column became weaker and erratic on March 11th.

April 6, 1953 - Naval reports: Lava pile bulged on east and west flank and increased in height in vent area.

June 2, 1953 - Naval photographs: Further growth of the lava mound on east flank occurred. Between April 6 and June 2 there were fresh additions overriding the lava surface.

June 17, 1953 - New lava was pouring out slowly from the vent. Vent was buried under lava. It was piling up at the source as well as spreading down northwest, west and northeast flanks.

June 30, 1953 - Evening: A patrol plane reported that an ash column was rising from the glowing vent of Trident. Through an analysis of documentary material from different agencies, Snyder (op. cit.) concluded that by March 11, 1953, 0.13-0.17 cubic mile of lava was extruded together with 0.015-0.029 cubic mile of ash. By June 17th, the total volume of the lava pile had risen to about 0.055-0.073 cubic mile (as compared to the 6 to 7 $mile^3$ total volume of pyroclastics erupted by Mt. Katmai in 1912 was around 6-7 cubic miles.

To date this is the best documented eruption of Mt. Trident. Since 1953 the record of volcanic activity from the recent cone is incomplete. Eruptive activity is continuing, even at present. The reconstruction of the post 1953-1954 volcanic history which follows is based on periodical reports by U.S. National Park Service rangers and sporadic air reconnaissance records coupled with chance observations. Reconnaissance geophysical investigations, carried out by Decker (op. cit.) in summer of 1963, added some more information and the present investigation commenced in 1965. The information available for the period 1954-1964 is summarized below (sources of information: Records of the U.S. National Park Service, Katmai National Monument, Courtesy Messrs. O. T. Dick and D. F. Coe, and Decker, op. cit. pp. 38-42).

1954:

June 18, 1954 - Reconnaissance flight by Richard W. Ward, Park Ranger at Brooks. The new lava flow had increased in size greatly. Comparison of photographs confirm this. (Emplacement of first lava flow occurred between February, 1953 and June, 1954).

1956:

September, 1956 - Report by Mr.W. Steenburgh, Park Ranger at Brooks: Dense air-borne dust was observed on September 8-9. Sulphurous odor and dust fall accompanied the same.

A photograph (plate 10b), dated August, 1957, obtained through the courtesy of U.S.N.P.S. shows two lavas, the 1953-1954 flow appearing on the left. The one to the right is reportedly a new 1957 flow. Between the flows, near the base of the cone a blocky mound (pumice covered) is observed for the first time. This is essentially a jumbled mass of blocks and broken crusts of the vent and must have moved down sometime between 1954 and 1957. (Specimen Nos. KT-12 and 13 were obtained from this blocky mound).

1958:

Annual Report by Mr. T. Roeder, Park Ranger, Brooks:

Mt. Trident continued to be active throughout 1958. Reconnaissance flight of September 8 showed a large new lava flow (a 1958 flow) partially covering 1953-54 flow. Small 1957 flow appeared on the east.

1959:

June 8, 1959 - Letter by Mr.T. Roeder: Trident volcano showed signs of a great deal of activity since fall, 1958.

1960:

August 10, 1960 - Report by Mr. R. Peterson, Park Ranger, Brooks: Bob Dewey and Bob Brown (U.S. Fish and Game Dept.) and Peterson observed violent activity. Lava was thrown to 10,000 ft (1960 overflow). Smoke column rose to 10,000-15,000 ft. After a reconnaissance flight Peterson reported:

(a) Cone appeared to be growing,
(b) Considerable ash discharge,
(c) Periodic smoke discharge and
(d) No enlargement of the lava.

1960:

August 21, 1960 - Peterson's report on the condition of Trident: Light grey slide areas were formed near the cinder cone. The cinder cone was breached. During the winter of 1959-1960 a new flow was extruded to the west of 1953-1954 and 1958 flows (plate 11a). Lava had apparently moved down the old flow part way, enlarging it and then spilled over the adjacent ridge. This lava flow must have taken place before July, 1960, when Peterson had carried out a reconnaissance flight (1959-1960 flow).

1961:

June 30, 1961 - An ash blow out was suspected. A photograph taken in 1961 by Mr. Peterson of U.S.N.P.S. (plate 11b), shows the development of the plug in the crater.

August, 1961 - The crater appeared to be smaller.

1962:

January, 1962 - Cone diameter had doubled. Smoke and ash eruptions were reported during the summer of 1961.

June 10, 1962 - 5:20 p.m. - Cinder cloud rose to 20,000 ft. Chuck Nickles, Bob Dewey (U.S. Fish and Game Dept.) and Dave Bogart, Park Ranger, Brooks, flew over the area at 7:30 p.m. The plug at the crater had blown out and a new crater had formed. Fumarolic activity at Katmai crater lake stopped at this time. (These two events have been correlated - Bordet et al, 1963, p. 30).

1963

April 1, 1963 - 9:00 a.m. - Bill Tolbert, Northern Consolidated Airlines representative at King Salmon, reported a huge cloud of volcanic dust from Trident. Radar estimates placed the height of the cloud around 40,000 ft. Dave Bogart flew over the area and reported that Trident had erupted in the same manner as in June, 1962. The crater was clear and emitting acid smokes at the time of flight. Post-eruption aerial photographs taken by Bogart (April 5, 1963) and the U.S. Navy (Decker, op. cit. p. 47, fig. 31) on August 5, 1963 showed a flow like stream descending down the south flank of the cone. Bogart considered this to be a mud flow. Decker and Ward (Decker, op. cit. p. 47) identified this to be a flow of blocks and ash (block avalanche), spilled down between the 1953-54 and 1957 flows. Photograph taken by Bogart (plate 12) also revealed that the plug had been blown out.

Plate 11a. Oblique aerial view of Mt. Trident, August, 1960, showing the disposition of the 1953-54, 1957, 1958, 1959-60 flows and the north western margin of the 1960 overflow (Photo - Mr. Peterson; courtesy of U.S. National Park Service).

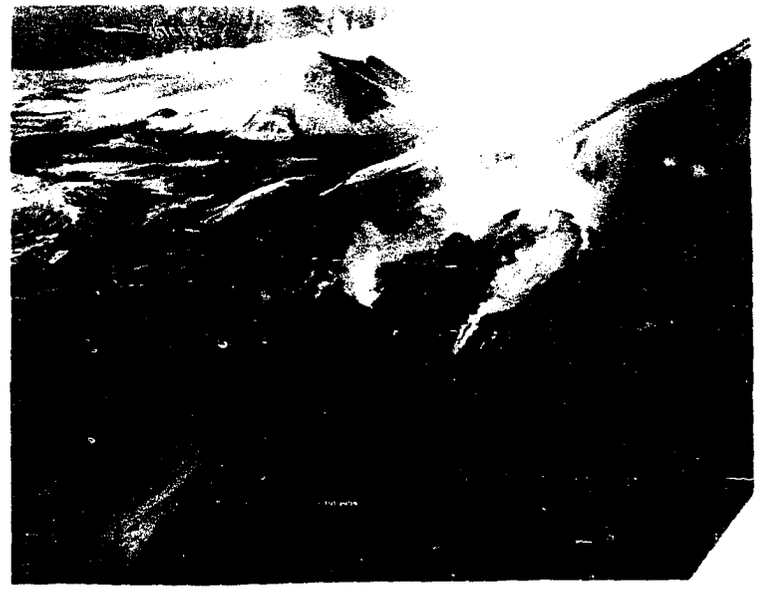

Plate 11b. Oblique aerial photograph of Trident crater, 1961, showing typical development of the vent-plug (Photo - Mr. Peterson; courtesy of U.S. National Park Service).

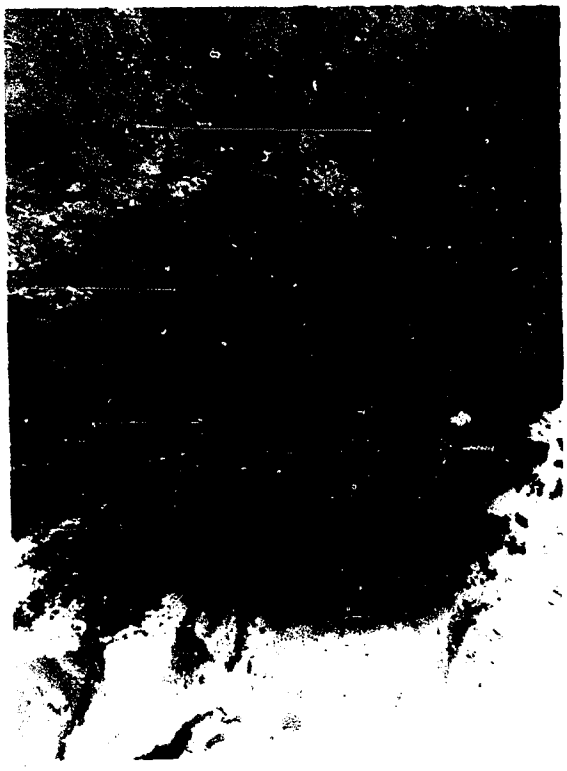

Plate 12. Vertical aerial photograph of Trident crater after the plug was blown out by a vent-clearing explosion in April, 1963 (Photo - Mr. D. Bogart, April 5, 1963, courtesy of U.S. National Park Service).

August 6-7, 1963 - (Decker, op. cit. p. 41). Together with P. Ward, Decker climbed the active crater of Trident and also prepared a sketch of the disposition of the different lavas (ibid. pp. 41-42, fig. 25). He reported that the small crater at 3850 ft on the SW ridge had developed a cone rising to an elevation, of about 4,700 ft. The crater was about 500 ft in diameter and showed heavy fumarolic activity and active solfataras encrusted with molten and crystalline sulphur. Temperatures exceeded 400°F. The flow fronts were steep (30° or more) talus slopes of vitreous porphyritic lavas. The flows near the head were between 100-200 ft thick and appeared to have moved in a highly viscous manner. Decker adds that subsequent to Snyder's observations eruptive activity had added 2 more sq. miles to the area covered by lavas or an addition of about 0.018 - 0.036 cubic mile of lava. According to him the 'black' flow of April 1, 1963 consisted essentially of block and ash avalanche.

November 17, 1963 - Afternoon - An explosive eruption took place. Ray Loesche, flying 30 miles from Trident was shaken by this. This was followed by a 10-minute growth of a large smoke column. Air Force radar installation estimated the height of cloud at 35,000 ft. (Decker, op. cit. p. 42 - information collected from Anchorage News Paper reports).

1964:

May 31, 1964 - 4:30 p.m. - Brooks Camp observed Trident eruption. The mushroom shaped cloud formed. Ash was spread all over Mt. Martin. The cone was breached and volcanic bombs were reported (Kent Smith, Ranger Naturalist, U.S.N.P.S.).

APPENDIX II

METHODS OF MINERAL SEPARATION

Magnetite

Bulk rock specimens were ground to about 100 mesh in a large agate mortar. Magnetite was recovered by a small hand magnet, from a water suspension agitated by vigorous stirring. Large glass beakers (500-1000cc) are usually required at this stage. The hand magnet was held against the outside surface of the beaker. Magnetite clings to the beaker wall near the magnet, and are easily separated from the non-magnetic fraction. After washing and drying at room temperature (∿ 70°F), further grinding of this magnetite concentrate was carried out in an agate mortar to ∿400 mesh, and the process described above was repeated using a smaller beaker and distilled water. This procedure was repeated at least four times for each sample. The samples, thus obtained, were about 96% pure. An acetone wash before final drying was found useful. The above method of magnetite separation, developed by Dr. T. Katsura, provides high purity magnetite samples.

Two or three samples of magnetite were prepared from most specimens for comparative chemical analysis.

Pyroxene and Groundmass Glass

Moderately thin slices were cut from the rock specimen, and oxidized zones and inclusions were eliminated. The slices were then ground in a mechanical mortar, and the sample was then washed and dried at room temperature (∿ 70°F). The (-100) - (+200) mesh fraction was recovered for separation of pyroxenes and glassy mesostasis. Magnetite was eliminated from this fraction in the low intensity magnetic separator, and the fraction was then run through Franz Isodynamic separator to eliminate the feldspathic

constituents. Pyroxenes were recovered from the magnetically susceptible concentrate (consisting chiefly of pyroxenes, rare olivine and glassy mesostasis with adherent plagioclase fragments) by progressive heavy liquid separations; bromoform followed by tetrabromoethane (sp. gr.- 2.9). The pyroxene concentrate was chiefly contaminated by magnetite rich groundmass material. The bromoform float was chiefly composed of glassy mesostasis with plagioclase and rare pyroxenes.

The pyroxene concentrate was washed, dried and ground lightly in an agate mortar to 180-200 mesh. This was followed by a steady rolling between two glass plates and finally a five-minute-dil. HCl wash. These stages were necessary to disaggregate compound grains, and to remove the iron-oxide stains and adherent magnetite. The final separation of the two pyroxenes in the Franz separator was preceded by a final cleaning with tetrabromoethane.

For separating ortho - vs clinopyroxenes, the most effective tilts of the Franz separator tray were found to be 17° toward west and 21° toward north. Concentrates up to 0.3 amp. were largely composed of impurities (stained and compound grains; olivine and groundmass charged groundmass). Orthopyroxene was obtained as the magnetic concentrate in the 0.3 - 0.4 amp. range and clinopyroxene was obtained as the magnetic concentrate in the 0.5 - 0.6 amp. range. The middling fraction obtained between 0.4 and 0.5 amp. was a mixture of the two types plus compound grains. The tails were mostly impure feldspathic fractions.

In the Franz separator the feed rate must be slow, and the pyroxene separates were further purified by successive runs in the Franz separator with minor current adjustments.

The lighter fraction, as previously obtained, was subjected to mild grinding in the agate mortar to disaggregate the adherent grains. The sample was then washed and dried. Heavy liquid separation with a mixture of bromoform and acetone (sp. gr. - 2.5) floated the glassy mesostasis away from heavier impurities. This separation was repeated several times to obtain samples of groundmass glass of suitable purity.

Plagioclase (Phenocrystal and Groundmass Phases).

Based on the size of the phenocrysts, thin slices from the rock specimen, devoid of oxidized sections and inclusions, were crushed in a steel mortar, and the (30-50) or (50-80) mesh fractions were extracted. This size range was found to be optimum for the separtion of phenocrystal vs groundmass plagioclase. The phenocryst fragments were picked by tweezers, and again ground to about 100-150 mesh. The sample was finally cleaned in the Franz separator.

This fraction consisted of fragments of plagioclase phenocrysts and fragments composed of groundmass plus bits of ferromagnesian phenocrysts, plagioclase and magnetite. The latter fragments are weakly magnetic and can be separated from fragments of plagioclase phenocrysts by a hand magnet. However, cleaning was done with a tweezer, and grains which did not visibly contain any felspar fragment were picked up and ground to about 200 mesh. After washing and drying this sample was run through the Franz separator to collect the groundmass plagioclase fraction as tailings. The last traces of adherent non-magnetic colorless glass fractions were eliminated by heavy liquid separation (mixture of bromoform and acetone - sp. gr. - $\sim$ 2.5). In specimens with predominantly colorless and non-magnetic glass, the last step had to be repeated several times to obtain samples of suitable purity.

REFERENCES

Akimoto, S., E. Komada and I. Kushiro, 1966, Preliminary experiments on the stability of natural pigeonite and enstatite, Proc. Jap. Acad., 42, 482-487.

Atlas, L. 1952, The polymorphism of $MgSiO_3$ and solid state enquilibria in the system $MgSiO_3$-$CaMgSi_2O_6$, Jour. Geol., 60, 125-147.

Aubouin, J., 1965, Geosynclines, Elsevier Pub. Co., Amsterdam.

Barth, T. F. W., 1951, Subsolidus diagram of pyroxenes from common mafic magmas, Norsk. Geol. Tidsskr., 29, 218-221.

Barth, T. F. W., 1962, Theoretical Petrology, John Wiley & Sons, New York.

Beloussov, V. V., 1962, Basic Problems in Geotectonics, McGraw-Hill Book Co., New York.

Benioff, H., 1951, Earthquakes and rock creep, Part. I - Creep characteristics and the origin of aftershocks, Bull. Seism. Soc. Amer., 41, 31-62.

Berg, E., J. Kienle and S. Kubota, 1966, Preliminary determination of crustal structure in the Katmai National Monument, Alaska, (Abstract), Amer. Geophys. Un. Meeting, August, 1966, Oregon, USA.

Bordet, P., G. Marinelli, M. Mittempergher and H. Tazieff, 1963, Contribution a l'etude volcanologique du Katmai et de la Vallee de dix Mille Fumees, Alaska, Mem. Soc. Belg. Geol. Paeontol. Hydrol., 8°, nr. 7, 1-114.

Bowen, N. L., J. F. Schairer, and E. Posnjak, 1933, The system CaO-FeO-SiO_2, Amer. Jour. Sci., 5th Ser., 26, 193-284.

Boyd, F. R. and J. L. England, 1965, The rhombic enstatite - clinoenstatite inversion, Carnegie Inst. Wash. Year b.64, 117-120.

Boyd, F. R. and J. F. Schairer, 1962, The system $MgSiO_3$-$CaMgSiO_3$, ibid, 61, 68-75.

Brown, G. M., 1957, Pyroxenes from the early and middle stages of fractionation of the Skaergaard intrusion, East Greenland, Miner Mag., 31, 511-543.

Brown, G. M., 1960, The effect of ion substitution on the unit cell dimensions of the common clinopyroxenes, Amer. Mineral, 45, 15-38.

Buddington, A. F. and D. H. Lindsley, 1964, Iron-titanium oxide minerals and synthetic equivalents, Jour. Petrol., 5, 310-357.

Burk, C. A., 1965, Geology of the Alaska Peninsula - Island Arc and Continental Margin, Pts. 1, 2 and 3, Mem. Geol. Soc. Amer. 99.

Burnham, C. W., 1965, Ferrosilite, Carnegie Inst. Wash. Yearb. 64, 202-204.

Carstens, H., 1958, Note on distribution of some minor elements in co-existing ortho- and clino-pyroxenes, Norsk. Geol. Tidsskr., 38, 257-60.

Chayes, F., 1965, On the level of silica saturation in andesite, Carnegie Inst. Wash. Year b. 64, 155-9.

Chudoba, F. F., 1933, The determination of the feldspars in thin section (Trans. W. Q. Kennedy), Murby, London.

Chudoba, F. F. and J. Frechen, 1943, Der Einfluss der Temperatur auf die Beziehung zwischen Optik und Chemismus der Olivine, N. Jahrb. Min. Monats. Abt. A., 91-98.

Clark, S.P.,J.F. Schairer and John de Neufville, 1962, Phase relations in the system $CaMgSi_2O_6$ at low and high pressures, Carnegie Inst. Wash. Year b.61, 59-68.

Curtiss, G. H., 1955, Importance of Novarupta during eruption of Mt. Katmai, Alaska (Abstract), Bull. Geol. Soc. Amer., 66, 1547.

Daly, R. A., 1933, Igneous rocks and depths of the earth, McGraw-Hill Book Co., New York.

David, I. and A. J. E. Welch, 1956, The oxidation of magnetite and related spinels. Constitution of gamma ferric oxide, Trans. Faraday Soc., 52, 1642.

Decker, R. W., 1963, Proposed volcano observatory at Katmai National Monument, a preliminary study (Unpublished report with Geophysical Institute, University of Alaska.)

Deer, W. A.,R. A. Howie and J. Zussman, 1962-63, Rock forming minerals,Vol. 2- Chain silicates, Vol.3-Framework silicates and Vol.5-Non-silicates, John Wiley & Sons, New York.

Eaton, J. T. and K. J. Murata, 1960, How volcanoes grow, Science, 132, 925-38.

Eicher, G. J. and G. A. Rounsefell, 1957, Effects of lake fertilization by volcanic activity on abundance of salmon, Limn. Oceanog., 2, 70-6.

Fenner, C. N., 1920, The Katmai region, Alaska and the great eruption, of 1912, Jour. Geol., 28, 569-606.

Fenner, C. N., 1923, The origin and mode of emplacement of the great tuff deposit in the Valley of Ten Thousand Smokes, Nat. Geog. Soc., Cont. Tech. Pap. 1, 1-74.

Fenner, C. N., 1926, The Katmai magmatic province, Jour. Geol., 34, 673-772.

Fenner, C. N., 1948, Immiscibility of igneous magmas, Amer. Jour. Sci., 246, 465-487.

Fenner, C. N., 1950, The chemical kinetics of the Katmai eruption, Pt. II, ibid. 248, 697-725.

Green, T. H. and A. E. Ringwood, 1966, Origin of the calc-alkaline igneous rock suite, Petrology of the Upper Mantle, Dept. Geophys. Geochem., Austr. Nat. Univ., Publ. No.444, 105-17.

Griggs, R. F., 1922, The Valley of Ten Thousand Smokes, Nat. Geog. Soc.,

Groves, A. W., 1935, The Charnockite series of Uganda, British East Africa, Quart. Jour. Geol. Soc. London, 91, 150-207.

Hess, H. H., 1949, Chemical compositions and optical properties of common clinopyroxenes, Pt. 1, Amer. Mineral., 34, 621-66.

Hess, H. H., 1952, Orthopyroxenes of the Bushveld type, ion substitutions and changes in unit cell dimensions, Amer. Jour. Sci., Bowen volume, 173-87.

Holmes, A., 1932, The origin of igneous rocks, Geol. Mag., 69, 543-58.

Hori, F., 1954, Effects of constituent cations on the optical properties of the clinopyroxenes, Sci. Pap., Coll. Gen. Ed., Univ. Tokyo, 71-83.

Howie, R. A., 1963, Cell parameters of orthopyroxenes, Min. Soc. Amer., Sp. Pap. 1, 213-22.

Katsura, T., 1964, Generalized titanomagnetite in Hawaiian volcanic rocks, Pac. Sci., 18, 223-8.

Katsura, T. and I. Kushiro, 1961, Titanomaghemite in igneous rocks, Amer. Mineral., 46, 134-45.

Keller, A. S. and H. N. Reiser, 1959, Geology of the Mt. Katmai area, Alaska, Bull. U.S. Geol. Surv. 1058-G, 261-98.

Kosminskaya, I. P., S. M. Zverev, P. S. Veitsman, Yu. V. Tulina and R. M. Krakshina, 1963, Basic features of the crustal structure of the sea of Okhotosk and the Kurile-Kamchatka zone of the Pacific Ocean from deep seismic sounding data, Izv. Geophys. Ser. (Eng. trans.), 11.

Kretz, R., 1961, Some applications of thermodynamics to coexisting minerals of variable composition, examples: orthopyroxene-clinopyroxene and orthopyroxene-garnet, Jour. Geol., 69, 361-87.

Kuno, H., 1950, Petrology of Hakone volcano and adjacent areas, Japan, Bull. Geol. Soc. Amer., 61, 957-1020.

Kuno, H., 1952, Cenozoic volcanic activity in Japan and surrounding areas, Trans. New York Acad., Sci., Ser. 2, 14, 225-31.

Kuno, H., 1953, Formation of calderas and magmatic evolution, Trans. Amer. Geophys., Un., 34, 267-80.

Kuno, H., 1954a, Geology and petrology of Ōmuro-Yama volcano group, north Izu, Jour. Tokyo Univ. Fac. Sci., Sect. 2, 9, 241-65.

Kuno, H., 1954b, Study of orthopyroxenes from volcanic rocks, Amer. Mineral, 39, 30-46.

Kuno, H., 1955, Ion substitution in the diopside-ferropigeonite series of clinopyroxene, Amer. Mineral, 40, 70-93.

Kuno, H., 1960, High alumina basalt, Jour. Petrol. 1, 121-45.

Kuno, H., 1965, Fractionation trends of basalt magmas in lava flows, Jour. Petrol., 6, 302-21.

Kuno, H. and H. H. Hess, 1953, Unit cell dimensions of clinoenstatite and pigeonite in relation to other common clinopyroxenes, Amer. Jour. Sci., 251, 741-52.

Kushiro, I., 1959, Preliminary note on alkali dolerite of Atumi district, northern Japan, Jap. Jour. Geol. Geog., 30, 259-72.

Kushiro, I., 1960, Si-Al relations in clinopyroxenes from igneous rocks, Amer. Jour. Sci. 258, 548-54.

Kushiro, I., 1962, Clinopyroxene solid solutions, Pt.I- The $CaAl_2SiO_6$ component, Jap. Jour. Geol. Geog., 33, 213-226.

Kushiro, I., 1965a, The liquidus relations in the systems Forsterite-$CaAl_2SiO_6$-Silica and Forsterite-Nepheline-Silica at high pressures, ibid, 64, 103-9.

Kushiro, I., 1965b, The coexistence of Nepheline and Enstatite at high pressure, ibid., 109-12.

Larsen, E. S., J. Irving, F. A. Gonyer, and E. S. Larsen III, 1936,38, Petrologic results of a study of minerals from the Tertiary volcanic rocks of the San Juan region, Colorado, Amer. Mineral, 21, 679-701, 23, 227-57.

Lewis, J. F., 1960, The occurrence of orthopyroxenes with low optic axial angle, Amer. Min eral, 45, 1125-6.

Lindsley, D. H, 1965a, Iron-titanium oxides, Carnegie Inst. Wash. Yearb. ibid., 64, 144-8.

Lindsley, D. H., 1965b, Ferrosilite, ibid., 148-50.

MacDonald, G. A. and T. Katsura, 1964, Chemical composition of Hawaiian lavas, Jour. Pterol., 5, 82-133.

McIntyre, W. L., 1963, Trace element partition coefficients - a review of theory and applications to geology, Geochem. Cosmochem. Acta, 27, 1209-64.

Morimoto, N., 1959, The structural relations among three polymorphs of $MgSiO_3$- enstatite, protoenstatite and clinoenstatite, Carnegie Inst. Wash. Yearb.58, 197-8.

Muan, A. and E. F. Osborn, 1956, Phase equilibria at liquidus temperatures in the system MgO-FeO-Fe_2O_3-SiO_2, Jour. Amer. Ceram. Soc., 39, 121-40.

Muir, I. D., 1951, The clinopyroxene of Skaergaard intrusion, eastern Greenland, Miner. Mag., 29, 690-714.

Muir, I. D.,C. E. Tilley and J. H. Scoon, 1957, Contributions to the petrology of Hawaiian basalts, I. The picrite basalts of Kilauea, Amer. Jour. Sci., 255, 241-53.

Nockolds, S. R., 1954, Average chemical compositions of some igneous rocks, Bull. Geol. Soc. Amer., 65, 1007-32.

Nockolds, S. R., and R. Allen, 1953, The geochemistry of some igneous rock series, Geochim. Cosmochim. Acta, 4, 105-42.

Ödman, O. H., 1932, Mineragraphic study on the opaque minerals in the lavas from Mt. Elgon, British East Africa, Geol. Fören. i Stockholm Förh. 54, 285-304.

Osborn, E. F., 1959, Role of oxygen pressure in the crystallization and differentiation of basaltic magmas, Amer. Jour. Sci., 257, 609-47.

Pauling, L., 1960, Nature of the chemical bond, Cornell Univ. Pr, 2nd. Ed.

Payne, T. G., 1955, Mesozoic and Cenozoic tectonic elements of Alaska, Misc. Geol. Inv. Map I-84, U.S. Geol. Surv.

Ramberg, H. and G. DeVore, 1951, The distribution of Fe^{++} and Mg^{++} in co-existing olivines and pyroxenes, Jour. Geol., 59, 193-21.

Ramdohr, P., 1940, Die Erzmineralen in gewöhnlicken magmatischen gesteinen, Abh, Preuss. Akad. Wiss. Math.-naturw. kl.

Sclar, C. B., L. C. Carrison and C. M. Schwartz, 1964, High pressure stability field of clinoenstatite and orthoenstatite-clinoenstatite transition, (Abstract), Trans. Amer. Geophys. Un. 45, 121.

Shimozuru, D., 1963, Poisson's ration of rocks at high temperature, seismological application, Geophysical Papers dedicated to Prof. K. Sassa, 517-521.

Shor, G. G., 1964, Structure of the Bering Sea and the Aleutian ridge, Mar. Geol., 1, 213-219.

Snyder, G. L., 1954, Eruption of Trident volcano, Katmai National Monument, Alaska, U.S. Geol. Surv. Circular 318, 1-7.

Spurr, J. E., 1900, A reconnaissance in southwestern Alaska in 1898, 20th. Ann. Rept., U.S. Geol. Surv., Pt. 7, 43-263.

Taylor, S. R. and A. J. R. White, 1965, Geochemistry of Andesites and the growth of the continents, Nature, 208, 271-274.

Thornton, C. P. and O. F. Tuttle, 1960, Chemistry of igneous rocks, I. Differentiation Index, Amer. Jour. Sci., 258, 664-84.

Tilley, C. E., 1950, Some aspects of magmatic evolution, Quart. Jour. Geol. Soc. London, 106, 37-61.

Tilley, C. E., and J. H. Scoon, 1961, Differentiation of Hawaiian basalts, Trends of Mauna Loa and Kilauea historic magma, Amer. Jour. Sci. 259, 60-68.

Tilley, C. E., H. S. Yoder Jr. and J. F. Schairer, 1965, Melting relations of volcanic tholeiite and alkali rock series, Carnegie Inst. Wash. Year b.64, 69-82.

Trögger, W. E., 1956, Optische Bestimmung der gesteinsbildenden minerale, Teil 1, 2 aufl., E. Schwiz. Verlags, Stuttgart.

Turner, F. J. and J. Verhoogen, 1960, Igneous and metamorphic petrology, McGraw-Hill Book Co., New York.

Wager, L. R., 1956, A chemical definition of fractionation stages as a basis for comparison of Hawaiian, Hebridean and other basic lavas, Geochim. Cosmochim. Acta, 9, 217-48.

Wager, L. R., 1960, The major element variation of the layered series of the Skaergaard intrusion and a reestimation of the average composition of the hidden layered series and the successive residual magmas, Jour. Petrol., 1, 364-98.

Waters, A. C., 1955, Volcanic rocks and the tectonic cycle, Sp. Pap. Geol. Soc. Amer. 62, 703-22.

Wilcox, R. E., 1954, Petrology of the Paricutin volcano, Bull. U.S. Geol. Surv., 965-C, 281-349.

Wilkinson, J. F. G., 1957, The clinopyroxene of a differentiated Teschenite sill near Gunnedah, New South Wales, Geol. Mag., 94, 123-34.

Williams, H., 1954, Preliminary notes on geological work done on Mt. Katmai and in the Valley of Ten Thousand Smokes, Int. Rept. by Luntey, U.S. Nat. Park Serv., 55-61.

Winchell, A. N. and H. Winchell, 1964, Elements of optical Mineralogy, Pt. 2, John Wiley & Sons, New York.

Wyckoff, R. W. G., 1960, Crystal Structures, 3, Chap. XII, 78, Interscience Pub., New York.

Yagi, K., 1953, Petrochemical studies on the alkalines rocks of the Morotu district, Sakhalin, Bull. Geol. Soc. Amer., 64, 769-810.

Yamaguchi, M., 1964, Petrogenic significance of ultrabasic inclusions in basaltic rocks from southwest Japan, Mem. Fac. Sci., Kyushu Univ., Ser. D. Geol., 15, 163-219.

Yoder, H. S. Jr., and C. E. Tilley, 1957, Basalt magmas, ibid., 56,156-61.

Yoder, H. S. Jr., and C. E. Tilley, 1962, Origin of basalt magmas: an experimental study of natural and synthetic rock systems, Jour. Pterol., 3, 342-532.

Yoder, H. S. Jr., C. E. Tilley, and J. F. Schairer, 1963, Pyroxenes and associated minerals in the crust and mantle, Carnegie Inst. Wash. Year b.62, 84-95.

Yoder, H. S. Jr., C. E. Tilley, and J. F. Schairer, 1964, Osothermal sections of pyroxene quadrilateral, ibid., 63, 121-9.